

TECHNOLOGICAL ASPECTS
OF QUANTUM DECOHERENCE
IN SUPERCONDUCTING JOSEPHSON QUBITS

by

Alessandro Bruno

SUBMITTED IN FULFILLMENT OF THE REQUIREMENTS FOR THE
INTERNATIONAL PhD PROGRAM ON
NOVEL TECHNOLOGIES FOR MATERIALS, SENSORS, AND IMAGING (XXIV CYCLE)
AT
UNIVERSITÀ DEGLI STUDI DI NAPOLI "FEDERICO II"
NAPOLI, ITALY
NOVEMBER 30TH, 2011



Coordinator: Prof. A. Andreone

UNIVERSITÀ DEGLI STUDI DI NAPOLI “FEDERICO II”
INTERNATIONAL PhD PROGRAM ON
NOVEL TECHNOLOGIES FOR MATERIALS, SENSORS AND
IMAGING (XXIV CYCLE)

The undersigned hereby certify that they have read and recommend to the examining committee for acceptance a thesis entitled “**Technological aspects of quantum decoherence in superconducting Josephson qubits**” by **Alessandro Bruno** in fulfillment of the requirements for the degree of PHILOSOPHIAE DOCTOR in Novel Technologies for Materials, Sensors, and Imaging.

Dated: November 30th, 2011

Scientific Thesis Supervisor:

Dr. Mikhail Lisitskiy
*Istituto di Cibernetica “Eduardo Caianiello”,
Consiglio Nazionale delle Ricerche, Pozzuoli (Na).*

Part of the experimental activity has been done in the Physics Institute of Karlsruhe Institute of Technology (KIT), Germany, in the group of Prof. Alexey Ustinov.

To my Family

Table of Contents

Table of Contents	iv
1 Quantum Computation: An introduction	1
1.1 Superconducting Quantum Bits	10
1.2 Phase Qubit	13
1.2.1 Flux-Biased Phase Qubit	13
1.2.2 Qubit Operation	18
2 Decoherence	22
2.1 External Sources	28
2.1.1 Control Lines	28
2.1.2 Bias Noise	28
2.1.3 Back Action	29
2.1.4 Sample Box Resonances	30
2.1.5 Electromagnetic and Thermal Baths	31
2.1.6 Other External Sources	32
2.2 Intrinsic Sources	33
2.2.1 Quasiparticle Dissipation	33
2.2.2 Critical Current Fluctuations	34
2.2.3 Flux Noise	36
2.2.4 Charge Noise	37
2.2.5 Surface Losses	39
2.2.6 Capacitive Coupling	39
2.2.7 Insulating Material Losses	40
2.2.8 Coupling to Discrete TLS	42
2.2.9 Other Intrinsic Sources	44
2.3 Theories	46
2.3.1 TLSs	46

2.3.2	Quasiparticles	51
2.3.3	Surface Spins	53
2.3.4	Metal-Induced Gap States	56
3	Qubit's Materials Research - State of the Art	57
3.1	Substrates and its Treatments	59
3.2	Superconductors	64
3.3	Dielectrics	66
3.4	Tunnel Barriers	69
3.5	Oxides and Interfaces of Superconductors	72
4	Hydrogenated Amorphous Silicon	82
4.1	a-Si:H	84
4.1.1	Material Analysis	86
4.2	Integration in Nb Technology	92
4.2.1	Nb:H - Superdiffusion	94
4.3	Results and Discussion	97
4.4	Conclusions	104
5	Superconducting Resonators	106
5.1	Resonator's Model	107
5.1.1	Quality Factors and Losses	109
5.2	Lumped Element Resonators	116
5.2.1	Design and Simulations	121
5.2.2	Measurement Technique	124
5.2.3	Fabrication	126
5.3	Results	129
6	Josephson Junctions for Qubit Devices	137
6.0.1	Junction Design	138
6.0.2	Trilayers	140
6.0.3	Characterization and Results	144
6.0.4	Junction Fabrication Perspectives	149
7	Qubit Design	154
7.1	Layout Project	155
7.1.1	The On-Chip Experiments	157
7.2	Dimensioning	157
7.2.1	Qubit's Loop and Junction	160

7.2.2	Isolation by Impedance Transformation	162
7.2.3	Read-out DC SQUID	165
7.2.4	Flux Bias	168
7.2.5	Microwave Transmission Line	171
7.2.6	Shunt Capacitor	172
8	Qubit Fabrication	174
8.1	Substrates	175
8.2	Trilayers	178
8.3	Junctions and Base Layer	179
8.4	a-Si:H liftoff	180
8.5	Wiring	185
8.6	Preliminary Test of Fabricated Qubits	185
9	Conclusions	189
	Bibliography	194

Acknowledgements

My doctoral thesis derived from the collective guidance and contribution of many people. I have been fortunate to work with Researchers, Professors, postdocs, and graduate students, who have educated, stimulated, pushed and supported me during my time at ICIB-CNR. As a graduate student, I grew both academically and personally and I am grateful to have had such a challenging experience. I would like to first thank my scientific research advisor Dr. Mikhail Lisitskiy for the opportunity to be a part of his research group. He is truly a generous advisor and educator. I have acquired a tremendous amount of knowledge and real-field experience from his deep understanding of solid state physics, particularly superconducting Josephson junction devices. I value his kind nature and positive attitude that he has provided within our research topic as well as in the ICIB-CNR community. My experience with him represent for me a lasting education in academic research and beyond. At ICIB-CNR, I had the opportunity to work directly with, and learn from, a group of great scientists. I want to kindly thank Dr. Maurizio Russo, for having given me the opportunity to work in the ICIB-CNR laboratories and for his financial help in the critic moments of the research, when everything seems lost; Dr. Berardo Ruggiero, for his unvaluable strategic support and wise guidance; Dr. Roberto Russo, for having always paused his activities to answer my many questions on Physics (but not only on that), and especially for having listened to my most bizarre ideas; Dr. Roberto Cristiano, for the interesting conversations we had; Dr. Carmine Granata and Ing. Antonio Vettoliere, for their support and competence in the manufacture processes;

Dr. Emanuela Esposito, for the beautiful course she held and for the sincere help she gave me; Dr. Ettore Sarnelli, for the great sailboat teachings he gave me; Dr. Carlo Camerlingo for the help with Raman analysis of a-Si:H films.

Moreover, I had the great opportunity to spend several month at the Karlsruhe Institute of Technology, Germany. Professor Alexey Ustinov offered me the best opportunities to develop the common research activities. There in Germany, not only I met many serious scientist and wise researchers, but I found also sincere friends, as Sebastian Skacel and Jürgen Lisenfeld.

During the PhD activities I have established a wide network of collaborations, and I want to thank all the people that, in a way or in another, helped me to achieve the results presented in this thesis: P. Delli Venieri and L. V. Mercaldo (ENEA, Portici), M. Iodice and G. Coppola (IMM, Napoli), U. Coscia and G. Ambrosone (UNINA-INFN, Napoli), D. K. Basa (Utkal University, Bhubaneswar, India), and P. Mengucci (University of Ancona).

Furthermore, I want to share this great moment in my life with all my friends, without their help and support this work would surely not have been possible;

I would like to thank my parents Federico, and Laura Taddei, and my sister, Teresa, for their unconditioned endless love and encouragement throughout my endeavor: their constant support made what I am today. For that, I am forever indebted to them.

Finally, a special and sweet thank is for my wife Hsin-Yi Chien that, with her care and determination, was able to give me the best gift of my life: Love.

Abstract

The aim of this thesis was to realize superconducting quantum bits by using novel fabrication techniques and materials in order to enhance the coherence time of the former devices. For the system to be studied we chose the flux-biased phase qubit, which consists of a Josephson junction integrated in a superconducting loop. This qubit realization has some advantages, which make it an ideal test-bed for different fabrication technologies and materials. Relatively large Josephson junctions can be used in the phase qubit realization, which are easy to be fabricated by using standard lithographic technology with the flexibility of employing various fabrication techniques and materials.

The coherence of current-generation of superconducting qubits seems to be limited by intrinsic sources of noise and energy loss, related to materials' defects (two-level systems, TLSs) on the surfaces and interfaces of the superconducting films, and in the bulk of the dielectric films used for the microelectronic realization of the circuits.

For this reason, we aimed our research activities on the realization of low loss dielectrics (a-Si:H), on its integration with Josephson junction technologies, on the protection of the superconducting films' surfaces from unwanted contamination, and on the optimization of the circuit design and fabrication processes.

Chapter 1

Quantum Computation: An introduction

A simplified view of the history of computing shows that computing was thought of mainly as mental processes in the 19th century; it was then thought of mainly as machine processes in the 20th century, and it is now thought of mainly as Nature processes in the 21st century.

A calculus process is, in fact, essentially a physical process, which can be executed on a hardware (no matter if mechanical, electronic or biological) and which obeys to certain physical laws. The classical computation theory is based on the abstract Turing Universal Machine, introduced by Alan Turing in 1936 and successively elaborated by John von Neumann in the years Forty. The principles and the functioning rule-set of the original Turing Universal Machine, representing an ideal mechanical device which computes in accordance to the laws of classical physics, are still the basic ones that govern even the most sophisticated computing technologies known nowadays.

In 1965, shortly after the advent of the integrated circuits (the hardware of modern

calculus tools), Intel Chairman Gordon Moore predicted that the number of transistors on a chip would double approximately every two years. Since the introduction of "Moore's Law", there have been two constants: predictions that the end of Moore's Law is just around the corner, and the semiconductor industry proving those predictions to be wrong by producing ever smaller transistors. Presently, there are three fundamental approaches which could in principle be pursued in order to increase the computational speed of a physical computing system: traditional transistor computing, molecular computing, and quantum computing.

The traditional approach has been to push microelectronic-transistor sizes to smaller and smaller gate-length scales. Current generation of Intel Tri-Gate transistor has gate lengths of 22 nm [102]; next generation Si CMOS (Complementary Metal-Oxide-Semiconductor) n-gate lengths will soon migrate to less than 10 nm. None the less, few would argue that the present astonishing rate of progress in computer speed and power can continue forever without major enhancements in fabrication technology. Multiple revolutionary developments in integrated circuit technology will be needed to maintain the present rate of growth of computational power in the next decade. The microelectronics industry faces several engineering obstacles as it continues to minimize device dimensions. Most importantly, reducing feature sizes presents an obstacle of a fundamental nature; classical physics-rules can not correctly describe the behavior of an electronic system as the device lengths shrink to near atomic scales. At these dimensions, the world of quantum mechanics begins to emerge as an unavoidable problem, and such an electronic system starts to behave quantum-mechanically.

Ideas and inspiration coming from the observation of the natural world had always represented an unvaluable tool, both in science and in computing, to find new solutions. For example, there have been many attempts in order to understand, mimic and harness the information-processing tools and power of the brain. Already finite automata have been developed as an abstraction of neuron activities, while neural

networks represent another model inspired by the brain; information processing of genetic mechanisms is a further source of inspiration. All these attempts are of interest and importance.

In accordance with the modern knowledge of Nature, it is possible to conclude that two radical approaches are the only feasible ways to increasing computational speed: *molecular computing*, based on the parallel time-evolution of huge number of suitably prepared and controlled molecules (such as DNA or organic solutions), and *quantum computing*, which relies inherently on the physical principles of quantum mechanics, namely superposition, interference, and entanglement.

Our world is, at least for our most accurate experimental observations, a quantum mechanical one. It is therefore natural, necessary, interesting, and important to explore the foundations and potentials of quantum-information processing. At the same time, the technologies and methods that allow the experimental realization of quantum-information processing systems should be explored.

Quantum computing is a very new, fascinating, promising, and puzzling scientific adventure, in which two of the most significant developments in science and technology of the 20th century, quantum mechanics and informatics, merge and mutually influence each other. An adventure, that may lead not only to the computer revolution, but also to a new scientific and technological basis for information processing in the 21st century.

A quantum bit, or qubit, is a quantum two-level system which can be in the two states $|0\rangle$ and $|1\rangle$, just as a classical bit can be in the two states 0 and 1 [168]. The difference between bits and qubits is that a qubit can be in a state other than $|0\rangle$ or $|1\rangle$: it is possible to form a linear combination of states, called superposition

$$|\Psi\rangle = \alpha|0\rangle + \beta|1\rangle \tag{1.0.1}$$

The numbers α and β are complex numbers, so that the state of a qubit is a vector in a complex vector space. The special states $|0\rangle$ and $|1\rangle$ are known as computational

basis states and form an orthonormal basis for this space (as visible from the Bloch-sphere representation of Fig. 2.1).

At the heart of quantum information processing lies quantum-mechanical entanglement. This property can be summarized by the idea that entangled objects are such that the state of one part of the system cannot be described in the absence of knowledge of the other parts. These linkages allow the phase space of available states in a quantum computer to grow exponentially without a similar growth in computing resources.

The first suggestions to exploit quantum mechanics in a (partially abstract) calculus device are due to P. Beinhoff in 1980, and to his speculations on the Reversible Turing Machine: a computation can always be executed backwards, so that it is possible to get to the initial state running back through the intermediate computational steps. Subsequently, R. Feynmann [76] demonstrated that no classic Turing Machine is capable of simulating certain physical (quantum) phenomena without incurring in an exponential decrease of its performances. On the contrary, Feynmann proposed that an Universal Quantum Simulator could perform such a simulation in a perfectly efficient way. In 1985 D. Deutsch [57] formalized these ideas in his Universal Quantum Turing Machine, representing the abstract model on which the modern theory of quantum computing is based.

However, it is only when practical quantum algorithms were proposed that the official scientific interest focused on quantum possibilities and on the reviewed notion of tractability in the field of computational complexity. In fact, the attraction of quantum computation lies in the existence of quantum algorithms that are in some cases exponentially faster than their best known classical equivalents.

Most famous are Shor's factoring algorithm [206] and Grover's search algorithm [90], demonstrating respectively that classically intractable problems (as number factorization) can be efficiently solved in a polynomial time, and that new and faster search algorithm schemes are possible. There has also been extensive work on the use of a quantum computer to simulate quantum physics [76, 137, 27, 215, 33], to execute

adiabatic algorithms [73, 38, 12] and quantum algorithms for differential equations [222], to find eigenvalues [2, 105], to perform numerical integration [3] and various problems in group theory [114, 159, 75] and knot theory [221, 252].

Since then, enormous efforts have been done towards the physical realization of such algorithms in a quantum-hardware based device, but only with very little and non scalable results. The technological challenge is still open and with no particular favorites.

D. P. DiVincenzo [61] clearly elucidated five criteria which must be satisfied by any quantum hardware in order to perform a useful quantum computation:

1. qubits should be clearly identifiable (constituting an enumerable Hilbert space) and it should be possible to scale them up in number;
2. it should be possible to initialize the state of the qubits to a simple fiducial state such as $|0000\dots 0\rangle$ (*e.g.* the ability to prepare them in their thermal ground state);
3. the qubits should have long relevant decoherence times, much longer than the gate-operation time, so that error correction techniques may be used in a fault tolerant manner (an approximate benchmark is a fidelity loss of 10^{-4} per elementary quantum-gate operation);
4. it should be possible to realize a universal set of quantum gates through the accurate control of the system's Hamiltonian, and thus to efficiently couple the qubits;
5. it should be possible to perform quantum measurements of the qubit state, in order to obtain the result of the computation.

Any candidates for quantum computing hardware should be assessed against the above DiVincenzo's checklist.

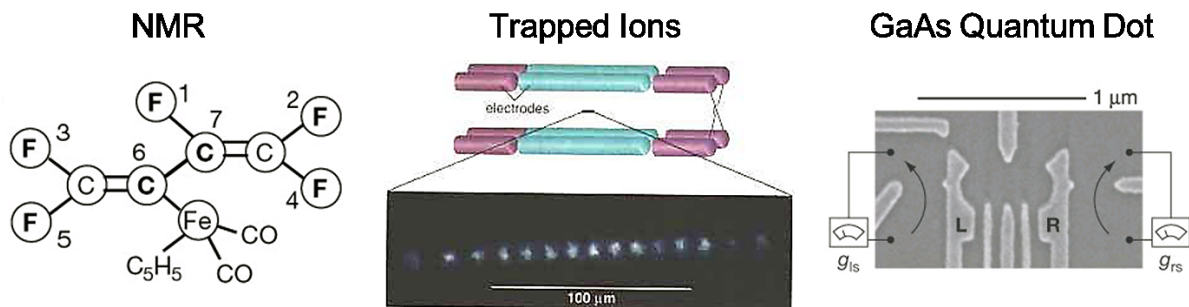


Figure 1.1: Various realization of quantum bits: (left) nuclear spins of molecules in solution (NMR) [229]; (center) trapped ions [43]; (right) electronic spin in quantum dots [106].

Over the last two decades, a number of two-level systems have been examined (theoretically and/or experimentally) as candidates for qubits and quantum computing. These include nuclear spins of molecules in solution (NMR) [83, 48, 229] (Fig. 1.1, left) or in solid state [110], ions in an electromagnetic trap [43, 42, 156] (Fig. 1.1, center), atoms in beams interacting with cavities at optical [113] or microwave frequencies (Cavity QED)[93], states of electrons on superfluid helium [187], linear and non-linear optics with single photons, quantum-Hall systems [190], and electronic [66] and spin states in quantum dots [139] (Fig. 1.1, right).

There are also macroscopic solid state implementations, such as flux states of superconducting circuits [26, 157, 78, 87], charge (single Cooper pair) states of sub-micrometric Josephson junctions [205, 164], phase states across a Josephson junction [149], and hybrid combination of the former such as the quantonium [237], fluxonium [143] and transmon [115].

Table 1.2 shows a comparison of the current performance of various qubit implementations. All these systems score well on some aspects of the DiVincenzo's checklist; however, some open questions remain. In fact, each physical system considered has its inherent advantages and disadvantages.

Usually, atomic, molecular, and optical (AMO) architectures are thought to be more easily isolated from their environment, in such a way to preserve their quantum

Type of Matter Qubit		Coherence			Benchmarking	
		$\omega_0/2\pi$	T_2	Q	1 qbit	2 qbit
AMO	Trapped Optical Ion ($^{40}\text{Ca}^+$)	400 THz	1 ms	10^{12}	0.1%	0.7%*
	Trapped Microwave Ion ($^9\text{Be}^+$)	300 MHz	10 s	10^{10}	0.48% [†]	3%
	Trapped Neutral Atoms (^{87}Rb)	7 GHz	3 s	10^{11}	5%	
	Liquid Molecule Nuclear Spins	500 MHz	2 s	10^9	0.01% [†]	0.47% [†]
Solid-State	e^- Spin in GaAs Quantum Dot	10 GHz	3 μs	10^5	5%	
	e^- Spins Bound to ^{31}P : ^{28}Si	10 GHz	60 ms	10^9	5%	10%
	Nuclear Spins in Si	60 MHz	25 s	10^9	5%	
	NV^- Center in Diamond	3 GHz	2 ms	10^7	2%	5%
	Superconducting Phase Qubit	10 GHz	350 ns	10^4	2%*	24%*
	Superconducting Charge Qubit	10 GHz	2 μs	10^5	1.1% [†]	10%*
	Superconducting Flux Qubit	10 GHz	4 μs	10^5	3%	60%

Figure 1.2: Comparison of the current performance of various qubits, both from AMO (Atomic, molecular, and optical) and solid-state implementations. The approximate resonant frequency of each qubit is listed as $\omega_0/2\pi$; this is not necessarily the speed of operation, but sets a limit for defining the phase of a single qubit. Therefore, $Q = \omega_0 T_2$ is a very rough quality factor, where T_2 is the qubit's dephasing time introduced in chapter 2. Benchmarking values show approximate error rates for single- or multi-qubit gates. Values marked with * are found by state tomography, and give the departure of the fidelity from 100%. Values marked with \dagger are found with randomized benchmarking. Other values are rough experimental gate-error estimates. Figure from arXiv:1009.2267.

state for longer time, but they lack of the possibility to scale up the interacting-qubit number without a tremendous technological effort.

Rather than relying on fundamental, naturally-occurring quantum systems such as spins, atoms, or photons, superconducting qubits are engineered circuits that consist of macroscopic objects (constituted of hundreds of trillions of atoms and visible with naked eyes), but that exhibit collective quantum behavior which makes them usable as qubits. The two key features are the superconductivity, which is a collective quantum behavior of many electrons that allows the entire circuit to be treated quantum mechanically, and the Josephson effect, which gives the strong nonlinearity required to make an effective two-level system (or qubit).

However, macroscopic objects have a large number of internal degrees of freedom, therefore making it difficult to preserve the coherence of the quantum system.

As will be shown in details in chapter 2, one of the greatest technical challenges to be overcome in realizing a quantum computer is the preservation of quantum coherence during the computation process; interaction with any external system or environment destroys this coherence.

The major problem of large scale quantum circuits is the interaction of the surrounding environment with the quantum components, leading to irreversible loss of information (its uncontrolled transfer to the environment), this process is called decoherence.

It is generally accepted that at least 10^4 gate operations must be completed before the effects of decoherence become significant for an error-free quantum computer [62]. This constraint is driving research efforts in Josephson junction devices in order to increase the coherence time by investigating both the environmental noise and the intrinsic noise in the quantum system. Although the time over which the coherence can be maintained is at present relatively short (~ 10 ns - 60 μ s) for such devices, the present research in the materials field (see chapter 3 appears to be promising for longer coherence times.

It is hard to foresee exactly where the research and development in quantum

computing will take us. However, we can safely say that something important will come out and that quantum computing is a challenge not only for informatics and physics - both theoretical and experimental - but also for science in general, for technology and society.

For informatics as a science, quantum computing may bring the most radical change in its main research aims, scope and paradigms. Indeed, so far informatics has been developed, largely, with the global aims of serving current and foreseeable information-processing technology. Quantum computing (and molecular computing) is perhaps the first significant challenge, chance, and necessity for informatics to free itself from this short-term role of servant of technology, and to start to concentrate more on its most basic long-term aims: to study the laws and limitations of the information processing world, to contribute to the development of new global theories and to deepen our understanding of various worlds, for example physical, biological, and chemical.

For informatics as a technology, the development of quantum-information processing technologies can make a revolutionary contribution to the capacity and security of information processing and communication systems. For theoretical physics, quantum computing can be seen as a new challenge and also as an important new source of aims, stimuli, scientific methods, and paradigms for dealing with the most basic problems of quantum theory. It also brings an opportunity to understanding more the role of information as an important resource and fundamental concept in physics and for the understanding of the physical world.

For experimental physics, especially for solid state physics and quantum optics, large needs of quantum computing in order to store, communicate, and process quantum information faithfully bring radically new challenges of astounding complexity and importance.

As a last remark, for me as an ICT engineer (and soon as a physics/engineering PhD) quantum computing offers new approaches to overcome classic informational limits in communication, processing, information security, and it is not so far the day

in which Quantum Engineers will ordinarily manipulate quantum state of suitable devices.

The research activity of my thesis is devoted to the investigation of different materials and technological aspects of the decoherence phenomenon in the field of superconducting quantum bits.

1.1 Superconducting Quantum Bits

Superconducting circuits based on Josephson tunnel junctions are regarded as one of the most promising approaches for the development of quantum computing [26, 142]. As was found over the past twenty years, these circuits exhibit macroscopic quantum phenomena such as Macroscopic Quantum Tunnelling (MQT) [241, 59], energy level quantization [150], and resonant and photon-assisted [196] tunnelling between quantum states.

Recent successes with superconducting qubits have enhanced the feasibility of implementing quantum computing with Josephson devices. Within the past few years, the observation of a superposition of macroscopic quantum states [78, 230] and of time domain coherent oscillations between quantum states [164, 162, 255, 237, 145, 39] has been reported in such devices.

The phase qubit has attracted significant interest because coupled phase qubits have been measured simultaneously [152], and quantum conditional-gates have been successfully realized leading to the demonstration of two-qubit algorithms with a superconducting quantum processor: Grover's search and Deutsch-Jozsa's quantum algorithms have been executed for the first time on a quantum hardware [60]. Moreover, quantum von Neumann architecture was fully implemented by means of a superconducting circuit, made of two phase qubits coupled through a quantum bus, two quantum memories, and two zeroing registers; two vital algorithms for quantum computing were executed: the quantum Fourier transform, with 66 % process fidelity,

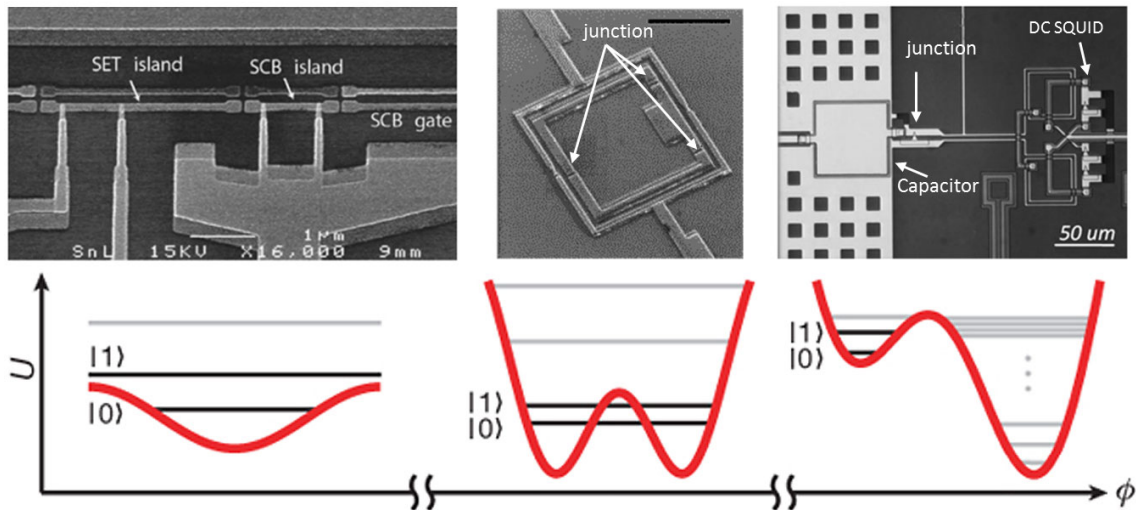


Figure 1.3: The main types of superconducting quantum bits and their relative computational basis (the $|0\rangle$ and $|1\rangle$ states) arising from the quantized energy-levels in their potential-energy landscape. (left) Charge qubit (Chalmers University, Sweden); (center) Flux qubit (Delft University, Holland); Phase qubit (UCSB, California).

and the three-qubit Toffoli OR phase gate, with 98 % phase fidelity [144]. Finally, recent advances in superconducting amplifiers have enabled high-fidelity measurement of the quantum state of a qubit, taking the first steps toward quantum-feedback.

As an application of qubits to fundamental physics, recent experiments could indeed address important questions in quantum mechanics: the extension of quantum entanglement from the microscopic to the macroscopic world, and the location and nature of the limit between the quantum and classical worlds. For instance, the accurate measurement of the correlations between two coupled qubits demonstrated the violation of Bell's inequalities [7], and showed that the collective variables of a macroscopic superconducting phase qubit circuits closely follow the predictions of quantum mechanics.

The major advantages of using Josephson junction devices as qubits are as follows:

- Relatively easiness of being measured, due to inherent macroscopic quantum nature of superconductivity
- Strong interaction with the wires of an electrical circuit, making possible their

integration with fast control and readout possible (microwave resonators, Rapid Single Flux Quantum circuits)

- Low dissipation of the circuits due to superconducting elements
- Reproducibility of identical sub-micrometric qubits is feasible by using the state of art lithographic technology
- The integration of large number of on-chip, widely separated, qubits, with tunable inter-qubit coupling and individual qubit addressing

The basic component of all superconducting devices considered for quantum computing is the Josephson junction. Being nonlinear, it is the fundamental circuit element that is needed for the appearance of usable qubit states. In contrast, linear circuit elements, such as capacitors and inductors, can form low-dissipation superconducting resonators, but are unusable for qubits because the energy-level spacings are degenerate. The nonlinearity of the Josephson inductance breaks the degeneracy of the energy-level spacings, allowing the dynamics of the system to be restricted to only the two qubit states. The Josephson junction is a unique nonlinear element because it combines negligible dissipation with extremely large nonlinearity: the change of the qubit state by the energy of a single photon can modify the junction inductance by an order of magnitude.

The superconducting tunnel junction consists of two superconductors separated by a thin insulating barrier. In the vast majority of superconducting qubit realized up to date, the superconductors are fabricated either from sputter-deposited niobium or from evaporated aluminum, and the Josephson junction barrier is formed by thermal oxidation of an aluminum layer realized in order to form an amorphous AlO_x tunnel barrier (see chapter 6). As was firstly shown by Josephson [108], with a sufficiently thin ($d \sim 10\text{-}30 \text{ \AA}$) tunnel barrier (Fig. 1.4), coherent tunnelling of Cooper pairs can occur, and the macroscopic wavefunctions of the two superconductors $|\Psi_L\rangle$ and $|\Psi_R\rangle$ can interact, yielding a Cooper pair current with density J and voltage V across

the junction that are related to the superconducting phase difference φ across the junction as

$$J = J_0 \sin \varphi \quad (1.1.1)$$

$$V = \frac{\Phi_0}{2\pi} \frac{d\varphi}{dt} \quad (1.1.2)$$

where J_0 is the critical-current density, the maximum Cooper pair current density that the junction can support, t is the time, and $\Phi_0 = h/2e \approx 2.07 \times 10^{-15}$ Wb is the magnetic-flux quantum [18].

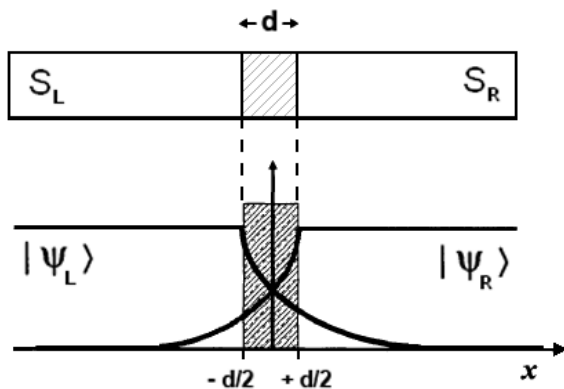


Figure 1.4: A superconducting tunnel junction consists of a thin insulating barrier sandwiched between two superconductors S_L and S_R . For sufficiently thin barrier thickness d , the macroscopic wavefunctions $|\Psi_L\rangle$ and $|\Psi_R\rangle$ of the superconductors interfere.

The superconducting devices considered for qubit realization generally have about 10^{12} Cooper-pair electrons, whose collective motion produces a relatively large flux ($10^{-3}\Phi_0$) or voltage (~ 1 mV) signals. Indeed, Josephson junctions have been shown to be ideal structures for the observation of macroscopic quantum effects.

1.2 Phase Qubit

1.2.1 Flux-Biased Phase Qubit

A phase qubit utilizes the phase difference φ across a Josephson junction as computational two-level basis. Although it is indeed possible to carry out phase qubit experiments on a directly current-biased Josephson junction [145, 173, 177, 63], a

rather complicated design of the bias lines is required in order to decouple the qubit from the environmental impedance of the bias lines Z_0 . Furthermore, in a directly-biased scheme the junction switches to the voltage state during read out, so that heating occurs and quasiparticles are created.

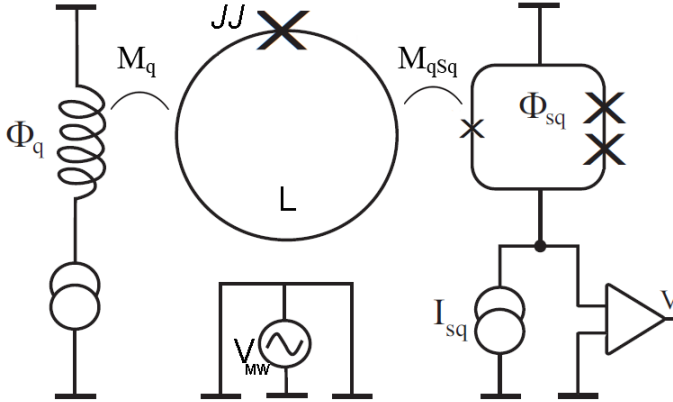


Figure 1.5: Schematics of a flux-biased phase qubit. The rf SQUID, with its inductance L , is inductively-coupled to the flux-line through the mutual inductance M_q , to the readout DC SQUID through the mutual inductance M_{sq} , and to the microwave-bias line.

These problems are all solved by placing the junction in a superconducting ring having an inductance L . In this way, the qubit remains always in the superconducting state, while it is biased by an inductively-coupled bias line and is read out by an inductively coupled DC SQUID (see Fig. 7.3). Furthermore, the impedance of the bias lines Z_0 is transformed into an effective impedance Z_{eff} (see section 7.2.2) so that the junction is practically decoupled from the low-impedance environment.

By embedding the junction in the superconducting loop, the circuit becomes an rf SQUID [18, 44]. This circuit, in spite of its simplicity, gives rise to a very interesting physics and can be used both as a phase and a flux qubit.

We will determine now the potential energy of the rf SQUID, and introduce some of the working principles of a phase qubit.

The flux quantization links the total flux Φ_q in the rf SQUID loop to the phase drop φ across the junction [18],

$$\varphi + \frac{2\pi\Phi_q}{\Phi_0} = 2\pi n \quad (1.2.1)$$

where n is an integer. From this equation, the phase-flux relation

$$\varphi = -\frac{2\pi\Phi_q}{\Phi_0} \quad (1.2.2)$$

is deduced for $n = 0$. The Josephson phase φ is in turn related by the first Josephson equation 1.1.1 to the supercurrent flowing in the loop, which using Eq. 1.2.2 reads

$$I_q = -I_0 \sin(2\pi\Phi_q/\Phi_0). \quad (1.2.3)$$

Due to the loop inductance L , this current I_q generates a magnetic flux which adds up to an externally applied flux Φ_{ext} . The resulting total flux threading the qubit loop Φ_q is therefore

$$\Phi_q = \Phi_{ext} + LI_q = \Phi_{ext} - LI_0 \sin(2\pi\Phi_q/\Phi_0). \quad (1.2.4)$$

The quantity

$$\beta_L \equiv \frac{2\pi LI_0}{\Phi_0} \quad (1.2.5)$$

is an important parameter to be taken into account for the qubit design (see chapter 7). For $\beta_L > 1$, the flux in the loop Φ_q is multivalued in some regions of the external flux Φ_{ext} , which causes Φ_q to switch in a hysteretic manner between flux states when the external magnetic flux is varied [258], and the switching between flux states is related to a reversal of the circulation direction of the loop current, while the current amplitude is always smaller than the critical current of the junction (*e.g.* the junction never switches to the resistive state).

The potential energy of the rf SQUID is thus the sum of the junction potential given by the tilted washboard potential equation [18]

$$U_\varphi = \frac{I_0\Phi_0}{2\pi} \left(-\frac{I}{I_0}\varphi - \cos\varphi \right) \quad (1.2.6)$$

and the magnetic energy $LI_q^2/2$ which is stored in the loop inductance L .

By rewriting Eq. 1.2.4 in order to obtain the circulating current in the form $I_q = (\Phi_q - \Phi_{ext})/L$, we arrive at the rf SQUID potential

$$U_\varphi = E_J \left[1 - \cos \varphi + \frac{(\varphi - 2\pi\Phi_{ext}/\Phi_0)^2}{2\beta_L} \right] \quad (1.2.7)$$

where the Josephson energy is $E_J = \hbar I_0/2e$. Here, \hbar denotes the Planck constant which reflects the scale of quanta in quantum mechanics. This potential has the form of a parabola centered at $\Phi_0 = 2\pi\Phi_{ext}/\Phi_0$ and modulated by a cosine. As it is shown in Fig. 1.6, for large values of β_L the potential has many minima, while for $\beta_L < 1$ only a single minimum exists.

Each minimum corresponds to a certain number of flux quanta in the loop, and accordingly the mentioned switching between flux states is associated with a transition between the wells.

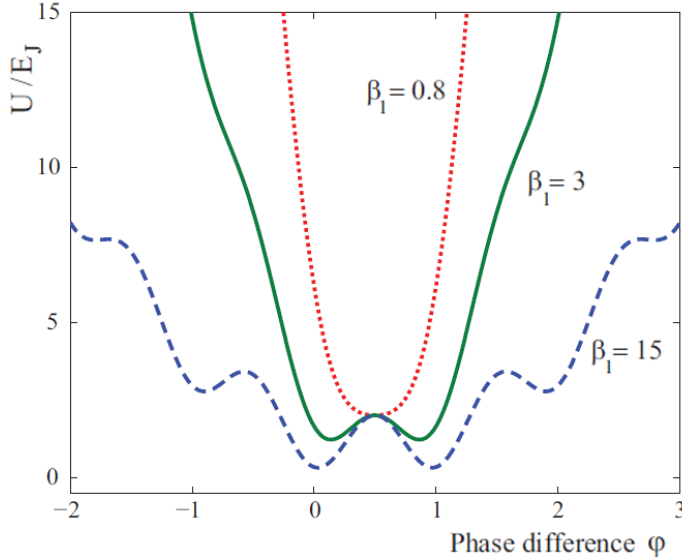


Figure 1.6: Potential of the rf SQUID for several values of the β_L parameter at an external magnetic flux of $\Phi_{ext} = \Phi_0/2$. Figure from [135].

Aiming at operating the rf SQUID as a phase qubit, for a given junction critical current the loop inductance is designed such that $1 < \beta_L < 4.6$. This results in a potential that has only two minima for all values of externally applied flux and one single minimum for $\Phi_{ext} \approx 0$.

If β_L is larger than 4.6, it is still possible to operate the rf SQUID as a phase qubit, but in this case more than two minima exist in the potential at all values of external flux, and therefore it becomes more difficult to initialize the flux state of the

qubit in a certain well.

By changing the external magnetic flux Φ_{ext} , the double well potential can be effectively tilted (see section 1.2.2). This allows to dynamically adjust the depth of the potential wells *in situ*. Analogously to the critical current I_0 of a biased Josephson junction, for the rf SQUID there exists a critical flux Φ_c where the potential barrier between the shallow and the deep well vanishes. Its value can be found from the condition that the inflection point of the potential coincides with the position of the minimum of the shallow well [119]. While the extrema of the potential Eq. 1.2.7 are located at a φ given by

$$\varphi - \frac{2\pi\Phi_{ext}/\Phi_0}{\beta_L} = -\sin\varphi \quad (1.2.8)$$

the inflection point which satisfies $U''(\varphi) = 0$ is located at φ_c , for which

$$\cos(\varphi_c) = -1/\beta_L \quad (1.2.9)$$

independently of the external flux Φ_{ext} . The insertion of the solution for φ_c into Eq. 1.2.8 results in the critical flux for a two-well potential [119]:

$$\Phi_c = \pi/2 + \sqrt{\beta_L^2 - 1} + \arcsin(1 - \beta_L). \quad (1.2.10)$$

For the phase qubit operation, the rf SQUID is biased right below its critical current I_0 , so that one potential well is made very shallow by adjusting the flux bias close to the critical flux such that $0 < \Phi_c - \Phi_{ext} \ll \Phi_c$.

Moreover, in each potential well the rf SQUID behaves as an anharmonic quantum oscillator, whose energy levels are unevenly spaced due to the non linearity of the Josephson inductance. The two lowest energy levels are thus used as the qubit ground-state $|0\rangle$ and the qubit excited state $|1\rangle$. Qubit operations can be carried out with a resonant microwave pulse, because the sufficiently large anharmonicity in the shallow well ensures that the junction is not excited to higher energy-levels.

In order to read out the qubit, the washboard potential is tilted a little further, by means of a short flux pulse, so that the tunnelling rate from the lowest energy level is still negligible while the rate from the second-lowest level is relatively high

(see Figure 1.7). In this way, since the two local minima correspond to opposite circulating currents, by reading the flux coupled in the read-out DC SQUID the qubit state $|0\rangle$ and $|1\rangle$ are mapped to different DC SQUID switching currents to the voltage state. Consequently, the occupation of the qubit states can be reconstructed with high fidelity by measuring its escape probability P_{esc} .

1.2.2 Qubit Operation

In order to extract information from a qubit, one must be able to discriminate whether it is in the ground-state $|0\rangle$ or in its (first) excited state $|1\rangle$. This is accomplished in two stages, which we refer to as "measurement" and "readout". As we described in the previous section, all the qubit operation are done through a sequence of applied flux bias and microwave frequency signals, as illustrated in Fig. 1.7.

I) Initialization.

To initialize the qubit, its flux state is reset to a defined value and its phase state to the one of lowest energy in the corresponding potential well. Given that the parameter $\beta_L < 4.6$, it suffices to switch the applied magnetic flux to zero such that only a single potential well remains. Keeping this flux level for a time much larger than the energy relaxation time T_1 ensures that the qubit is initialized in the ground state $|0\rangle$. For larger values of $\beta_L > 4.6$ there exist always more than one potential minima. Initialization in a certain well in this case is still possible by using the so-called "shaker" technique [128], in which an oscillating external flux is applied to induce escape from all potential wells of higher energy towards the global minimum.

II) Preparation.

The external flux Φ_q is adjusted adiabatically to a value near the critical flux Φ_c to make the potential well in which the phase is confined very shallow. While the exact value of Φ_q can be chosen to result in the desired energy difference between the two qubit states, it underlies two limitations. On the one hand, it must not be too large such that the first excited state does not escape from the shallow well during the

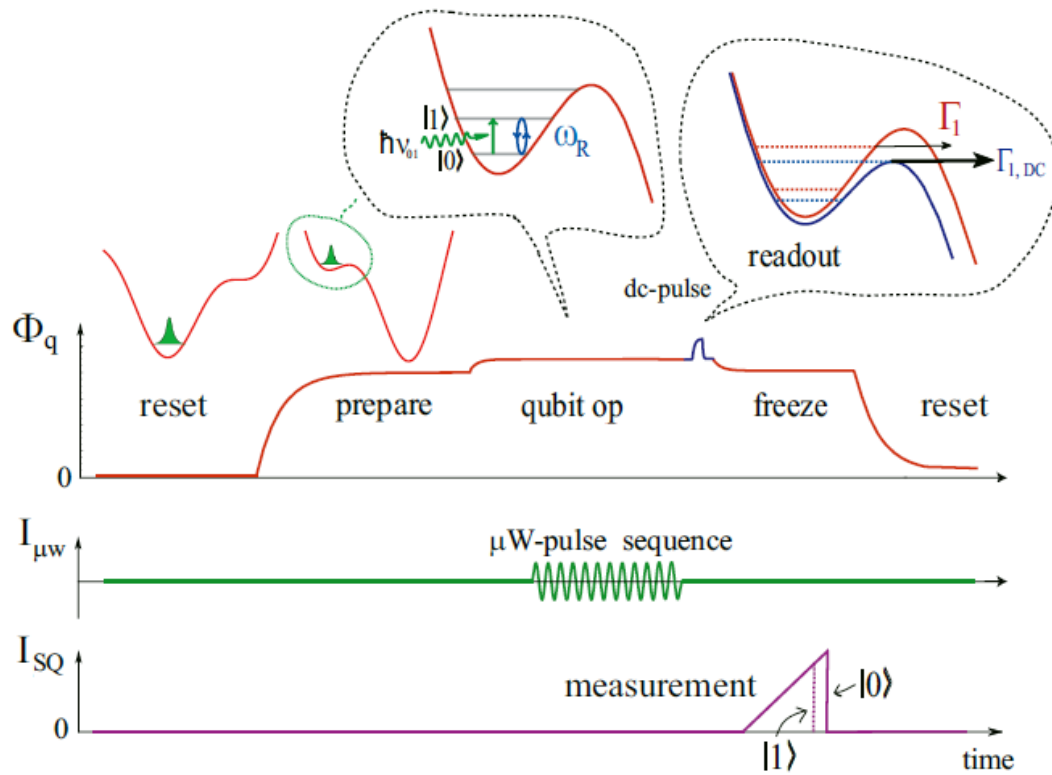


Figure 1.7: Top: Timing profile of the magnetic flux bias Φ_q applied to the qubit. Middle: microwave pulse sequence for the logical qubit operations. Bottom: Bias current sent to the readout SQUID. Figure from [135]

qubit operation. On the other hand, a smaller value of Φ_c results in a deeper potential well which is more harmonic, *i.e.* the transition frequencies between neighboring states are less distinct from each other. The external flux must hence be large enough to result in a potential well of sufficient anharmonicity, ensuring that higher excited states are not populated by a microwave tuned to the $|0\rangle$ to $|1\rangle$ transition frequency.

III) qubit operation.

After the external flux has reached the working point, logical qubit operations are performed by a sequence of dc-currents and resonant microwave pulses. Since microwave pulses of frequency $\omega_{\mu w} = (E_1 - E_0)/\hbar$ change the individual state population undergoing Rabi oscillation, they can be used to realize the Haddamard transformation and the logical NOT gate. A dc-pulse can be used to implement the phase gate by introducing a small detuning which changes the Larmor frequency and hence the precession velocity of the Bloch vector.

IV) qubit measurement.

The measurement of the qubit's state consists to shortly reduce the potential barrier of the well which contains the qubit states to allow the excited state of higher energy to tunnel into a macroscopically distinguishable state. The ground state remains in the initial well in this readout procedure. In flux-biased phase qubits, this is accomplished by applying a dc-pulse of flux which increases the total flux in the qubit loop.

Indeed, after sending the microwave pulse, a short but still adiabatic dc-flux pulse is applied which raises the excited state close to the top of the potential barrier. Its effect is to provide an additional tilt in the qubit potential as shown in the readout inset of Fig. 1.7, increasing the escape rate towards the neighboring potential well for all states which are contained in the shallow potential well.

It is possible to adjust the amplitude and duration of this measurement pulse such that only the excited state tunnels to the deep right well, whereas the ground state

remains in the shallow left well, since the escape rate of the excited state is typically a factor of $10^2 - 10^3$ higher than the one of the ground state, it is possible to adjust the duration and amplitude of the flux pulse such that during its application only the excited state escapes at large probability.

Thereby, the phase eigenstates $|0\rangle$ and $|1\rangle$ are mapped to macroscopically distinct flux states in the shallow and deep wells, respectively. This technique [47] allows to distinguish the phase eigenstates with a fidelity [257] close to 100%.

IV) State readout.

After application of the measurement dc-pulse, the applied magnetic flux is reduced, hereby increasing the barrier height separating the two wells in order to avoid further inter-well transitions. Whether the qubit is now in the left or right well is determined by measuring the corresponding magnetic field in the qubit loop by means of an inductively coupled DC SQUID.

Starting with the standard Nb/Al/AlO_x/Nb and NbN/AlN/NbN trilayer junctions, in chapter 6, I will explain the optimizations we realized at the ICIB-CNR on both the design and fabrication processes involved in the test-junction realization. Details about the design and dimensioning of a phase qubit will be discussed in chapter 7, while in chapter 8 the complete fabrication steps for the qubit realization will be analyzed. The understanding of the fabrication process is vital to know the limitations on the circuit parameters and, more importantly, to quantifying and reducing possible mechanisms of decoherence or dissipation in these devices. Lisenfeld007

Chapter 2

Decoherence

Decoherence is the entanglement of a quantum state of a system with its environment, and the consequent collapse of the system's wavefunction. A consequence of quantum decoherence is, indeed, the emergence of the classical or probabilistically additive behavior: decoherence is the mechanism by which the classical limit emerges out of a quantum starting-point, and determines the location of the quantum-classical boundary. Decoherence occurs when a system interacts with its environment in a thermodynamically irreversible way.

Decoherence can be viewed as the loss of information from a system into the environment. Thus, it is acknowledged that no system is, in reality, perfectly isolated, but rather every system is loosely coupled with the energetic state of its surroundings. Viewed in isolation, the system's dynamics is non-unitary (although the combined system plus environment evolves in a unitary fashion). Moreover, the dynamics of the system alone, treated in isolation from the environment, is irreversible. As with any coupling, entanglements are generated between the system and the environment, which have the effect of sharing quantum information with - or transferring it to - the surroundings.

It appears evident that, if the system under consideration is either a single atom in an ion trap, or a single photon, or a single spin (all controllable and measurable by

means of remote EM fields), the obtainable degree of isolation from their environment could be reasonably high with current state-of-the-art technologies; however, if our system is a macroscopic piece of metal, built on a crystalline substrate and coupled to the outer environment by means of wires and other circuits, then the degree of isolation becomes one of the main concerns.

In fact, for a two-level quantum system, the coherence time of the quantum state is a very important figure of merit, being related to the number of qubit operations that can be performed without error [104]. Despite significant advances during recent years, with coherence times of the order of several tenths of μs reached [175], decoherence due to the coupling between the quantum circuit and the degrees of freedom of the environment is still a major limitation for the development of a quantum processor [168], even with a small number of qubits.

Although better understanding of the decoherence sources could help in reducing qubit decoherence, real quantum-error correcting-codes will be mandatory for quantum computing. These codes are known to require error rates smaller than about 10^{-4} depending on the nature of the errors for each logic gate. Presently, the gate error rate can be estimated at a few percent for single qubit gates, and significantly more for two qubit gates. The coherence time is about a few thousands times longer than the duration of a single qubit-gate operation in the case of the best-performing superconducting qubit at present time, and is at best a few hundreds times the duration of a two-qubit gate.

Since decoherence is equivalent to a qubit error-source, the qubits require an improvement of coherence time of two or three orders of magnitude. Thus, the operation of a quantum processor based on superconducting circuits, or on any other technology presently developed appears to be a significant challenge. However, this is not a reason to give up, because conceptual and technical breakthroughs are everyday-news in the rather new field of quantum circuits.

Thus the quantitative characterization and understanding of decoherence processes and sources, both during the free evolution of the qubit and during its driven

evolution, is presently a central issue for the development of qubit circuits.

Decoherence is commonly described by two phenomenological parameters T_1 and T_2 , that govern respectively longitudinal and transverse relaxation of the qubit state [153]. In order to qualitatively describe this two processes, it is useful to consider the Bloch sphere (Fig. 2.1), which enables any arbitrary quantum superposition of the quantum states $|0\rangle$ and $|1\rangle$ to be considered as a vector. The states $|0\rangle$ and $|1\rangle$ point along the positive and negative z axis, respectively. The superpositions $|0\rangle \pm |1\rangle$ lie along the $\pm x$ axes, and the superpositions $|0\rangle \pm i|1\rangle$ along the $\pm y$ axes. Thus, a given point on the surface of the sphere defines a specific superposition of these states, which corresponds to the generic Hilbert vector $|\Psi\rangle = a|0\rangle + b|1\rangle$.

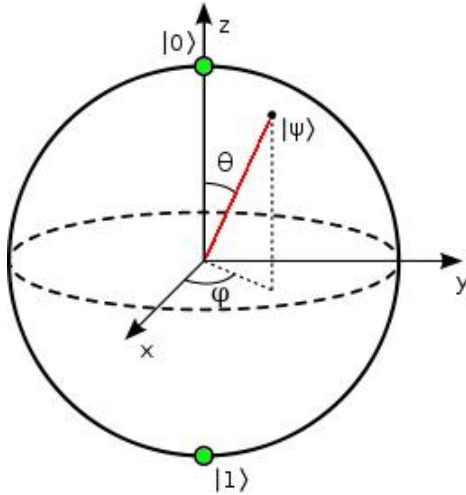


Figure 2.1: Bloch-sphere representation of the qubit state. The ground state $|0\rangle$ is represented by a vector pointing to the north pole, the state $|1\rangle$ corresponds to a vector pointing to the south pole and all equally weighted superpositions are found along the equator for $\Theta = \pi/2$.

Physically, both longitudinal and transverse relaxation are due to fluctuating fields of microscopic origin that induce spurious rotations of the state vector on the Bloch sphere. At low temperatures $T \ll \hbar\omega_{10}/k_B$, stimulated transitions between the qubit levels due to thermal photons are greatly suppressed, and longitudinal relaxation proceeds via spontaneous decay of the qubit's excited state $|1\rangle$ toward thermal equilibrium ground-state $|0\rangle$. This process corresponds to random fields in the (x,y) plane (it can be imagined as a shortening of the state vector), and its decay rate is intimately connected to the real part of the admittance shunting the qubit junction [146, 104]

$$\frac{1}{T_1} = \frac{\text{Re}(Y(\omega_{10}))}{C} \quad (2.0.1)$$

where C is the junction's capacitance.

In the longitudinal relaxation, $\text{Re}(Y(\omega_{10}))$ has contributions from several parallel dissipation channels. First of all, the electrical leads that are connected to the qubit to perform low-frequency biasing, high-frequency control, and readout all contribute to the spontaneous emission from the qubit. However, the effective impedance seen by the qubit as it looks into the control and readout lines can be made quite large by appropriate use of broadband inductive and capacitive impedance transformers (see section 7.2.2).

An alternative approach to prevent the spontaneous emission from the qubit, is to couple the qubit to the outside world via a resonant cavity or a transmission line resonator [242], which has the effect of suppressing the spontaneous emission at qubit frequencies far from the cavity resonance, a phenomenon analogous to the Purcell effect in atomic physics. Thus, by appropriate circuit design, one can effectively suppress energy dissipation induced by the electrical leads.

A more serious source of dissipation are microscopic material-defects inherent in the amorphous thin films that are used to implement the qubit (see section 2.2.7 and references therein). While the energy gap of the superconductor provides a natural barrier against dissipation, charged defects in the amorphous dielectrics of the circuit provide a high density of low-energy sub-gap states to which the qubit can couple.

Transverse relaxation of the qubit receives contributions from spontaneous decay, from pure dephasing, and from inhomogeneous broadening, given by

$$\frac{1}{T_2} = \frac{1}{2T_1} + \frac{1}{T_\Phi} + \frac{1}{T_\Phi^*}. \quad (2.0.2)$$

The first term, $1/2T_1$, means that any process which causes energy relaxation will also dephase the qubit at a rate $\Gamma_1/2$. The second term is the pure dephasing rate $1/T_\Phi$, and is caused by intrinsic processes (low-frequency fluctuations, which occur during the course of a single experiment, *e.g.* during one decay time) that randomly

modify the effective transition frequency of the qubit (the energy separation between the qubit states), which cause the qubit to accumulate a random phase a rate Γ_Φ [146, 104]. Dephasing could be represented as a "smear" of the state vector on the Bloch sphere, and the process corresponds to a random field along the z axis.

$$Q_\Phi = \omega_a/\Gamma_\Phi \quad (2.0.3)$$

is commonly defined as a dephasing quality factor, and represents the the number of coherent oscillations before the qubit will accumulate a random π phase shift.

Finally, there are fluctuations which occur on longer timescales T_Φ^* , from experiment to experiment, creating an dephasing ensemble denoted by the rate $\Gamma_\Phi^* = 1/T_\Phi^*$. Among these, non-thermal sources of noise, such as fluctuations from room-temperature laboratory control and measurement equipment, as well as active circuit-elements operating in the vicinity of the quantum device (SQUIDs, RFSQ circuitry, *etc.*) will contribute to the decoherence of the qubit in ways that are unique to different experimental realization and configurations.

This last type of fluctuations on a $1/T_\Phi^*$ timescale is analogous to spatial-magnetic field inhomogeneities in nuclear magnetic resonance (NMR), and is often referred to as inhomogeneous broadening. Like its NMR counterpart, because it is not intrinsic to a single experiment, it can be reduced using spin-echo techniques. Though it is possible to compensate for inhomogeneous broadening, doing so can be the bane of practical experiments, because inhomogeneous broadening often represents drifting conditions, which significantly complicate experimental protocols.

As the dephasing time T_2 can never exceed twice the relaxation time T_1 , it is the relaxation time which ultimately defines the limit on qubit coherence. The low-frequency spectrum of such fluctuations, $S_\lambda(\omega)$, is not white, but is singular at low frequencies, with a spectrum that scales inversely with frequency $S_\lambda(\omega) \propto 1/\omega$.

This so-called $1/f$ noise is generic for all disordered materials (for a review, see *e.g.* [246]), and is typically understood as arising from the fluctuations of an ensemble of underlying two-level systems, (TLSs), or sometimes also called two-level fluctuators,

(TLFs), with a broad distribution of characteristic relaxation-times [64, 195, 232]. Thus, in the presence of bias noise, a coherent superposition of the qubit states decays in time with a Gaussian envelope [153] such as:

$$f(t) \approx \exp \left[- \left(\frac{\delta\omega_{10}}{\delta\lambda} \right)^2 A \ln \left(\frac{1}{\omega_m t} \right) t^2 \right]. \quad (2.0.4)$$

where λ is the control parameters that determine the energy separation between the qubit states, and ω_m is

Low-frequency noise is specifically harmful since it is difficult to filter it out by finite band filters. Moreover, while the deleterious effects of low-frequency bias noise can be mitigated by the use of spin-echo-type refocusing techniques [210], the effectiveness of refocusing pulses is limited unless dephasing times are much longer than gate times, a situation which is typically not realized. An important step in this direction has been accomplished [237]. The authors showed that dephasing can be significantly reduced by biasing the qubit at an optimal point, where its resonance frequency is stationary with respect to its control parameters, which in that case are gate voltage and magnetic flux.

It is important to develop a deeper understanding of all potential sources of low-frequency noise and dephasing in superconducting circuits and to quantitatively identify the various microscopic mechanisms, in order to point out the direction to strategies to overcome the dephasing effects, the realization of materials with a reduced defect density, and the design of circuits with improved noise control properties.

In the following paragraphs, I will review the experimental evidences circa the microscopic origins of several noise channels which were identified and studied up to now by the superconducting qubit community. Moreover, I will introduce the theoretical frameworks that were developed in order to model the decoherence sources.

In conclusion, it will be evident that the concepts of charge-, critical current-, and flux-noise, have much in common: all the three noise sources take origin from a not well identified material defect (which is not said that should be of the same microscopic nature for the three phenomena), and all three could be well modeled in

a theoretical framework of random tunnelling of TLSs with an associated charge; flux noise, in addition, involves the concept of spin locking and the random direction of the magnetic moment associated with the tunnelling charge.

2.1 External Sources

2.1.1 Control Lines

The most common source of extra noise during an experiment is the noise coupled from the external control-lines. This is not likely the cause of the observed noise in recent realization of superconducting qubit for a number of reasons. As shown by Paik *et al.* [173], decoherence is not caused by insufficient bias-line filtering or bias noises. Filtering was one of the first aspects to be carefully investigated and improved in order to preserve and isolate the delicate quantum state. Engineerization of filters lead to excellent narrow- and broad-band filters which ensure that the noise level at the mK stage is not the main decoherence channel [140]. Furthermore, as we will see in section 7.2.2, the impedance of the bias lines Z_0 is inductively transformed into an effective impedance Z_{eff} so that the junction is practically decoupled from its low-impedance environment.

2.1.2 Bias Noise

Martinis *et al.* [146] calculated the decoherence of the qubit state from noise and dissipation due to the finite impedance of the current bias, in the case of current-biased Josephson junction phase qubit. Noise in the control currents produces decoherence in the qubit, with noise at microwave frequency SQUIDting the relative population between the ground and excited state, and noise at low frequency affecting the phase of the state. The finite impedance of the current bias produces decoherence in a manner

that can be calculated semiclassically by appropriately adding thermal and zero-point noise, and the authors showed that with careful engineering of the circuit, this channel decoherence .

Longobardi *et al.* [138] have ruled out the the noise in the flux bias line as the main source of decoherence by developing an integrated thin film shunt on chip with a dedicated resistor to heat the shunt past its transition temperature. This technique allowed to trap a desired amount of flux in a superconducting loop in order to bias the inductively coupled qubit, with the ability of controlling the current level without warming up the whole qubit box.

Another approach to reduce the bias noise is the use of a π -junction for flux qubits to realize degenerate quantum levels without external magnetic field [111]. This type of phase-bias can avoid dephasing due to noise in external flux and is called as a quiet qubit.

2.1.3 Back Action

Back action from the magnetometer (a readout DC SQUID) is another potential source of decoherence [47]. As for the noise coupled to the qubit loop from the bias and control lines, also the coupling with the DC SQUID may have detrimental effects, specially because usually the readout magnetometer is strongly coupled to the qubit, and because in order to perform the readout operation it is driven to its normal state (see section 1.2.2), thus introducing quasiparticles in the system.

For this reason, in section 7.2.3 I will introduce a 3 junction asymmetric-design for the DC SQUID, in which the magnetometer is operated in a switching current mode, in that it is "silent" until the moment to perform the measurement. When the measurement is performed, a voltage is established across the DC SQUID junctions creating quasiparticles which, being generated closely to the rf SQUID of the qubit, can affect its state.

However, after the measurement the magnetometer's bias current is rapidly ramped back to zero and left there long enough that the quasiparticles disperse.

The design of the magnetometer realized in this work is such that the only current that couples strongly to the qubit is the circulating current. The flux and current biases can be set at a point where the derivative of the circulating current with respect to the bias current goes to zero. At this point, fluctuations in the bias current do not couple to the qubit (at least to the first order, see section 7.2.3), in such a way that the magnetometer is not a major source of decoherence.

Nevertheless, several other readout schemes have been proposed and realized in the last years including, for example, dispersive-readout [249] involving non-linear SQUID resonators or CPW resonators coupled to the qubit loop. These approaches allow little back-action, while showing a large measurement contrast, negligible dissipation, quantum nondemolition (QND) measurements, and fast operation rates. However, also in this case, seems that the overall coherence time of the qubits was not limited by any dissipation or noise channels related to the readout method.

2.1.4 Sample Box Resonances

The sample box is an important part of the experimental qubit set-up that must satisfy a number of requirements. The box should serve as a shield against external radiation that might heat the qubit, and also against external magnetic flux that might dephase the qubit by causing fluctuations in its working frequency. For this purpose a superconducting box, or an Al-platted copper box are often used.

In addition, the qubit box must allow access to microwave and DC control lines to operate the qubit, which may have dramatic impact on qubit coherence times. Spontaneous emission of transmon qubits in a circuit QED architecture is strongly influenced by far off-resonant modes of the cavity [97]. The authors clearly demonstrated that, beside a well known mechanism of relaxation through the circuit's lossy dielectrics, the transmon qubits relaxation-times are controlled also by spontaneous emission through the cavity, by the so called Purcell effect [192].

Near the cavity resonance, spontaneous emission is Purcell-enhanced and T_1 is

short. Away from resonance, the cavity protects the qubit from decay and the relaxation time is substantially longer than expected.

With careful design, it should be possible, together with the realization of sample boxes in order to avoid accidental resonances, also to realize filters to minimize dissipation.

2.1.5 Electromagnetic and Thermal Baths

Superconducting qubits are normally operated at the base temperature of dilution fridges (~ 20 mK), so that the condition $k_B T \ll \hbar/\omega_{10}$ is largely fulfilled ($\omega_{10} \sim 10$ GHz). Therefore, the thermal bath should not provide enough energy to excite the qubit to its excited states.

Moreover, the sample box is usually well shielded with respect to its electromagnetic environment: the external magnetic flux is shielded by multiple superconducting shields and Cryoperm cylinders surrounding the sample holder.

However, recently it was proposed and verified [17] that not-well filtered stray light, electromagnetic waves in the range of terahertz to infrared radiation, seems to be responsible for short coherence times in phase qubits and for frequency noise in coplanar waveguide (CPW) resonators, due to the generation of quasiparticles. Careful shielding of high frequency radiation (higher than 30 GHz) should be arranged, in order to prevent the samples to be irradiated by a not-so-well characterized electromagnetic environment. In fact, common microwave components (attenuators, filters, circulators, etc.) and the standard (Al-plated copper) sample housing, may let energy (and noise) from the terahertz to infrared frequency spectrum reach the qubit sample.

For this reason, additional carbon-based coatings are nowadays routinely applied in the inner thermal-shields of the dilution fridge, and the sample housings are buried inside a "brick" of iron-based microwave-adsorbing materials like eccosorb [65].

2.1.6 Other External Sources

Several other sources of decoherence, located out of the volume occupied by the qubit itself, have been investigated during the last decade. Among them, it was calculated that cosmic rays have a flux of $\sim 0.6/\text{cm}^2\text{s}$ and deposit an energy of $\sim 1 \text{ MeV}/\text{mm}$, yielding for a 50 mm^2 chip of thickness 0.5 mm a power 0.02 pW [148]. Energy deployed in the qubit volume by natural background radioactivity is typically of the order of that coming from cosmic rays [148], and in both cases little, if nothing, could be done to limit the incoming cosmic rays flux or the natural decay of unstable isotopes.

As a conclusion of present section 2.1, it worths to be noted that, although being thoroughly studied in the last decade, the decoherence phenomenon still eludes its fully understanding. However, step by step, we are learning what decoherence is NOT, or namely which decoherence sources are NOT limiting the current technological implementations:

- Decoherence is not caused by insufficient filtering of bias line, or bias noises [173],
- Decoherence is not strongly dependent on temperature (in the $15 \text{ mK} - 200 \text{ mK}$ range) [136],
- Decoherence is not influenced by the readout magnetometer coupled to the rf SQUID loop, nor by the back-action during measurements, if the qubit decoupling is properly engineered,
- Decoherence is not due to the junction intrinsic dissipation, even for subgap resistance $R_s \geq 1 \text{ G}\Omega$ [179],
- Decoherence is not depending on the size of the superconducting loop, which could have excess loss at low power levels [117].

2.2 Intrinsic Sources

Taking into account most of the potential external sources of decoherence in the qubit external environment (sample box, cables, bias noises, *etc.*), the evidence seems to point towards intrinsic qubit sources as the major ones of the decoherence. This is corroborated by old observations of flux noise of unknown origin in SQUIDs [77, 224, 248], and more recently in persistent current qubits [254].

With "intrinsic sources" we mean here the qubit system itself, which, being a macroscopic structure, consists of many superconducting and insulating films with all their volumes, surfaces, and interfaces, used to create the needed circuital elements as the Josephson barriers, insulating layers, wirings, inductors, and capacitors.

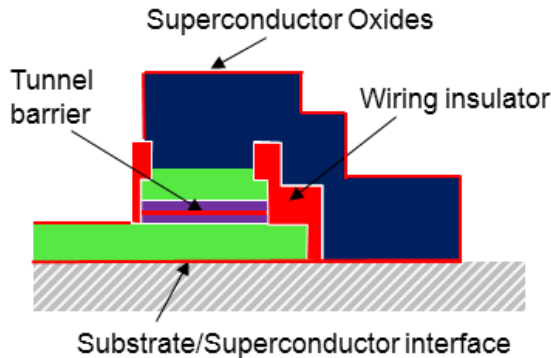


Figure 2.2: Intrinsic sources of decoherence due to microscopic TLS in the qubit's local environment.

The major source of decoherence in the qubit's local environment was originally predicted to reside in the Josephson junction, in the form of quasiparticle dissipation and critical current fluctuations, but recently many other channels have necessarily been considered, and not only localized in the junction itself, in order to explain the well hid - but always present - phenomenon of the decoherence.

2.2.1 Quasiparticle Dissipation

The dissipation in a Josephson junction is usually quantified through the subgap resistance R_s of the junctions. Patel *et al.* [179] have found that devices having a

subgap resistance of the order of a $1 \text{ G}\Omega$ or greater (at 400 mK) exhibit coherence times not longer than the values measured in other qubit with much lower level of quasiparticle dampening.

In a superconductor the density of unpaired electrons (quasiparticles) should theoretically vanish when approaching zero temperature [225].

Instead, it is experimentally observed that the quasiparticle density decreases exponentially with decreasing temperature, but saturates below 160 mK to a quasiparticle density of $25\text{-}55 \text{ /}\mu\text{m}^3$ [58] in an aluminum thin film. It was also experimentally demonstrate [148] that quasiparticles can be a significant source of decoherence in a Josephson qubit, and thus it appears important to understand how to minimize their presence and effects.

Non-equilibrium quasiparticle populations might be reduced by adding a normal-metal quasiparticle-trap to the box or, in the case of a charge qubit, by making the two halves of the CPB out of superconductors with dissimilar gaps, creating a barrier to quasiparticle tunnelling.

Very recently, the "3D cavity" approach, firstly introduced by the Yale group [175], demonstrated that the junction itself (at least small Al/AlO_x/Al junctions) and the quasiparticle population are not the source of energy relaxation which is limiting currently-observed T_1 times ($T_1 = 60\mu\text{s}$).

In Section 2.3.2 I will present in more detail the theory about dissipation from incoherent quasiparticle tunnelling.

2.2.2 Critical Current Fluctuations

Josephson junctions usually show low-frequency fluctuations of their critical current with a $1/f$ power density spectrum. However, the Josephson energy $E_J = I_0\Phi_0/2\pi$ is a crucial parameter determining the qubit energy landscape and, depending on the critical current I_0 , all superconducting qubits are susceptible of dephasing from excess of low-frequency critical-current noise.

These critical current fluctuations have thus the effect of modulating the barrier

height of the rf SQUID potential, resulting in fluctuations of the energy spacing between coupled states.

The microscopic mechanism and the source of the fluctuations on the critical current in a Josephson junction are long-standing open problems. These fluctuations are widely believed to arise from charges tunnelling, or hopping between different localized states in the barrier forming glass-like two-level states (TLSs) that locally modify the barrier transmissivity [46].

A simple model assumes that these defects are TLSs switching between two states that correspond to an open and a closed tunnelling channel through the junction. The distribution in the energy splitting of these TLSs is thought to be very broad and to extend above the transition energies of Josephson qubits. This picture is supported by the observation made by Simmonds *et al.* [207] of a coherent coupling between a phase qubit and uncontrolled TLSs randomly distributed in frequency. The same authors also observed that avoided level crossing in the spectroscopic data implies a strong coupling between the qubit and the unknown TLS, that was later eliminated by annealing the sample at room temperature. These observations suggest that TLSs located in the tunnel barriers not only generate low-frequency critical current fluctuations, but can also play an important role in the relaxation of Josephson qubits.

However, a more detailed comparison with other experiments revealed an important problem: the experimentally observed noise spectrum [247, 232] was proportional to T^2 , which is incompatible with the assumption of constant TLS density of states.

New experiments [68] on fluctuations in small Al junctions, similar to those used in several types of qubits [39, 145, 237], in normal state brought a new puzzle. It turned out that the temperature dependence of the noise power spectrum in the normal state is linear, and the noise power is much less than that reported for large superconducting contacts. A plausible explanation of such behavior is given in [71], where it is suggested that the critical current noise is due to electron trapping in - and tunnelling between - shallow localized subgap-states that might be formed at

the superconductor-insulator boundary, a mechanism similar to the one suggested to describe the charge noise in paragraph 2.2.4.

Van Harligen *et al.* [232] studied the critical-current fluctuations of Josephson tunnel barriers of different areas, and transmissivities, and fabricated in different amorphous technologies: as expected, they observed the proper linear scaling ($S_{I_0} \propto I_0^2/A$) of the noise spectral density, S_{I_0} , with the junctions area, A , beneath the same technology and having assumed independent TLS fluctuators. Moreover, it was found that all amorphous tunnel-barriers show roughly the same levels of critical-current noise measured at 4.2 K and at 1 Hz [232]

$$\frac{\sqrt{AS_{I_0}}}{I_0} \approx 10 \mu\text{m pA/Hz}^{1/2}/\mu\text{A} \quad (2.2.1)$$

a sort of "universal" density of microscopic defect within all the tested materials.

Within the model of Van Harligen *et al.*, the critical-current fluctuations in the present qubit devices seem to be orders of magnitude too small to explain the measured level of decoherence. Nevertheless, measurements on the critical-current noise of an rf SQUID operated in the dispersive mode (so that the junction is maintained in the supercurrent state) reveal a junction noise-magnitude which is similar to that observed in experiments where the junction is biased in the finite voltage state [160]. Thus, it is expected that critical-current noise will farther limit the dephasing times of superconducting qubits even though, presently, the coherence times of superconducting qubits is more severely affected by excess of low-frequency charge- and flux-noise, or by dissipation.

2.2.3 Flux Noise

Studies of the flux noise in superconducting structures, such as DC SQUIDS, have a long history. As early as in the 1980s it was demonstrated that it is the flux and not the critical current noise that limits the ultimate sensitivity of DC SQUIDS [117].

The interest in this problem was recently renewed when it was realized that flux noise can limit the coherence in flux and phase superconducting qubits [254, 146].

In fact, both in SQUIDS [248] and in Josephson flux qubit [24], it is universally observed a flux noise of unknown origin whose power spectral density exhibits a $1/f$ behavior with magnitude of $1\mu\Phi_0/\sqrt{Hz}$ measured at 1 Hz [254].

All experiments surprisingly agree on the magnitude of the noise at frequency $f \sim 1$ Hz and on its area independence. Moreover, the same magnitude is observed in devices fabricated by an extremely wide range of materials, and it is universally observed that the noise does not decrease at very low temperatures.

Koch *et al.* [116] have suggested a model for $1/f$ flux noise in SQUIDS and qubits, where the noise is generated by magnet moments of electrons in the defects of the insulating materials. Due to thermal effects, unpaired electrons hop on and off defect centers in which the electron orientation is locked in one of the two Kramers-degenerate ground states. The orientation is random from trap to trap, and the time an electron resides in a given trap varies over orders of magnitude. The uncorrelated spin orientations sum up to give a $1/f$ power spectrum. When applied to qubits loops, this model results in scaling of the noise amplitude as the fourth root of the area.

An alternate source for the decoherence has been proposed due to the non-exponential spin-lattice relaxation of paramagnetic dangling-bonds at the amorphous semiconductor-oxide interface [56]. The scaling of the flux noise with size is similar to the previous theory, but since it is an effect of the interface the flux noise should not depend in this case on the defects in the substrate.

Thus, despite more than 20 years of research ruled out many potential sources of flux noise, the microscopic mechanism is still eluding its perfect knowledge and will require more sophisticated investigations and material-growth techniques.

2.2.4 Charge Noise

Charge noise mainly affects only qubits and devices operating in the Coulomb blockade regime, like single electron transistors (SETs) and small-area Josephson qubit as a single Cooper-pair-box or the quantronium [237, 162]. These devices are subject to

a background charge-noise due to microscopic charged TLSs acting as uncontrolled electrostatic bias at the gate charge (N_g), resulting in a random accumulation of phase between the electrodes.

It may sound obvious to relate the source of the charge-noise random telegraph process (RTP) to charges which jump (trapped and detrapped) between two different locations in space. However, where these charges are actually located and what the two states physically are, it remains unclear.

Works by Zorin *et al.* [260] have shown that the charged TLSs are partly located in the substrate, partly in the oxide layer covering all the electrodes, and partly in the oxide barriers of the tunnel junctions themselves. It has been suggested that some TLSs contribute both to the critical current noise and to the charge noise [117].

In order to reduce its detrimental effects on the qubit operation, echo sequences in the qubit's state manipulation-protocol can substantially suppress inhomogeneous dephasing of qubit due to low-frequency charge noise. From the fabrication point of view, although there is some indication that charge noise is lower in SETs that are electrostatically isolated from the substrate [122], there has been little progress in the the development of novel materials or circuit designs that display a reduced level of charge noise.

Although the whole collection of TLSs produces a noise whose spectral density approximately follows a $1/f$ law [259, 238, 181], RTP charge noise due to some well-coupled TLS-qubit system can be observed as well [29].

The first attempt of a model to explain qubit decoherence by means of charge noise appeared in [176], where electron tunnelling between a localized state in the insulator and a metallic gate was studied. Despite recent progresses in order to understand the temperature dependence of charge noise in small area qubit (a T^2 scaling dependance between 200 mK and 1K [10]), and despite of several recent models based on thermal activation of TLSs [112] in an asymmetric double-well potentials, or on an assumed linear dependence of the defect density of states on frequency [204], a detailed microscopic picture is still lacking.

Having briefly introduced the charge noise, it is certainly good to note that charge noise contribution is negligible in the typical phase qubit due to the relatively large junctions required, which operate far from Coulomb blockade regime.

2.2.5 Surface Losses

Despite its superconducting state, the thin superconducting films used in Josephson qubit fabrication could potentially have unexpected losses. Even though the superconducting films have the expected values of transition temperature, implying no expected conduction losses at low frequencies, superconducting films can show losses at high frequencies. These losses are usually attributed to the kinetic inductance of the Cooper pairs and of surface defects (like the presence of oxides, photolithography imperfections, variable etching profiles, *etc.*), and are usually quantified in terms of surface resistance R_{surf} and introduced frequency noise.

The losses of superconducting films at high frequencies (tens of GHz) have been extensively tested by measuring the intrinsic quality-factors of coplanar waveguide resonators (CPWs) and will be explained in further detail in section 3.5, where several material, process, and design improvements in order to reduce these decoherence channels are discussed.

2.2.6 Capacitive Coupling

Capacitive coupling to bias leads can be a dominant source of dissipation, and therefore of decoherence in the form of spontaneous emission via electric-dipole transitions, even for galvanically-floating flux/phase qubits which were thought to be immune to such mechanism of decoherence.

Such dissipation channel is well known for charge qubits [104], but it was not considered for flux/phase qubits before the study of Steffen *et al.* [218]. The authors showed that the assumption that the connection of the qubit to ground is poor, and therefore such qubits are immune to capacitive coupling, is incorrect; indeed, it

becomes significant at microwave frequencies, while the capacitance to ground C_g is basically fixed by the overall physical size of the qubit device, and cannot be altered significantly by details of device shape or geometry. Moreover, Steffen *et al.* showed that most floating qubits so far realized have a strong capacitive coupling to ground, because the C_g of an isolated object scales only with its linear dimension, and is thus appreciable for all but the smallest flux-qubit designs. For a typical qubit loop with a radius R of $\sim 10\text{-}100\ \mu\text{m}$, the obtained $C_g > 10\ \text{fF}$ which is a not negligible capacitance and could, in fact, represent a significant relaxation channel.

By considering C_g in Eq. 2.0.1, together with the junction capacitance C and any capacitance from the bias leads C_c , one gets a T_1 of $\sim 10\ \text{ns}$, which is a typical T_1 value for the first generation of qubits. Similarly to C_g , values of C_c of the order of $\sim 10\ \text{fF}$ are easily present between the qubit and bias loops and/or measurement SQUIDs, particularly because the capacitance only scales logarithmically with distance.

In accordance with the model described in [218], the relaxation times can be improved by designing floating qubits that couple symmetrically to the bias leads, *i.e.* by configuring the bias leads in such a way that no circulating currents can be generated in the qubit, and by realizing bias and measurement lines in such a manner that their inductance to ground are as small as possible. More on this geometric optimization will be discussed in chapter 7.

2.2.7 Insulating Material Losses

Recently, there is a strong evidence [208, 47] that the common insulating materials used for qubit fabrication (AlO_x , SiO , SiO_2) have ubiquitous TLS defects which affect the coherence times of superconducting qubits. All the dielectrics involved in the qubit fabrication, such as the substrates, the insulation under the wiring layer (wiring insulation) and the Josephson barrier itself, are considered as candidates to be studied and optimized in order to reduce the qubit's decoherence.

In particular, Martinis *et al.* [147] showed in 2005 that the same TLSs causing dielectric loss in superconducting-microwave resonators (see section 3.3 and chapters

4 and 5) are also responsible for the main decoherence-mechanism in superconducting phase qubits.

The density of TLS defects, as evaluated by the loss $\tan \delta$, determines the magnitude of decoherence; TLSs in qubit's vicinity couple to the qubit and extract energy from it.

The authors in [147] are also the first to investigate the possibility of improving the coherence times by choosing the materials with which the qubits are built of.

Furthermore, they suggest that OH^- defects are the dominant source of the TLS in their amorphous chemical vapour deposited (CVD) SiO_2 and AlO_x dielectrics, as previous experiments have measured the intrinsic loss in undoped and doped bulk-quartz at 100 to 1000 ppm concentrations C_{OH} . The loss tangent was found to scale roughly as $\tan \delta \cong 3.0 \times 10^{-5} + 0.4 \cdot C_{\text{OH}}$.

In figure 2.3, it can be seen that the decoherence is stronger if dielectrics with high dielectric losses (quantified by higher loss $\tan \delta$) are used in qubit fabrication.

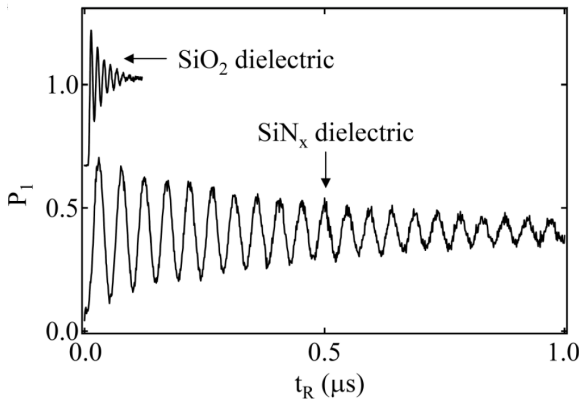


Figure 2.3: Rabi Oscillations for a phase qubit using CVD SiO_2 (top trace, offset) and SiN_x (bottom trace) as a dielectric for the crossover wiring. In the case of SiN_x , the decay of the Rabi oscillations is consistent with the measured relaxation time of $T_1 \approx 0.5 \mu\text{s}$, which is about 20 times better than previous experiments with a SiO_2 dielectric. Figure from [147].

The authors realized phase qubit circuits using CVD silicon nitride (SiN_x) which, being made from precursor gases without oxygen, showed intrinsic loss tangent about 30 times smaller than for SiO_2 , confirming the importance of reducing the OH^- concentration. Thus, with SiN_x identified as a superior dielectric, Martinis *et al.* showed that the TLSs which are responsible for the qubit decoherence and the for dielectric losses are indeed identical.

Efforts in the fabrication of qubits with ultra-low $\tan \delta$ wiring-insulators (discussed

in section 3.3 and in chapter 4) and crystalline tunnel barrier (see section 3.4) lead to remarkable result in terms of improved coherence time. Moreover, experiments based on extremely high quality factor ($Q > 400000$) superconducting CPW revealed that TLS are also associated with native superconductor-oxides residing in a 3 nm thick surface volume [81]. Thus, also the superconductor surfaces and interfaces have to be investigate in order to characterize and avoid the TLS contribution; more on this argument will be discussed all through chapter 3.

In collaboration with the IMS and KIT, Germany, we have characterized several dielectric material by means of the lumped LC-resonator technique (see chapter 5), a direct measurement to test the quality of the insulating layers at the typical frequencies of interest for the qubit. In this framework, we have established a solid fabrication protocol (see section 8.4) to integrate the niobium technology with the best known amorphous dielectric, namely the hydrogenated amorphous silicon (a-Si:H), the latter introduced in section 3.3 and extensively discussed in chapter 4.

2.2.8 Coupling to Discrete TLS

While a continuum of TLS in bulk dielectrics can lead to energy relaxation, coupling of the qubit to the discrete TLS bath in the Josephson tunnel barrier itself can lead to the quantum-coherent transfer of energy between the qubit and the single TLS, and result in fidelity loss. The interaction of individual TLS dipole-moment with the resonant electric field of the junction capacitance can be observed both spectroscopically [208, 47] and in the time domain [5].

Interaction between the qubit and a resonant TLS gives rise to an avoided level-crossing in the qubit spectroscopy; the size of the energy splitting is S/h , where h is the Planck constant. Spectroscopy of the qubit performed over a broad range of frequencies reveals a density of TLS-induced splittings around $0.5 \text{ GHz}^{-1} \mu\text{m}^{-1}$ [217].

Fig. 2.4 shows the peak-value of the occupation probability of the qubit excited-state ($|1\rangle$) as a function of excitation frequency and qubit bias. Along with the

expected bias dependence, the data also exhibit avoided two-level crossings (splittings) that arise from the qubit state resonating with an individual TLS in the tunnel barrier. The density of splittings in the conventional design is high enough that the qubit is almost always coupled to at least one TLS. The state occupation of $|1\rangle$ is consequently diminished, giving rise to decoherence and thus reducing the qubit performance.

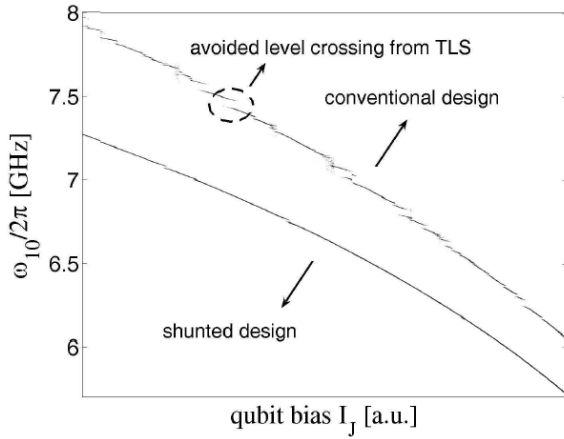


Figure 2.4: Qubit frequency versus qubit bias for the conventional (top trace, shifted for clarity) and the capacitively shunted design (bottom trace). The flux bias tunes the frequency of the qubit. The smaller area / shunted junction design has about one tenth of the area and consequently exhibits a reduction in the number of avoided level crossings by approximately a factor of ten. Figure from [217].

These splittings have been observed in phase qubits, flux qubits, and charge qubits. In the case of phase qubits with large junction area of order $100 \mu\text{m}^2$, qubit T_1 is directly determined by the loss tangent of the tunnel barrier dielectric, as predicted by Eq. 2.3.6 (with $\alpha = 1$).

For smaller-area charge, phase, or flux qubits, the density of splittings is reduced, due to the reduced junction area [217], although larger splittings are observed in the smaller junctions, and the splitting reduction have been found to linearly depend on the junction area A as

$$S_{I_0} \propto I_0^2/A \quad (2.2.2)$$

Recent works have demonstrated the possibility to use a single TLS as a quantum memory [47, 166], and it was found that the coherence time of a single TLS could be of orders of magnitude more than the qubit's coherence times itself. Moreover,

the fidelity of the memory operation was tomographically measured [166], and many defect-models have been quantitatively evaluated [45].

A part from using a single TLS as a quantum memory, more generally the coupling of the qubit to resonant TLS can be suppressed by operating the qubit so that it is far detuned from dominant TLS defect states. However, in many instances, during practical manipulation of a qubit, it is necessary to tune its frequency, either to perform measurements or to realize gate operations. In this case, the qubit resonance is swept through the resonance frequencies of several TLSs and, for a finite bias-sweep rate, there is the possibility that the qubit's state evolves to the ground state, while the TLS evolves to its excited state: the excitation is swapped from the qubit to the TLS with associated loss in the fidelity of the qubit operation.

Moreover, the effect of spectroscopically un-resolved qubit-fluctuators is still un-explored.

2.2.9 Other Intrinsic Sources

Among the minor sources of coherence decay that have been considered for the superconducting qubit is piezoelectricity. If there is any piezoelectricity or magnetostriction in any of the nearby materials, the electromagnetic oscillations in a superconducting qubit could lose energy in the form of phonons [103].

For this reason, piezoelectric materials, like quartz and aluminum nitride, are not considered good insulators to be used in the fabrication of low decoherence qubits.

Another noise source arises from the magnetic vortices or magnetic flux-tubes moving in the superconducting electrodes of the devices: the superconducting films used for the qubit fabrication may trap magnetic flux in the form of quantized Abrikosov vortices [28], if the external fields during the sample's cool down are non properly shielded. The motion of those vortices between pinning centers, under microwave-field biasing, leads to vortex noise and dissipation. Vortices density might be reduced by better magnetic shielding of the sample, and their pinning strength may be enhanced by intentionally putting an array of holes, defects, or inclusions in the superconducting

wires [213].

In section 7.2.1 I will discuss how to dimension the width of the superconducting wires by taking into account the detrimental presence of the trapped vortices.

Local radioactivity arising from the naturally-occurring unstable isotopes of the materials used for qubit fabrication, together with the nuclear spin fluctuations, have been taken into consideration as additional decoherence sources [116], but it seems not likely that these two processes could explain the observed T_1 and T_2 in superconducting qubits.

As a last possible decoherence channel, it may be possible that vacuum fluctuations play a role in the observed noise at quantum-scale. The concept of vacuum energy has been deduced from the concept of virtual particles, which is itself derived from the energy-time Heisenberg uncertainty principle. The effects of vacuum energy can be experimentally observed in various phenomena such as spontaneous emission, the Casimir effect, the van der Waals bonds, the supposed Hawking radiation, and the Lamb shift. Virtual particles also mediate the exchange of all forces between particles. For example, when an electron experiences electrical repulsion from another electron, it is actually exchanging virtual photons with that other electron. Higher-energy virtual photons are allowed by the uncertainty principle to exist for short periods of time, as shown by the uncertainty equation, they may have a visible effect in the real world. For example, a metal plate experiences a storm of fleeting impacts from virtual particles (of all natures, either bosons or fermions) on its surfaces; this "vacuum pressure" is equal on both sides of the plate, and so cancels out. If, however, two parallel metal plates are too closely spaced to allow the quantization of the virtual fields in the space between them, the vacuum pressure between the plates is less than that on their outer surfaces, and they experience a net force pushing them together. This force is termed the "Casimir effect" after Dutch physicist H. Casimir, who predicted its existence in 1948, and the force was experimentally measured in 1997 [124]. It would not be so surprising if the constant bombardment of virtual particles should be found to be responsible for the observed "noisy" behavior of the

superconducting surfaces, when investigated at the quantum regimes.

2.3 Theories

Similarly to any quantum object, the phase qubit is subject to decoherence due to its interaction with uncontrolled degrees of freedom in its environment, including those in the device itself. These degrees of freedom appear as noise - induced in the parameters entering the qubit Hamiltonian - in terms of energy exchange with a noise source on one hand, and in terms of random dephasing between states $|0\rangle$ and $|1\rangle$ due to adiabatic variations of the transition frequency on the other hand.

2.3.1 TLSs

Low-energy two-level systems, TLSs, are associated with not-well-identified defects in the dielectrics, namely in the wiring insulators, in the tunnel barriers, in the capacitors, and in all the surfaces/interfaces of the superconductors, for what it concerns the qubit realization.

They are responsible for wide number of anomalous properties of glasses at low temperature, including the specific heat that varies linearly with temperature T [256], a T^2 dependence of the thermal conductivity [256, 240, 185], a strong enhancement of acoustic and dielectric absorption [188], the universal electronic low-frequency noise observed in any device (from semiconducting field-effect transistors [64, 246] to SQUIDs [117]), the microwave losses at low excitation regimes [169], and the energy splittings in the high frequency qubit spectroscopy [217].

The microscopic origin of the TLSs is thought to be related to the rearrangement of dynamic two-state crystalline (or amorphous structure) defects, to the electron hopping between traps in which their spins have fixed but random orientations [115], to electrons that flip their spins due to interaction with tunnelling TLSs and phonons [56], to spin diffusion along the surface of a superconductor [72], or more generically

to the random switching of fluctuators between its two metastable states (1 and 2).

However, among these models, only the one presented in [72], implying the presence of magnetic impurities in superconductor's surface oxides, seems to agree with recent experiments [24, 199] on measurements of the $1/f$ noise generated by an ensemble of TLSs.

We now introduce the "TLS tunnelling" model in its most generic form, readily adaptable to describe any real physical system.

In fact, no matter which is the real microscopic origin, a TLS (an ideal one) produces a random telegraph-noise. This process is characterized by the switching rates γ_{12} and γ_{21} for the transitions $1 \rightarrow 2$ and $2 \rightarrow 1$.

One of the basic assumptions of the tunnelling model is the occurrence of configurations of two local minima with nearly equal energy and spatially adjacent sites of equilibrium in the potential-energy landscape, which could for example be taken into account for the amorphous structure of a dielectric.

Such a configuration can be described by a double-well potential, between which the particle can hop via either thermal activation or quantum mechanical tunnelling. At low temperatures, the thermal energy is not high enough for particles to overcome the potential-well barrier, so that only the tunnelling through the barrier will occur.

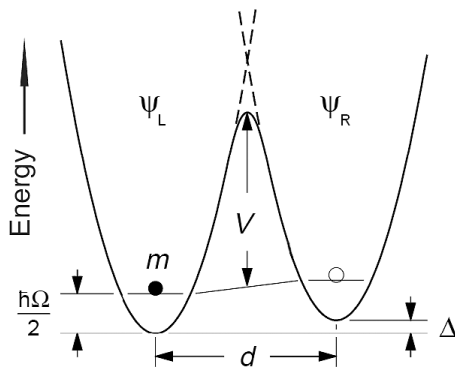


Figure 2.5: A particle in a double-well potential. Asymmetry energy, Δ : well distance, d ; energy of the ground state of the particle in an isolated well, $\hbar\Omega/2$; potential barrier, V . The figure is taken from [67].

Formally, a TLS is simply a particle with mass m in a double-well potential, as in Fig. 2.5. For reasons of simplicity this potential is considered as if composed of two identical, nearly-harmonic wells with ground state energy $\hbar\Omega/2$, separated by

the distance d . For glasses an asymmetry in the depth of the wells, with asymmetry energy Δ , can be assumed because of their structural disorder.

By solving the Schrödinger equation for the left and the right well-associated wavefunctions, and assuming a weak overlap of the latter, we can obtain an expression for the energy splitting [67]

$$E = E_+ - E_- = \sqrt{\Delta^2 + \Delta_0^2} \quad (2.3.1)$$

where the tunnel splitting term, Δ_0 , can be obtained by the Wentzel-Kramers-Brillouin method as $\Delta_0 \approx \hbar\Omega e^{-\lambda}$. Under all made approximations, the tunnelling parameter, λ , is determined by the mass, m , and the shape of the potential as $\lambda \approx \frac{d}{2\hbar}\sqrt{2mV}$ [67].

Due to the irregular structure of glasses, the introduced characteristic parameters Δ and Δ_0 are different for different TLSs. A basic assumption of the tunnelling model is, that Δ and Δ_0 are independent of each other and that their values are nearly uniformly distributed [185]. This assumption, in spite of its phenomenological origin, is in excellent agreement with the experimental data.

It is interesting to report, as from [67], the coupling of TLSs to electric field. If there is a charge associated with the defect state, there will be an electric dipole moment \vec{p} corresponding to the configurational change that takes the defect from $|L\rangle$ to $|R\rangle$. For a typical TLS defect in an amorphous dielectric, it is expected an electric dipole moment of order 1 Debye [153] (roughly 1 electron charge times the Bohr radius).

The application of an external electric field to the TLS normally do not change the shape of the potential - which would have an influence on the separation of the wells d and on their barrier height V - and thus do not change Δ_0 . Instead, external perturbations of the electric field change the local environment of the TLS and therewith Δ . The perturbation theory predicts that the small change in asymmetry energy $\delta\Delta$ will vary linearly with the strength of the electric field

$$\delta\Delta = 2\vec{p} \cdot \vec{F} \quad (2.3.2)$$

where \vec{F} is the strength of the applied electric field.

Various low-temperature properties of solids containing defects or structural disorder like glasses evolve from relaxation processes. In the following, relaxation processes of TLSs coupling to electric field will be discussed in detail, leading to descriptions which are important for the results within this thesis.

At low temperatures, absorption or emission of single phonons can induce transitions between the levels. As always only one phonon participates in this phenomenon, relaxation of a TLS from its excited state into its ground state is called a "one-phonon" or a "direct process".

The loss tangent $\tan \delta$ of the dielectric is defined as the ratio of the energy absorbed per unit volume per radian of oscillation to the maximum energy density of the electric field

$$\tan \delta = \frac{2P_a}{\omega \varepsilon_0 \varepsilon_r E^2}, \quad (2.3.3)$$

where ε_0 and ε_r are the absolute and relative electric constant.

The dielectric loss induced by the TLS is thus expressed as [153]

$$\tan \delta = \frac{\pi \rho \vec{p}^2 \tanh(\hbar\omega_T/2k_B T)}{3 \varepsilon_0 \varepsilon_r \sqrt{1 + \omega_r^2 \gamma_1^{-1} \gamma_2^{-1}}}, \quad (2.3.4)$$

where ρ is the TLS energy density of states per unit volume, and ω_r the Rabi frequency of the TLS's coherent oscillations.

Note that the loss tangent of the amorphous dielectric decreases, due to the population of the TLS excited state: as thermal or external microwave transitions saturate the TLS, the dielectric becomes transparent to resonant irradiation, and the loss decreases. In the case of qubit experiments, however, one typically works at a temperature around 20 mK and at extremely low microwave drive powers, corresponding to one microwave photon loaded into the anharmonic qubit resonance. In this case, we are interested in the intrinsic low-temperature ($k_B T \ll E$), low power ($\omega_R = 0$) loss tangent of the amorphous dielectric

$$\tan \delta = \frac{\pi \rho \vec{p}^2}{3 \varepsilon_0 \varepsilon_r}. \quad (2.3.5)$$

For the parameters $d = 1$ Debye, $\rho = 10^{46} J^{-1}m^{-3}$, and $\varepsilon_r = 4$ (characteristic of

amorphous SiO [184]), we find a large intrinsic loss tangent $\tan \delta \approx 3 \cdot 10^{-3}$. This number is typical of amorphous-oxide thin films, as from table 3.1.

The qubit's dissipation from the amorphous dielectric can be expressed as a lossy capacitance in parallel with the junction. In such a case, Eq. 2.0.1 could be read as

$$T_1 = \frac{1}{\alpha \omega_{10} \tan \delta}. \quad (2.3.6)$$

In the case of a large qubit junctions, with area $\gg 10 \mu\text{m}^2$, the tunnel barrier itself contains a quasi-continuum of resonant TLS, and dissipation from these states can induce qubit energy relaxation. In this case, the qubit is given by Eq. 2.3.6 with $\alpha = 1$, and where now δ refers to the lossy tunnel-barrier dielectric. The large intrinsic loss tangent of amorphous AlO_x accounts for the relatively short coherence-times (tenths of ns) of the first-generation phase qubit having large junction-areas [145].

It is interesting to note that only the TLSs with energy splitting E less than $k_B T$ (thermal TLSs) contribute to the qubit dephasing, since the TLSs with large level splitting are frozen in their ground states. As long as $E < k_B T$, the rates γ_{12} and γ_{21} are close in magnitude, and without loss of generality one can assume that $\gamma_{12} \approx \gamma_{21} \equiv \gamma$, *i.e.* the fluctuations can be described as a random telegraph process (RTP). A set of such random telegraph fluctuators with exponentially broad distribution of relaxation rates, γ , produces low-frequency charge and dielectric noise with a $1/f$ power spectrum, and in last analysis contribute to qubit energy dephasing.

On the other hand, for $E > k_B T$, (quantum) TLS defects behave like a "spin bath" in the quantum regime, giving rise to such unusual properties as enhanced dielectric loss at low temperature, and low microwave drive power [80], and in last analysis contribute to qubit energy relaxation.

In chapter 4, I will extend the discussion on the TLSs, by giving more details on the microscopic and experimental aspects.

2.3.2 Quasiparticles

At the low temperatures typically used in Josephson qubit experiments (10 - 50 mK), the equilibrium quasiparticle-density is computed to be exponentially small.

Moreover, no equilibrium quasiparticles are expected in a superconductor well below the critical temperature $T \ll T_c$, because of the exponential suppression of excitations from the superconducting gap Δ . However, an experiment on Cooper-pair boxes has measured a significant quasiparticle density $n_{qp} \sim 10/\mu\text{m}^3$, arising from an unknown source in an Al charge qubit [200]. Once excited, quasiparticles can readily tunnel through a Josephson junction. Charge associated with quasiparticles allows a tunnelling event to couple energy between the quasiparticle and the qubit, and the decay of qubit from its excited state could add energy to the final quasiparticle state.

However, because in some superconducting-qubit implementation the state-measurement procedure produces a voltage across the junction, a significant number of quasiparticles are produced and remain in the system even after the qubit is reset into the zero-voltage state. These quasiparticles, with densities far exceeding the equilibrium value, then cause decoherence, perturbing the proper operation of the qubit. Recently, it has been shown [34] that, being the quasiparticle tunnelling-amplitudes flux-dependent, as a consequence also the qubit decay-rate induced by quasiparticle tunnelling is flux-dependent.

Lang *et al.* [125] showed qualitatively that quasiparticles create decoherence. Decoherence from quasiparticles can arise via either energy relaxation or dephasing. For example, quasiparticles tunnelling across the junction create shot noise in the current bias. Noise at the qubit transition-frequency, ω_{10} , causes unintended state transitions, whereas noise at low frequencies alters the junction bias-current and hence ω_{10} , leading to unintended variations in the phase evolution [146]. Quasiparticles also affect the critical current, I_0 , of the junction by changing the effective Josephson supercurrent of the conduction channels [85]. Fluctuations in I_0 produce decoherence as with bias-current noise. Finally, quasiparticles provide a mechanism for energy

dissipation that can result in unintended transitions from the qubit's excited to ground states.

One method to minimize the creation of quasiparticles is to limit the time the qubit remains in the voltage state. However, quasiparticles are observed in the circuit even in the absence of junction switching.

The number of quasiparticles present in the junctions could be further decreased by two methods: by reducing the creation rate with current shunts, and increasing the depletion rate with normal-metal traps. Experimental data demonstrated that both methods are required to significantly reduce the number of quasiparticles and increase the system's coherence [125].

The first method to minimize quasiparticle creation is to place a current shunt in parallel with the junction. Because the rate of quasiparticle creation is proportional to the quasiparticle current flowing through the junction, the reduction of this current reduces the generation rate by a factor of about 10^3 .

The second method is aimed to increase quasiparticle recombination. In a superconductor, quasiparticles recombine into Cooper pairs at a rate proportional to their density. At high density, this is a rapid depletion mechanism; however, to effectively remove quasiparticles when the density is low, alternative channels for quasiparticle decay must be created. One such channel is a quasiparticle trap, that consists of a normal-metal island in good electrical contact with each of the superconducting leads of the Josephson junction.

The traps are for the quasiparticles as an effective potential well of depth Δ , when they diffuse to the traps they are captured and dissipate their energy to the normal metal [49]. Provided that the temperature of the normal metal is much less than Δ/k , the normal metal will only be a sink, and not a source of quasiparticles.

Finally, quasiparticle energy is ultimately removed from the superconductor by recombination and emission of a phonon with energy $\geq 2\Delta$. Because phonons are long-living at low temperature, especially for crystalline substrates, they may ballistically travel across the chip and have their energy redeposited as quasiparticles

anywhere in the superconductor. All of these estimates imply that a conservative design should have quasiparticle trapping structures of millimeter or greater size, not just local structures placed around the tunnel junctions.

Quasiparticle normal-metal traps could be realized by evaporating a 3 nm adhesion layer of Ti followed by 0.1 μm of AuCu (25 wt.% Cu).

Moreover, engineered spatial profile of the superconducting gap by controlled oxygen doping [11] was also shown to provide an effective potential barrier, able to keep the quasiparticle far from the junction area. More recently, the authors of [163] showed another example of superconducting-gap engineering, by using a NbN counter-electrode and a NbTiN wiring layer, so that non-equilibrium quasiparticles are trapped in the wiring layer and do not diffuse into the junctions due to the smaller energy gap of the NbTiN compared to NbN.

We conclude that in order to greatly decrease the number of quasiparticles, a qubit needs a combination of both decreased quasiparticle generation with the shunt and more rapid removal of the quasiparticles by the trap.

Anyway, as shown also by the very recent "3D cavity" experiment [175], quasiparticle dissipation seems not to be the major source of decoherence in present generation of superconducting qubits. On the contrary, the authors of this experiment highlighted the participation of defects present on metallic and dielectric surfaces in high frequency losses, by the coupling of a transmon qubit with a large dipole moment with a three-dimensional C band microwave cavity, yielding coherence times of tens of microseconds.

2.3.3 Surface Spins

Recent experiments have revealed clear evidence for a high density of unpaired surface-spins in thin-film SQUIDs [199], and suggest that these spins are the source of the excess low frequency flux noise.

Several theoretical models of low-frequency flux-noise have then been proposed [116, 24, 56, 72]. For example, Koch *et al.* [116] developed a model of low-frequency

flux-noise by using a flux qubit whose configuration contains a superconducting loop. In their model, decoherence is caused by unpaired electrons trapped in defects, where their spins have fixed, random orientations. An electron can be trapped by a defect for a long period of time with the direction of its spin remaining unchanged at low temperature [120] due to spin-orbit coupling [1].

In order to estimate the low-frequency flux-noise using Koch's model, the authors first assume that the defects with density n are uniformly distributed over a simple toroidal model of a SQUID loop with inner and outer radius respectively r and R , and loop width W , covered by a surface density of spins σ_s .

Three regions were defined: the superconducting loop, the exterior region, and the hole region that is enclosed within the SQUID loop. A small current loop was used in order to simulate mutual inductance $M(x, y)$ between electron's magnetic moment and the SQUID loop. The loop area of A had a current i flowing in it so that $A \cdot i = \mu_B$, where $\mu_B = 9.27 \times 10^{-24}$ J/T is the Bohr magneton. The flux per Bohr magneton coupled into the SQUID loop has been calculated to be $\Phi_0/\mu_B = M(x, y)/A$, and the total mean-square normalized flux-noise from three regions coupled into the SQUID is obtained:

$$\langle (\delta\Phi_{st})^2 \rangle = 8n\mu_B^2 \int_0^{L_r+R} dx \int_0^x dy [M(x, y)/A]^2 \quad (2.3.7)$$

where L_r is the distance beyond the SQUID loop in the integration. For reasons of simplicity, taking the upper limit of $M(x, y)$ to be $1 \text{ n}\Phi_0/\mu_B$ and assuming the range of integration from 10^{-4} Hz to 10^9 Hz, the $1/f$ spectral density of the flux noise could then be expressed as

$$\frac{S_\Phi(f)}{\Phi_0^2} \approx \frac{\langle (\delta\Phi_{st}/\Phi_0)^2 \rangle}{30f}. \quad (2.3.8)$$

Note that this model predicts that the magnitude of the rms (root mean square) flux-noise depends not on the total area of the SQUID, but on the ratio of the linear dimension of the SQUID, for a constant aspect-ratio R/W . Models for $1/f$ flux noise from surface spins are indeed attractive, as they yield a noise spectral power that is only weakly dependent on the overall scale of the device, compatible with the

”universal” character of the noise [24].

Instead of the $1/f$ flux noise caused by unpaired electron-trapping as described in Koch’s model, de Sousa’s proposal of the magnetic flux-noise is linked to the spin flips of paramagnetic dangling-bonds at the amorphous-semiconductor/oxide interface [56]. The dangling bond forms the trapping center near the Fermi energy ($\varepsilon_F \pm k_B T$) for interface conduction-electrons with spin flips due to the interactions with the local structural defects at the interface, for example, in Si/SiO₂ and in other amorphous-oxide interfaces that are typically used as the substrate for superconducting qubits. Also in this case, the corresponding noise has a $1/f$ frequency dependency.

Moreover, Sendelbach *et al.* [199] measured the flux threading a Nb SQUID that was cooled (down to 20 mK) with vortices intentionally trapped into the Nb film. The flux threading the SQUID increased as as temperature was lowered and the flux change was proportional to the density of the initially trapped vortices. The experimental data is compatible with the thermal polarization of unpaired surface-spins in the trapped fields of the vortices.

Furthermore, the authors inferred from the magnitude of the temperature-dependent flux change a surface spin-density of $5 \times 10^{17} \text{ m}^{-2}$, that is once again compatible with densities inferred from electron-spin resonance studies of the disordered Si/SiO₂ interface [56], and with the MIGS theory [40] (see section 2.3.4).

The most recent flux-noise model, presented in [72], considers interacting spins at the superconductor-insulator interface that interact via the RKKY mechanism, and which diffuse in the nonuniform surface magnetic fields of the SQUID. In all the previous models, surface spin interactions were clearly neglected, despite significant experimental evidences [199]. In [72], interactions between spins are essential to the noise mechanism.

Thus, it is not unreasonable that spin densities of this order exist at the interface between the insulating substrate and the superconductor, or between the superconductor and its insulating native oxide, even if the precise microscopic nature of the surface spin states that give rise to the excess flux noise is still unknown and object

of intense investigation.

In chapters 6 and 8 I will discuss some preliminary attempt to perform suitably surface treatments, both to the substrates and to the superconductors, in order to produce passivation against natural-oxide formation and reduction of the material defects.

2.3.4 Metal-Induced Gap States

Choi *et al.* [40] showed that, in the presence of potential disorder at the metal-insulator interface, some of the metal-induced gap states become localized (by means of Andreev localization) and produce local moments. TLS are associated with localized Metal-Induced Gap States (MIGS) at the Metal-Insulator Interface, and a modest level of disorder yields the observed areal density of magnetic defect, as those revealed by a scanning SQUID microscope investigation of the surfaces of common amorphous and crystalline materials normally used in microfabrication [25].

An areal density of unpaired electrons of about $5 \times 10^{17} \text{ m}^{-2}$ under and/or on superconducting thin films could be responsible for the "universal" $1/f$ flux noise at low temperatures, with the characteristic noise spectral-density of a few $\mu\Phi_0\text{Hz}^{-1/2}$ at 1 Hz.

Since the origin of MIGS is the local metal-surface disorder, its density could be reduced by epitaxial growth of metal layers and by its surface treatments.

As we will discuss in chapter 3, a large consensus has emerged that the $1/f$ flux noise arises from fluctuating spins of localized electrons with an areal density of $5 \times 10^{17} \text{ m}^{-2}$. We will see that also other experiments, different in nature, will conclude that on the superconductor's surfaces/interfaces there are defects having similar areal density.

Chapter 3

Qubit's Materials Research - State of the Art

As we have seen from the previous chapter, quantum superposition and entanglement are fragile, particularly when they exist in solid-state systems such as a superconducting qubit, that is tightly coupled to numerous environmental degrees of freedom.

The efficiency of the future devices for quantum information processing will be limited mostly by the finite decoherence rates of the qubits. Recently, substantial progress was achieved in enhancing the time within which a solid-state qubit demonstrates coherent dynamics. This progress is based mostly on a successful isolation of the qubits from external decoherence sources. Under these conditions, the material-inherent sources of noise start to play a crucial role. In most cases, the noise that the quantum device demonstrates has a $1/f$ spectrum. As we saw, this suggests that the environment, that destroys the phase coherence of the qubit, can be thought of as a system of two-state fluctuators, which experience random hops between their states.

Since the microscopic origins of the device $1/f$ noises are still not completely understood, the material research to improve the quality of the superconducting circuit, in terms of defect density, remains a vastly unexplored field with potentially

important consequences. The research over the last several years has shown that qubit performance is limited by spurious coupling of the qubit to microscopic TLSs in the materials that are used to implement the qubit circuit [153], where these TLSs shall be thought as defects (of various nature) in the dielectrics, in the superconductor/substrate interfaces, and/or native oxides.

Superconducting qubit-community demands for material research directed at redistributing, reducing or removing such TLS states. This effort is similar to the one that led to the semiconductor revolution in the second half of 20th century, carried on by improving the growth of high quality silicon single crystal and by optimizing the Si-SiO₂ interface.

Most of the significant progress in improving the coherence times of superconducting qubits has been based on existing fabrication technologies utilizing standard materials, such as Al and Nb, with AlO_x tunnelling barrier. However, recently many groups have found that they are precisely these materials and fabrication technologies that are the limiting factors to further increases of coherence times [208, 47, 147].

Careful studies and solutions to these issues are vital to the future progress of quantum computation using superconducting qubits. The time and resources necessary to measure coherence times of superconducting qubits make it impractical to use these measurements alone to investigate changes in the materials and/or the fabrication process. In fact, if we consider that, in first approximation, both coplanar waveguide resonators and qubits could be realized with the same fabrication technique, namely double-angle aluminum evaporation, then it could be reasonable to think about a common microscopic origin of both loss of resonator's quality factor and of qubit's decoherence, respectively. As shown in Fig. 3.1, the two systems are made of the same materials (Al films with surface oxides), and during their operation they both could be driven by single microwave photon energies, even though the local electromagnetic field densities may be different by several orders of magnitude.

Due the similarities in the process for fabricating CPW and qubit samples, one

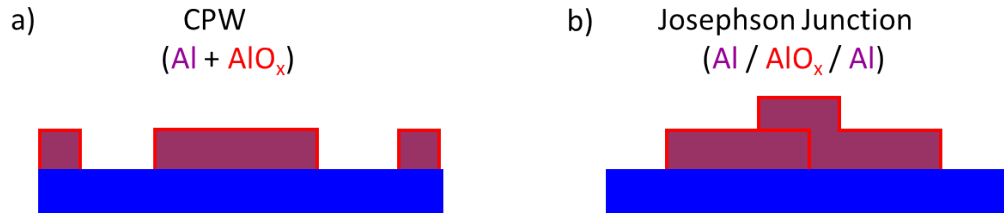


Figure 3.1: Schematics cross-section of coplanar waveguide resonators and qubits. Both could be realized with the same materials and fabrication techniques, *e.g.* aluminum evaporation. The study and reduction of the losses in the resonator may help to enhance the coherence of the qubits.

could in principle study frequency noise and quality-factor dependencies in superconducting resonators and gain insights in the microscopic origin of TLS $1/f$ noise and decoherence in superconducting qubits.

In this chapter we discuss the material origin of dissipation and dephasing in superconducting qubits, and the loss of quality-factor for superconducting microwave resonators. Having identified the main sources of energy relaxation and dephasing processes to reside in material defects giving rise to TLSs, there are plenty of aspects that could be studied and optimized in the device fabrication process, like the substrate choice and its pre-treatments, the wiring crossover insulator, the tunnel barrier, and the growth of epitaxial, non-oxidizing superconductors, in order to defeat decoherence. Thus, we will focus our attention on the underlying material-physics that governs decoherence in superconducting circuits, and outline some of the approaches that are currently being pursued to realize systems with improved coherence properties.

3.1 Substrates and its Treatments

The coplanar waveguide (CPW) resonator are useful for studying many of the different materials and fabrication techniques common in superconducting qubits. This section will review results of studies of the resistivity of the substrate, of the effect of different

resists used for liftoff, and of plasma etching on the intrinsic quality factor Q_0 of the resonator. These aspects are not independent of each other, and the results must be analyzed within the overall context of the fabrication process. The substrate makes up a good portion of the local environment of both the coplanar waveguide resonators and superconducting qubits. They interact with the substrate, including impurities, via electric and magnetic fields. This interaction provides a mechanism of loss that can cause decoherence in a qubit, and reduce the Q_0 of a coplanar waveguide resonator. The loss of the substrate is proportional to the number of impurities and hence related to the resistivity of the substrate.

The effect of the substrate on decoherence can be studied by fabricating and measuring qubits on different substrates. However, when the substrate is changed it can have other effects on the fabrication process, like changing the lattice or the growth of the overlying films.

The detailed description of a CPW resonator will be done in section 5.1.

Let us see in detail how coplanar waveguide resonators were used to investigate to what extent the substrate and fabrication steps affect the high-frequency loss of an rf SQUID qubit. The Q of any resonant structure is a function of the intrinsic loss-mechanisms associated with the electromagnetic fields in the resonator and the coupling of the resonator to losses in the rest of the circuit. The intrinsic loss-mechanisms for a planar transmission-line resonator are made up of the conductor loss (Q_ρ), the dielectric loss (Q_ε), and the radiative loss (Q_{rad}), and hence the intrinsic Q_0 is

$$\frac{1}{Q_0} = \frac{1}{Q_\rho} + \frac{1}{Q_\varepsilon} + \frac{1}{Q_{rad}} \quad (3.1.1)$$

$Q_\varepsilon = 1/\tan \delta$ where $\tan \delta$ is the loss tangent of the dielectric substrate. The Q_ρ is dependent on the the geometry of the coplanar waveguide, but in general $Q_\rho \propto f_0/R_s$ where R_s is the surface resistance of the conducting film [98]. Q_{rad} is determined by the distribution of the fields in the structure, and is dominated by radiation leaking out the ends of the resonator.

The loaded Q_L is given by

$$\frac{1}{Q_L} = \frac{1}{Q_0} + \frac{1}{Q_{ext}} \quad (3.1.2)$$

where Q_{ext} is the external quality factor, taking into account the coupling to the rest of the circuit.

The coplanar waveguide resonator is simple to fabricate by one-step photolithographic process because the ground and signal conductors are in the same layer. The resonator is realized by coplanar waveguide gaps at each end of the half-wavelength resonant portion. The external Q_{ext} is set by the size of these gaps, the microwave frequency, and the impedance of the resonator and input ports. For a linear coplanar waveguide resonator, Q_{rad} increases with decreases in the width of the center strip [79] and should not effect Q_0 for the 10 μm wide strip used for the all the resonator considered here. If Q_{ext} and the Q_{rad} are large enough, then the resonator can be used to measure the smaller of Q_ε and Q_ρ . Thus, the coplanar waveguide resonator is a suitable structure to study the loss from the superconducting films and various dielectrics of the rf SQUID qubit.

The authors of [35] measured the Q_0 of Al CPWs as a function of the substrate resistivity (0.5 Ωcm - 20 $\text{K}\Omega\text{cm}$) and for a few different resist (ZEP520A and PMMA), under different baking conditions. They clearly demonstrated that the Q increases, and hence the loss decreases, with increasing resistivity.

The resonators patterned with ZEP520A showed both higher Q values than the ones patterned with PMMA and improvement with increased bake temperature. When changing the ZEP520A bake temperature from 120° C to 180° C, the chance of the resist outgassing during deposition is reduced, and the measured Q is increased. This is consistent with resist outgassing known to degrade deposited Nb films when PMMA is used as a lift-off mask [96]. The measured Q for the sample fabricated using PMMA on a the highest resistive Si substrate (20 $\text{K}\Omega\text{cm}$) is much lower than for ZEP520A on the same resistivity substrate. This is most likely due to the outgassing of the PMMA being worse on the high resistivity silicon, which has lower thermal conductivity, allowing more heat to build up in the wafer.

On the other hand, the authors of [15] demonstrated that the same Al CPWs, built on sapphire or on silicon substrate, have a very different frequency-noise spectra (as from Fig. 3.2) depending on the choice of the substrate. The resonator built on silicon has a reduction of the frequency-noise magnitude of the order of ~ 9 dBc/Hz (decibels relative to the carrier per Hertz) compared to his twin built on sapphire.

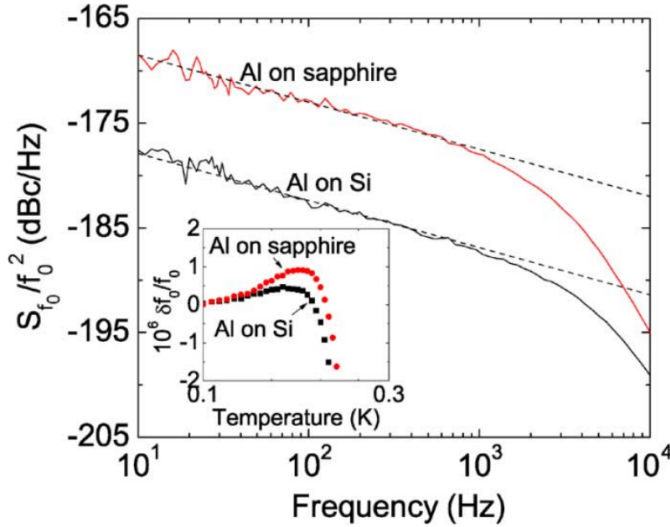


Figure 3.2: Frequency noise spectra of Al CPWs realized on silicon and sapphire substrates, with equal geometry and similar resonance frequency, 4.22 GHz and 4.57 GHz respectively, measured at an internal power of -40 dBm at a bath temperature of 100 mK. The roll-off is due to the resonator-specific response time. The inset shows a more pronounced non-monotonicity in the temperature dependence of the resonance frequency for Al on sapphire (red) compared to Al on Si (black). Figure from [15].

Moreover, the same authors showed that by removing unnecessary parts of the dielectric substrate (in the gap between the superconducting central-strip and the grounds) by means of KOH wet etching [16], NbTiN resonators gained 7 dBc/Hz in terms of frequency noise, probably by etching away a consistent amount of TLSs that were residing in that volume of substrate.

A counter-example is provided by magnesium oxide (MgO) substrates, which show once more how the substrate choice does play an important role in the resonator's Q_0 . Although being the optimal substrate for NbN growth (in terms of lattice match), it seems that it is not suitable for the realization of high quality CPW [169] due to the suspected presence on its surface of magnetic impurities [169] and to a non linear dielectric microwave-response [94].

Furthermore, it was demonstrated that also quasiparticle recombination-time in superconducting resonators depends on the substrate [233]. The author of this experiment showed an increased (one order of magnitude higher) quasiparticle recombination time in superconducting resonators on a SiN_x membrane, compared to identical resonators on a SiN_x/Si wafer, due to higher phonon temperature in the membrane.

In another interesting experiment [250] performed at NIST, the authors showed that both the roughness of the exposed substrate surface in the CPW gap, and the interface between the superconducting metal and the substrate, can have a large effect on the total loss of microwave resonators. However, the TLS contribution to the loss is not affected by the gap roughness, while it is significantly reduced if the Si surface is hydrogen terminated prior to Nb deposition. This work was one of the first to give importance to the method of cleaning and preparing the substrate's surface before the first metal deposition. Among the typical methods, we will briefly comment on the resulting substrate/metal interface quality.

Argon ion milling (or rf-clean) is an effective way to clean crystalline substrates, both from organic and metallic impurities. Being an *in situ* process, the resulting surface should be contaminant-free but, being a physical attack, it is very likely to induce the creation of an amorphous defective layer which may also influence the growth of the overlying metal.

Acid etch is another common method to clean substrates, and the protocol may largely depend on the substrate to be cleaned (*e.g.* a combination of HNO_3 and HF for sapphire substrate, diluted HF for $< 100 >$ silicon, *etc.*). Being an *ex situ* method, the cleaned surface may get contaminated (*e.g.* oxidized) before the substrate could be loaded in the deposition system. The authors of [250] showed that, by performing a fast load (within 3 minutes from the HF dip) into the vacuum chamber, the oxidation of a silicon substrate could be minimized and surface keeps "H-terminated", which means that the deposited metallic atoms will bind directly to a pure silicon surface. At ICIB-CNR, during my PhD work, we established our protocol to realize this cleaning method, and we applied it to all the silicon substrates utilized for the qubit fabrication

(see chapter 8).

3.2 Superconductors

As the choice of the substrate, also the choice of the superconducting material to be employed in the resonator and qubit fabrication is not trivial as may seem.

Most superconducting qubits with long coherence times are made of Al/AlO_x/Al junctions [104, 23], prepared by a double-angle shadow Al evaporation-process that has an intermediate *in-situ* oxidization step, to create a thin layer of AlO_x for the Josephson barrier formation. For many years, aluminum has been the material of choice for highly-coherent qubits, but no strong reason was ever found to discard niobium technology (if not the easiness in the fabrication processes). Moreover, it seems that Al- and Nb-fabricated circuits share the same amount of $1/f$ flux noise and similar coherence levels could be obtained.

Nevertheless, it is very interesting to discuss some results coming from the CPW field.

Recently, rhenium (Re) has attracted a considerable interest [243], due to several of its properties, such as the negligible amount of natural surface oxides, the possibility of epitaxial growth, and the ability to support the growth of epitaxial Al₂O₃ on its surface (see 3.4). Nevertheless, CPWs realized out of rhenium performed well, but only slightly better than the analogous made of Nb or Ta, with a maximum improvement of the Q_0 of a factor 2.

Instead, a very different result came out from CPWs made of TiN [239], which showed the highest Q_0 ever observed for CPW resonator (2×10^7 at high power as from Fig. 3.3). Titanium nitride is an interesting and promising disordered-superconductor to be employed in high quality resonator and qubit also due to the possibility to tune its T_c with N₂ stoichiometry during the deposition, spanning from a (novel) superinsulating regime [236] to $T_c = 4.5$ K.

Also niobium titanium nitride (NbTiN) was recently candidate for the realization

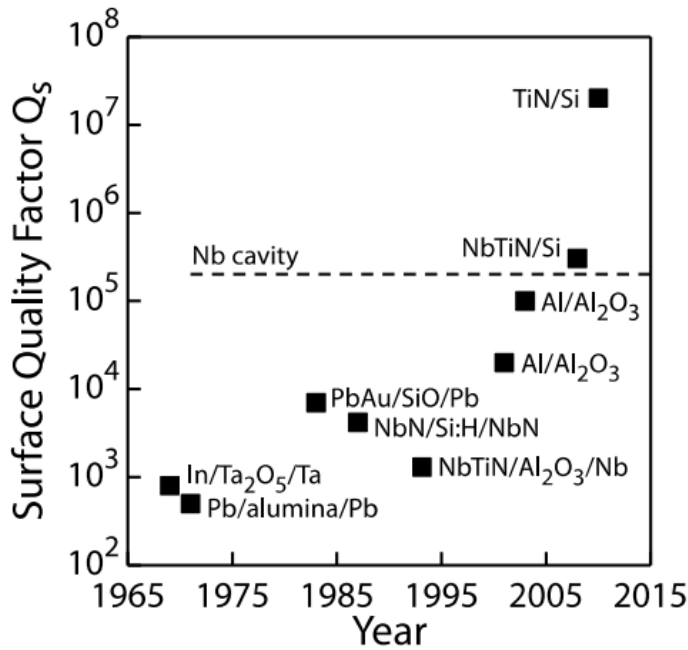


Figure 3.3: Current trend in the improvements of the CPWs resonator's surface quality-factor Q_s . Titanium nitride grown on high-resistivity silicon substrates is currently the material that exhibits the lowest losses, although suffers of aging problems. Figure from T. Klapwijk.

of high-quality superconducting resonators [16]. It is a strongly disordered superconductor, which has a relatively high critical temperature ($T_c \approx 17$ K), a large superconducting gap ($2\Delta \approx 5.9$ mV), and one of the lowest surface resistivity ($R_s \approx 1n\Omega$). NbTiN is already widely used for critical application where the losses are a serious concern, such as mixers for low-noise terahertz receivers, low-loss accelerating rf-cavities, CPW resonators, low-noise superconducting single-photon detectors, *etc.* NbTiN has been shown to follow Mattis-Bardeen theory more closely than Nb, Al or Ta, indicating that it has a minimal dielectric layer compared to the latter materials [14].

If we compare Fig. 3.4 with Fig. 3.2, it is possible to notice how CPWs having the same geometry, but realized out of different superconductor (NbTiN and Al), have ~ 15 dBc/Hz difference in frequency noise spectra, while keeping the same dependence with regards of the choice of the substrate (~ 9 dBc/Hz reduction of noise magnitude for the CPW built on silicon).

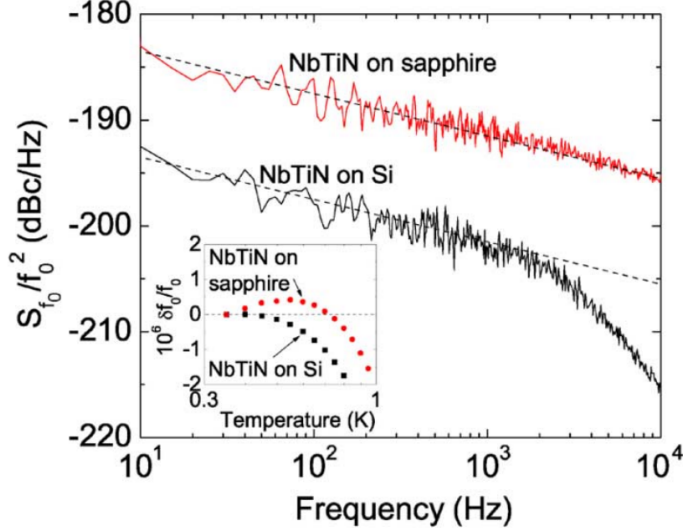


Figure 3.4: Frequency noise spectra of NbTiN CPWs realized on silicon and sapphire substrates, with equal geometry and similar resonance frequency, 3.70 GHz and 3.76 GHz respectively, measured at -30 dBm of internal power and at a bath temperature of 350 mK. The roll-off is due to the resonator-specific response time. The inset shows monotonic temperature dependence of the resonance frequency for NbTiN on Si (black) and a non-monotonic one for the NbTiN on sapphire (red). Figure from [16].

3.3 Dielectrics

The loss tangent for common amorphous dielectrics has generally been ignored, because materials have been assumed to exhibit low loss at low temperatures (see chapter 4). Indeed, microwave loss is negligible ($\tan \delta \sim 10^{-9}$) for the crystalline Si and Al_2O_3 substrates, while it appears to be not negligible for amorphous, glassy dielectrics, as shown in Tab 3.1.

Thus, it is not the nonlinear Josephson inductance – the key to the realization of a superconducting qubit – that limits energy relaxation-times; rather, it is the ”simple” linear self-capacitance of the qubit [153], because it is typically realized by amorphous AlO_x or SiO_2 dielectrics.

The dielectric layer between the junction layer and wiring layer (wiring crossover insulators) and the dielectric used to realize parallel-plate capacitors are then potential sources of the observed decoherence.

It is straightforward to probe the intrinsic loss of candidate dielectric-materials by fabricating and characterizing thin-film linear tank-circuits (LC resonators) in which the material under study forms the capacitor dielectric. At millikelvin temperatures

Table 3.1: $\tan \delta$ values for common microelectronic materials at low temperature and single photon energies. For Nb_2O_5 the $\tan \delta$ value is taken at 4.2 K.

Material	$\tan \delta$
Al_2O_3	[30] $\sim 10^{-9}$
c-Si	$\sim 10^{-9}$
a-Si:H	$2\text{-}10 \times 10^{-5}$
SiN_x	$1\text{-}2 \times 10^{-4}$
Thermal SiO_2	3.0×10^{-4}
AlO_x	1.6×10^{-3}
AlN	1.8×10^{-3}
CVD SiO_2	2.7×10^{-3}
SiO	3.0×10^{-3}
Nb_2O_5	$1\text{-}4 \times 10^{-3}$
MgO	$5\text{-}8 \times 10^{-3}$

and at low microwave drive powers, the internal quality factor of the tank is the inverse of the intrinsic loss tangent of the capacitor dielectric (as extensively discussed in chapter 5). Such measurements were used to demonstrate the high intrinsic loss of the anodically grown Nb_2O_5 , thermal evaporated SiO films used in the first-generation phase qubit circuits, and of plasma-enhanced chemical vapour deposited (PECVD) SiN_x [109].

A recent survey of several candidate dielectrics for qubit circuits indicates that, among amorphous dielectrics, hydrogenated amorphous silicon (a-Si:H) has a particularly low intrinsic loss tangent of order [169].

While at present there is no detailed understanding of the microscopic material origin of dielectric TLS, it is clear that a high density of OH^- defects in amorphous dielectrics leads to significant dissipation at microwave frequencies. Previous experiments on bulk samples of doped quartz revealed a dielectric loss tangent that scaled linearly with OH^- impurity concentration [240]. Typical PECVD-grown SiO films are expected to contain OH^- impurities of a few atomic percent, and the measured loss tangents in these thin films are compatible with an extrapolation of the bulk measurements on doped quartz. By contrast, PECVD-grown SiN_x films grown from

SiH_4 and N_2 precursors display intrinsic dielectric loss tangents more than a factor of 20 lower than SiO films grown in the same deposition system (see Tab. 3.1).

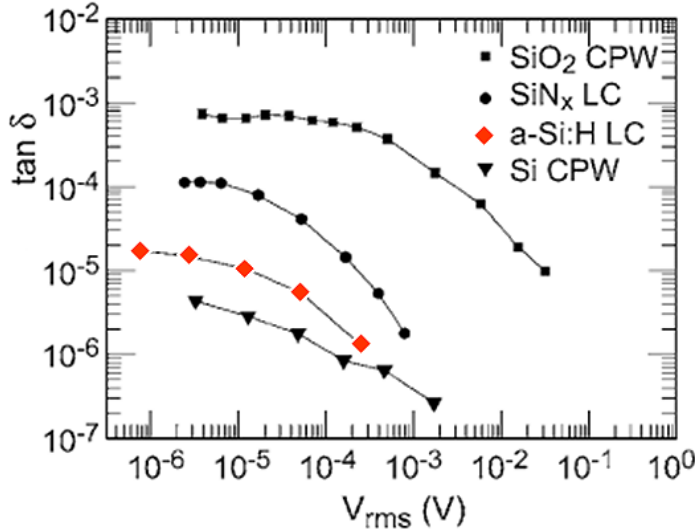


Figure 3.5: Loss tangent versus microwave power for CPW and LC resonators. Data labeled as SiO_2 and Si correspond to 300 nm PECVD SiO_2 on single-crystal Si, and 100 Ωcm single-crystal Si, respectively. In red, PECVD a-Si:H exhibit the lowest losses among amorphous materials. All resonators had Al electrodes. Measurements made at $T \leq 100$ mK. Figure from [169].

As already discussed in section 2.2.7, the straightforward experiment realized by Martinis *et al.* [147] clearly demonstrated how the substitution of low-loss SiN_x instead of lossy SiO , for the realization of the crossover insulator (and by reducing the superconducting area covered by the dielectric), resulted in a significant increase (a factor of 20) in the decay time for the observed Rabi oscillations, jumping from tenths to hundreds of nanosecond, as from Fig. 2.3

In order to avoid losses coming from TLSs in the bulk dielectrics, Cicak *et al.* presented a special design of plate capacitors without dielectric between the plates [41]. the implementation of this type of vacuum-gap capacitors (VGCs) into resonators and qubits showed that VGC-based devices have very low losses, although a slight power-dependent behavior of the losses similar to those arising from TLSs was observed. This leads to the conclusion that, even in VGCs, TLSs exist namely on the Al-oxides and in the small dielectric volume in order to realize the pillars to sustain the standing structure.

Clearly, it is desirable for the capacitance shunting the qubit junction to be entirely free of low-energy defect states. Efforts to incorporate defect-free, crystalline dielectric

thin films into qubit circuits are underway, and some successes were recently obtained by Siddiqi's group [244] and McDermot's group in the USA, by using *c*-Si membranes from SOI (silicon on insulator) wafer and evaporated Al on both sides.

At the same time, a scalable superconducting qubit-architecture, involving a complex circuit-topology with numerous wiring-interconnects, will most likely require a reliable, low-loss amorphous wiring dielectric. Optimization of the growth of the amorphous dielectric films for this purpose will require a deeper understanding of the microscopic physics that drives TLS-induced microwave loss, and a thorough exploration of the phase space for dielectric film growth. This aspects will be covered in more detail in chapter 4, where I will describe how we optimized the growth of high quality a-Si:H and we successfully integrated it in Nb- and NbN-based superconducting qubit.

3.4 Tunnel Barriers

Energy splitting in the energy spectroscopy of phase qubit are generally attributed to TLSs residing in the tunnel barrier: during the last years they have been extensively characterized in terms of their statistics [208, 47] and manipulation [47, 166].

A very recent experiment [86], developed in Ustinov's group at KIT, aimed to study the dependance of the barrier's TLSs on the AlO_x film stress. Introducing a mechanical strain to the qubit during its operation, by means of a piezoelectric placed beneath the sample, the amorphous tunnel-barrier experiences a distortion of the structural lattice of the order of less than a nanometer, which is enough to follow the spectroscopic evolution of each single TLS in its potential landscape.

In order to minimize energy relaxation due to TLS in the qubit tunnel barrier, it is necessary to reduce the density of resonant TLS [153]. This can be achieved in a straightforward way by reducing the area of the Josephson junction. However, reduction in junction area leads to an increase in the coupling matrix element between the qubit and the TLS, and raise the qubit's operational frequency over the 15-18

GHz limit of commercially-available microwave components. This problem can be circumvented by reducing the area of the junction, and then shunting the junction with a thin-film capacitor to maintain the same coupling matrix element between the junction and any remaining TLS. This strategy was employed successfully in the second-generation phase qubit circuits described in [217] (see Fig. 2.4). The resulting devices displayed measurement fidelity approaching 90%, sufficient to perform the first high-fidelity tomography on a coupled phase qubit circuit [216]. An alternative approach is to reduce the density of TLS by improving the quality of the barrier material.

Nearly all superconducting qubits studied to date have employed amorphous aluminum oxide barrier. Studies of junction critical-current noise suggest that the TLS densities in all amorphous oxide barriers are similar [232]. Therefore, reduction of the defect density in the junction will likely require a radically new approach to junction fabrication.

One novel approach, developed at ICIB-CNR during this thesis work, is to realize Josephson barriers made of nitrides, instead of oxides, like AlN or SiN_x, and to perform a nitridization step directly on the barrier, during the trilayer fabrication, in order to test if the barrier uniformity could be further improved and nitrogen vacancies could be filled by the plasma nitridization (see section 8.2).

Another, more radical, approach is to employ a defect-free, single-crystalline barrier for the Josephson junction. While the epitaxial growth of an insulator on a metal is a daunting challenge, there has been some progress in the molecular beam epitaxy (MBE) growth of Re/Al₂O₃/Al junctions with epitaxial barriers [170]. Re and Al₂O₃ are lattice-matched to within 1%; however, growth conditions must be optimized to prevent formation of three-dimensional clusters and promote the two-dimensional growth of the oxide. The critical step is to evaporate the Al at low temperature in a small partial pressure of O₂, and then to crystallize the oxide with a high-temperature anneal at 800° C.

The epitaxial Re/Al₂O₃/Al junctions display a density of TLS reduced by a factor

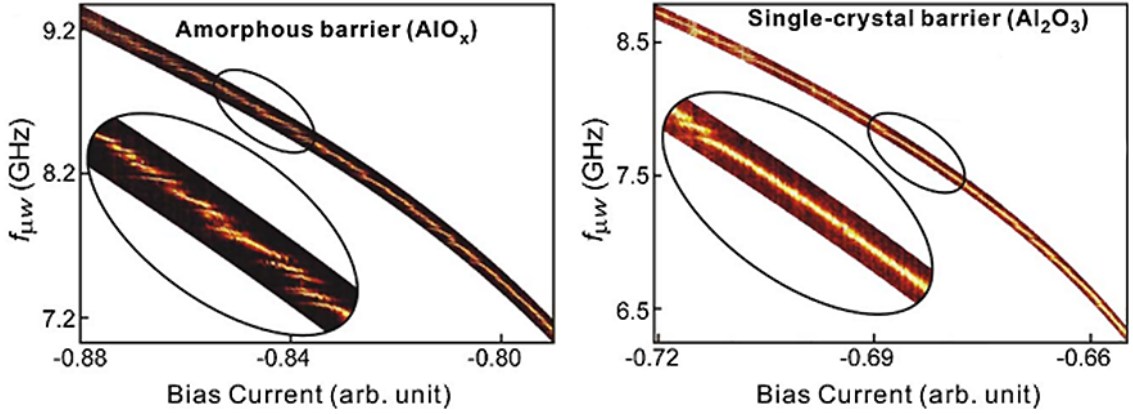


Figure 3.6: Left: qubit spectroscopy of an amorphous-barrier qubit (polycrystal-Al/amorphous-AlO_x/ polycrystal-Al). Right: qubit spectroscopy of an epitaxial-barrier qubit (epitaxial-Re/epitaxial-Al₂O₃/polycrystal-Al). Both qubits have an identical design (qubit junction area of 70 μm²) and the only difference is the tri-layer structure. The amorphous-barrier qubit shows many spectral splittings, while in the case of epitaxial-barrier qubit the density of splittings is substantially lower. Figure from [171].

of five with respect to a typical amorphous junction [171]. There is a suspicion that the remaining TLS reside at the amorphous oxide formed at the interface of the crystalline Al₂O₃ and the amorphous Al counterelectrode, which is grown at low temperature. It is possible that more advanced growth-techniques could circumvent this problem.

We report here another very recent realization [163] of a transmon qubit realized by a fully-epitaxial NbN/AlN/NbN trilayer, showing an energy-relaxation time and a spin-echo decay time of ~500 ns.

Moreover, despite recent progress in the development of crystalline barriers, to our knowledge there have been no experiments in order to investigate the noise in these junctions. During this thesis work, I also started the investigation of epitaxial growth of NbN/AlN/NbN trilayers at high substrate temperature (see section 6.0.2) for the realization of an all-epitaxial junction.

As a final remark in this section, it is important to note that other types of Josephson junctions, namely weak-link devices, are also being pursued as an alternative to conventional tunnel junctions. These geometrically defined junctions can potentially avoid the decoherence associated with amorphous insulating layers. However, the challenge is to ensure that sufficient nonlinearity can be achieved in a robust fashion without any additional loss mechanisms, such as quasiparticle generation. Although weak-link junctions have been studied since the 1970s [133], most measurements have been conducted near the critical temperature where the correlation length diverges and Josephson behavior is observed. At the same time, however, operation at such high temperatures is associated with significant loss and is thus incompatible with quantum circuits. Recent improvements in nano-scale lithography and numerical studies to optimize the performance of weak-link junctions [234] have permitted the current-phase relation and transport current to be engineered with a reasonable level of control [235] and suggest the plausibility of producing weak-link qubits [130]. Another proposal employing phase-slip centers is currently under investigation [158].

3.5 Oxides and Interfaces of Superconductors

I will now introduce some results from several experiments on CPW resonators, which are clearly showing how the loss mechanisms that limit the quality factor of such devices, at low temperature and low power, have to be found in the interfaces between the superconducting layer and both the substrate and superconductor's native oxides.

In 2006, Barends *et al.* investigated the quality factors and phase noise of coplanar waveguide resonators made from Nb and Ta on dielectric substrates at GHz frequencies [13]. In Fig. 3.7 it can be seen that the quality factors saturate below $T/T_c < 0.25$, and that the saturation level increases with the readout power. This effect could not be explained by Mattis-Bardeen theory (according to Eq. 5.1.40) related to superconductivity mechanisms. The power dependence of the quality factor was attributed to a decrease of microwave losses for increasing power levels.

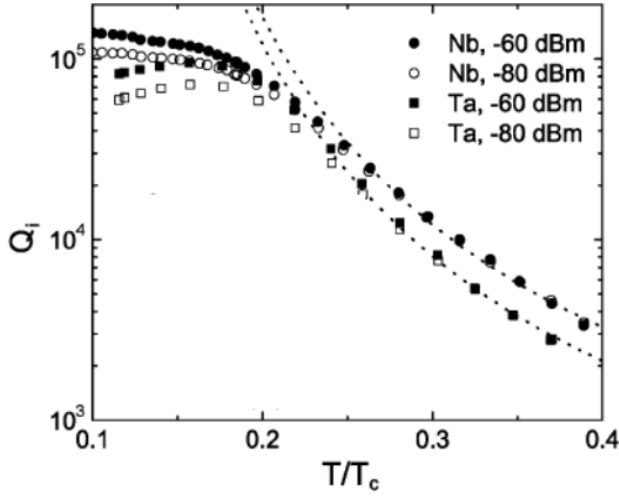


Figure 3.7: Unloaded quality factor of Nb and Ta resonators as a function of the reduced temperature. For very low T/T_c the quality factors deviate from normal Mattis-Bardeen behavior (dotted lines) and saturate due to TLSs in the surfaces. Both materials show the same behavior. The figure is taken from [13].

Furthermore, the resonance frequency showed a non-monotonic temperature-dependence. In Fig. 3.8 it can be seen that above a tenth of T_c the resonance frequency increases with decreasing temperature, whereas below a tenth of T_c the resonance frequency decreases with decreasing temperature (see inset of Fig. 3.8). The temperature dependence of the resonance frequency above a tenth of T_c could be explained by superconductivity-related mechanisms, while below such value the temperature dependence was assumed to be due to TLSs among the substrate. Additionally, an observed $1/f$ like slope of the phase noise of the resonators were suggested to arise from two-level systems among the dielectric substrate. This assumption was confirmed by the interesting fact that, although the materials used for fabrication were different, their quality factors, shifts of resonance frequency, and noise showed the same behavior at low temperatures.

The discoveries of Barends *et al.* have been confirmed in 2007 by Kumar *et al.* [123]. Detailed investigations of the temperature and power dependence of the resonance frequency and frequency noise in quarter-wavelength CPWs made from Nb at GHz frequencies were carried out. In Fig. 3.9 it can be seen that below a temperature of 1.2 K a shift of resonance frequency could be detected, which increased with temperature, while the Mattis-Bardeen theory (see dashed line in Fig. 3.9) would predict a much smaller shift opposite in sign.

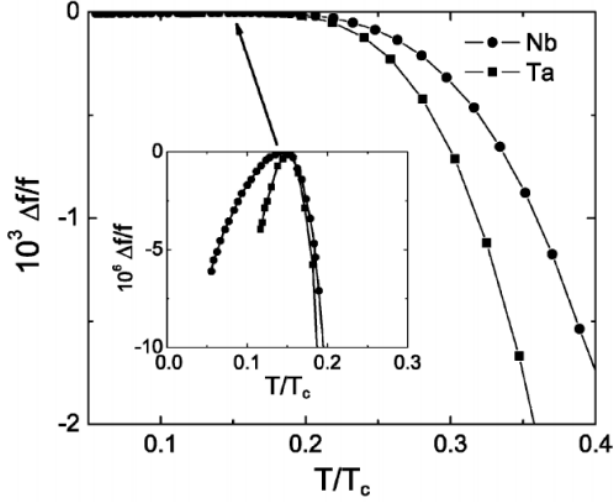


Figure 3.8: Resonance frequency versus temperature. Above a temperature of a tenth of T_c the kinetic inductance decreases with decreasing temperature and the resonance frequency increases subsequently. The inset reveals that the slope changes sign for temperatures below a tenth of T_c . This is assumed to be due to TLSs among the substrate. The figure is taken from [13].

This temperature dependence of the frequency shift was reported to be constant over a range of readout power (which is the applied power) of -96 to -72 dBm and for $T < 900$ mK it could be shown to be proportional to [123]

$$\frac{\Delta f_0}{f_0} \propto C \left[\text{Re} \psi \left(\frac{1}{2} + \frac{hf_0}{2\pi i k_B T} \right) - \log \left(\frac{hf_0}{k_B T} \right) \right] \quad (3.5.1)$$

which is the mathematical expression of a change of permittivity, due to resonant interaction of TLSs in amorphous dielectrics according to the tunnelling model. In 3.5.1 C is a prefactor, f_0 denotes the resonance frequency of the resonator, and ψ is the complex digamma-function. This direct link between the change of permittivity due to TLSs and the change of the resonance frequency of a microwave resonator was a striking evidence of the TLS nature of dielectric losses among superconducting microwave resonators.

In order to find a quantitative relation for the proportionality in 3.5.1, the prefactor was chosen to be $C = \frac{F\alpha}{\pi}$, where α is the density of states n of the TLSs and their dipole moments p . F was called the forming factor, and takes into account the distribution of the electric field in the resonator. It should be quantified the portion of field in the TLSs volume to figure out where the TLSs are situated in the resonator. An obtained value of $F \approx 10^{-2}$ consistent with a reasonable thickness of order of 3

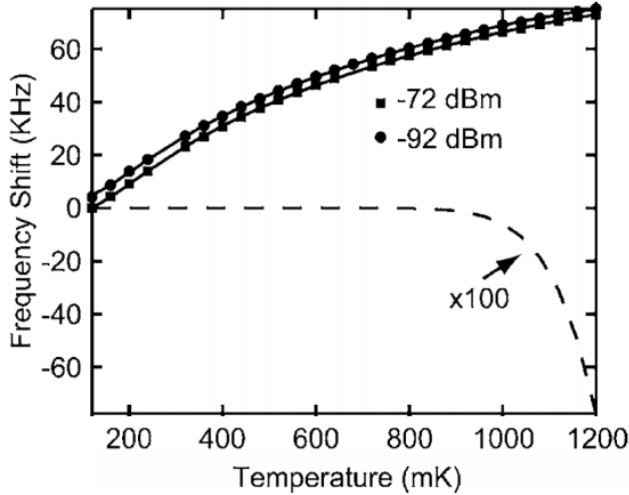


Figure 3.9: The resonance frequency shift, defined as $\Delta f_0 = f_0(T, P) - f_0(120 \text{ mK}, -72 \text{ dBm})$, is plotted as a function of temperature for a readout power of -72 dBm (circles) and -92 dBm (squares). The solid lines represent fits to (3.5.1) due to TLS theory, a further indication for the existence of TLSs in the surfaces. The figure is taken from [123].

nm, led to the conclusion that TLSs are situated in thin layers on the surface of the resonator, *e.g.* are due to oxidation of it. In addition, the temperature dependence of noise of the resonator could be modeled by the TLS theory (for more information the see [123]), emphasizing the assumption of surface distributed TLSs.

In a closely-related work, Gao *et al.* investigated the influence of variation of the center-strip width w of a CPW on its excess frequency-noise [82]. A rapid decrease of frequency noise was found by increasing w , scaling as $1/w^{1.6}$, and a semi-empirical model for TLS noise in superconducting microresonators was deduced, and such model is able to describe this noise effect quantitatively. In this model, a uniform spatial distribution of TLSs within a volume V_h of TLS-hosting material was assumed. V_h occupies some quantitative portions of the total resonator volume V . Furthermore, the authors were able to show that such a volume V_h could be either the substrate interface or the oxide surface, but not the inner volume of the superconducting resonator. This led to the conclusion that in the CPWs dielectric losses arise from surface TLSs, and that the influence of the TLSs can be tuned by the geometry.

The next step was to determine the exact location of the TLSs in a CPW. Therefore, Gao *et al.* used the same CPWs with varying center-strip widths and investigated this time the temperature dependence of the resonance frequency [81]. All resonators showed the same temperature dependence of the shift of the resonance frequency, but

with decreasing center-strip width the magnitude of the frequency shift increased (see Fig. 3.10).

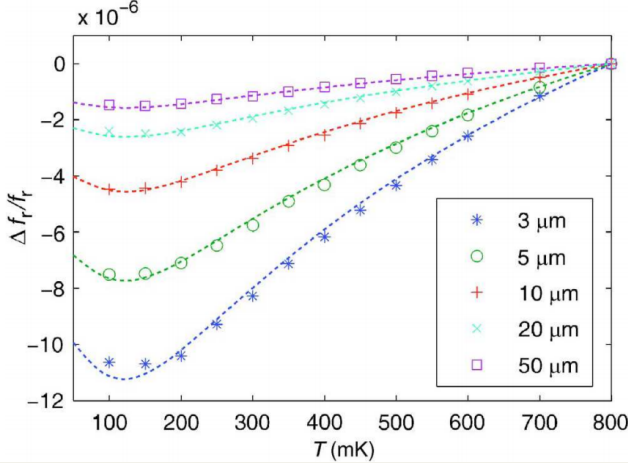


Figure 3.10: The colored lines show the fractional frequency shifts $\frac{\Delta f_0}{f_0}$ as a function of temperature. The markers represent different resonator geometries, as indicated by the values of the center strip width w in the legend. The dashed lines indicate fits to the TLS theory outlined in 3.5.1. The figure is taken from [81].

The forming factor F , introduced in [123], was used to try to gain some information about the location of the TLSs: if TLSs were in the bulk substrate with dielectric constant ϵ_r , the forming factor could be modeled by $F \approx \epsilon_r/(\epsilon_r + 1)$ independent of the center strip width; if instead the TLSs were in a surface layer, F would be dependent on w . The measurement results showed a dependence of F on w (as it can be seen in Fig. 3.10), confirming the existence of surface TLSs in a layer thickness of the order of a few nanometers. Estimation whether the TLSs are situated on the metal surface or the substrate surface, performed by introducing geometrical factors, showed similar values for metal and substrate surfaces. Thus, the exact location stays still unclear.

Another crucial experiment on the temperature dependence of the resonance frequency and frequency noise was done by Barends *et al.* [14] for CPWs made from NbTiN fabricated on different dielectrics, like oxidized silicon, sapphire and hydrogenated silicon. Furthermore, the resonators were partly covered with 10, 40 or 160 nm of sputtered SiO_x .

Interesting conclusions arose from this investigation. On one hand, it could be observed that the temperature dependence of the resonance frequency scales linearly with thickness of the SiO_x layer. In Fig. 3.11 (left), it can be seen that the thicker

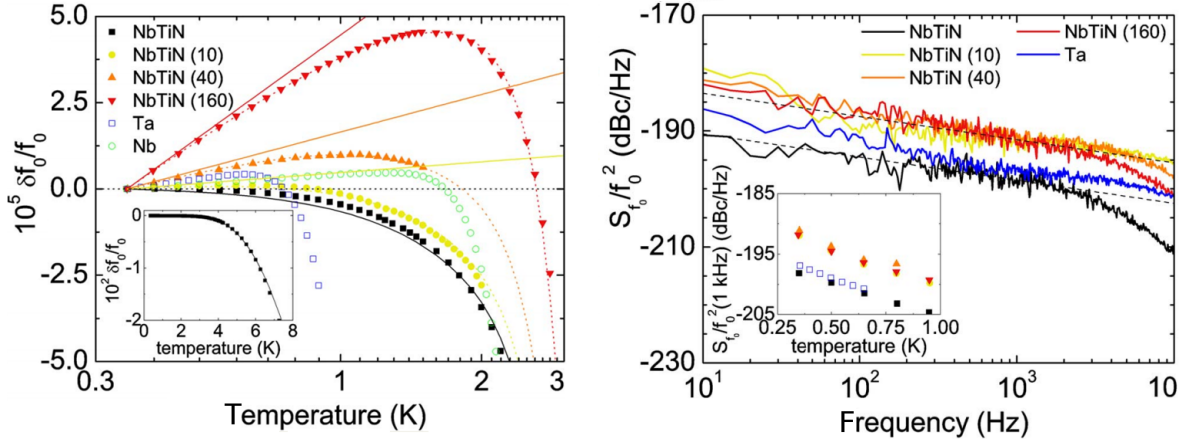


Figure 3.11: Left: The resonance frequency for NbTiN resonators closely follows Mattis-Bardeen theory, unlike Nb, Ta and Al, and depends on volume of the dielectrics deposited on top of the NbTiN. Right: The magnitude of the frequency noise does not depend on the volume of the dielectrics, thus indicating a noise originating on the surfaces/interfaces of the superconductor. Figure from [14].

the SiO_x layer on the NbTiN resonator the more pronounced the shift of the resonance frequency increasing by increasing the temperature below 1.5 K (due to TLSs-based mechanism), while decreasing by increasing the temperature above 1.5 K (due to superconductivity-based mechanisms) [14]. This is the same observation as that made in figure 3.7. On the other hand, the observed increase in noise is noticeably independent of the thickness of the SiO_x layer, as from Fig. 3.11 (right). These observations were interpreted as that the resonant-frequency temperature-dependence is due to TLSs in the dielectric volume sputtered on top, whereas the observed increase of the noise is due to the interface between superconductor and SiO_x layer. Moreover, the noise level of Ta and uncovered NbTiN was very similar, whereas the resonance frequency dependence showed to be clearly non-monotonic (caused by TLSs) for Ta, while for uncovered NbTiN it followed Mattis-Bardeen theory (caused by kinetic inductance, see 5.1). This observation suggested that the contribution of surface TLSs is dependent on the superconducting material itself. It is possible to interpret this result as that there are less TLSs on the NbTiN's surfaces than on the Ta's one. In addition, the noise increased when using sapphire instead of silicon as a substrate,

indicating that the choice of crystalline substrate affects the frequency noise. This again points towards an influence to noise by the superconductor-dielectric interface. This conclusion was even strengthened by the fact that, for NbTiN on sapphire, the non-monotonic temperature dependence of the resonance frequency was analogous to that of NbTiN on Si covered by SiO_x . This led to the conclusion that TLSs are situated in superconductor-dielectric interfaces as well as in superconductor-substrate interfaces. The hydrogenation of the Si substrate showed a strong decrease of loss, which led to the conclusion that the TLSs were present in the form of dangling bonds in the dielectric. A recent investigation of Lindström *et al.* confirmed the assumption that TLSs are situated in the superconductor-substrate interface [132]. Investigating half- as well as quarter-wavelength CPWs, the temperature and power dependence of the dielectric loss could be shown to arise directly from resonant absorption processes of TLSs.

Moreover, it shall be mentioned that investigations of Macha *et al.* [141] led to the same conclusions as discussed in the work of Lindström, when investigating the temperature and power dependence of dielectric losses (see Fig. 3.12). Interestingly, the influence of the TLSs is of the same order of magnitude for all investigated superconductor (Nb, Al)-substrate (Si, sapphire) combinations, thus confirming the suggestion of a common nature of TLSs in CPWs surface/interface defect-states.

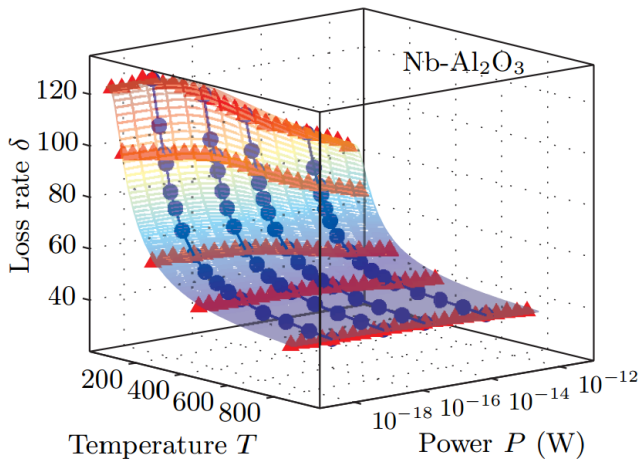


Figure 3.12: The complete description of the loss illustrated for a Nb on sapphire sample. The grid is generated using the theory described in [132], and is separated in the temperature and the power dependence part. Blue circles and red triangles show the measured data of the temperature- and of the power-dependence, respectively. The figure is taken from [141].

By comparing this result with the ones obtained with CPWs made from NbTiN

(see [14]) and Re, it can be assumed that it is possible to reduce the influence of surface distributed TLSs by using superconductors with reduced amount of natural-growing surface-oxides.

Also the geometry of the resonator does play a consistent role in the overall frequency noise of the system, most likely due to the variation in the electric fields densities with the resonators dimension. In Fig. 3.13 it is possible to observe how the frequency noise of a NbTiN on Si CPW resonator, measured at 350 mK, decreases by increasing the CPW width S and gap W .

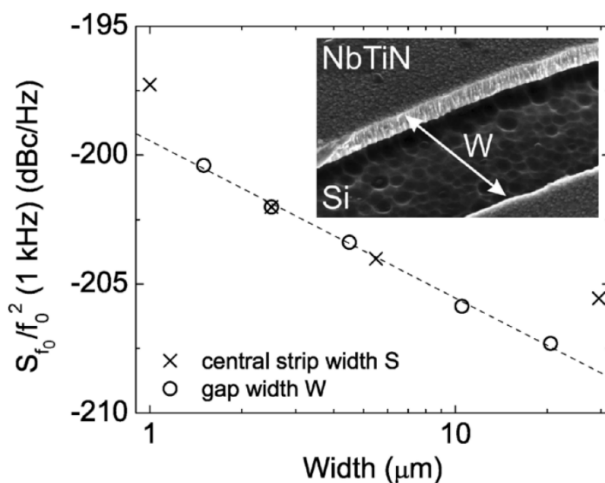


Figure 3.13: The frequency noise of a NbTiN on Si CPW resonator, measured at 350 mK, decreases by increasing the CPW width S and gap W . Figure from [15].

It is interesting to discuss also the results obtained by Koch *et al.* [116], who, by studying the $1/f$ flux noise in SQUIDS and qubits, indicated that the observed noise-levels are in reasonable agreement with the recurring defect's density of $5 \times 10^{17} \text{m}^{-2}$ [153, 199].

There are many candidates for defect centers. In amorphous SiO_2 , they include E' center variants, the nonbridging oxygen hole center (NBOHC), and the superoxide radical [89]. In addition, the amorphous oxides of superconductors, such as AlO_x and NbO_x , contain large densities of defects of various sorts: for example, the concentration of OH^- defects in AlO_x can reach several percent [147, 198]. Moreover, the defect density of thermal NbO_x is $\sim 10^{20}$ defects/ cm^3 near the surface and less in the bulk (the atomic density is $\sim 10^{23}$ atoms/ cm^3) while Titania (TiO_2) has a defect

density which is 4 orders of magnitude lower than NbO_x , namely $\sim 10^{16}$ defects/cm³.

The value of $5 \times 10^{17} \text{m}^{-2}$ is 6 orders of magnitude higher than the value of about 10^{12}m^{-2} reported from measurements of two-level systems in Josephson junctions [147]. However, the two situations are physically very different. The thickness of the tunnel barrier is 2-3 nm, and the barrier is protected with a metallic layer immediately after its formation, before it is exposed to any contaminants. In contrast, the SiO_2 layer on a Si wafer is typically 100-300 nm thick and, because of its exposure to processing chemicals and the atmosphere, it is covered by contaminants that are likely to be highly disordered. For a 100 nm thickness, an areal density of $5 \times 10^{17} \text{m}^{-2}$ corresponds to 1 defect in 10^4 atoms, which does not seem unreasonable. This areal density is also comparable with estimates of trap densities on silicon surfaces that have been exposed to similar atmospheric conditions [211]. Furthermore, room-temperature scanning tunnelling microscope (STM) experiments [118] on ultraclean silicon surfaces, that were exposed to a low level of oxygen in an ultrahigh vacuum system, revealed as many as eight near-surface two-level systems in an area of $2 \times 10^{17} \text{m}^{-2}$ in a 10-500 Hz bandwidth, corresponding to $2 \times 10^{18} \text{m}^{-2}$ over 13 decades of frequency. Thus, the areal density of $5 \times 10^{17} \text{m}^{-2}$ does not seem beyond the realm of possibility.

Having located the TLSs, responsible for the observed losses in CPW resonators and decoherence in qubits, to reside on the substrate/superconductor interface, and on the surfaces of both the substrate and the superconductor, many authors are starting the investigation of possible surface treatment, in order to reduce the TLSs' density. In an unpublished research done in McDermott group [180], they studied flux-noise in SQUIDs after the deposition of thin layers of Fe (0.01 - 0.3 nm) and they found that the flux-noise magnitude increases by one order of magnitude, while the inductance-noise decreases by the same amount. Surface treatments with fluoroalkyl-trichlorosilane (FTS – a self-ordering magnetic polymer) showed similar results.

In this context, among the various treatments that could be performed to the surfaces (carbideization, fluoridization, and other treatments discussed in section 4.2),

one is attracting considerable interest: the deposition of a thin layer of copper monoxide (CuO) in its monoclinic crystallographic phase. This material manifests a well known antiferromagnetic ordering at low temperature ($T_N = 230$ K) [84]. It was recently discovered that the magnetic ordering could be induced by proximity effect [161]: the so-called proximity effect manifests itself as a mutual induction of physical properties from one material into an adjacent one, across their interface. In the most famous example, superconducting electron pairs are induced in a neighboring normal metal, and conversely, normal electrons in the metal permeate the superconductor. However, at the interface between a metal and an insulator, one would not expect such a behavior.

On the contrary, the authors of [161] showed the evidence for a subtle proximity effect, that arises between a normal metal and CuO, an antiferromagnetic Mott insulator, where strong Coulomb interactions prohibit electronic conduction. This new phenomenon may also provide a new mechanism to control spins at solid-state interfaces, as well as possible applications in spintronic and superconducting qubit devices.

Chapter 4

Hydrogenated Amorphous Silicon

In 1971, Zeller and Pohl [256] showed that the low temperature behavior of glasses drastically differs from that of perfect crystals. Even more fascinating was the discovery of almost universal thermal properties among glasses. This caused an increasing interest in the understanding of glasses, and glass physics arose as an intensively pushed field of natural science. At that time, the thermal properties of dielectric solids (like glasses) at low temperatures were expected to be determined by phonons of long wavelength. Phonons are characterized by the elastic behavior of the medium averaged over a distance comparable with their wavelength. At temperatures $T < 1$ K, the wavelength of the dominant phonons is a thousand times larger than the interatomic distance. Therefore, no difference between the behavior of glasses with their disordered structure and that of crystals with their regularly constrained lattice was expected [9].

However, observed anomalous phenomena of the specific heat and the thermal conductivity of glasses [219] pointed out to have their origin in the disordered structure. In 1972, independent of each other Anderson [6] and Phillips [185] worked out a theoretical description, which was able to explain the anomalous low-temperature properties of glasses. In this description, defects in amorphous solids were expressed by double-well potentials leading to the assumption of two-level systems (TLSs) in

the amorphous solids which are able to tunnel through the potential-well barriers. Thus, this model was called the *tunnelling model*. With the help of this model, the anomalous specific heat of glasses could be deduced from the relaxation effects of TLSs with a broad distribution of energy splittings between their levels [67]. Observed nonlinear ultrasonic attenuation [9], dielectric loss [220], as well as variations of the dielectric permittivity, and the sound velocity in glasses could be explained by the tunnelling model in terms of resonant absorption of phonons or photons by TLSs at very low temperatures and low-energy excitations.

In very recent times, new interest in the anomalous properties of glasses at low temperatures arose from the field of superconducting quantum-engineering. For instance, the superconducting phase qubit, has been reported to suffer from two-level tunnelling systems (TLSs) in its vicinity, which couple to the qubit and extract energy from it leading to strong decoherence [147]. In principle, a superconducting phase qubit consists of a superconducting loop interrupted by a Josephson junction (JJ). It was shown that decoherence is stronger if dielectrics with high dielectric losses are used in phase qubit fabrication [147]. This showed that the TLSs responsible for the qubit decoherence and for the dielectric losses are identical.

Consequently, dielectric loss in amorphous thin films was intensively investigated in the last years, leading to remarkable results. Investigations with superconducting microwave resonators were able to show that TLSs are situated in the bulk dielectric materials [169], as well as in thin layers on the surfaces of such devices [13, 123, 81]. These TLSs were shown to be of the same origin as those found in glasses three decades ago, in perfect agreement with the predictions of the tunnelling model [132, 141, 178]. Although a wide understanding of TLS processes in superconducting microwave devices could be established, open questions remained. Especially absolute values of dielectric losses and their dependence on frequency have not been reliably investigated yet. On the other hand, this fact is of great importance for qubit development. According to investigations of dielectric loss in bulk glasses [240] and to recent results in this regard by superconducting microwave devices, the TLS density of states is

assumed to be constant in regard to dielectric loss [132, 141]. However, investigations of the specific heat of glasses [219] have figured out that the TLS density of states is indeed frequency dependent.

Moreover, it is very important to note that currently there is no direct knowledge of the low-temperature quality of the dielectrics at low frequencies, which may be crucial in order to improve coherence times in qubits.

We have already discussed about the TLS tunnelling model in section 2.3.1, and about several dielectric materials in 3.3: now it is time to introduce our dielectric of choice, namely the hydrogenated amorphous silicon.

4.1 a-Si:H

As showed by O’Connell *et al.* [169], the lowest-defective amorphous material with extremely low $\tan \delta$ among conventional dielectrics (such as SiO, SiO₂, SiN_x) is hydrogenated amorphous silicon (a-Si:H), having a high structural coordination number and defects passivated by hydrogen. Because of its low $\tan \delta$, it is considered as the best amorphous dielectric material for superconducting qubit and microwave resonator applications [149].

This is compatible with data on acoustic attenuation in a-Si:H and a-Ge:H that suggest a TLS density of states which is two orders or magnitude lower than that of typical glass films [188]. There has been speculation that the fourfold coordination in these covalently bonded films tends to overconstrain atomic-scale defect-states and thereby suppress the density of low-energy excitations [185].

One of the methods for low-defective a-Si:H film growth, widely used for fabrication of solar cells, optical waveguides, and MEMS, is the plasma enhanced chemical vapour deposition (PECVD) [53], where silane (SiH₄) is plasma-decomposed in hydrogen ions and other reactive species, and condensation of a-Si:H takes place on a heated substrate (150-300 ° C, typically) to form an amorphous hydrogen-rich film [54]. From the microelectronic point of view, a-Si:H is a suitable material both for

the fabrication of wiring insulator and of Josephson junction's tunnel barrier [121].

In the framework of the PhD activities, our ICIB-CNR group established several collaborations with other institutes in order to acquire the best know-how to deposit and analyze the a-Si:H. All the fabricated qubit and resonators employing a-Si:H were realized at the ENEA (Portici), which is an Italian leading institution for what it concerns the photovoltaic applications of a-Si:H, in collaboration with Dr. P. Delli Veneri and Dr. L. V. Mercaldo. At IMM-CNR (Napoli), we tested an alternative deposition system and we characterized the resulting films by means of FTIR analysis, in collaboration with Dr. G. Coppola and Dr. M. Iodice. At Unina-INFN (Napoli), and in collaboration with Prof. D. K. Basa (Utkal University, Bhubaneswar, India), we discussed about the possibility to extend our studies to another promising material, namely hydrogenated amorphous silicon carbide (a-SiC:H).

After several preliminary depositions of a-Si:H, exploring the deposition parameter-space along the temperature (150° - 250° C) and the silane/hydrogen dilution (1:0-1:2) axes, we determined the optimal receipt in order to: obtain the best a-Si:H adhesion on both silicon substrate and niobium films, avoid interface-bubble formation, maximize the FTIR peaks relative to Si-H stretching mode and Si-H bending mode (seen next section) and, of course, reduce as much as possible the low temperature dielectric losses (as will be extensively discussed in chapter 5).

The deposition parameters that ensured the lowest defective a-Si:H films were:

- $P_{SiH_4} = 200$ mTorr 40 sccm
- Power = 5 W
- $f = 100$ MHz
- $T_s = 250^{\circ}$ C
- Rate = 3 nm/s

The PECVD requires a high process temperature (250° C) and the presence of

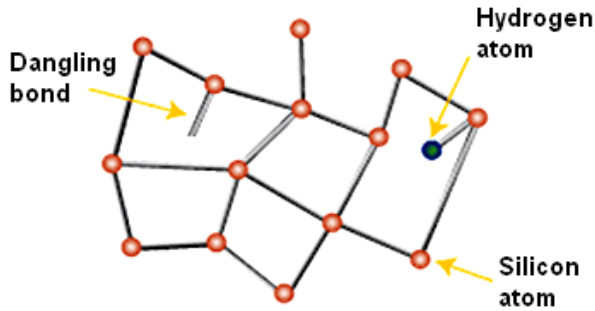


Figure 4.1: The structure of amorphous silicon is typically highly defective due to a large number of unsaturated silicon bonds. The incorporation of hydrogen atoms in the film structure has the effect to lower the defectivity by saturating the dangling bonds.

energetic hydrogen ions during the a-Si:H layer growth. Therefore, the incorporation of PECVD a-Si:H deposition into the Nb technology requires attention due to the possible degradation of the superconductivity of the Nb films by two physical processes: 1) oxygen diffusion from the surface Nb oxides and 2) hydrogen diffusion inside the Nb films. We studied the influence of the a-Si:H deposition by the PECVD on the superconducting and crystalline properties of 20 nm Nb films treated by two surface protection methods: plasma nitridation and thin protective Si layer.

4.1.1 Material Analysis

The thin a-Si:H films (typically ~ 250 nm), deposited under the optimal conditions, were investigated by means of several techniques. Optical microscopy and SEM analysis confirmed the absence of macroscopic interfacial defects, such as bubbles and cracks, between the grown material and the substrate. The average surface roughness of 3.3 nm (Fig. 4.2) and a good step coverage were observed.

Moreover, Raman investigation confirmed the pure amorphous nature of the material under investigation. Indeed, in Fig. 4.3 are clearly identifiable the 480 cm^{-1} peak, typical for the amorphous Si, and the LA and LO structures, characteristic for hydrogenated a-Si, as from the Raman peak analysis performed in [22]. It is significant to note the complete absence of the peak relative to the crystalline phase of the Si-Si bonds, namely the 520 cm^{-1} peak, which once more confirms the good properties of the deposited insulator.

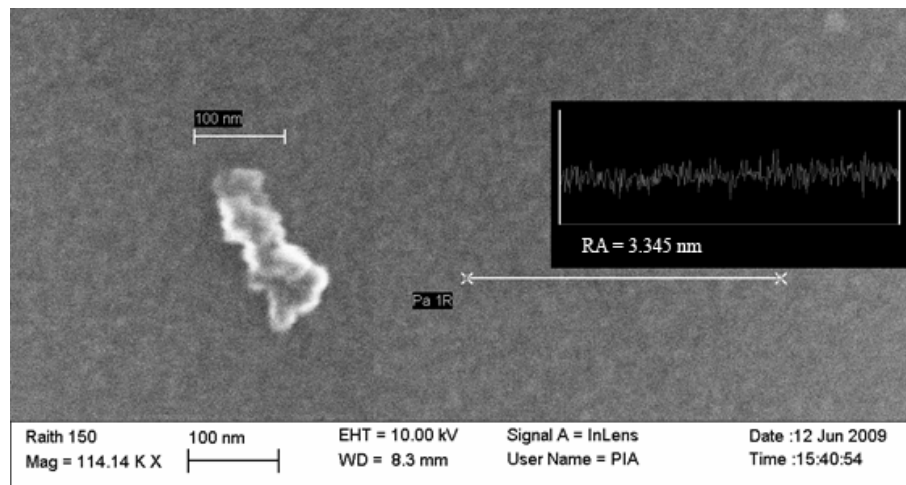


Figure 4.2: SEM investigation of the a-Si:H surface, in terms of the average surface roughness.

FTIR characterization of a-Si:H deposited at the IMM institute of CNR, Napoli, by means of an OXFORD PlasmaLab PECVD reactor, gave us other information about the quality of the deposited a-Si:H at the chosen parameters, by quantitative analysis of the atomic bonds in the amorphous structure.

The a-Si:H was deposited with the following parameters:

- $P_{SiH_4} = 600$ mTorr (600 sccm)
- $T_s = 250^\circ$ C
- RF Power = 2 W
- Deposition rate = 32,4 Å/min

Several substrates have been used, among which Si $\langle 111 \rangle$ wafers and R-plane sapphire (from ICIB-CNR), and Si $\langle 100 \rangle$ and $\langle 110 \rangle$ wafers (from IMM).

It has to be noted that some of the a-Si:H was grown on a previously photolithographically-patterned niobium-layer present on the samples, in order to incorporate the a-Si:H in the circuit as capacitor's dielectric and as wiring insulator.

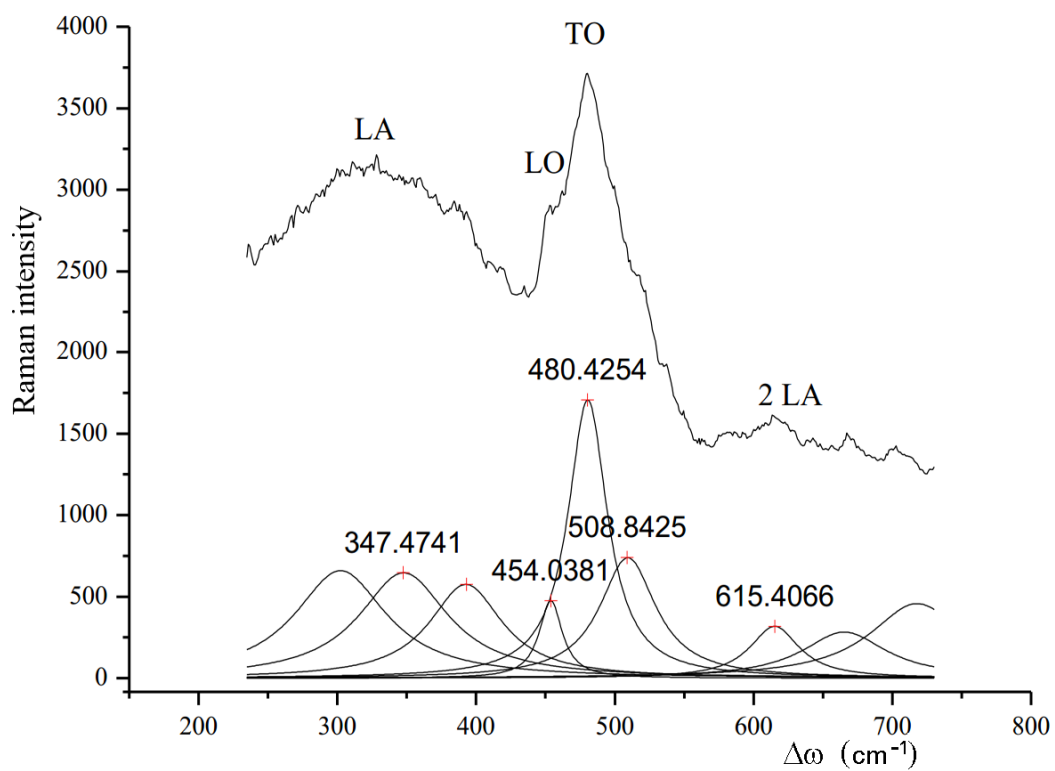


Figure 4.3: Raman peak analysis performed as from [22]. The 480 cm^{-1} peak, typical for the amorphous Si, and the LA and LO structures, characteristic for hydrogenated a-Si, are clearly identifiable.

The FTIR characterization started with the acquisition of the substrate spectral-absorbance in the 400 - 4000 cm^{-1} range. Here is the data collection information and spectrometer description for a typical FTIR analysis:

Number of sample scans: 64

Source: IR

Detector: DTGS KBr

Beamsplitter: KBr

Mirror velocity: 0,1581

Aperture: 100,00

Sample gain: 8,0

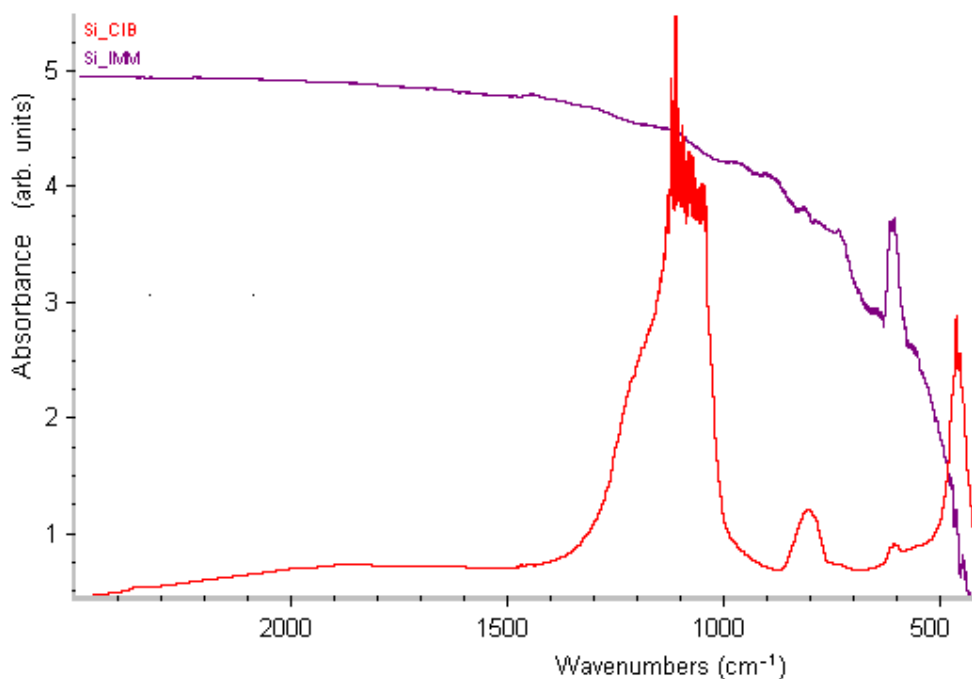


Figure 4.4: Comparison of the FTIR spectra of ICIB c-Si substrate and the typical IMM ones.

Every spectral curve is acquired after a background noise acquisition. This process is important to get rid of the (large) noise introduced by atmospheric attenuation

(CO₂ and H₂O) in the optical path, which in principle could be reduced by fluxing N₂ inside the FTIR instrument (not yet installed at the time of this analysis).

Another reason to perform the background acquisition is to take into account the presence of the substrate and be able to subsequently cancel out its presence, as if the FTIR spectra are only due to the material under observation, with (at least in principle) no substrate influence.

All the IMM silicon substrate's absorbance spectra were closely resembling the typical fingerprint expected for c-Si, with no difference on thickness, doping, crystallographic orientation, resistivity, *etc.* Instead, as it could be easily seen from Fig. 4.4, the silicon substrates from ICIB showed a spectral fingerprint which is completely different from the expected one, and the origin of this difference is still of unknown nature.

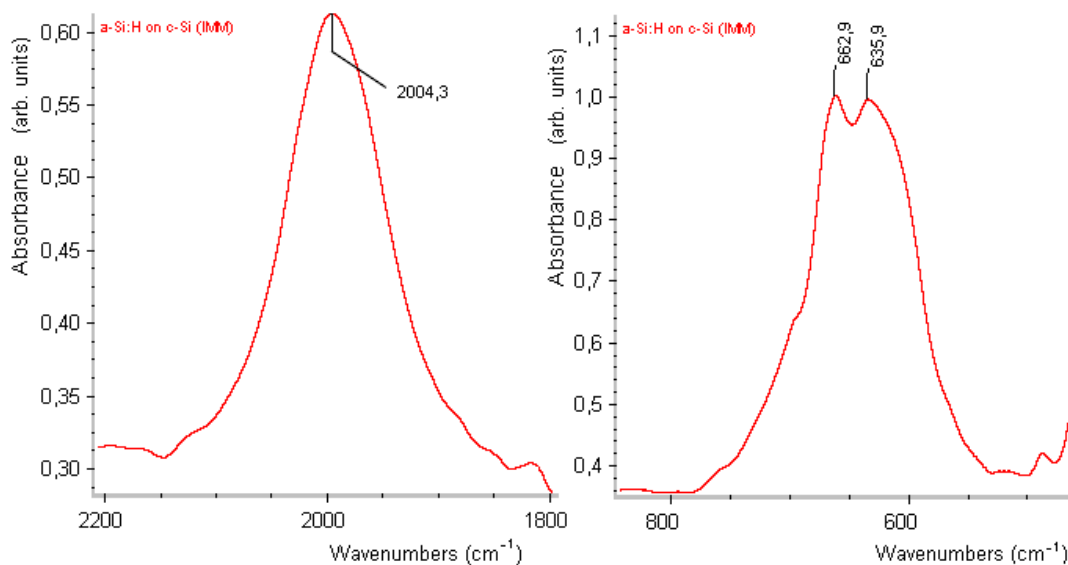


Figure 4.5: Transmission infrared absorption spectrum of 260 nm thick PECVD a-Si:H film deposited on IMM c-Si substrate at 250° C. Left panel: the $\sim 2000 \text{ cm}^{-1}$ Si-H stretching mode. Right panel: the $\sim 640 \text{ cm}^{-1}$ Si-H bending mode.

By analyzing the a-Si:H deposited on the IMM substrates, we clearly identified the $\sim 2000 \text{ cm}^{-1}$ and the $\sim 640 \text{ cm}^{-1}$ adsorption peaks, due to the Si-H stretching mode and Si-H bending mode, respectively (see Fig. 4.5). Also in the reflectivity

analysis and in the SAGA (grazing angle) analysis, we could identify the same peaks as expected.

By analyzing the a-Si:H deposited on the ICIB c-Si substrates, it has to be noted that the difference of substrate absorbance (Fig. 4.4) could not be compensated by removing the contribution of the substrate during the FTIR data analysis: we have not been able to find the fingerprint peaks of the a-Si:H at $\sim 2000 \text{ cm}^{-1}$ or $\sim 640 \text{ cm}^{-1}$ by means of any type of investigations (absorbance, reflectance, SAGA).

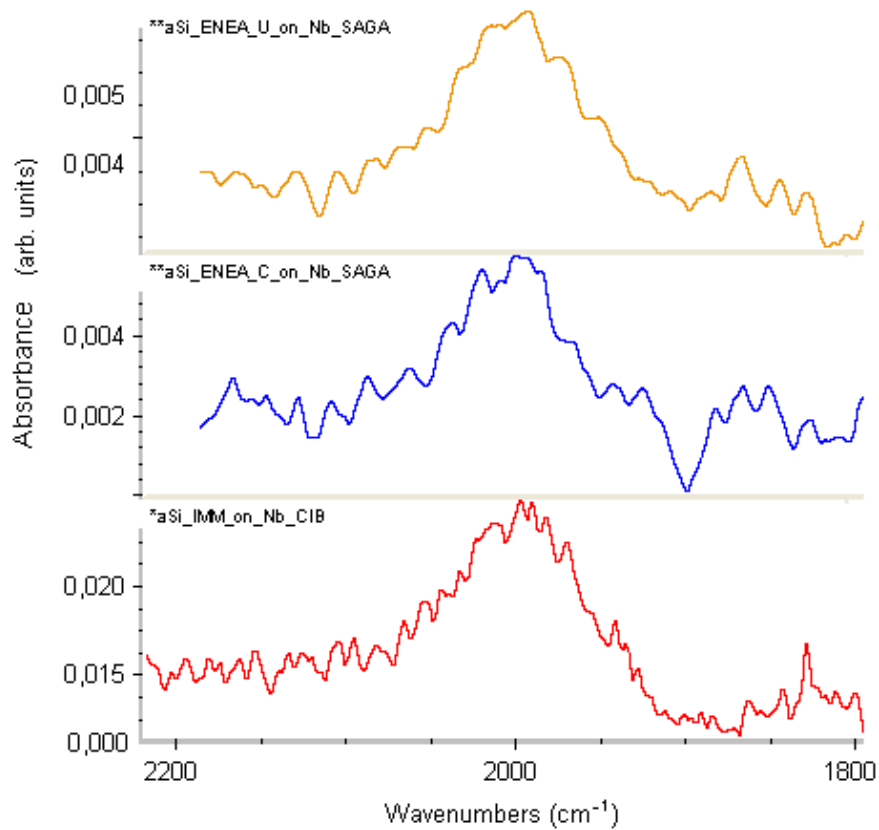


Figure 4.6: SAGA characterization of the $\sim 2000 \text{ cm}^{-1}$ peak of different a-Si:Hs on Nb. Top: a-Si:H deposited at ENEA (family "U"). Middle: a-Si:H deposited at ENEA (family "C"). Bottom: a-Si:H deposited at IMM.

The only method that was found to be suitable in order to highlight the presence of the peaks due to hydrogen inclusion in the a-Si:H films was the analysis of the reflectivity spectra coming from the material deposited on the niobium layer, with

allowed us to get rid of the strong and anomalous contribution from the ICIB *c*-Si substrates.

By means of SAGA characterization of a-Si:H on Nb, we also compared the IMM deposited material with similar a-Si:H previously deposited by PECVD at ENEA (Portici) (Fig. 4.6). We confirmed the repeatability of the sample FTIR spectral characteristics and the reliability of the deposition conditions.

As a result of the investigations with the FTIR method and even in the absence of a Gaussian deconvolution software to analyze the weight of the 2000 and 2100 cm^{-1} peaks, it seems that the 2000 cm^{-1} one is by far the spectral main peak, confirming the quality of the deposited a-Si:H at the chosen parameters. In fact, the peak at $\sim 2100 \text{ cm}^{-1}$, which is caused by Si-H₂ stretching-mode vibrations, is evidently absent in the characterized a-Si:H films (see Fig. 4.5 and 4.6).

4.2 Integration in Nb Technology

Niobium, as a refractory superconductor, is still considered as a fundamental material for fabrication of robust and reliable Josephson devices for a number of key applications, such as biomedical SQUID application, high-speed superconducting digital circuits (RSFQ), mm-wave receivers and sub-millimeter wave mixers, and as voltage standard. The high robustness and reliability of Nb Josephson devices, as well as Nb high thermal and chemical stability, attracted the researchers to apply the Nb technology for realization of superconducting qubit based on Josephson effect [136, 245, 19].

It is important to note that, for a qubit realization, the a-Si:H film has to be deposited on the top of patterned superconductor layers which locally act as metal substrate for the PECVD process. The requirement of a relatively high substrate-temperature and the presence of energetic hydrogen-ions during the PECVD process can easily deteriorate the Nb superconducting properties by means of two physical processes: (1) the oxygen diffusion from the surface oxide, naturally present before

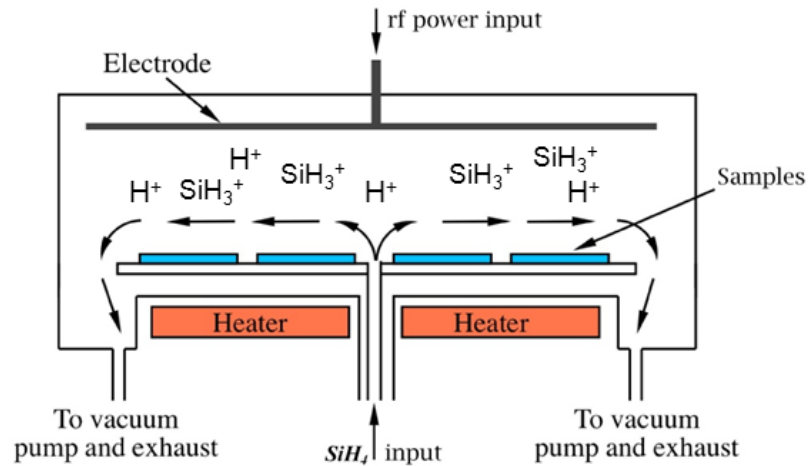


Figure 4.7: Schematics of the PECVD reactor used for the a-Si:H deposition. In the chamber, the samples are subject to heating at $\sim 250^\circ\text{C}$ and to a highly reactive hydrogen plasma.

the insertion of the sample inside the PECVD chamber, and (2) the penetration of the hydrogen inside the metal during the a-Si:H deposition.

In fact, it is commonly known that the addition of interstitial oxygen and hydrogen to Nb deteriorates its superconducting properties, specially its superconducting transition temperature T_c [95, 55, 251]. The dissolution of the natural oxide-layer on a Nb surface, accompanied by the oxygen diffusion into the Nb bulk, has been observed to start at 150°C and reach a maximum at $\sim 300^\circ\text{C}$ [52], as from Fig. 4.8. This effect is also expected during the PECVD process, when the Nb film must be heated up to $\sim 250^\circ\text{C}$ in order to produce high quality a-Si:H films.

Furthermore, it is well known that, since Nb is a strong getter material, the hydrogen is efficiently adsorbed and diffused into the films, leading to the so called "hydrogen Q disease", a degradation of the quality factor of superconducting Nb RF-cavities [8]. Thus, it is clear that the incorporation of PECVD a-Si:H into the Nb technology requires careful attention, due to the possible degradation of the superconductivity of the Nb films.

All the available data show that there are two main methods to prevent the oxygen

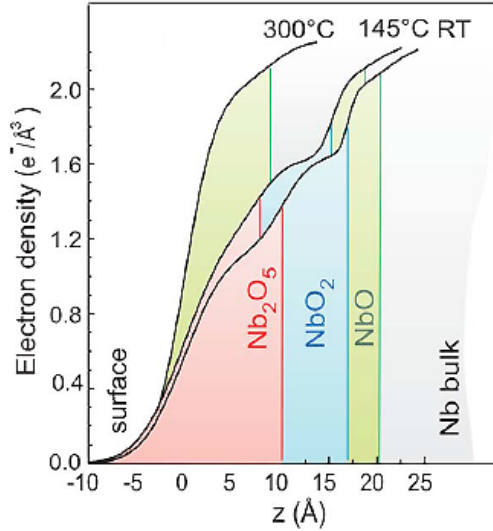


Figure 4.8: Diffusion of natural-occurring Nb-oxides due to the increase of the temperature. The process starts at $\sim 145^\circ\text{C}$. Figure from [52].

and hydrogen diffusion inside a Nb film. The first is the plasma nitridation of the Nb surface, which has been successfully utilized in order to prevent the oxygen diffusion in Nb wiring and to maintain its superconductivity after annealing at 300°C [201]. The plasma nitridation seems to be an effective method also to prevent the hydrogen diffusion inside a Nb film because of the trapping of hydrogen by additional interstitial sites produced by nitrogen trapping near the film surface [182, 155]. It is important to note that the trapping effect takes place also in case of interstitial oxygen and interstitial carbon [182]. The second method is the deposition of a sputtered thin ($\sim 3\text{ nm}$) amorphous silicon (a-Si) layer on the Nb film. As was reported in [121], the Nb base electrode was protected from the hydrogen diffusion during the fabrication of a-Si:H tunnel-barrier Josephson junctions by the use of this method.

4.2.1 Nb:H - Superdiffusion

In this section, we investigate the effect of the PECVD of the a-Si:H film on the superconducting properties of a Nb film. In particular, the measurements of the superconducting transition-temperature T_c and residual resistivity ρ_0 were correlated

with the X-ray diffraction (XRD) analysis applied to estimate the oxygen and hydrogen diffusion inside the Nb films. Nitridation of Nb films and deposition of a sputtered thin a-Si layer on the Nb films (in both cases made *in situ* after the Nb-film deposition) were investigated as methods to protect the Nb films during the PECVD process.

Nb films were deposited at ICIB-CNR on 3 inches Si-substrates by DC magnetron sputtering in a cryo-vacuum deposition-system, at an Ar pressure of 2.0×10^{-3} Torr at room temperature. The base pressure was in the 10^{-9} Torr range. The Nb films were fabricated at low deposition rate (0.35 nm/s). Films of niobium with thicknesses of 20.6 ± 2.2 nm, 51.1 ± 6.4 nm, and 90.6 ± 2.1 nm were deposited, as measured by a Tencor AlphaStep 100 profilometer.

The minimal thickness of ~ 20 nm was chosen as a compromise in order to satisfy two requirements: to obtain a measurable effect of the oxygen and hydrogen diffusion on the superconducting properties (a thinner film is favorable) and to provide sufficient material thickness for the XRD analysis (a thicker film is favorable). Some of the 20 nm thick samples (identified as Nb(20)) were left untreated after the deposition and subsequently exposed to natural oxidation in air. Another part of the 20 nm thick samples was treated *in situ* by RF-nitrogen plasma-process for 3 min before breaking the vacuum. We identify these samples as Nb(20)/Nb Nitride. The nitrogen pressure was 2.0×10^{-2} Torr and the DC bias voltage was -200 V; these conditions seem to give an efficient growth of a 3-5 nm thick nitride layer [201]. The last part of the 20 nm thick samples (identified as Nb(20)/Si) were protected *in situ* by a 3 nm thick RF-sputtered a-Si film, before breaking the vacuum. The 50 nm and 100 nm thick Nb samples were not subjected to any surface protection treatment.

Subsequently, all the films were patterned by UV photolithography and etched by reactive ion etching (RIE) in a $\text{CF}_4 + 5\% \text{O}_2$ atmosphere. The sample design (Fig. 4.9) comprises a Nb strip (50 μm wide and 2000 μm long) whose superconducting properties were measured by four-point DC technique, and a sufficiently large Nb area in order to perform XRD analysis. This sample design allows to investigate the

superconducting properties and to make the XRD measurements on the same sample.

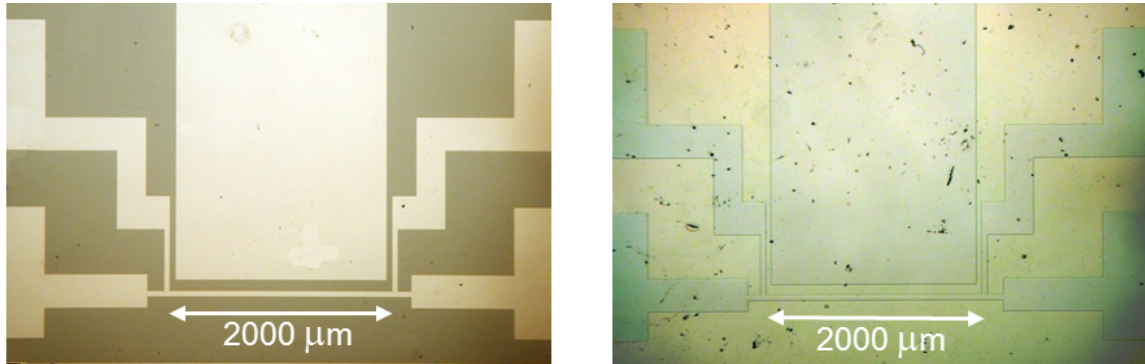


Figure 4.9: Micrograph of a patterned 20 nm Nb film. Left: before the PECVD a-Si:H deposition. Right: after the deposition. The 2000 μm long strip for the electrophysical four-point DC measurements and the large Nb area for the X-ray analysis are clearly visible.

It is important to note that all the samples which were treated by nitrogen plasma were exposed to nitrogen plasma for a second time also after the patterning (under the same RF-nitrogen plasma conditions used for the top surface), in order to form a nitride layer also on the sidewalls of the Nb films [203].

The samples destined to the a-Si:H deposition (with and without protective surface treatment) were covered by a 300 nm thick a-Si:H film grown at ENEA by very high frequency (VHF) PECVD at 100 MHz, using pure silane (SiH_4) at substrate (*i.e.* Nb films) temperature of 250° C [53]. In order to distinguish the heating effect, mostly acting on oxygen diffusion, from the effect of hydrogen diffusion, caused by the exposure of the films to high energy hydrogen ions, we also investigated the effect of a simple thermal annealing on a selected group of samples (identified as annealed), heated inside the same PECVD chamber at 250° C at a pressure of 5×10^{-7} Torr (no gas was introduced) and for a time identical to that of the 300 nm a-Si:H deposition.

All the samples were characterized in terms of both superconducting and microstructural properties. The dependence of the Nb stripline resistance R on temperature was measured by a four-point DC technique, with a temperature accuracy

of 0.01 K. The superconducting transition temperature T_c was evaluated as the midpoint between the resistive transition and the superconducting transition width ΔT_c , defined as the temperature interval between the two points associated with the 10% and 90% of the resistance taken just before the superconducting phase transition [134]. The value of $R(10\text{ K})$ was utilized for estimation of the residual resistivity ρ_0 .

The crystallographic properties of the Nb films, namely the orientation normal to the substrate surface, the crystal lattice parameter, a , along this direction, and the crystalline grain size, L , were investigated by XRD analysis by using a Bruker D8 Advance diffractometer with Cu-K α radiation source in Bragg-Brentano geometry.

4.3 Results and Discussion

The experimental data from the measurements of the electrophysical properties and from the XRD analysis are summarized in Table 4.1.

height	Sample	T_c (K)	ΔT_c (K)	a (Å)	ρ_0 ($\mu\Omega\text{cm}$)
A	Nb(20) reference	7.27	0.19	3.330 ± 0.003	17.22
B	Nb(20) annealed	5.69	0.13	3.330 ± 0.003	17.22
C	Nb(20)/a-Si:H	4.29	0.25	3.372 ± 0.002	39.43
D	Nb(20)/Nb Nitride reference	8.16	0.02	3.289 ± 0.005	10.99
E	Nb(20)/Nb Nitride annealed	7.05	0.04	3.310 ± 0.005	18.92
F	Nb(20)/Nb Nitride/a-Si:H	6.59	0.06	3.311 ± 0.004	21.52
G	Nb(20)/Si reference	8.44	0.03	3.288 ± 0.006	30.01
H	Nb(20)/Si annealed	8.28	0.02	3.293 ± 0.003	10.97
I	Nb(20)/Si/a-Si:H	8.02	0.04	3.303 ± 0.003	11.91

Table 4.1: Superconducting transition temperature T_c , superconducting transition width ΔT_c , crystal lattice parameter a , and intrinsic resistivity ρ_0 of the 20 nm thick Nb samples, with different surface treatment, before and after annealing at 250° C and PECVD growth of the a-Si:H layer.

Results from X-ray refraction analysis (as in Fig. 4.3), performed in collaboration with Prof. P. Mengucci, from the Università Politecnica delle Marche (Ancona),

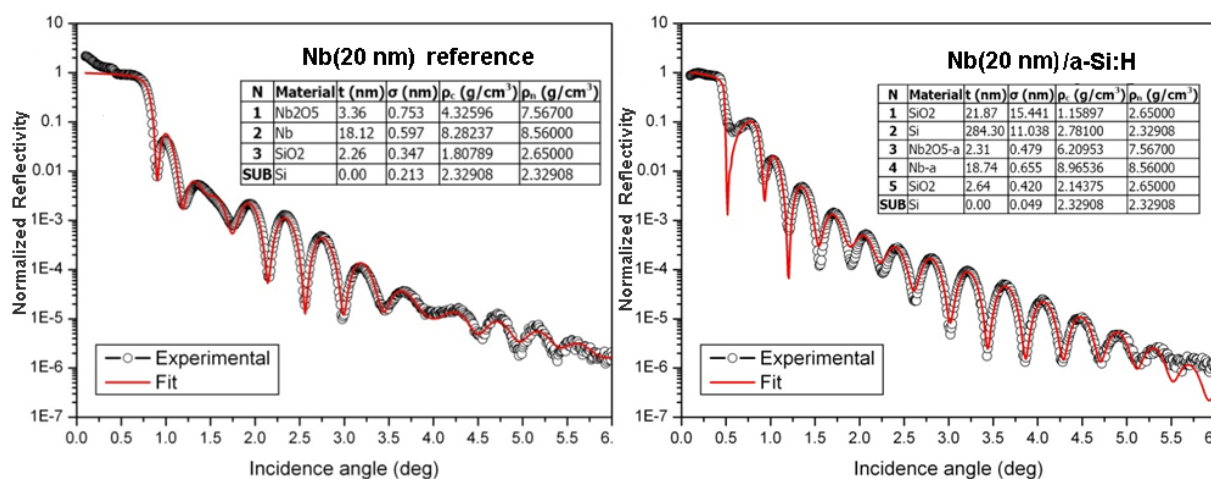


Figure 4.10: X-ray refraction analysis on samples Nb(20 nm) reference and Nb(20 nm)/a-Si:H, and the fitting procedure based on the known bulk material densities.

helped to measure the thickness of the various films and the smoothness of the interfaces formed between them, by means of fitting procedure based on the known bulk-material densities.

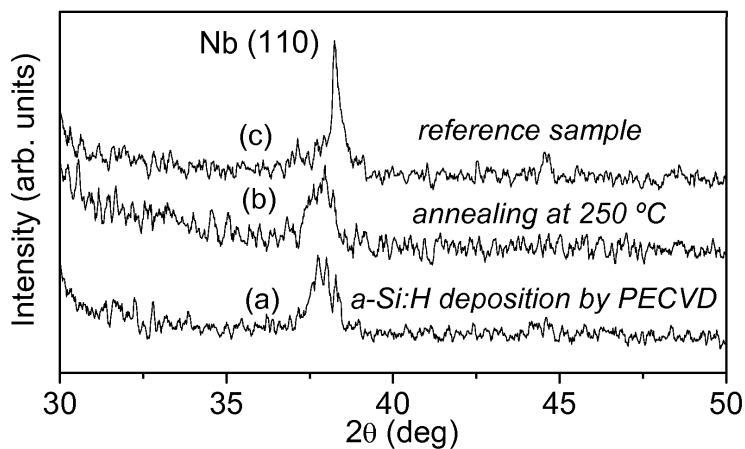


Figure 4.11: X-ray diffraction patterns of Nb(20) films without any surface treatment. (a) reference sample; (b) sample after annealing; (c) sample after a-Si:H deposition. Curves (b) and (c) evidently show the shift of the peak position to lower angles and, hence, demonstrate the expansion of the Nb crystal lattice caused by the oxygen and hydrogen diffusion.

The XRD measurements of all the Nb films revealed a polycrystalline structure with the main diffraction peak corresponding to the Nb (110) planes parallel to the substrate surface. As an example, curve (a) of Fig. 4.11 shows the $\theta - 2\theta$ XRD

pattern of the reference Nb(20) film.

In spite of the small film thickness, the sensitivity of the XRD method was sufficient in order to distinguish the small Nb (110) diffraction peak from the large peaks associated with the Si substrate. The values of the crystalline grain size L , estimated from the breadth of Nb (110) diffraction peak of the reference samples, were between 7.6 Å and 11.7 Å.

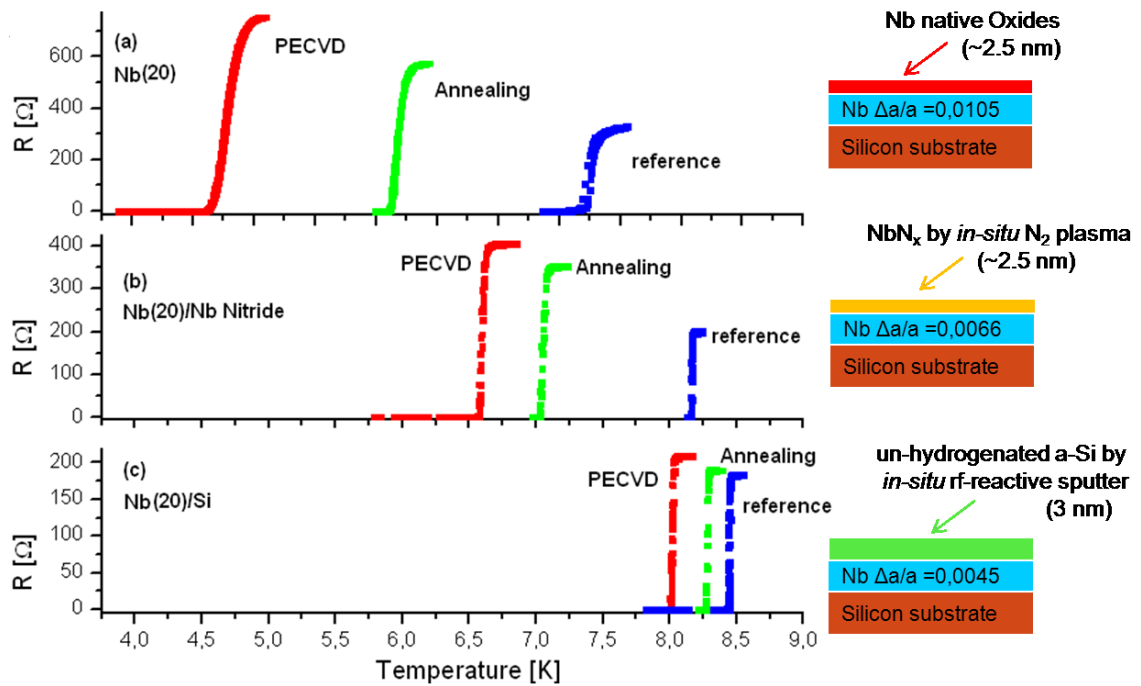


Figure 4.12: Superconductive transition curves of the 20 nm thick Nb films with different surface treatment before and after both the annealing at 250° C and the PECVD a-Si:H deposition. (a) 20 nm thick Nb film without any surface treatment; (b) 20 nm thick Nb film with nitridation; (c) 20 nm thick Nb film covered by the 3 nm thick Si layer. It may be appreciated how the surface treatments and the two sample processing in the PECVD chamber substantially decrease the T_c , deteriorate the sharpness of the transition together with the increase of its width, and noticeably increase the Nb residual resistivity ρ_0 .

The superconducting transition curves of the 20 nm Nb films, with different surface treatment before and after both annealing at 250° C and a-Si:H deposition by PECVD, are shown in Fig. 4.12.

The deposition of the 300 nm a-Si:H layer by PECVD resulted in a deterioration of the Nb superconducting properties, namely, in the reduction of T_c and increase of the superconducting transition-width. This deterioration of the superconductivity is accompanied by an enlargement of the crystal lattice parameter, a , and by an increase of the residual resistivity, ρ_0 . However, the extent of the deterioration depends on the surface treatment made before the PECVD process. Indeed, the maximum degradation as a result of the PECVD step was observed for the untreated Nb(20) film with $T_c^A - T_c^C = 2.98$ K and $\Delta a_{AC} = 0.042$ Å, where A and C identify the samples as indicated in Table 4.1.

The deterioration of the superconducting properties were accompanied by a shift of the Nb (110) peak position on the XRD pattern to lower angles θ , *i.e.* by an increment of the crystal lattice parameter a . The degree of the deterioration depended on the surface treatment made before the PECVD process (see closed symbols in Fig.4.13). Indeed, the maximum effect of the PECVD was observed for the unprotected Nb(20 nm) (closed circle in Fig.4.13, $\Delta T_c = 2.98$ K, $\Delta a = 0.042$ Å). The plasma nitridation protected the Nb film in such a manner the PECVD detrimental effect was diminished to $\Delta T_c = 1.57$ K, $\Delta a = 0.022$ Å (closed square in Fig.4.13). Small variations of the T_c and the a ($\Delta T_c = 0.42$ K, $\Delta a = 0.015$ Å) were observed for Nb(20 nm)/Si(3 nm) sample (closed triangle in Fig.4.13).

It is interesting to note that the annealing of the samples at 250° C, performed with the purpose of distinguishing the effect of the oxygen diffusion from that of hydrogen diffusion, also resulted in a significant deterioration of the superconductivity and in an increase of the crystal lattice-parameter. The effect can be attributed to the partial dissolution of the native oxide layer and the following oxygen diffusion into the Nb film, leading to an enhancement of the interstitial oxygen-concentration underneath the film surface [52]. Thus, after annealing we observed a significant decrease of T_c and increase of a for the Nb(20) film and for the Nb(20)/Nb Nitride film. The T_c difference in the first film was of 53 % of the T_c drop caused by the PECVD process, while in the second annealed film the T_c drops was of 70 % of the case of the PECVD

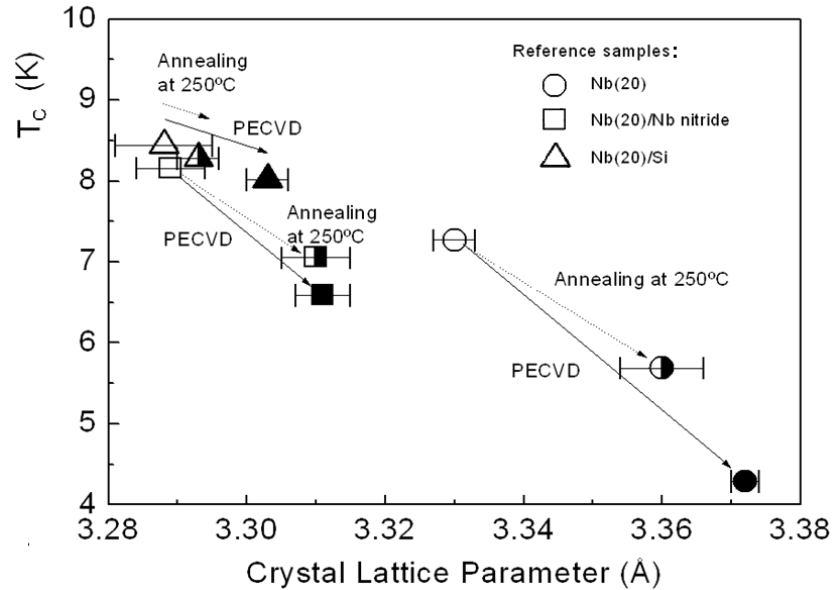


Figure 4.13: Superconducting transition temperature T_c versus crystal lattice parameter a , for Nb(20 nm), Nb(20 nm)/Nb Nitride, and for Nb(20 nm)/Si(3 nm) before (open symbols) and after a-Si:H deposition by PECVD (closed symbols). Semiclosed symbols report the results for annealing at 250° C in high vacuum.

process. Moreover, the difference of a in both cases was less than that observed after the PECVD process. On the other hand, for the Nb(20)/Si sample there was no drastic deterioration of T_c and expansion of the crystal lattice parameter a after the annealing step; the T_c difference was of 38 % of the value obtained after the a-Si:H growth by PECVD, and the difference of a was of 33 %.

These results show that a significant role in the deterioration of the superconductivity during the PECVD process is played by oxygen diffusion, as an undesirable effect of the required substrate heating. The annealing at 250° C seems to be detrimental even on the films with nitridation. Interestingly, the sputtered a-Si buffer layer effectively prevents the formation of the native Nb surface-oxide and its decomposition with subsequent oxygen diffusion caused by the heating up to 250° C. Moreover, the a-Si seems to work as a protective layer, which efficiently blocks also

the hydrogen diffusion during the a-Si:H layer growth.

A very interesting result was that, for all the samples, we found that the variations in the crystal lattice parameter a were correlated with the difference in the superconducting transition temperature T_c .

As it can be seen from Fig. 4.13, the reference Nb(20 nm) film (open circle) manifested lowest value of the T_c and highest expansion of the crystal lattice in comparison to the values of the reference samples, while the highest value of T_c (8.44 K) and $a = 3.288 \pm 0.007 \text{ \AA}$ – slightly less than the crystal lattice parameter for stress-free Nb film (3.295 \AA from [101]) – were achieved on the reference Nb(20 nm)/Si(3 nm) film (open triangle).

The slight difference in the crystal lattice-parameter can be explained by difference in the film thickness: low thickness (20 nm) of the films of the present research and high thickness ($> 100 \text{ nm}$) of the Nb film of [101]. Moreover, we note that the values of the T_c and of the a for the reference Nb(20 nm)/Nb Nitride were slightly different from the parameters of the reference Nb(20 nm)/Si(3 nm) films (see Fig.4.13, open square). The expansion of the crystal lattice and the decrease of the superconducting transition temperature T_c in the the case of the reference samples are described by oxygen interstitially added into the Nb crystal at a concentration below the solubility limit [223].

The polycrystalline film-structure with small grain size (as in our case) can favor the oxygen migration through the grain boundaries. From the linear experimental dependence of the crystal lattice-parameter on the oxygen content reported in [223], the increment of the atomic-percent oxygen ΔC_{O_2} is related to the crystal lattice expansion Δa by the empirical formula

$$\Delta C_{O_2}(\text{at}\%) = 250.5 \cdot \Delta a \text{ (in \AA)} \quad (4.3.1)$$

By Eq. 4.3.1 we estimated the oxygen content for the reference samples, 10.5 at%O for Nb(20 nm) and 0.25 at%O for Nb(20 nm)/Nb Nitride, considering Nb(20 nm)/Si(3 nm) as a sample with negligible oxygen content and using its crystal lattice parameter as the oxygen-free reference value (Fig.4.14).

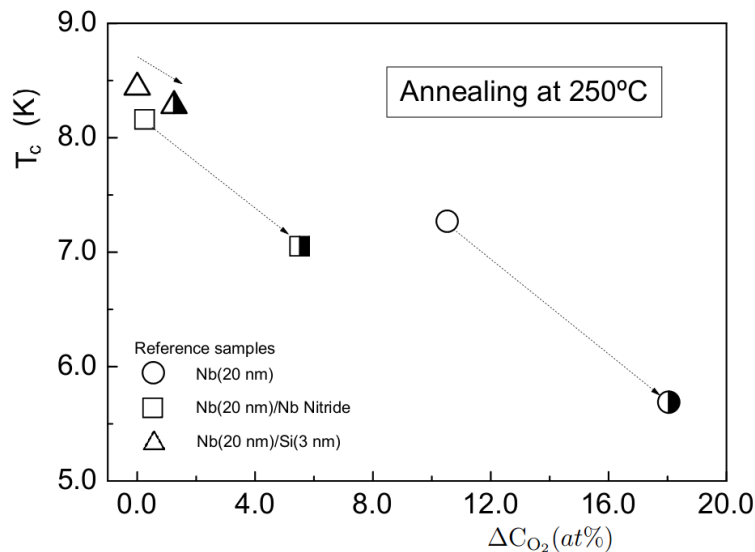


Figure 4.14: Modification of the T_c , before and after annealing at 250° C, as a function of the oxygen concentration. Circles: Nb(20 nm); Squares: Nb(20 nm)/Nb Nitride. Triangles: Nb(20 nm)/Si(3 nm).

Fig. 4.14 shows that for the Nb(20 nm) films with nitridation and without any surface treatment, the interstitial oxygen, created during the annealing, decreased the T_c by 0.21 K/at%O. This means that in our experiment the nitridation did not protect well the Nb film from the oxygen diffusion during annealing processing.

As was found in [201], NbN_xO_y is formed on the surface of the nitridated Nb films when exposed to air at room temperature. It is possible to assume that, similarly to the native oxide of unprotected Nb film, the NbN_xO_y reduces and the oxygen diffuses into Nb film during the annealing at 250° C at high vacuum. On the contrary, the nitridation surface treatment effectively protected the Nb film from hydrogen diffusion: during the a-Si:H deposition by the PECVD, the additional hydrogen contribution to the total T_c suppression was of 30% for Nb(20 nm)/Nb Nitride film, while in case of the Nb(20 nm) film without surface protection, the hydrogen contribution to the complete T_c suppression was 47% (see Fig.4.13). This protection phenomenon can be

attributed to the interstitial nitrogen in the Nb nitride surface-layer which prevented the hydrogen diffusion inside the Nb film [182, 155]. In the case of Nb(20 nm)/Si(3 nm) sample, the annealing resulted in the decreasing of the T_c by 0.13 K/at%O – practically by the same ratio as for natural degradation of the T_c for Nb(20 nm) film exposed in air at room temperature (0.11 K/at%O). The T_c suppression caused by the oxygen diffusion during the sample heating was 38% of the total suppression during the PECVD. Si layer effectively prevented the formation of the native Nb surface oxide, its decomposition, and the oxygen diffusion caused by the sample heating up to 250° C. Anyway, the a-Si layer blocked well the hydrogen diffusion from the pure silane plasma during the PECVD.

The interstitial oxygen and hydrogen expand the crystal lattice of Nb film. This expansion results in the increase of the residual resistivity ρ_0 (see Table 4.1 and Fig. 4.12). Moreover, we found a direct relation between the suppression of the T_c and the increase of the residual resistivity ρ_0 . Therefore, the decrease of the T_c can be attributed to the smearing of the sharp density of state at the Fermi level which, in terms of the McMillan analysis, leads to decrease of the coupling constant λ [154].

Finally, Fig. 4.15 shows the suppression of T_c of the Nb films without any surface treatment and with different thicknesses, after the annealing step and after the a-Si:H deposition: in both cases the effect decreases with the increase of the Nb film thickness.

In the view of realizing superconducting circuits with 200 nm thick niobium wires, this result is giving us a solid confirmation that, despite superficial effects enhanced by the small thickness of the thinnest samples, the "bulk" superconducting properties will not be affected by the annealing nor by the PECVD a-Si:H deposition.

4.4 Conclusions

We studied the influence of the a-Si:H deposition by PECVD on the superconducting and structural properties of Nb films treated by two surface protection methods:

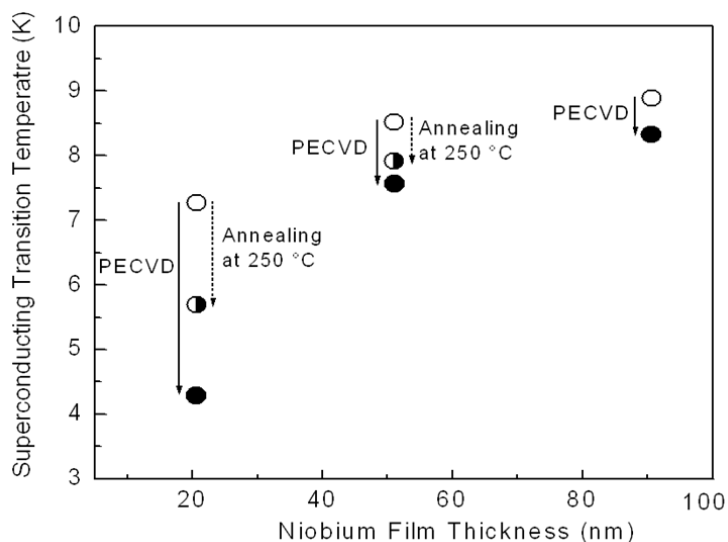


Figure 4.15: T_c suppression by the annealing and by the PECVD process for Nb films with different thicknesses without any surface treatment. Open symbols: results for the reference samples. Semiclosed symbols: results for the annealing process. Closed symbols: data obtained after the a-Si:H deposition by PECVD.

plasma nitridation and deposition of a thin a-Si layer. We observed that the main T_c suppression mechanism was the decomposition of the Nb native surface-oxides and oxygen diffusion caused by the heating of the sample at 250° C, required for the growth of high quality a-Si:H. We demonstrated that *in situ* sputtered thin a-Si layer works well as a protective method against both the oxygen and hydrogen diffusion. We note that the plasma nitridation effectively protected the Nb film from the hydrogen diffusion, but was inefficient for the protection from the oxygen diffusion. Moreover, we found that the extent of the T_c suppression caused by the annealing and by the complete PECVD process inversely depends in both cases on the Nb film thickness.

Nevertheless, the incorporation of the a-Si:H by PECVD with the Nb technology for the qubit realization will not require the utilization of either a Si thin layer deposition or the surface plasma nitridation as a surface protective technique, because of the negligible variation of the niobium's superconducting properties of 200 nm thick wires after both annealing and a-Si:H deposition. Instead, surface treatments like the N_2 plasma could be considered as first attempts to treat the superconductor's surface in order to reduce the surface's density of defects.

Chapter 5

Superconducting Resonators

In this chapter, it will be described the measurement method, the lumped-element (LE) superconducting microwave-resonator technique, that was extensively used in order to evaluate the absolute values of the dielectric loss as well as their dependence on frequency.

The LC lumped-resonator technique is a reliable and powerful tool for the loss tangent ($\tan\delta$) characterization of any dielectric at the typical conditions at which a qubit device is operated, namely at low cryogenic temperatures (20 mK), microwave frequencies (150 MHz-12 GHz), and low excitation power (10^{-7} - 10^{-3} V).

Bulk losses of various dielectrics commonly used in qubit fabrication were compared at low temperatures and low excitation energies. This was done in order to find useful low-loss dielectrics improving qubit performances. In order to explain the method and the obtained experimental results, the theoretical background introduced in chapter 4 will be used. By means of this technique, we studied the influence of fabrication processes of the insulator, *e.g.* different substrate temperatures, SiH_4/H_2 ratio, on a-Si:H loss tangent ($\tan\delta$), in order to investigate the origin of the loss mechanisms in a-Si:H thin films. For the resonator realization, the Nb technology was successfully incorporated with the a-Si:H PECVD technologies (see section 4.2).

In the following sections the basics of microwave resonators will be deduced, different types of losses will be introduced, and two important types of such resonators will be presented, namely the coplanar waveguide (CPW) and the lumped element (LE) resonators. Afterwards, the measurement method developed at the IMS/KIT/ICIB-CNR will be described, and important enhancements of its design will be explained. Finally, experimental results on the low temperature measurement of the losses of a-si:H will be presented.

5.1 Resonator's Model

In order to deduce the basic properties of a microwave resonator, the electric components of the resonator are considered to be physically very small in relation to the electrical wavelength. Thus, even distributed resonators can be modeled by an equivalent RLC lumped-element circuit.

Series Resonant Circuits

The input impedance of a series RLC resonant circuit (see Fig. 5.1.a) consists of the resistance R and the reactance X as

$$Z_{in} = R + X = R + i\left(\omega L - \frac{1}{\omega C}\right), \quad (5.1.1)$$

where ω denotes the frequency, L the inductance and C the capacitance of the

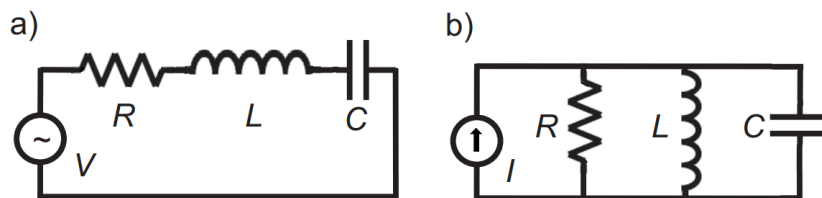


Figure 5.1: Schematics of an RLC circuit. a: in series. b: in parallel.

resonant circuit. Since the current I through all elements is equal, the complex

power delivered to the resonator can be given as

$$P_{in} = \frac{1}{2}Z_{in}|I|^2 = \frac{1}{2}|I|^2 \left[R + i \left(\omega L - \frac{1}{\omega C} \right) \right]. \quad (5.1.2)$$

The first term of the power expresses the dissipation by the resistor:

$$P_{loss} = \frac{1}{2}|I|^2 R, \quad (5.1.3)$$

while the average magnetic energy stored in the inductor is given by

$$W_m = \frac{1}{2}|I|^2 L, \quad (5.1.4)$$

and the average electric energy stored in the capacitor is given by

$$W_e = \frac{1}{2}|I|^2 \frac{1}{\omega^2 C}. \quad (5.1.5)$$

Equation (5.1.2) can now be written as

$$P_{in} = P_{loss} + 2i\omega(W_m - W_e). \quad (5.1.6)$$

In the case of resonance, $W_m = W_e$, the input resonance Z_{in} gets minimal and the the resonance frequency is defined as

$$f_0 = \frac{1}{2\pi}\omega_0 = \frac{1}{2\pi\sqrt{LC}}. \quad (5.1.7)$$

Parallel Resonant Circuits

Figure 5.1.b shows the schematics of a parallel lumped-element circuit. The input impedance in this case is given by

$$Z_{in} = \left(\frac{1}{R} - \frac{i}{\omega L} + i\omega C \right)^{-1}. \quad (5.1.8)$$

Since in a parallel circuit the voltage V across all elements is equal, the complex power can be written as

$$P_{in} = \frac{1}{2}Z_{in}|I|^2 = \frac{1}{2}|V|^2 \frac{1}{Z_{in}^*} = \frac{1}{2}|V|^2 \left(\frac{1}{R} + \frac{i}{\omega L} - i\omega C \right). \quad (5.1.9)$$

The dissipated power is then

$$P_{loss} = \frac{1}{2}|V|^2/R, \quad (5.1.10)$$

and the average electric and magnetic energies are

$$W_e = \frac{1}{4}|V|^2/C, \quad (5.1.11)$$

$$W_m = \frac{1}{4}|V|^2 \frac{1}{\omega^2 L}, \quad (5.1.12)$$

The power can also be written as (5.1.6), which, in the resonant case $W_m = W_e$, leads to the same resonance frequency f_0 as from Eq. 5.1.7.

5.1.1 Quality Factors and Losses

The quality factor Q_0 of a resonant circuit is defined as

$$Q_0 = \omega \frac{(\text{average energy stored})}{(\text{energy loss/second})} = \omega \frac{W_m + W_e}{P_{loss}} \quad (5.1.13)$$

At resonance $W_m = W_e$, this leads to the following expressions for the loss

$$Q_0 = \begin{cases} \frac{1}{\omega_0 RC}, & \text{for series circuits,} \\ \omega_0 RC, & \text{for parallel circuits.} \end{cases} \quad (5.1.14)$$

The quality factor Q_0 introduced here is not influenced by any loading effects caused by external circuitry. This means that it is an intrinsic characteristic of the resonator itself, so that it is called the unloaded quality factor Q_0 . In order to calculate the loss in a resonator, one has to use the angle δ between the imaginary part X of the complex impedance Z and the impedance itself in the complex plane. The tangent of this loss angle is defined as $\tan \delta_{tot} = R/X$, ratio of the real part R of the complex impedance to the imaginary part X . This ratio is called the loss tangent of a resonator. This loss tangent is directly connected to the unloaded quality factor Q_0 by the relation

$$\tan \delta_{tot} = \frac{1}{Q_0}. \quad (5.1.15)$$

Now, the behavior at frequencies $\omega = \omega_0 + \Delta\omega$ close to resonance (*i.e.* $\Delta\omega = \omega_0$) will be considered. Then, in a series-circuit, the complex impedance can be approximated (as from [31]) as

$$Z_{in} \cong R + iRQ_0 \frac{2\Delta\omega}{\omega_0} = R + iRQ_0\gamma \quad (5.1.16)$$

where γ is the double-sided fractional bandwidth. Since $Z_{in} = R$ at resonance (because $W_m = W_e$), the maximum power absorption by the resonator can be found at resonance. At all other frequencies, one can find less power absorption by the resonator, which can formally be described by [31]

$$|Z_{in}|^2 = R^2/p. \quad (5.1.17)$$

Here, the power fraction p ranges between $0 < p < 1$, and denotes at which power (being $p = 1$ at maximum power) the bandwidth $2\Delta\omega$ is to be taken. *E.g.* $\gamma(p = 0.5)$ means that the bandwidth is measured at half-power, *i.e.* at the half of the maximum amplitude of a resonance curve with the ordinate in linear scales. As long as the frequency is close to resonance, (5.1.17) can be substituted in (5.1.16). This leads to a more general expression of Q_0 in relation to the power fraction p

$$Q_0 = \frac{1}{\gamma(p)} \sqrt{\frac{1-p}{p}}. \quad (5.1.18)$$

Again, $\gamma(p)$ denotes the bandwidth at the power fraction p . Usually, the bandwidth is measured at $p = 0.5$, which leads to the result

$$Q_0 = \frac{1}{\gamma(p = 0.5)} = \frac{1}{\tan \delta_{tot}}. \quad (5.1.19)$$

The same result can be deduced for a parallel circuit. In practice, there are lots of influences on the overall quality factor Q_L caused by the coupling to other circuitry and the environment. Thus, the overall quality factor Q_L , which is called the loaded quality factor, is lower than Q_0 . The loaded and unloaded quality factors are connected via the external quality factor Q_e

$$\frac{1}{Q_L} = \frac{1}{Q_0} + \frac{1}{Q_e} \quad (5.1.20)$$

which takes all environmental influences into account. The influence of an external load on an RLC circuit can be expressed by an additional load resistor R_L shunted to the resonator

$$Q_e = \begin{cases} \frac{\omega_0 L}{R_L}, & \text{for series circuits,} \\ \frac{R_L}{\omega_0 L}, & \text{for parallel circuits.} \end{cases} \quad (5.1.21)$$

In order to obtain the quality factors of a resonator, one has to measure either the transmission $|S_{21}|$ through the resonator or the reflection $|S_{11}|$ from one port back to itself. The measurement to be performed depends on the type of resonator, which will be explained in the following. This measurement method can be explained by introducing the scattering theory. In this model, the resonator is assumed to be a scatterer for the currents coming from both ports connected to the resonator. The incoming and outgoing currents at each port can be expressed as wavefunctions connected by the scattering matrix

$$\begin{pmatrix} \psi_{1,out} \\ \psi_{2,out} \end{pmatrix} = \begin{bmatrix} S_{11} & S_{12} \\ S_{21} & S_{22} \end{bmatrix} \cdot \begin{pmatrix} \psi_{1,in} \\ \psi_{2,in} \end{pmatrix}. \quad (5.1.22)$$

A typical measurement curve of the transmission through a resonator is shown in figure 5.2

Here, an absorption dip can be seen for each resonating frequencies (in this case for a 4 series-connected resonator). Q_0 is measured at $\gamma(p = 0.5)$ above the minimum of $|S_{21}|$ while Q_L is measured at $\gamma(0.5)$ below the maximum. A factor of $\gamma(p = 0.5)$ means at half power. In units of dB, as given here, one can obtain the value of $P = 3\text{dB}$ for half power by using

$$P[\text{db}] = 10 \log_{10} \left(P = \frac{P[\text{W}]}{P_0[\text{W}]} \right) \quad (5.1.23)$$

where $P[\text{dB}]$ denotes the power level for a reference power P_0 in W.

There are various contributions to the intrinsic loss $1/Q_0$ from the resonator itself. These contributions compose the total value of Q_0 like

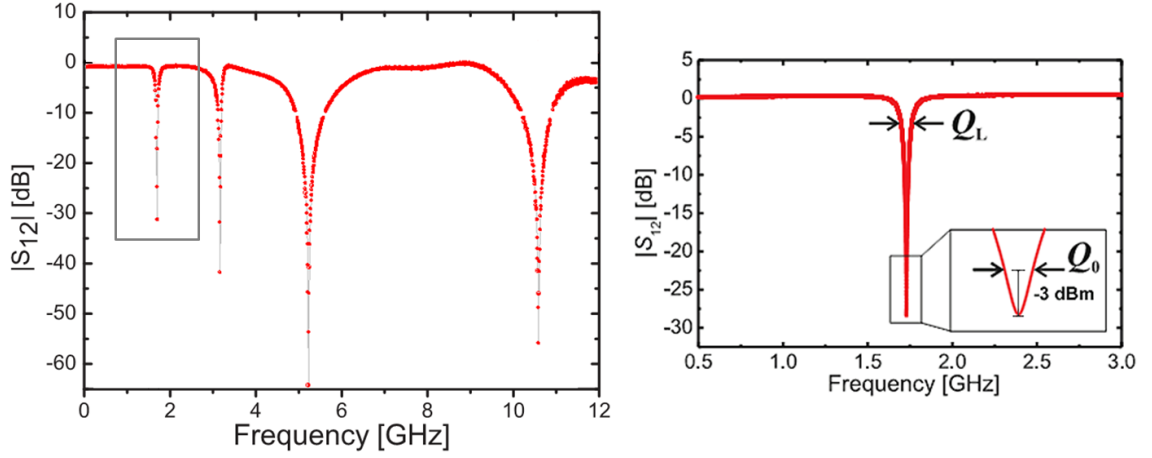


Figure 5.2: Experimental $|S_{21}|$ data from a 4-multiplexed a-Si:H resonators. Left: all 4 resonances measured in a single frequency sweep (0 -12 GHz). Right: detail of the gray-box area from the previous graph, showing the loaded quality factor Q_L . Inset: the intrinsic quality factor Q_0 directly extracted from the resonance dip by calculating $Q_0 = 1/\gamma(0.5) = f_0/\delta f$, where δf is the bandwidth of the resonance dip at $|S_{12}| = \sqrt{|S_{12,min}|^2/(1 + |S_{12,min}|^2)}$.

$$\frac{1}{Q_0} = \frac{1}{Q_\varepsilon} + \frac{1}{Q_{rad}} + \frac{1}{Q_\rho} \quad (5.1.24)$$

where, Q_ε denotes the dielectric, Q_{rad} the radiation, and Q_ρ the conductor losses.

Various types of resonators can be described by the idealized RLC circuit. It is important to distinguish between series- or parallel-resonators connected in series or in parallel to the environmental circuitry [31]. Beside this consideration, the physical implementation of the used components R , L , and C is important. In this section, lumped element resonators, consisting of discrete elements, and coplanar waveguide resonators, consisting of distributed elements, will be described.

Lumped Element Resonators:

As long as electrical components can be considered small in electrical size, meaning that their physical dimensions are much smaller than the electrical wavelength, which is the length of a transmission-medium element expressed as the number of

wavelengths of the signal propagating in the medium, they can be treated with the formulas of the previous section.

In a lumped element, voltage and current do not vary in magnitude and phase over its length. A typical lumped element in microelectronics is a plate capacitor with a size in the μm range. The capacitance C of such a small capacitor can be obtained by the well-known formula

$$C = \varepsilon_0 \varepsilon_r \frac{A}{d} \quad (5.1.25)$$

where, ε_0 denotes the electric constant, ε_r the permittivity of the dielectric between the plates, and A the area of a plate and d the distance between the parallel plates.

Coplanar Waveguide Resonators (CPWs):

In contrast to the lumped element resonator consisting of concentrated elements, the coplanar waveguide resonator consists of a symmetrical coplanar waveguide transmission line. This transmission line has an inner conductor line of width w separated from the surrounding ground plane by two gaps of width s (see Fig. 5.3).

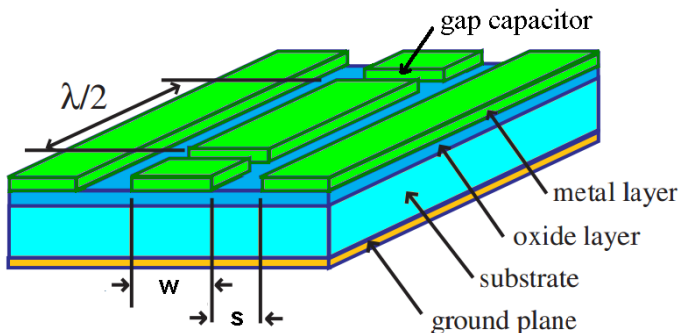


Figure 5.3: Schematics representation of a CPW resonator. w is the width of the central conductor, and s the width of the gap between the central conductor and the ground plates. Figure from [35]

Although this type of resonator consists of distributed elements, it can be modeled by a lumped-element circuit. For this, the resistance load per unit length R' , the inductance per unit length L' , and the capacitance per unit length C' are introduced as normalized parameters [92]:

$$L' = \frac{Z_L \sqrt{\varepsilon_{r,eff}}}{c_0}, \quad (5.1.26)$$

$$C' = \frac{\varepsilon_{r,eff}}{L'c_0^2}, \quad (5.1.27)$$

$$R' = \frac{\alpha}{2Z_L} \quad (5.1.28)$$

where Z_L denotes the characteristic impedance, $\varepsilon_{r,eff}$ the effective permittivity, α the attenuation constant, and c_0 the vacuum speed of light.

The length of the transmission line determines the resonance frequency of the resonator. Typical CPWs have the length l of a quarter- or half-wavelength of the corresponding resonance frequency f_0

$$l_{half} = \frac{\lambda}{2} = \frac{1}{2} \frac{c_0}{f_0(\varepsilon_{r,eff})^{1/2}}, \quad (5.1.29)$$

$$l_{quarter} = \frac{\lambda}{4} = \frac{1}{4} \frac{c_0}{f_0(\varepsilon_{r,eff})^{1/2}}, \quad (5.1.30)$$

and the effective dielectric constant of a CPW depends on the ratios $w/(w + 2s)$ and s/h , with h denoting the substrate thickness. For thick substrates, $h \rightarrow \infty$ can be assumed leading to a saturated value of the effective dielectric constant $\varepsilon_{r,eff} = (\varepsilon_r + 1)/2$. The components R , L , and C of a CPW can be deduced by treating the CPW as a lumped-element parallel circuit:

$$L = \frac{8l}{\pi^2} L', \quad (5.1.31)$$

$$C = \frac{l}{2} C', \quad (5.1.32)$$

$$R = \frac{Z_L}{\alpha l}. \quad (5.1.33)$$

With these values, the resonance frequency and the unloaded quality factor of the CPW can be calculated as

$$f_0 = \frac{1}{2\pi\sqrt{LC}}. \quad (5.1.34)$$

$$Q_0 = 2\pi f_0 RC. \quad (5.1.35)$$

Normally, a microwave resonator is fabricated out of metal. By applying an electric field to the resonator forces the charge carriers, here the electrons, to move, which leads to a current flow. In 1900, Drude proposed a model to explain the transport properties of electrons in metals [151]. In terms of this model, an electron passing through a metal is scattered at the ions, other electrons, phonons, *etc.* of this metal. This leads to a relation between the current density \vec{J} of the electrons and the applied field \vec{E}

$$\vec{J} = \left(\frac{nq^2\tau}{m} \right) \vec{E}. \quad (5.1.36)$$

This equation is nothing else than Ohm's law with the conductivity $\sigma = \left(\frac{nq^2\tau}{m} \right)$. Here, n is the density, q the charge, m the mass and τ the mean free time of the electrons. Thus, a change of the field will cause a change of the current density. For a time-dependent electric field with frequency ω , the Drude model predicts a complex conductivity [151]

$$\sigma(\omega) = \frac{\omega_0}{1 + i\omega\tau} = \sigma' - i\sigma''. \quad (5.1.37)$$

The reason for this behavior is the finite relaxation time τ . It describes a delay in the response of the electron to the external force. For $\tau \rightarrow \infty$, which is the case at high frequencies and in high carrier mobility conductors (especially superconductors), the imaginary part becomes noticeable, which is related to the so-called kinetic inductance. This kinetic inductance L_{kin} can be treated as an additional series inductance to the normal geometrical inductance L_g , which leads to

$$L = L_g + L_{kin}. \quad (5.1.38)$$

This additional inductance component has to be considered in superconducting resonators as it causes a shift of resonance frequency f_0 like

$$f_0 = \frac{1}{2\pi\sqrt{(L_g + L_{kin})C}}. \quad (5.1.39)$$

From further theoretical considerations, Mattis and Bardeen, by using the two fluid model showed that the quality factor of a superconducting resonator is given by

$$Q_{MB} = \frac{2 \sigma''}{\alpha \sigma'} \quad (5.1.40)$$

with

$$\alpha = \frac{L_{kin}}{L_g}. \quad (5.1.41)$$

5.2 Lumped Element Resonators

In chapter 3, we described the possibility to investigate the dielectric losses of superconducting microwave circuits. Not only CPWs, but also lumped element resonators are suitable to be used for such investigation: in the following sections investigations of "bulk" dielectric losses with lumped element resonators will be presented.

The investigation of dielectric loss using lumped element resonators has not been pushed as intensively as those using CPWs. One reason for that is the disadvantage of low quality factors in lumped element resonators in comparison to coplanar structures. However, the advantages of compact size and easily-computable electrical variables still make lumped element resonators interesting, *e.g.* for Kinetic Inductance Detectors (KIDs) [51].

For Lumped Element Kinetic Inductance Detectors (LEKIDs) the compact size is an advantage for the fabrication of whole arrays of these LEKIDs on a small suitable chip size. For these LEKIDs, interdigitated capacitors (IDCs) are employed. Since these capacitors are coplanar elements without any dielectric between the two electrodes, they show similar influences from surface distributed TLSs [41]. Another realization of lumped element capacitors are standard parallel plate capacitors which consist of two superconducting electrodes separated by a dielectric layer. In 2008 O'Connell *et al.* used such capacitors to set up an equivalent circuit for CPWs suitable for the determination of the contributions of TLS induced loss to CPWs [169]. The facts that the capacitance of a parallel plate capacitor can be computed easily

by 5.1.25, and that the entire electric field is stored in the dielectric between the capacitor plates were used to investigate the influence of TLSs in the bulk dielectric. In contrast, in a CPW the electric field permeates a large volume around the CPW, which may be not filled only by the dielectric of interest and, therefore, the fraction of dielectric energy has to be calculated using finite-element methods. Thus, using lumped element resonators with parallel plate capacitors, the values of the intrinsic dielectric losses can be achieved much more directly and reliably.

In the investigations of O’Connell *et al.* such lumped element resonators were decoupled capacitively from the load-lines to establish an equivalent circuit of a half-wavelength CPW. Firstly, this means that only the loaded quality factor is directly readable from the measurement curve, but not the unloaded one. Thus, this method is not direct. Secondly, the fact that the resonator is situated between the load-line and ground (see Fig. 5.4.a) leads to additional parallel load resistors which have to be considered by extracting the dielectric losses from measurements.

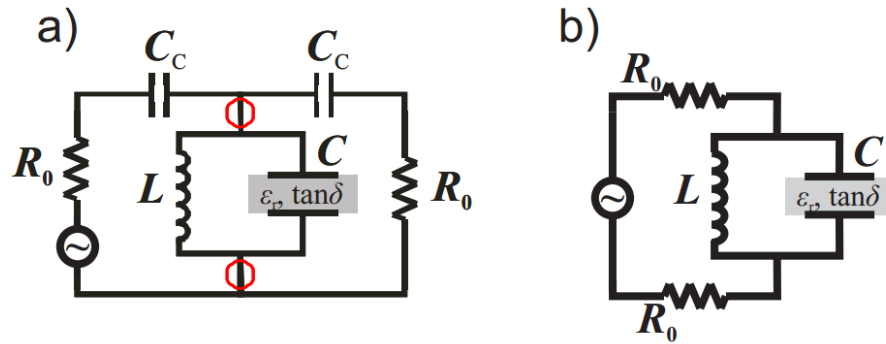


Figure 5.4: a) Schematics of a lumped element resonator with coupling capacitors C_c as an equivalent circuit for a half-wavelength CPW. The red circles emphasize additional load lines essential for this technique. These load lines have influences on the measurement (as explained in the text). b) Schematics of a lumped element resonator designed at the IMS, and used in this work, omitting disturbing coupling capacitors and load lines. Fig. from [209].

Thirdly, the values of C_c and the pieces of load-lines marked with red circles around (see figure 5.4.a) are unknown, and this fact makes the results not quantitatively reliable. Thus, there was a need of a reliable and direct determination of dielectric

losses. In order to avoid additional coupling capacitors and parallel load resistors, a pure LC circuit was designed consisting of a parallel plate capacitor and an inductance realized by a microstrip line directly connected to the load lines (see Fig. 5.4.b and 5.5)

The Lumped LC Resonator consists of a superconducting inductive coil and superconducting parallel-plate capacitor containing the dielectric under investigation.

For what it concerns capacitors (Fig. 5.7), the energy loss comes from dissipation in the insulator (with dielectric constant ϵ), which is conventionally described by the loss tangent $\tan \delta = \text{Im}\{\epsilon\}/\text{Re}\{\epsilon\}$ [147]. Small values of loss tangent ($\tan \delta \leq 10^{-5}$) are desired, with the number of coherent oscillations in the qubit given by Q_0 .

The Lumped LC Resonator technique allows to measure directly the loss tangent of the dielectric via the intrinsic quality factor $Q_0 = 1/\tan \delta$, using no fitting parameters. The bulk material losses exceed interfaces losses by far, thus the measurement is entirely referred to the dielectric under study.

By varying the area of the capacitor plates and the geometry of the inductance, a wide frequency range was covered (150 MHz to 15 GHz).

By achieving the same resonance frequency with different geometries, the redistribution of losses between the inductance and the capacitance could be investigated. The comparison between different resonator geometries was also employed at IMS to optimize the inductor design and avoid capacitive coupling within the meanders.

The Lumped LC Resonator technique is a reliable and powerful tool for loss tangent characterization at mK temperatures, at which a qubit device is operated, and allows to characterize the loss tangent dependencies of insulator material on the following parameters:

- temperature (20 mK-4.2 K)
- frequency (150 MHz-10 GHz)
- power ($10^{-6} - 10^{-3}$ V)
- resonator geometry

- fabrication processes of the insulator

Thus, this technique may also help to develop a deeper understanding of loss mechanisms in dielectric thin films.

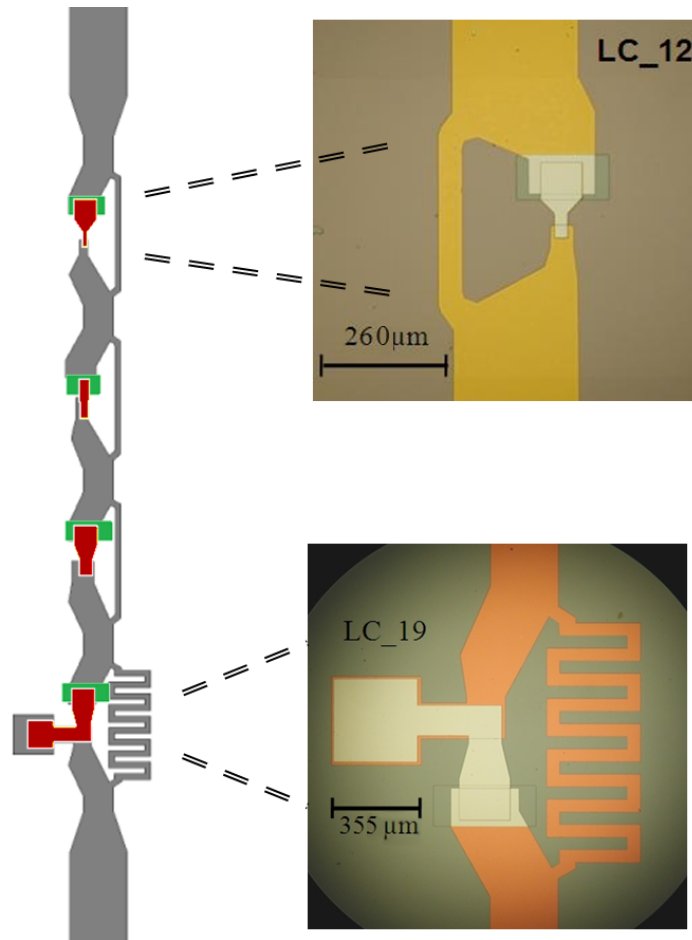


Figure 5.5: Optical photographs of two Nb/a-Si:H/Nb LC resonators. These resonators were optimized by Ustinov's group for different resonant frequencies, and fabricated in the ICIB-CNR by RIE method (see text).

When measuring the magnitude of transmission $|S_{21}|$ of such a superconducting resonator, one normally obtains the loaded quality factor Q_L , which is given by 5.1.20. There, Q_e is a measure of how much the resonator is decoupled from its environment. Q_0 is the intrinsic quality factor and denotes the loss in the resonator itself.

It is composed of three contributions as it is given by 5.1.24. There, $1/Q_\epsilon = \tan \delta$ denote the dielectric, $1/Q_{rad}$ the radiation and $1/Q_\rho$ the conductor losses. For a carefully designed superconducting resonator with matched lines and a closed housing, $1/Q_{rad}$ should be negligible. As for the resonators, the surface impedance amounts for $R_s = 0.32\mu\Omega \text{ GHz}^{-2} \cdot f^2$ [109], $1/Q_\rho \approx 1 \times 10^{-7}$ at 100 MHz, and $1/Q_\rho \approx 1.5 \times 10^{-5}$ at 15 GHz (all at 4.2 K) can be estimated. Since R_s decreases exponentially with temperature [92], the described method would be especially suitable for the characterization of low-loss materials for qubit applications, since $1/Q_\rho$ is negligible (orders of magnitude lower than all measured $1/Q_0$ values) already at 300 mK. The fact that conductor or inductor losses do not enter in the measured Q_0 values has also been confirmed by simulations and experiments. Altogether it can safely be assumed that in the presented method $1/Q_0 = 1/Q_\epsilon = \tan \delta$. This means that, by measuring the transmission $|S_{21}|$, the total dielectric losses at the resonance frequency can be obtained from the measurement data.

As this type of resonator has no coupling capacitors, it can be seen as a notch filter. The advantage of such a notch filter is that multiplexing is possible by putting resonators in series which cannot be done for the resonator's design introduced by O'Connell *et al.*, or half-wavelength CPWs, because these act like bandpasses. With a multiplexed resonator, losses at several frequencies in a broad frequency range can be investigated in one cooldown, which is a striking advantage in the face of very time-consuming measurements like low temperature measurements in dilution fridges. An obtained measurement curve of a sample with four resonators in series is shown in Fig. 5.2. It can be seen that all four resonances exist. By extracting the values of the loss tangent it could be shown that the values obtained by single resonators could be reproduced to a precision better than 0.1% by the multiplexed ones. This validated the idea of multiplexing the resonators.

5.2.1 Design and Simulations

At IMS and KIT, Germany, they have a long-time experience in the design of microwave resonators: altogether over 40 different resonators were designed by S. Skacel and Ch. Kaiser, covering a frequency range from 150 MHz to 15 GHz for various types of dielectrics with different values of ϵ_r . By varying L and C relative to each other, the same resonance frequency was achieved for different geometries. Thus, it could be proved that the losses extracted from the measurements were equal at one frequency independent of the resonator design. Multiplexed resonators were successfully designed by implementing up to six resonators in series. Obviously, the maximum number of resonators in series only depends on the chip size.

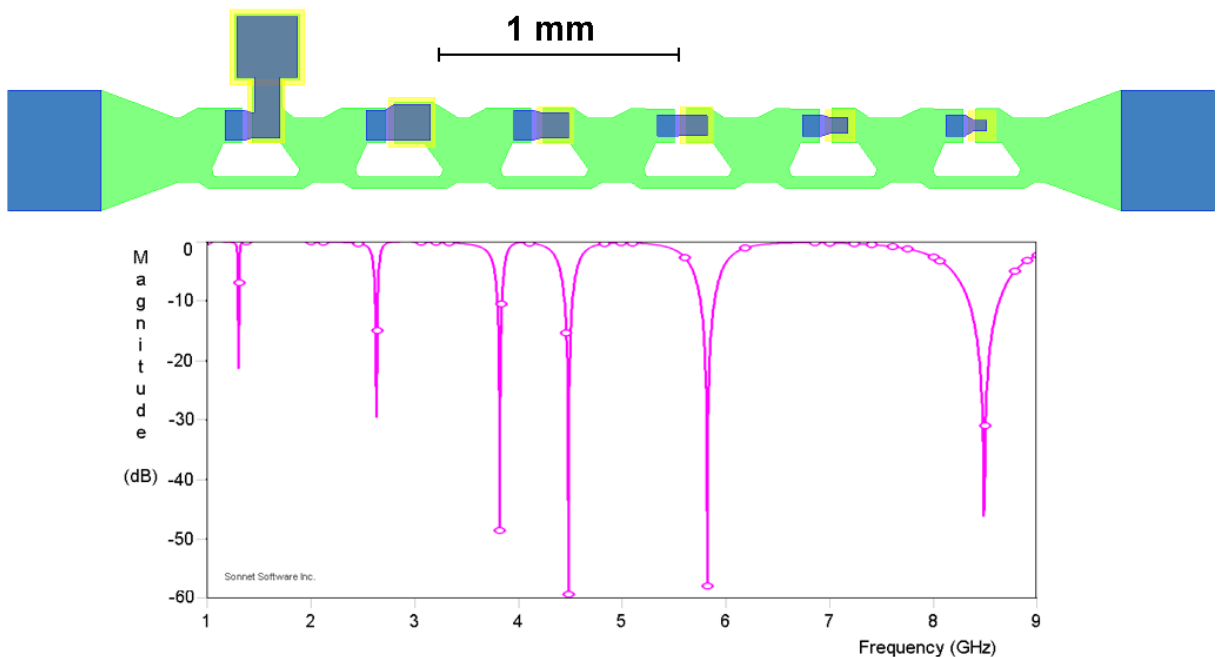


Figure 5.6: (Top) The newest layout with 6 multiplexed resonators and high temperature a-Si:H lift-off process. Green: base superconducting layer; yellow: dielectric layer; blue: superconducting wiring layer. (Bottom) Sonnet $|S_{12}|$ simulation of the same circuit.

In the actual experimental setup [109], the resonators under investigation are directly coupled to the microwave cables through microwave SMA connectors and

indium contact bonding, *i.e.* no coupling capacitor are inserted in series on the line. This configuration realizes a stop-band notch filter, in contrast to the majority of CPW or lumped element superconducting resonators so far realized, which are band-pass filters [141, 174].

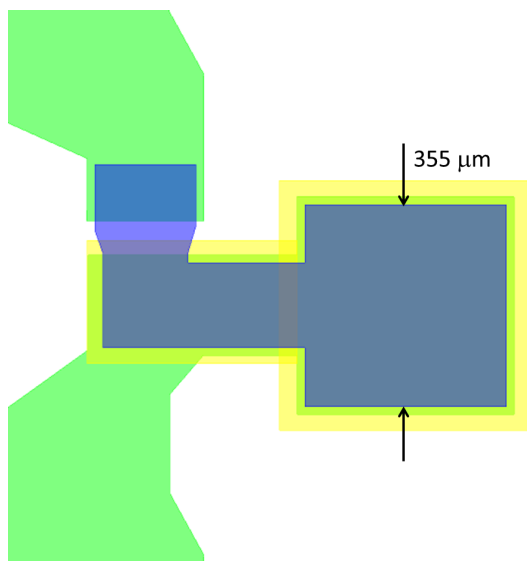


Figure 5.7: Detail of the layout of a parallel plate capacitor with large area ($> 350 \times 350 \mu\text{m}^2$). Green: base superconducting layer; yellow: dielectric layer; blue: superconducting wiring layer. Such capacitors were realized without pinholes and electric short-circuits despite the large area, sign of a good quality of the deposited thin films.

Careful electromagnetic simulations lead to a design of 4 and 6 multiplexed resonator in series, with orthogonal resonances and negligible cross talk interference, as shown in the left panel of Fig. 5.2 in the case of a 4 series circuit.

During the design process, the simulation of the resonators were done in order to figure out if the designs were suitable for measurement. For this purpose, the commercial software Sonnet [214] was used. With this software it was possible to simulate any superconducting parameters (*e.g.* surface impedance, kinetic inductance, *etc.*) and geometrical parameters, as well as material properties based on Maxwell equations. A typical simulation file of a sample with 6 resonators in series simulated in Sonnet is shown in Fig. 5.6.

In the simulations, all parameters (Nb as superconductor, the values of ϵ_r of the different dielectrics between the plates and of the substrate, and the physical sizes) were inserted. The loss calculated as $\tan \delta = 1/Q_0$ out of Q_0 extracted from the simulated resonance curves was always equal to the loss value of the dielectric between the

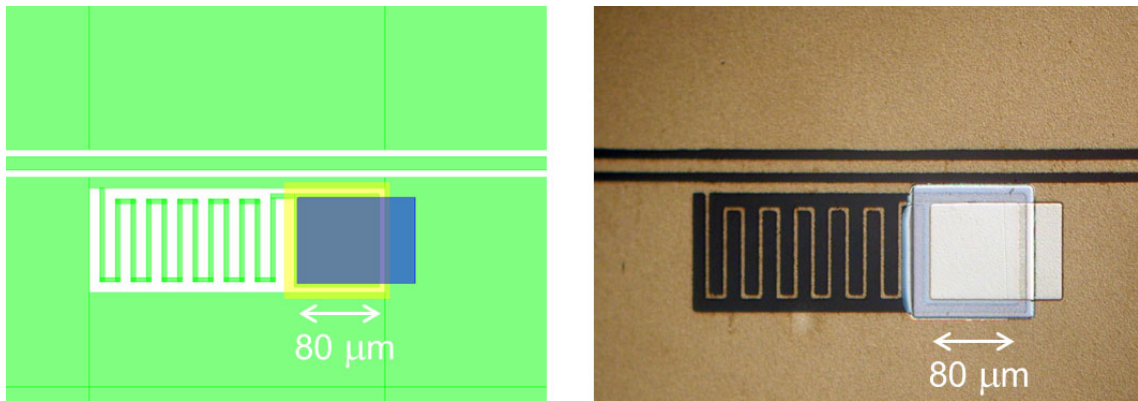


Figure 5.8: Design (left) and realization (right) of "hanging" LC resonator fabricated by means of high temperature a-Si:H lift-off process.

capacitor plates inserted in the simulation. This was plausible, because the additional contributions (besides the dielectric loss Q_ϵ) were assumed to be negligible, as it was shown in the previous section. In order to achieve a 50Ω matching and thereby avoid radiation loss, the width of the line connecting the resonators (see Fig. 5.6) were simulated by using the software *tx Line* [227]. For a 200 nm thick microstrip line on a $300 \mu\text{m}$ thick silicon substrate (with $\epsilon_r = 11.9$), the typical line width is $240 \mu\text{m}$. As the type of substrate and its size determines the width of the microstrip line, it has to be calculated for all substrates used. As the SMA connectors were $500 \mu\text{m}$ wide, the microstrip line was tapered linearly from $500 \mu\text{m}$ to $240 \mu\text{m}$ in order to keep close to a 50Ω matching. As a linear taper showed no influence on the simulated loss value, it was used to connect the contact plate with the microstrip. The fact that solely the dielectric loss of the amorphous dielectric between the plates determined the simulated measurement results, which were independent of the dielectric parameters chosen for the substrate, lead to the conclusion that entire dielectric field is stored in the capacitor.

Thus, this measurement method could be called a direct measurement method of dielectric loss of thin films. In the case of the multiplexed resonators, it was simulated how far the resonators have to be placed apart in order to get no crosstalk between them. The simulations showed that the resonators could be placed directly next to

each other without causing crosstalk.

As we will discuss in section 5.3, we recently designed a newer layout, showed in Fig. 5.8, in order to solve several spurious coupling and circuital-loss sources, that were hindering the low temperature of a-Si:H resonators. This design is called "hanging" LC resonator by several groups (*e.g.* [174]), and is developed in order to avoid ground-losses due to the use of CPW feeds instead of microstrip launchers.

5.2.2 Measurement Technique

Another important part of the experimental method is the measurement setup. In the following, the measurement setups used at 30 mK in a dilution refrigerator will be described.

In order to characterize a resonator, first of all the latter was mounted into a sample housings, and its resonances were measured by analyzing the $|S_{21}|$ parameter with a 40 GHz network analyzer.

During the pre-characterization at 4.2 K, the housed samples were connected via SMA connectors to two un-attenuated semi-rigid cables matched to 50Ω .

Especially at higher frequencies, noise comes into play, disturbing the smoothness of the measurement curves. Two possibilities to find a remedy were to reduce the internal bandwidth (1 Hz in all the measurements) of the network analyzer and repeat the measurement several times and to average over the curves, because the noise has stochastic nature and therefore it can be averaged out to a certain degree. An average factor of 100 up to 600 was chosen. The measured curves were analyzed by Matlab using the 3 dB method.

The measurements at very low temperatures ($T < 1$ K) and powers (single photon regime) required the installation of broadband and filtered microwave lines into the dilution refrigerator at KIT. At low cryogenic temperatures ($T < 1$ K) it is standard to install attenuators to the cables going down to the sample in order to attenuate the signal in the order of several magnitudes. Resistors are used as attenuators to reduce the noise coming to the sample and thermalize the cable's inner conductor,

which otherwise would be floating and directly connecting the room temperature electronics with the sample at the lowest temperature. The samples are not He-bath cooled, but placed in an evacuated chamber and thermally anchored to a cold stage.

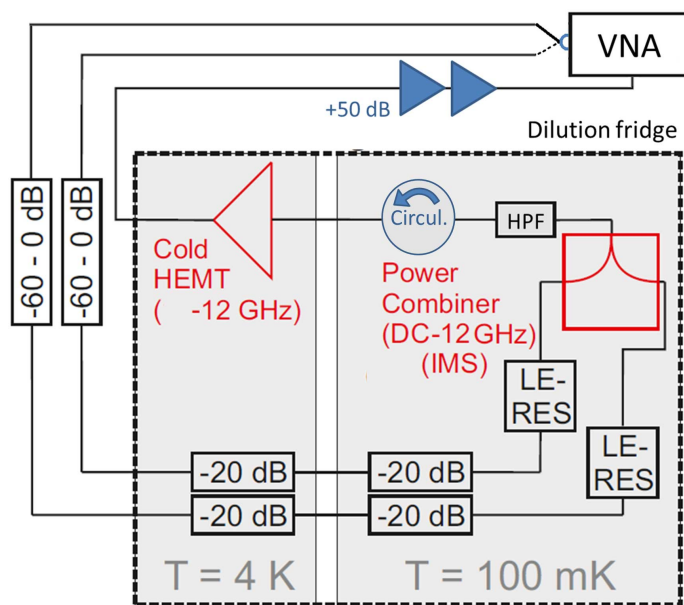


Figure 5.9: Schematics of the microwave set-up for the resonator characterization at 30 mK. See the text for a description of the components. Fig. readapted from [209].

For the dilution fridge measurements at the KIT an Oxford Kelvinox 400 was used. By attenuating the signal, one is able to apply very low powers to the sample built into the cryostat. In Fig. 5.9 one can see a -20 dB attenuator thermally anchored at 4 K. -20 dB is equal to a dissipation of 99 % of the applied power. Another -20 dB attenuator is thermally anchored at the coldest stage. In combination with the cables, which have an attenuation of -15 dB, and a step attenuator, which is able to vary the attenuation in steps from 0 to -60 dB, a maximum attenuation of -115 dB could be achieved, without considering the adjustable output power of the network analyzer. With the two anchored -20 dB attenuators, the thermal noise temperature could be reduced to 30 mK at the coldest stage. In the outgoing line, the signal has to be amplified again to be able to measure the signal back at room temperature. At this side, the sample has to be protected from noise coming from the amplifier input, which is thermally anchored at 4.2 K. For this purpose, the standard technique is to use a circulator (5-12 GHz) and a high pass filter ($f_c = 4$ GHz) at the coldest stage.

Moreover, we chose to use a power combiner, with an average attenuation of -8 dB in the bandwidth of interest, in order to measure multiple sampler during the same cooldown.

The outgoing signal is amplified at 4 K by a broadband (from 4 GHz to 12 GHz) cryogenic Russian amplifier (+25 dB amplification), and at room temperature by 2 MicroCircuits amplifiers having each a gain of +25 dB.

While at high powers (around -55 dBm) only an average factor of 1 to 2 is needed for usable measurement whit 200 to 300 points in the measured bandwidth, at low powers (below -105 dBm) an average factor up to 1000 has to be used.

5.2.3 Fabrication

The a-Si:H films studied in this work were deposited by high-frequency plasma enhanced chemical vapour deposition (PECVD) [53] on silicon substrates, on which 200 nm thick niobium-films were already been deposited and patterned with several geometries of inductors and capacitors.

During the PECVD no photoresist was present on the samples, in order to avoid the contamination of both the deposited a-Si:H and the reactor chamber, but also because the high temperatures required to obtain the highest quality a-Si:H ($\sim 250^\circ$ C) would have permanently burnt any conventional photoresist (see Fig. 5.10).

The PECVD parameters were optimized during several preliminary depositions of a-Si:H; by exploring the deposition parameter-space along the temperature (150°-250° C) and the silane/hydrogen dilution (1:0 - 1:2) axes, we determined the optimal receipt in order to: obtain the best a-Si:H adhesion on both silicon substrate and niobium films, avoid interface-bubble formation, maximize the FTIR peaks relative to Si-H stretching mode and Si-H bending mode (seen next section), and, of course, reduce as much as possible the low temperature dielectric losses (by means of the same fabricated resonators).

The optimal deposition parameters were found at a silane pressure of $P_{SiH_4} = 200$ mTorr, at an incident power of 5 W; the plasma was driven at 100 MHz and the

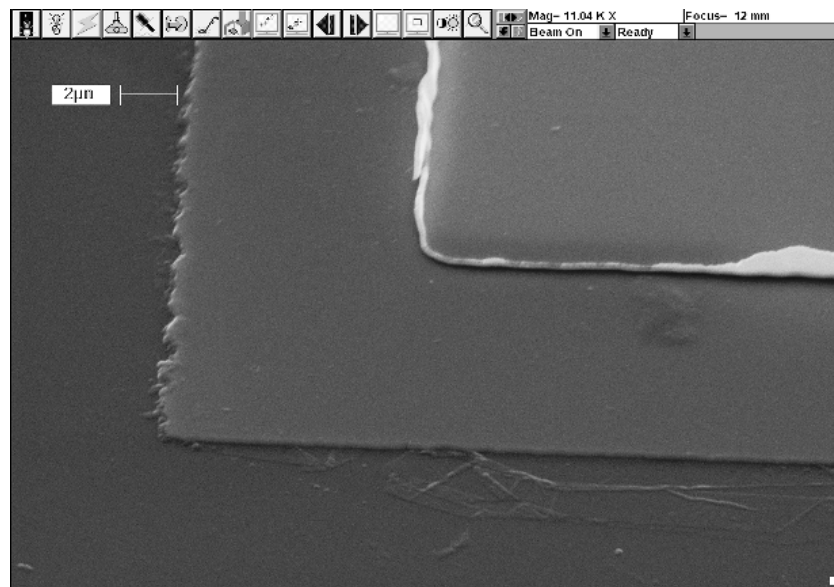


Figure 5.10: SEM image showing a border of an a-Si:H parallel plate capacitor. The lower layer is the Si substrate, followed by a patterned Nb base electrode and a Nb counter electrode. The a-Si:H, being an insulating material, is essentially not visible. The rough photolithography on one edge, and the presence of photoresist residues (veils), are to be noted.

substrate temperature was set at 250° C in order to obtain the lowest defective films.

After the deposition, the a-Si:H films covered uniformly all the sample's surfaces: it was necessary to open a contact via through the insulating film by means of CF_4/O_2 reactive ion etching before completing the capacitor fabrication with the niobium counterelectrode lift-off deposition (Fig. 5.11).

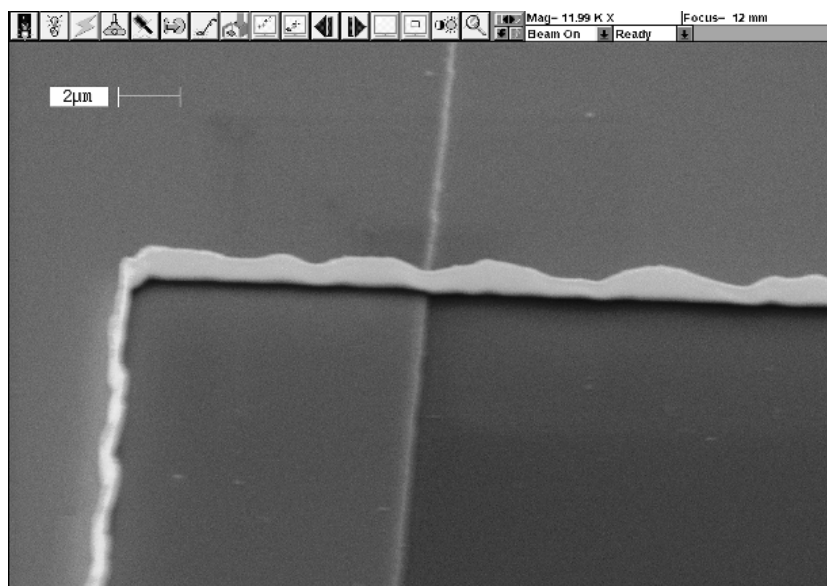


Figure 5.11: SEM image showing a detail of the wiring layer of an a-Si:H parallel-plate capacitor. The upper layer is the Nb counterelectrode, which shows pronounced defects due to the lift-off process (afterwards optimized).

In addition to the conventional RIE process for definition of the a-Si:H layer, a high temperature lift-off process based on the PMGI resist was also developed and successfully applied for patterning the a-Si:H film (see section 8.4).

In fact, in order to realize high quality superconducting resonators or qubits, it is preferable to reduce the dielectric coverage of the underlying superconductor [147, 32, 14], limiting the contamination of the superconducting surfaces by hydrogen and dielectric inclusions. In order to perform lift-off at the high-required temperature, we demonstrated that a PMGI/Nb bilayer, suitably patterned and conditioned, is capable of high temperature (up to 200° C) lift-off of a-Si:H.

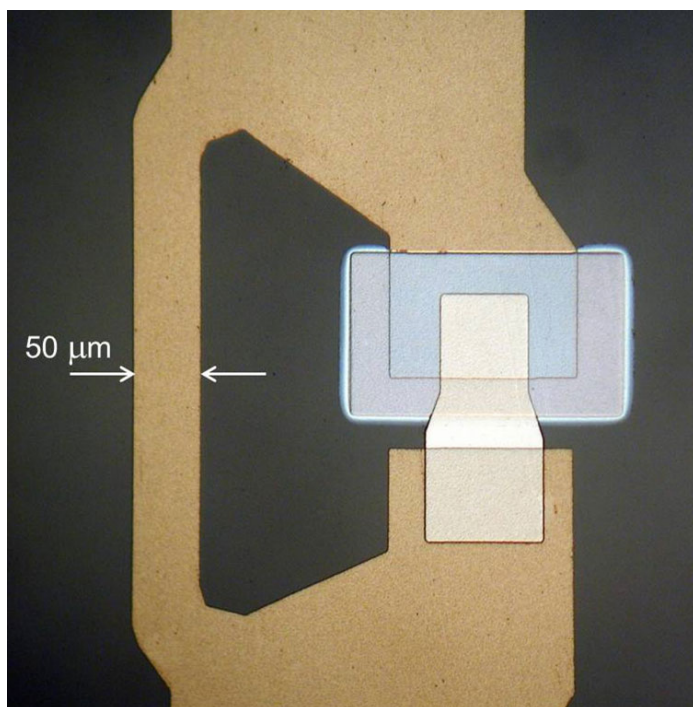


Figure 5.12: An LC resonator fabricated with the novel high-temperature a-Si:H process. The dielectric is deposited only where necessary, and the superconducting surface are left uncontaminated by hydrogen and silicon diffusion.

Finally, we developed a fabrication protocol that is suitable for both the resonators and the qubits fabrication, as extensively discussed in chapter 8. Indeed, the last-fabricated resonators were co-fabricated on the same chip with the qubit, in order to investigate in the same experimental condition both the dielectric losses and the decoherence of the qubits.

5.3 Results

The present analysis of a-Si:H resonators came right after an extensive survey of commonly used dielectrics: a first set of measurements involved Nb_2O_5 resonators, where the anodic niobium oxide was grown under different conditions and chemistries in order to determine the dependence of the quality factor on the oxide preparation; then SiO_2 and SiN_x resonators were characterized, showing the expected increase in the quality factor due to their less defective dielectrics [109]. All these measurements were done in a brass sample housings at IMS. With such configuration, the frequency

dependencies of the dielectric loss of such insulating materials were measured with great reproducibility at $T = 4.2$ K.

After our effort to develop a reliable method for the integration of low-defective a-Si:H in the standard fabrication of superconducting circuits based on Nb Josephson junction technology [32] (see section 4.2), we realized superconducting LC lumped resonators consisting of a superconducting inductive coil and superconducting parallel-plate capacitor containing the dielectric under investigation, as in Fig. 5.6.

At ICIB-CNR we realized LC resonator with both evaporated SiO and PECVD a-Si:H. In collaboration with IMS and KIT, we participated to a large materials-characterization survey, started one year before by Kaiser *et al.* [109], but we performed also independent measurements at the ICIB-CNR since we recreated the suitable microwave experimental set-up in our laboratories.

For all investigated materials, no dependence of the losses on the dielectric film thickness was found. This is not surprising for such lossy amorphous materials and shows that the losses in the film volume exceed the electrodes interface losses by far. The frequency dependencies of $\tan \delta = 1/Q_0$ for amorphous thin films of Nb₂O₅, SiO, SiO₂, SiN_x and a-Si:H are shown in Fig. 5.13. The rather large spread of the measured $1/Q_0$ values for each material is apparent. This spread was not caused by the measurement procedure and found to be the same for samples from different or the same processing runs.

Loss tangent is also $\tan \delta \sim \chi''$, where χ'' is the imaginary part of the electric susceptibility [167]. The loss tangent depends on the frequency, because $\chi'' \cong \omega^{n-1}$ with $0 < n < 1$ ("Universal Law") [107]. Mutual interactions between TLS dipoles determine the exponent n :

- $n = 0$ for no interaction
- $n \sim 0.5$ for nearest-neighbor interaction
- $n > 0.6$ for many body interaction.

Dielectric losses could be written as $\tan \delta \sim \chi''$, where χ'' is the imaginary part

of the electric susceptibility [167]. The $\tan \delta$ data recorded for the different materials at 4.2 K and at different resonant frequencies were fitted by the "Universal Law" $\chi'' \approx \omega^{n-1}$ with $0 < n < 1$ and ω being the resonant frequency. The exponent n is indicative of the mutual interactions between TLS dipoles: for $n = 0$ there is no interaction, for $n \sim 0.5$ nearest-neighbor interaction is prevalent, and for $n > 0.6$ many-body interaction is the main defect-defect one.

In the case of the above mentioned materials it was measured $0.63 < n < 0.68$, indicating that the TLS interaction could be described by the many-body interaction model.

Such a behavior can be expected for the investigated amorphous and hence glass-like materials. Knowledge of the mutual coupling of the TLS would also be important for the understanding of decoherence mechanisms in superconducting qubits. In general TLS modeling [186] as well as qubit related publications [204, 153], the TLS are simply assumed to be non-interacting. At first sight, dielectric loss measurements in the qubit working regime should allow to reveal whether this is true or not. In this regime, however, the dominant loss mechanism will always be resonant absorption. In this case, only the TLS in resonance with the MW frequency will contribute to the losses so that the mutual coupling of the dipoles cannot be probed. Although it is not *a priori* clear whether the results obtained in the relaxation regime at $T = 4.2$ K can be directly transferred to the behavior of TLS in the qubit working regime, these results revealing the mutual coupling of the TLS should at least be considered in the context of qubit decoherence.

Nb_2O_5 has been shown to be a very lossy material [109]. As it is a standard material in Nb based Josephson junction fabrication, it would be desirable to avoid its use in device fabrication, and possibly limit its presence. Investigation of the influence of the anodization condition for the growth of Nb_2O_5 on its dielectric losses showed that the losses are practically constant and do not depend on the anodization time or voltage.

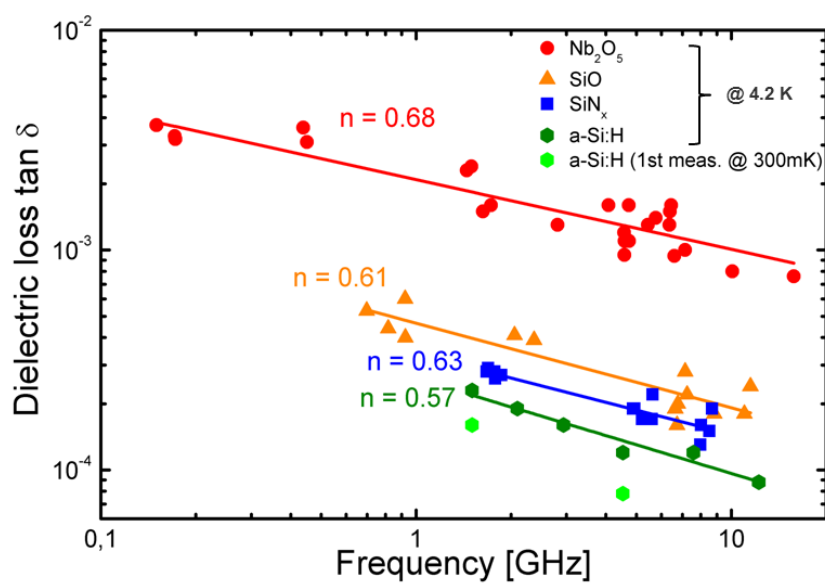


Figure 5.13: Experimental results obtained at $T = 4.2$ K for Nb-based LC resonators with different insulating materials. Nb₂O₅ was grown by anodic oxidation in aqueous solution (sample from IMS); SiO was deposited by thermal evaporation technique (sample from IMS); SiN_x was grown by PECVD (sample from PTB); a-Si:H was grown by PECVD (sample from ICIB-CNR). Results for a-Si:H at $T = 300$ mK are also reported. Figure from [109].

It can be seen in Fig. 5.13 that the absolute values of the losses in different materials compare to each other as expected, for example from [147], where it was predicted that the losses in silicon compounds should decrease with increasing coordination number. We found that especially a-Si:H is a material with very low losses.

As soon as we started to measure the resonators with a-Si:H as capacitor dielectric, it appeared evident that the measured quality factors were somehow "limited" to Q_0 values lower than 9000, by unknown reasons, instead of the expected unloaded quality factor $Q_0 \sim 30000$ for such resonators at 4.2 K. Moreover, for these resonators, the Q_0 were also strongly and anomalously dependent on the applied microwave power, unlike the case of all the perviously measured resonators.

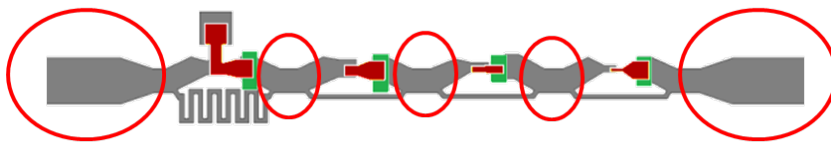
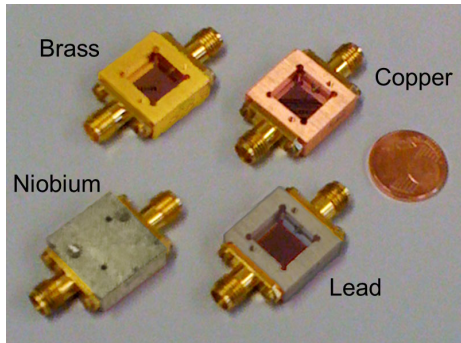


Figure 5.14: Layout of a series-resonator with the microstrip sections, responsible for inducing current in the ground of the sample housings, highlighted in red.

Further analysis, and accurate simulations using Sonnet [214] Electromagnetic Field Solver pointed out that the limiting factor had to be found in the sample housing and, in particular, in the choice of its constituting material. Simulations of the housing influence on quality factors showed that superconducting housing reduces the housing influence to an absolute minimum. In fact, it came out that the on-chip microstrip launchers, used to connect the SMA connectors to the lumped element resonator, although being well matched (50Ω) to groundplane by means of their width and tapered design, induce currents in the groundplane (see Fig. 5.14). The latter, in the brass-housing experimental setup, is the lossy and rough brass-housing surface underneath the chip substrate. Moreover, under the superconducting lumped inductor, there is no need of a groundplane, and ideally there should not be at all. Thus,

having a lossy ground plane is the most undesirable condition in our experimental setup.



Housing material	Sonnet Q_0	Experimental Q_0
Brass	9255	8391
Copper	13724	12740
Lead	29000	19598
Niobium	29000	26400

Figure 5.15: Left: photo of the samples boxes with installed SMA connectors and bonded samples (for the niobium housing, the Nb cover is also installed). Right: simulated and measured quality factors for a ~ 4.5 GHz a-Si:H resonator varying the sample housing material.

The low values of the loss tangent of a-Si:H (up to 2.5×10^{-5} at 4.2 K) required the development of superconducting housing for the resonators in order to eliminate a spurious dependence of $\tan \delta$ on the microwave power, by reducing losses which were not originated in the dielectric itself. The results of the simulations agree well with the experiments.

For the above reasons, we realized new versions of the sample housing, as shown in Fig. 5.3. We have been able to measure very low losses in the a-Si:H resonators (as low as $\tan \delta = 2.5 \times 10^{-5}$ at the highest frequencies, and as expected from amorphous silicon at 4.2 K), initially by means of housings made of copper, then of superconducting lead, and finally of superconducting niobium.

Thus, in order to measure the dielectric losses of an extremely low lossy material, like a-Si:H, with our microstrip-coupled lumped element resonators, one needs to ensure that the dielectric losses have to be the dominant losses in the measurement setup. Furthermore, the difference between the measurements performed in lead and in niobium housings (right table in Fig. 5.3) could be indicative of the higher losses expected from lead oxides compared to niobium oxides.

In order to improve the resonator’s design for the next fabrication run, we designed, simulated, and realized LE resonator with a new ”hanging” design [174] (see section 5.2.1), and they are currently under measurement.

Having minimized the spurious losses present in our experimental setup by using superconducting housings, we proceeded to correctly characterize the a-Si:H material, and we extracted a parameter $n = 0.57$, showing that the nature of the TLS interaction in such material seems to be closer to the nearest-neighbor one, which is indicative of a lower density of TLS defects.

In addition, we have investigated resonators having the same resonance frequencies, but realized with different combination of the inductor length and capacitor area, demonstrating that the quality factor Q_0 is independent of the resonator geometry. Moreover, for all the investigated materials, no dependence of the losses on the dielectric film thickness was found.

The a-Si:H resonator were measured also in a He³ cryostat at 300 mK, and the measured losses are plotted in Fig 5.16: as expected, the loss tangent decreases with decreasing temperature reaching the 10^{-5} range.

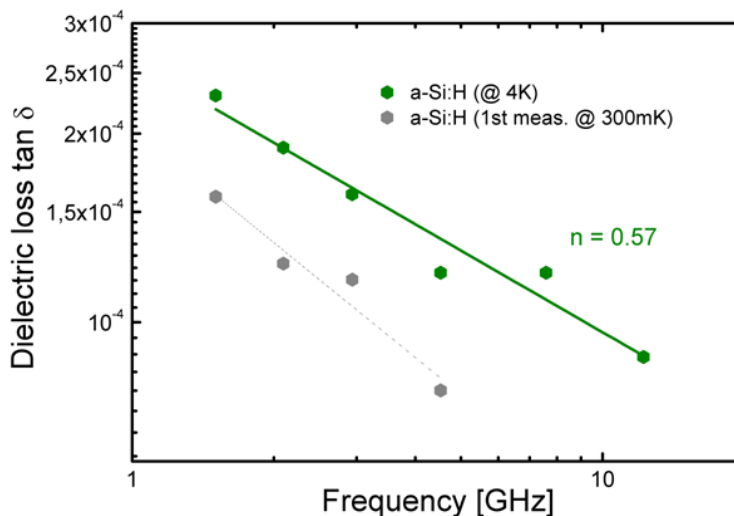


Figure 5.16: Large-scale plot of the frequency dependencies of the a-Si:H loss tangent measured at two temperatures (4.2 K and 300 mK). As expected, the loss tangent decreases with decreasing temperature reaching the 10^{-5} range.

The obtained loss tangent results at $T=4.2$ K and at $T=300$ mK (together with work-in-progress measurements at 30 mK) confirm the suitability of fabricated a-Si:H films to be employed as dielectric layers for the realization of qubits with longer coherence times.

Many other interesting investigations are on the way to be realized. In order to avoid a possible additional loss in the Nb caused by the hydrogen diffusion in the Nb electrodes during the a-Si:H PECVD, we fabricated resonators with the Nb base electrodes covered by a thin protective film: 3 nm a-Si by sputtering, NbN layer by plasma nitridization (for both, see section 4.2), and 3 nm Al film. Moreover, in order to compare Nb-based resonator with non-Nb ones, we fabricated full-aluminum resonators.

Furthermore, having minimized the spurious losses of our setup, we showed that the improved lumped LC lumped resonator method is a reliable direct measurement of low temperature dielectric loss and thus we opened the door for a new survey of a number of ultra-low loss amorphous (such as a-SiC:H, DLC, *etc.*) or single crystalline [244] dielectric candidates, in a quick and accurate way.

As a last remark, it could be very interesting to characterize losses of LC resonators and coherence times of qubits in the same measurement, to correlate the two phenomena at the same experimental conditions and in the same deposited material, by means of co-fabricated circuits. In chapter 7 we will further develop this idea, by designing both phase qubits and LE resonators on the same photolithographic mask.

Moreover, the developed high-temperature lift-off process (section 8.4) is capable to integrate the high-temperature PECVD deposition of a-Si:H with existing Nb Josephson technology, fulfilling the above mentioned requirements of reduced coverage of the underlying superconducting films.

Chapter 6

Josephson Junctions for Qubit Devices

Having extensively discussed about the theory of decoherence (chapter 2) and the state of the art of the materials research (chapter 3), and having introduced the high quality dielectric of interest (the a-Si:H, in chapter 3 and 4), the next step in order to implement a superconducting quantum bit is the realization of the Josephson junctions, the heart of such circuit.

In this chapter I will describe the strategies which were followed in the junction design, fabrication, and characterization. I will show our approach in the integration of novel processes aimed to reducing the intrinsic decoherence source at the junction level, namely the epitaxial growth of the superconducting base layer (and the tentative realization of a full-epitaxial trilayer), the avoidance of any anodization process, the surface treatments to passivate surface TLSs, the reduction of the oxide content, integration of a-Si:H with the junction fabrication, and the reduction of the superconductor's area covered by dielectrics.

6.0.1 Junction Design

As was demonstrated in [217], small junction-area qubits show fewer energy splittings (although larger) in high-frequency spectroscopy experiments, so that the number of TLS defects may be dramatically reduced with small-area designs.

However, loss of coherence from TLS depends both on the density and size of the splittings [217], and for low density it scales as the square of the tunnel-junction area divided by the total junction's capacitance:

$$loss \propto \frac{A_2}{C}. \quad (6.0.1)$$

So, a reduction in junction area reduces the number of barrier defects but also linearly reduces the capacitance C . Dramatic improvement in fidelity can thus be achieved by reducing the area of the tunnel junction to sub-micron sizes while keeping its critical-current constant, and the total capacitance constant by adding an external low-loss capacitor.

Even though modern lithographic and charged-beam techniques have made sub-micron and nano-scale size Josephson junctions a reality, the superconducting devices studied in this thesis were fabricated using standard i-line UV photolithography. This choice comes from the fact that we were intentioned to study the influence of several junction barrier materials on the coherence time of the qubit itself. Reducing the junction area would *de facto* reduce the overall barrier TLS number, and hence improve the coherence time, but will also make it more difficult to distinguish for an improved coherence time due to higher-quality barrier-material. Moreover, smaller junction sizes would also complicate the integration of novel barrier material in the circuits, drastically lowering the probabilities to successfully realize working qubit devices.

Our approach was then to use micron-size Josephson junction realized by trilayer processes and study the possibility to reduce the tunnel-barrier defects by changing its material (AlO_x , AlN , SiN_x) and their deposition processes. By the optical photolithographic process available at ICIB-CNR, test-junction with diameters ranging

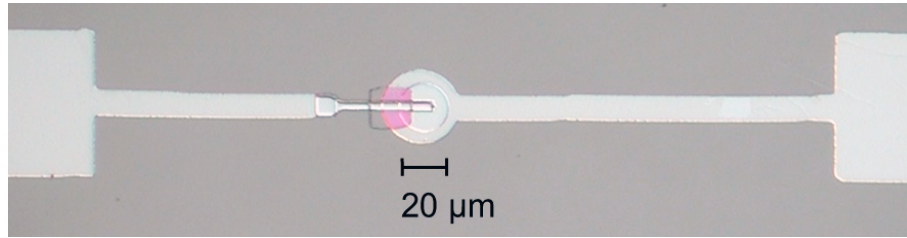


Figure 6.1: Optical image of a 20 μm diameter NbN/AlN/NbN Josephson junction with SiO wiring insulator and small-area wiring layer.

from 4 μm to 20 μm (Fig. 6.1) have been realized and characterized at $T = 4.2$ K.

Our optimizations started by considering the conventional fabrication processes based on Nb/ AlO_x /Nb trilayer and by incorporating it with the a-Si:H as wiring crossover. First of all, the deposition of a-Si:H by PECVD has been improved and optimized in order to minimize the circuital loss sources, as explained in chapter 3 and 4. We also paid attention on the possible degradation of the junction properties during the PECVD due to the high temperature necessary in such process.

The main technological aspects that we introduced in order to improve the qubit coherence-performance are as follows:

- the avoidance of any anodization step,
- the compatibility of the junction fabrication with PECVD a-Si:H technology for the fabrication of junction shunting-capacitor and wiring-insulator (SiO_2 replaced by a-Si:H),
- the reduction of the dielectric area in contact with the superconductors,
- the reduction of the wiring layer dimensions in favor of the base ones (the latter has better quality, and could be grown epitaxial)

We have successfully tested at $T=4.2$ K the feasibility of all the mentioned improvements by realizing several Nb/ AlO_x /Nb and NbN/AlN/NbN Josephson junctions whose parameters (in terms of critical-current density J_c) were already optimized for its application for superconducting phase qubits.

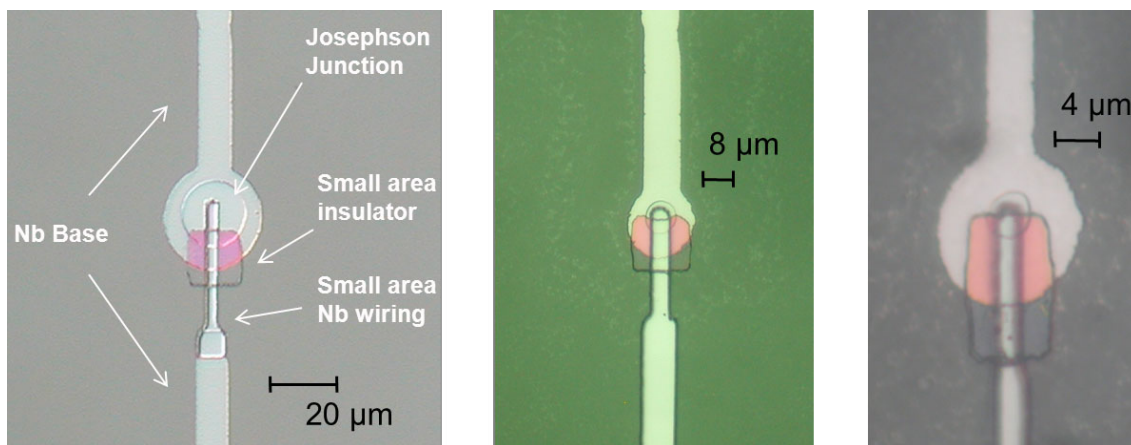


Figure 6.2: Design improvements applied to several test-junctions fabricated with a Nb/ AlO_x /Nb trilayer with critical-current density $J_c = 25 \text{ A/cm}^2$. The indicated dimensions refer to the relative junction-diameters.

6.0.2 Trilayers

During the realization of the test-junction, we focused mainly on Nb/ AlO_x /Nb and NbN/ AlN /NbN trilayers, for several reasons. Nowadays Nb/ AlO_x /Nb tunnel junctions are basic elements of most low- T_c superconducting electronic devices and circuits. Since its fabrication protocol was proposed in 1983 by Gurwitsch [91], it has been a solid technology, and in particular the junctions realized at ICIB-CNR for SQUID [88] and radiation detector [50] applications, and for physical research of Josephson devices [127] have been proven to have excellent Josephson characteristics. In addition to Nb technology, in the qubit community the Al/ AlO_x /Al junctions are more commonly utilized: first, there was the suspect that fluctuations and dissipation may arise from trapping sites in the Nb trilayer tunnel barriers; second, several research groups have achieved long coherence and energy relaxation times with Al junctions [237, 129].

Nevertheless, we utilized Nb/ AlO_x /Nb technology in order to compare the results coming from the other trilayers introduced during the qubit's fabrication (see section 8.2). We realized high quality junctions utilizing an approach derived from the radiation detector field: the realization of symmetric trilayer by the deposition of a

bilayered counterelectrode, namely 7 nm of Al and the standard Nb (the reverse of the base electrode) [189].

NbN/AlN is an alternative fabrication technology, which has been chosen in order to test qubit fabricated with material which differs from the traditional Nb/AlO_x and Al/AlO_x. NbN is considered as promising to increase the superconducting qubits decoherence times [163] because it can be epitaxially grown at room temperature. In addition, it is a superconducting material that forms a smaller amount of a native surface-oxide in comparison with Al and Nb, has a high superconducting transition temperature ($T_c \approx 17$ K), and has a large superconducting gap ($2\Delta = 5.9$ mV). To our knowledge, the realization of a first-generation current-biased phase qubit with NbN as superconductor and AlN as barrier material [255] showed a surprisingly long coherence time of the order of 5 μ s (although recently there were suspects regarding the credibility of this results).

In order to deposit thin films of NbN, we found the optimal conditions in terms of sputtering power and Ar/N₂ ratio during the deposition, as showed in Fig. 6.3. Moreover, we tested several substrate's surface pre-treatments: Propanol sonification, rf-argon cleaning, and wet acid etching (HNO₃ + HF)), in order to establish if these processes could influence the T_c of the grown films.

Furthermore, the choice of the substrate was made with care, for the reasons introduced in section 3.1. Even more, different substrates could lead to different crystalline structure of the sputtered material. For example, the authors of [69] simultaneously grew ultra-thin films (2.5–10 nm) of NbN by DC reactive sputtering at 600° C on A-, M-, and R-plane orientations of sapphire substrate. The obtained films demonstrated that NbN on R-plane are (135) oriented and suffer from detrimental disoriented twin domains. On the contrary, NbN on M-plane sapphire is shown to be untwined, leading to a lower room-temperature resistivity, to an increased critical current density ($J_c > 4$ MAcm⁻² at 4.2 K), and to a higher critical temperature ($T_c = 11.3$ K for a 4.4 nm thin film)

Our attempt to realize the epitaxial growth of NbN/AlN/NbN trilayers begun

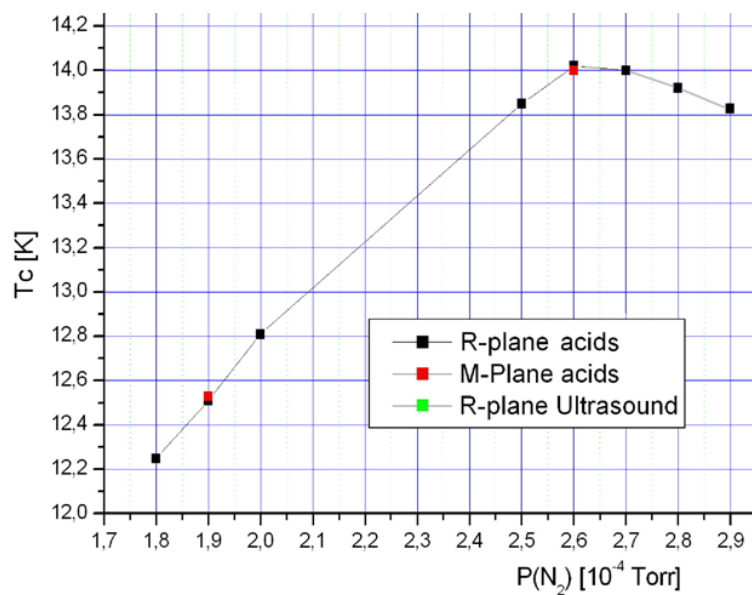


Figure 6.3: Niobium Nitride critical temperature versus N_2 partial pressure during the DC reactive-magnetron sputtering deposition of 200 nm thin films at 500 W. Different substrates and pre-cleaning procedures were also tested and are reported.

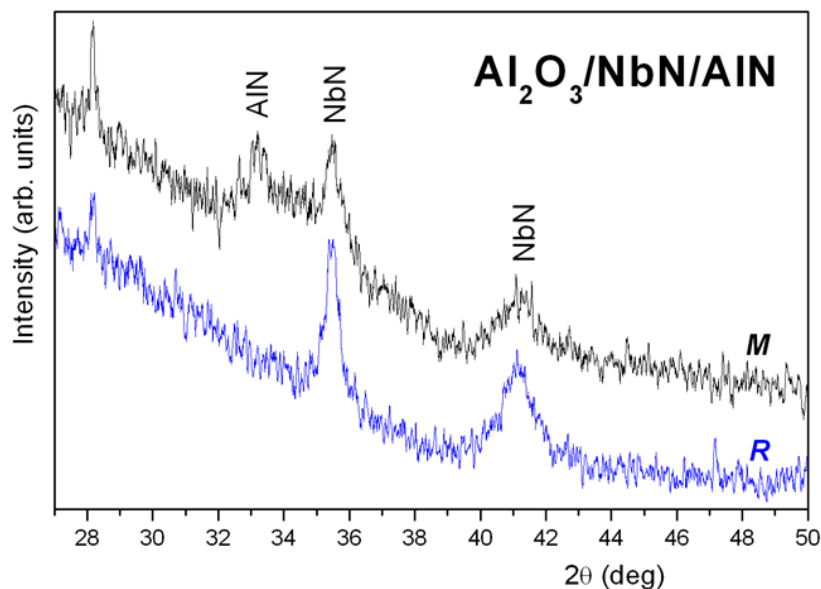


Figure 6.4: X-Ray diffraction patterns of NbN/AlN bilayers deposited on M- and R-plane sapphire at room temperature. The AlN peak is clearly observed only in the case of M-plane sapphire orientation.

with the comparison of the X-Ray diffraction properties of thin AlN films deposited *in situ* on NbN films, in a process similar to the trilayer realization (Fig. 6.4). It was a surprise to observe a difference in the appearance of the crystallographic phase of the AlN layer due to a change in the substrate orientation, which was accompanied by an apparently unchanged crystalline structure of the NbN layer.

This result seemed to be encouraging, and the next straightforward step was to increase the substrate temperature from room temperature up to 900° C, in order to promote the epitaxial growth of NbN and to improve the quality of the substrate/superconductor interface. Unfortunately, the high-vacuum heater ceased to work during the first high-temperature reposition, prematurely closing this branch of research on superconductor's epitaxial growth.

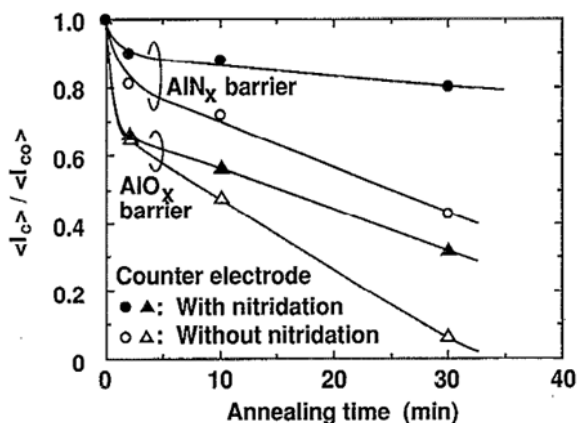


Figure 6.5: Annealing time dependence of critical current for AlO_x and AlN barrier junctions both with and without nitridation on the Nb counterelectrode. $\langle I_{c0} \rangle$ and $\langle I_c \rangle$ are medians of the critical currents, before and after annealing. The junctions were annealed at 250° C. Figure from [202].

Moreover, we tested if the fabricated junctions could sustain the high temperature ($\sim 200^\circ$ C) during the a-Si:H deposition. Annealing effects on the Nb/AlO_x/Nb Josephson junction barrier were studied in detail by Oliva *et al.* [172]. Generally, a marked decrease of J_c is observed with increasing anneal temperature/time, the normal-state resistance R_n is increased, and no changes in the junction capacitance are observed. Moreover, the authors reported a neat improvement in the barrier-quality in terms of the parameter $V_m = 0.7I_g \cdot R_s$, where I_g is the quasiparticle current at the energy gap voltage, $R_s = 2\text{mV}/I_{2\text{mV}}$ is the static resistance at the subgap voltage $V = 2$ mV and the factor 0.7 is reminiscent of the strong coupling

correction for the critical current of Nb-Nb superconducting tunnel junctions.

These considerations lead us to the idea that the junction could indeed benefit from the annealing process (under certain limits), resulting in a more compact and uniform barrier with lower defect density, because of an increase in the barrier height due to relaxing and rearrangement of TLSs and unbonded atoms in the barrier and at the interfaces.

Concerning the AlN barrier, the studies by Shiota *et al.* [202] showed that AlN barrier junction exhibited improved annealing stability as compared to AlO_x barrier junctions. For the AlN barrier junction, the decreases in critical current during annealing at 250° C are remarkably suppressed, as from Fig. 6.5. Moreover, by performing a N₂ plasma treatment on the Nb counterelectrode (a situation similar with the case of a NbN counterelectrode), the authors clarified the evident role of the oxygen penetration from the surface of the counterelectrode as responsible for the junction degradation after the annealing process.

6.0.3 Characterization and Results

The test Josephson-junctions were fabricated by the optimized junction geometries described in section 6.0.1 and were characterized at $T = 4.2$ K in a custom low-noise measurement system at the ICIB-CNR. The quality parameters extracted from the I-V characteristics are analyzed and discussed in the following. The I-V of a 20 μm diameter NbN/AlN/NbN Josephson junction with SiO wiring insulator and small-area wiring layer is shown in Figure 6.6. Figure 6.7 shows the I-V curve of a 20 μm diameter Nb/AlO_x/Nb junction with the same geometry.

As from the relative I-V graphs, the Nb/AlO_x/Nb exhibits low-subgap resistance R_s and good V_m quality factor, while the NbN/AlN/NbN Josephson junction has poor characteristics in terms of R_s and gap voltage V_g ; however, we can consider that the obtained quality will be suitable for the realization of qubits.

The critical current densities scaled as expected with the junction diameter, an important indication that the photolithographic junction definition (patterned by Cf₄

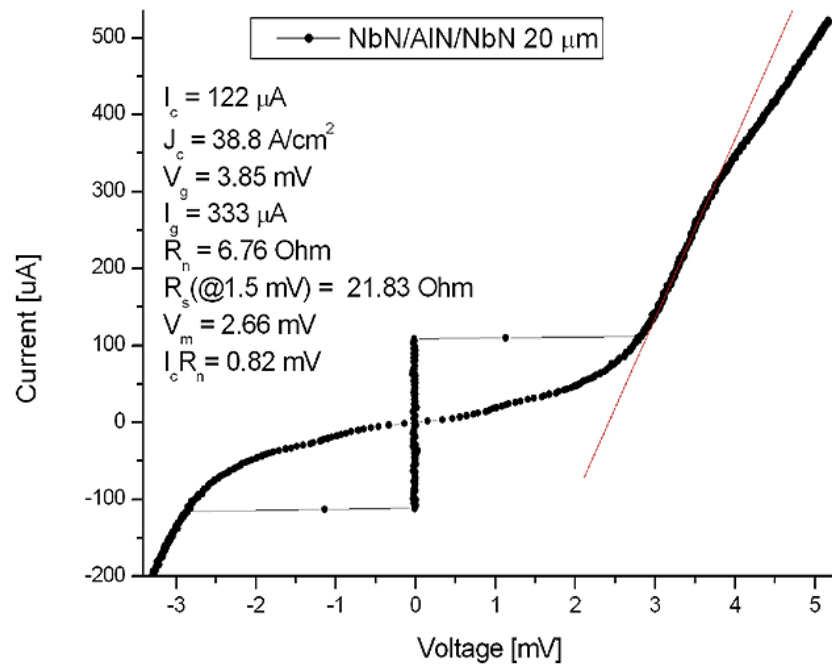


Figure 6.6: I-V curve of a 20 μm diameter NbN/AlN/NbN Josephson junction with SiO wiring insulator and small-area wiring layer, measured at $T = 4.2 \text{ K}$.

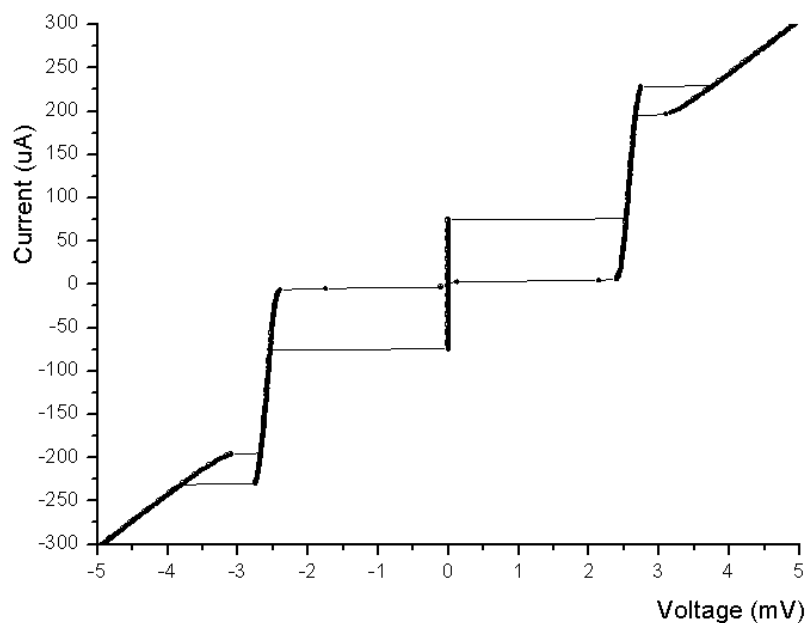


Figure 6.7: I-V curve of a high quality 20 μm diameter Nb/ AlO_x /Nb Josephson junction with SiO wiring insulator and small-area wiring layer, measured at $T = 4.2$ K.

RIE) is clean and not defective. Fig. 6.8 shows the I-V curve of a 4 μm diameter NbN/ AlN /NbN Josephson junction.

In Figure 6.10 we present the I-V curve and magnetic-pattern temperature dependence of a 10 μm diameter NbN/ AlN /NbN junction.

We also believe that the study of the junction's internal resonances (Fiske steps) could provide useful information on the barrier quality factor: the barrier volume is indeed a cavity comprised between two metal electrodes, and the physical meaning of the Fiske steps is indeed of junction resonances of the tunnel-barrier electromagnetic-modes. The voltage position of the Fiske steps and the relative amplitudes may reveal useful information about the quality factor of the underlying resonant cavity. In Fig. 6.10 we plotted the first Fiske steps, obtained by varying an uniform external magnetic field parallel to the junction's barrier plane.

We have estimated the junction's self-capacitance C_j from the analysis of the Fiske step voltage-position. Taking into account the dependance of the Swihart velocity on

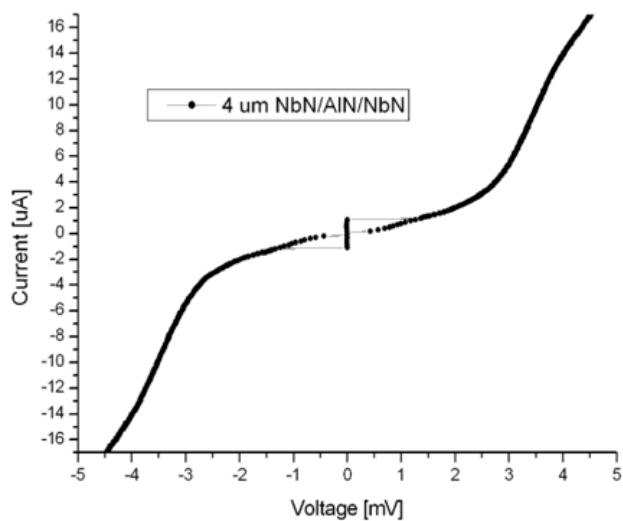


Figure 6.8: I-V curve of a 4 μm diameter NbN/AlN/NbN Josephson junction with SiO wiring insulator and small-area wiring layer, measured at $T = 4.2$ K.

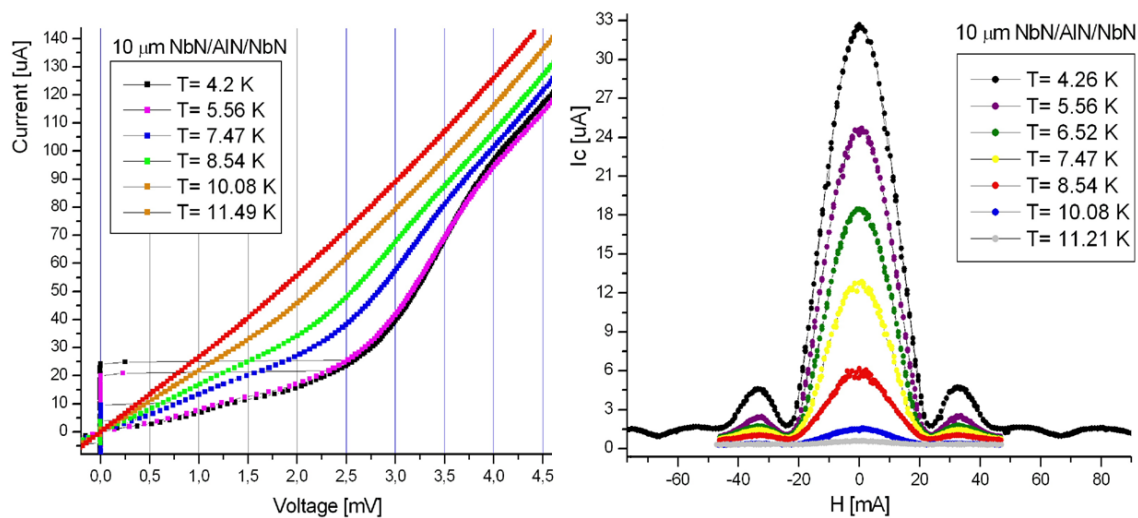


Figure 6.9: I-V curve (left) and magnetic-pattern (right) temperature-dependence of a 10 μm diameter NbN/AlN/NbN junction.

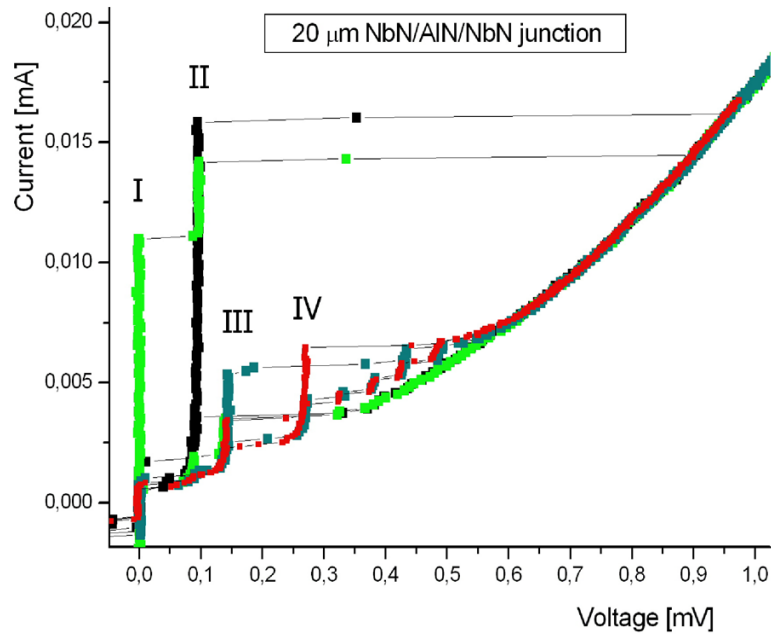


Figure 6.10: Fiske steps of a 20 μm diameter NbN/AlN/NbN junction, obtained by varying an uniform external magnetic field parallel to the junction's barrier plane.

the barrier thickness and the relative dielectric permeability of the barrier material, the obtained a value $C_j = 0.6$ pF seems to be plausible.

As a conclusion, it is important to note that, although the standard junction-quality-factor (such as V_m and V_g) are not sufficient in order to determine the performances of a qubit realized with such junction (performances that are typically characterized by spectroscopy and Rabi-oscillation decay-time experiments), it was in any case a considerable result the success of integrating the PECVD a-Si:H technology in the Nb and NbN junction technology. Passing from SiO to a-Si:H for wiring's insulators and capacitor's dielectric, will certainly have beneficial effects in terms of the qubit's coherence times, while having demonstrated (see section 8.6) that the junctions showed no detrimental effects from hydrogenation and from the annealing during the PECVD process is in my opinion a considerable result.

6.0.4 Junction Fabrication Perspectives

I would speculate here about some interesting aspects emerged from the above research activities. First of all, the epitaxy of the superconducting base layer, or even better of the full-trilayer is a promising path to be explored, especially keeping in mind the teachings coming from the experiments on CPW resonators and the theories such as the MIGS. Interfaces qualities and surface uniformity would greatly benefit from epitaxial growth of the films.

Moreover, the exploration of novel tunnel barriers may lead to interesting insights on the dynamics or on the nature of the barrier's TLSs. In fact, if the TLSs have a microscopic origin (and they indeed HAVE a microscopic origin), it will not be surprising to observe that some particular signature of the TLSs of an alternative barrier-material (such as SiN_x) will reveal some more information on its microscopic origin.

In section 8.2 I will introduce trilayers realized for the qubit fabricated by a NbN/ SiN_x /NbN trilayers.

As a conclusion, I will briefly discuss a fabrication technique that I consider at the same time forgotten and promising: the Edge Junction fabrication technique. This technique was commonly utilized in the Seventy for the realization of ultra-high-quality Josephson junction [100] with V_m quality factors up to 270 mV. I will present here a model of a fabrication process for a complete Josephson junction circuit. It is based on the use of an e-beam evaporator or an Ion Beam sputterer, both assisted by an extra ion beam (representing the so-called IBAD - ion beam assisted deposition), for what it concerns the depositions of the metals and insulators. The same Ion-Gun could be employed also for the etches, and in particular for the *in situ* barrier etch, as we will see briefly.

IBAD technique offers the possibility of low deposition rates ($5 \text{ \AA}/\text{min}$), low gas pressures ($\sim 10^{-5}$ Torr, implying low contaminations), accurate control of the implanted-ion energy ($0.5 - 3 \text{ KeV}$) and of the sputter incidence angle. Moreover it is suitable for the reactive deposition of oxides and nitrides, and, since small target

are required, it is suitable for material testing. Fundamental will be the ability to perform *in situ* etching and surface cleaning before the tunnel barrier deposition, in order to realize reproducibly sub-micrometric Josephson junctions.

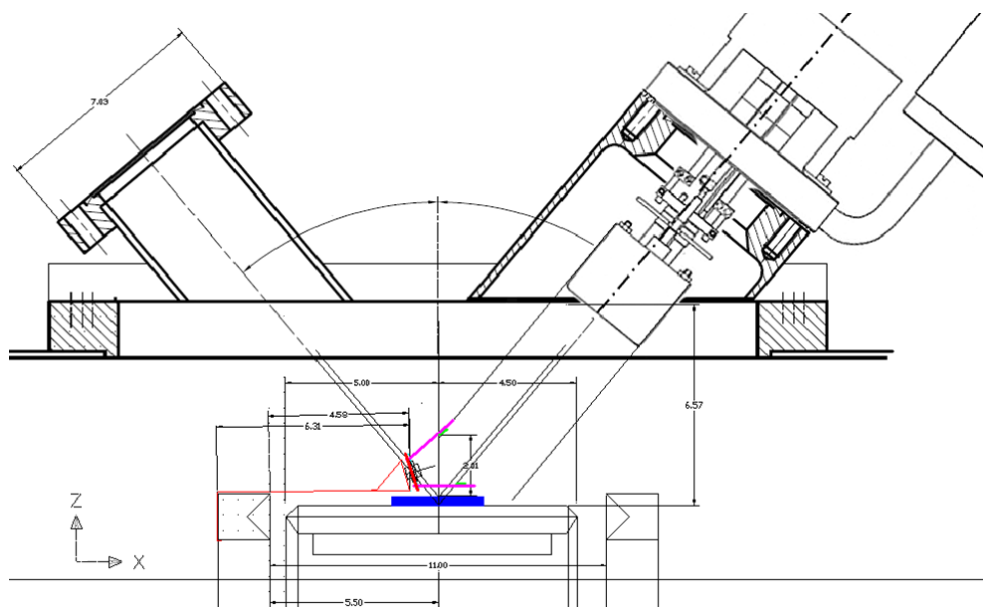


Figure 6.11: The IBAD technique was projected to work in the Ion-gun equipped load-lock of the MRC sputter machine at ICIB CNR.

The IBAD process was initially thought to be realized in the Ion-gun equipped load-lock of the MRC sputter machine at ICIB CNR, for the deposition of NbTiN from a 55% Nb 45% Ti sputter target, as in Fig. 6.11; however, it is relatively easy, due to the versatility of an ideal e-beam evaporator, to deposit the most exotic materials (like CuO, as discussed in section 3.5, in order to deposit antiferromagnetic surface layers of tunnel barriers) by means of this technique.

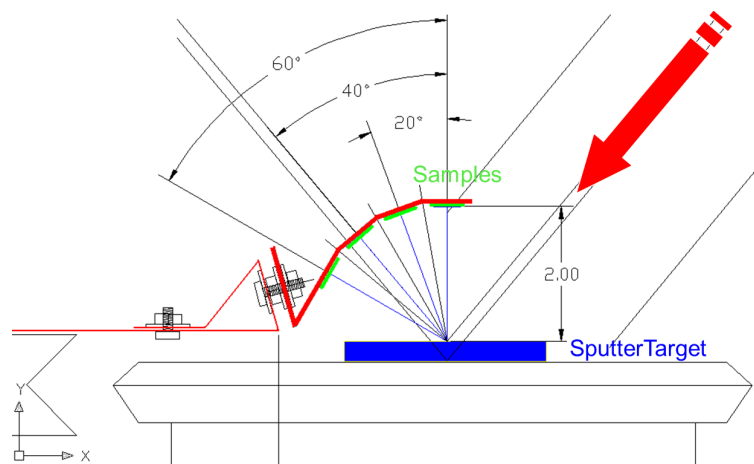


Figure 6.12: Ion Beam Sputtering - Project of a substrate support to study the influence of the deposition angle on the crystalline and superconducting properties of the material physically ejected by argon ions from the sputter-target.

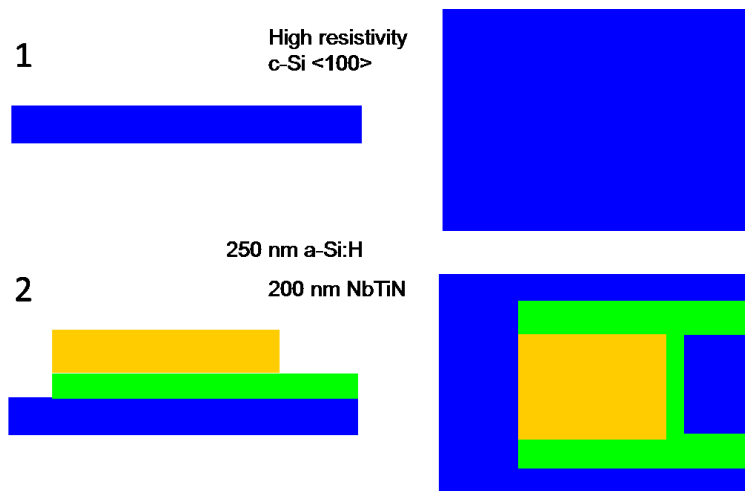


Figure 6.13: Initial steps of Josephson edge-junction fabrication by IBAD processes (Left: side view, Right: top view). 1 - c-Si Substrate preparation (HF dip).

2 - NbTiN base layer and insulator deposition and patterning through standard lithography (the materials are chosen as an example).

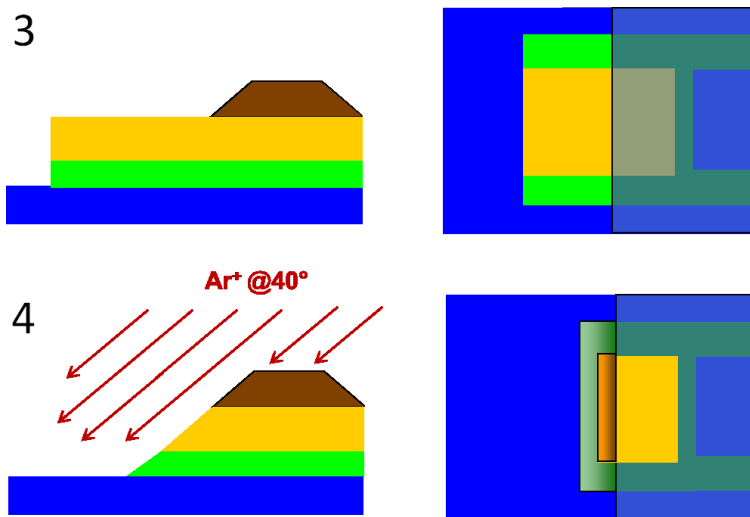


Figure 6.14: 3 - optical photolithography step with controlled resist-slope during the develop process.

4 - *in situ* ion beam etch at a 40° angle to expose and clean the base electrode.

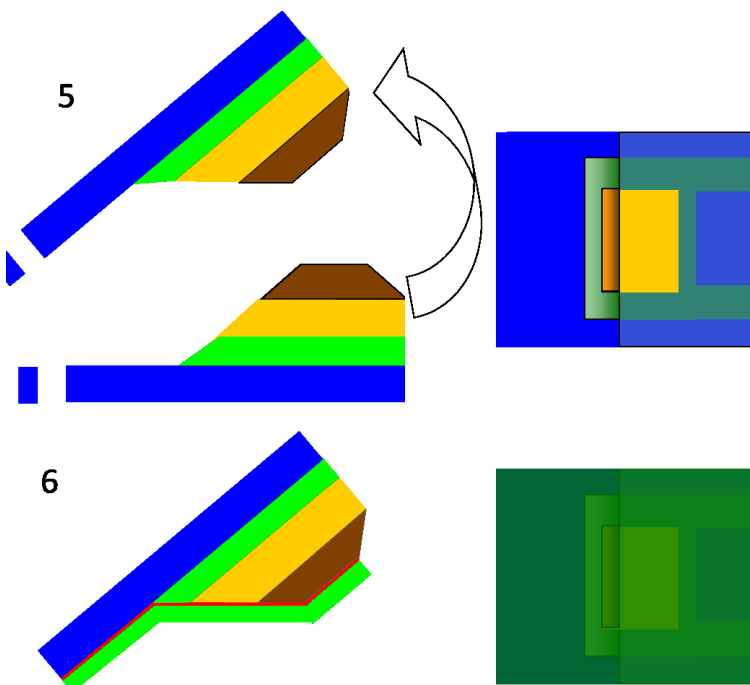


Figure 6.15: 5 - *in situ* sample holder rotation.

6 - *in situ* ion beam assisted deposition of the junction barrier and counterelectrode.

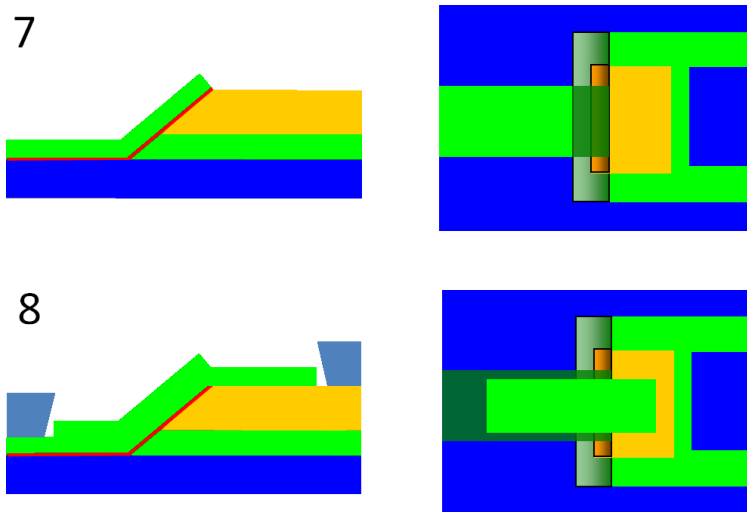


Figure 6.16: 7 - Photoresist patterning, deposition and liftoff-definition of the wiring.

8 - 2nd wiring for capacitor (optional).

Chapter 7

Qubit Design

A number of considerations must be taken into account in order to design a phase qubit, which we can broadly divide into three categories: the design of the qubit circuit itself; the design of the measurement circuit; and the design of the electromagnetic environment of the qubit to appropriately decouple it from the environment in order to prevent the decoherence. In practice, of course, these three categories are not so cleanly separated and must be considered together. For example, the measurement circuit forms an important part of the qubit's electromagnetic environment, so that the effects of the measurement circuit on qubit coherence must be very carefully considered.

In this chapter, I will introduce the qubit design-rules, describe the planned qubit and resonator experiments to be included in the layout, and follow the complete design and dimensioning flowchart for all the critical components, including the qubit loop, the insulation network, the readout DC SQUID, the flux-bias, the microwave antenna, and the shunt capacitor.

7.1 Layout Project

The qubit mask project was done in collaboration with KIT, in particular with the support of Dr. J. Lisenfeld, while the physical photolithographic masks were realized at ICIB-CNR by means of a Laser Writer system.

The layout of the qubit circuit has been drawn in AutoCAD[®], and it is very similar to a design originally suggested by J. Lisenfeld [135]. The qubit Josephson junction is embedded in a loop to form the rf SQUID. The size of the loop was chosen to result in a suitable β_L parameter determined by the critical current of the smallest manufacturable junction. Loop and mutual inductances were calculated using FastHenry [74].

Since the same mask was used to fabricate several chips, with a variety of trilayers, we had to take it into account for the expected variations of critical current densities J_c due to the very different trilayer's materials and for the uncontrollable deviation from targeted J_c .

Thus, the layout of a phase qubit circuit was made compatible with the fabrication processes with current density ranging from 5 A/cm² to 50 A/cm² by replicating the same circuit with different rf SQUID inductance (Fig. 7.2). For each replica, circuital dimensioning have been optimized.

As we will see in chapter 8, four different trilayers (Nb/AlO_x/Nb, NbN/AlN/NbN, NbN/SiN_x/NbN, and Al/AlN/Al) have been employed for the realization of a total of 24 chips, each of the latter containing a number of experiments described in the next section.

We chose to realize all the couplings to the rf SQUID by means of inductive-couplings. This approach allows an easy to implement isolation by impedance transformation (as described in section 7.2.2) and should minimize the possibility of inducing vortices due to the qubit's control pulse-currents and the diffusion of quasi-particles, since the qubit loop is galvanically decoupled from the rest of the circuit's lines.

The size and position of the readout DC SQUID loop were chosen to result in

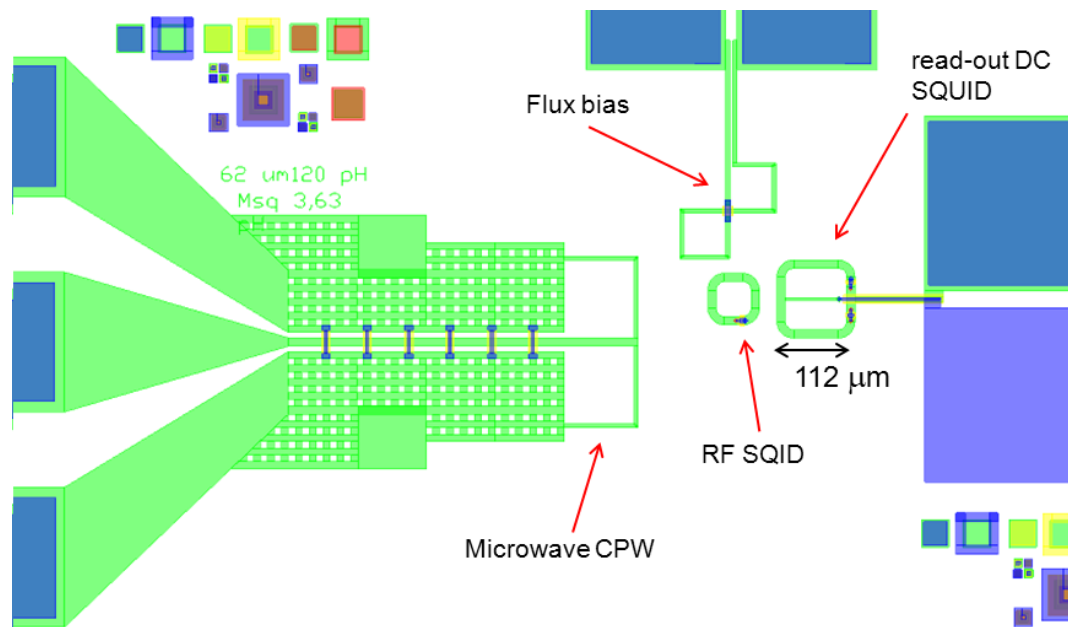


Figure 7.1: Layout of a complete phase qubit circuit.

a sufficiently large mutual inductance, typically about 1 to 8 pH (depending on the qubit J_c), in order to realize the lowest coupling to the SQUID noises at the cost of losing the possibility to detect qubit flux state in a single-shot measurement (see section 7.2.3). Moreover, the bias and voltage lines are connected symmetrically to the DC SQUID loop such that an applied bias current would divide equally between the two branches if their inductances were equal. In this case, no net magnetic flux is generated in the qubit loop and the qubit remains protected from fluctuations in the DC SQUID bias current. To keep this advantage for an asymmetric DC SQUID, a single junction is placed in one branch of the DC SQUID, while the other branch contains a series combination of two junctions of twice the critical current each [208].

Since the Josephson inductance

$$L_J = V \left(\frac{dI}{dt} \right)^{-1} = \frac{\hbar}{2e I_0 \cos \varphi}, \quad (7.1.1)$$

obtained by combining the first (1.1.1) and the second (1.1.2) Josephson equations, is inversely proportional to the critical current, a series combination of two junctions has the same inductance as a single smaller junction of half the critical current. Thus,

as long as no bias current is applied, the SQUID remains symmetric. The DC SQUID self-resonances have been calculated and are always greater than 30 GHz at the typical working conditions. Detailed calculation of the DC SQUID dimensioning and coupling to the qubit loop will be discussed in section 7.2.3.

7.1.1 The On-Chip Experiments

During the definition of the photolithographic mask, we planned to put on the chip the following circuits (see Fig. 7.2):

- 5 phase qubits with different rf SQUID loop-sizes (from 50 to 260 pH) in order to tolerate the variation of critical currents (from 5 A/cm² to 50 A/cm²) due to the multi-material fabrication
- 5 phase qubits analogous to the previous, but with a capacitance shunting the qubit's junction, in order to test the qubit at lower working-frequencies
- 2 LC resonators with 6-multiplexed lumped-element
- 4 "hanging" lumped-element resonators
- 4 Capacitors for low-frequency dielectric loss investigations

7.2 Dimensioning

The design of a phase qubit usually starts from considerations on the qubit junction's critical current I_0 . Having fixed the junction diameter to 6 μm due to photolithographic reasons, this means a constrain on the junction's current densities J_c .

Aiming at operating the rf SQUID as a phase qubit, for a given junction critical current the loop inductance is then designed in such a way that $1 < \beta_L < 6$. This results in a potential that has not more than two minima for all values of externally

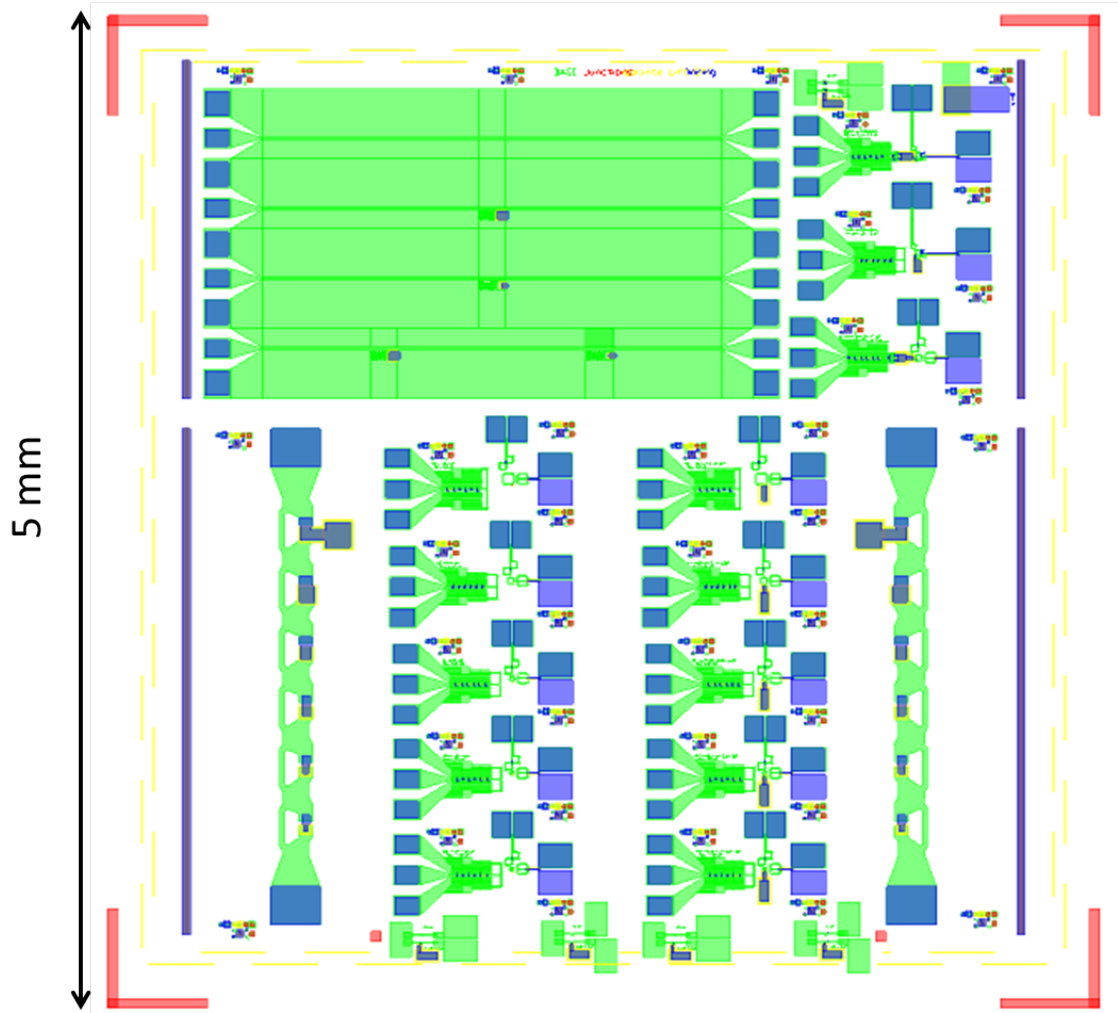


Figure 7.2: The complete layout of the fabricated samples. It comprises 4 "hanging" lumped-element resonators (top-left), 2 LC resonators with 6-multiplexed lumped-element each (bottom-left and bottom-right), 5 phase qubit circuits with different inductances L (middle-left), 5 shunted phase qubit circuits with different inductances L (middle-right), and a series of auxiliary test junctions and capacitors.

applied flux and one single minimum for $\Phi_{ext} \approx 0$. Thus, from constrain on $\beta_L \equiv \frac{2\pi LI_0}{\Phi_0}$, the rf SQUID loop inductance L is determined

Near the critical current, where the device will be biased, the qubit frequency is primarily determined by the junction critical current I_0 and the junction self-capacitance C , with the inductance L and flux bias essentially playing the role of current bias in the tilted washboard model, but having very little effect on the actual shape of the qubit potential. In order to achieve low operating-frequency of ~ 3 -4 GHz, one may consider to intentionally put an external shunt capacitor C_s in parallel to the junction (see section 7.2.6).

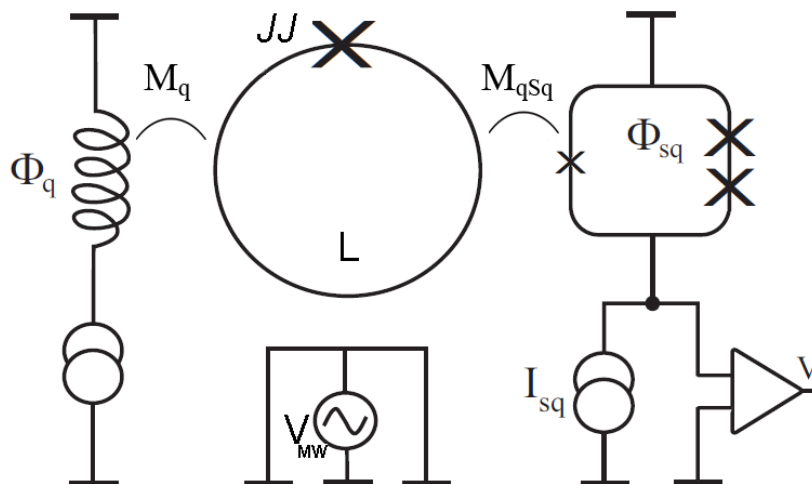


Figure 7.3: Schematics of a typical phase-qubit circuit, made of the qubit inductance L , the readout DC SQUID, the flux bias Φ_q , and the microwave bias. The respective mutual inductances with the qubit loop itself are also shown.

On the other hand, if the inductance L is increased, the qubit circuit could be made less sensitive to magnetic flux-noise in the qubit loop, which could be a desirable feature. At the same time, however, this would create a potential with more than two wells, which makes it difficult to reset the qubit. The resetting requires that we return the qubit state to the original well, and doing so is difficult when there are more than two wells. This is one of the many trade-offs that must be considered when designing these circuits.

7.2.1 Qubit's Loop and Junction

Since the rf SQUID is the heart of the qubit, it is worth to consider how to optimize its design.

For example, there is evidence which shows that the intrinsic low-frequency flux-noise increases linearly with the inductance of the flux qubit [193]. In a systematic analysis of the dependance of flux-noise on qubit geometry [126], the levels of flux-noise systematically varied between qubit designs with strong dependence upon qubit wiring length and wiring width. Qubit wiring lengths ranged from 350 μm to 2.1 mm, and wiring widths ranged from 1.4 to 3.5 μm . The authors showed that the power spectra of the flux-noise for their qubits decreased as the qubit loop was smaller, and as the line widths increased [126]. It is interesting to note that when they used a "shielding" Nb layer *under* the qubit circuit (essentially a Nb buffer between the substrate and the circuit, although the authors did not specify how they further isolated the shielding from the qubit), the flux noise systematically exhibited a lower value compared to the case of "no shielding" or "upper shielding". According to the authors, this effect should be due to the effective isolation of the qubit from the magnetic impurities at the substrate Si/SiO₂ interface, only present in the "under shielding" case.

Other authors [72] predict that the magnitude of the low frequency $1/f$ flux noise does not depend on the area of the rf SQUID, as long the ratio R/W remains constant (R denotes the radio of the squid, and W the width, respectively; see section 2.3.3 for the theoretical model based on spin dynamics together with the spatial dependence of the surface current density). The authors demonstrate that low-frequency $1/f$ flux-noise spectral-density due to surface spin dynamics is

$$\langle \Phi^2 \rangle = \frac{4}{\pi} (\mu_0 \mu_B)^2 \sigma_s \frac{R}{W} \frac{1}{f}, \quad (7.2.1)$$

where σ_s is the surface density of paramagnetic spins $\frac{1}{2}$, and μ_0 and μ_B are the material's absolute and relative magnetic permeabilities, respectively. The typical value of R/W for the commonly realized qubit loops is ~ 10 [72]; however, the details

of diffusion in SQUIDs having $R/W \sim 1$ might be different.

Since the designed rf SQUIDs have a 12 μm wide wire (W), and the 5 different qubits have different loop-size (with radius R between 16 μm and 55 μm , see section 7.1.1), the resulting qubits have values of the R/W ratio between 1.4 and 4.5.

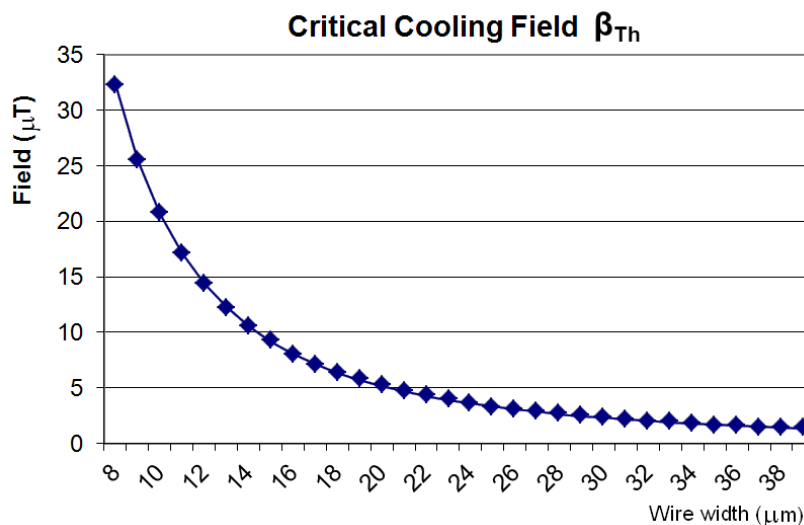


Figure 7.4: Calculation of the critical magnetic-field versus line-width (Eq. 7.2.2). Above β_{th} during field-cooling it is more likely to trap magnetic field in the superconducting wires.

Having realized several version of the same circuit with different rf SQUID inductances (see section 7.1), we have already varied R between 17 and 55 μm . Increasing the width of the qubit's wire would be the next step. However, the actual trend in all the fabricated qubits so far is to make the wires narrower, not wider. This is because the probability to trap a magnetic flux in superconducting thin-film wires (in the form vortices) increases with increasing of the wire's width W . The critical magnetic-field β_{th} , above which it is likely to trap magnetic field in the superconducting wires during field-cooling, is defined as [212]

$$\beta_{th} = \frac{\Phi_0}{W^2}. \quad (7.2.2)$$

Thus, taking the width of 12 μm of the superconducting wires used in this work (Fig. 7.5), the threshold value of field-cooling is of the order of 14 mT, a value

that is safely higher than the residual magnetic field present in the multiple-shielded sample-holder (a superconducting-lead shield and two cryoperm ones) where the qubit resides.

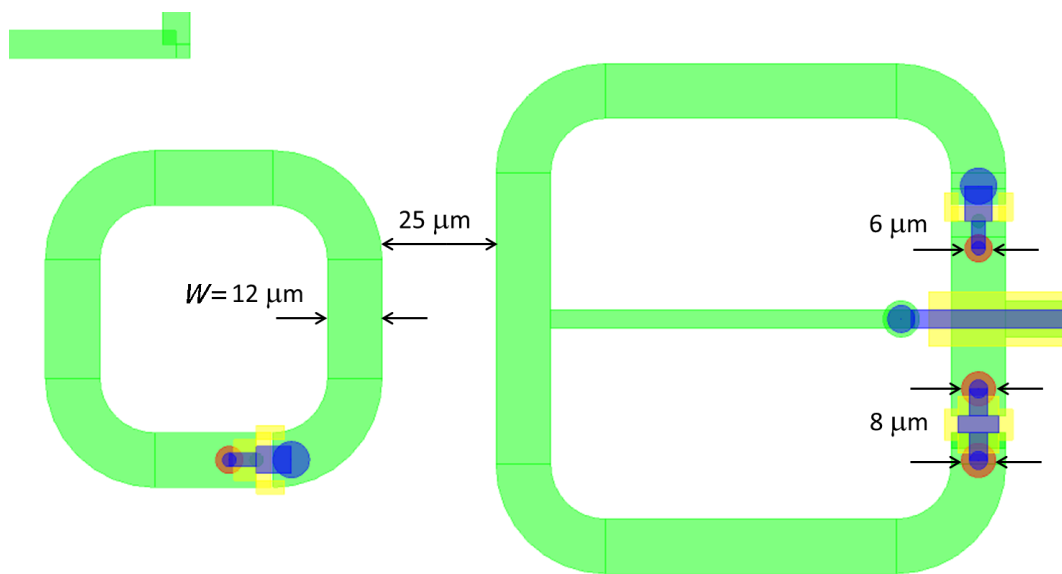


Figure 7.5: Detail of the layout of the inner qubit circuit: the rf SQUID (left) and the DC SQUID (right).

Moreover, increasing the width of the wires is partly similar with the result of the experiments performed with CPWs resonators and presented in section 3.5: the rf SQUID is itself a resonating structure, and the intrinsic losses and noises could have a similar dependence on the geometry, material choice, and fabrication processing.

7.2.2 Isolation by Impedance Transformation

For a phase qubit, any source of dissipation can be thought of as contributing to an effective shunting resistance across the qubit junction. The net effective resistance R_{eff} shunting the qubit junction due to all dissipation sources can then be found from

$$1/R_{eff} = \sum_i 1/R_i, \quad (7.2.3)$$

where the sum is taken over all sources of dissipation. The energy relaxation time of the qubit is then

$$T_1 \leq R_{eff}C, \quad (7.2.4)$$

where C is the total effective capacitance of the qubit junction, which includes the geometrical capacitance of the Josephson junction plus any shunting capacitance that was added across the qubit junction. Note that 7.2.3 sets an upper bound on the coherence time, because some other sources of dissipation might not have been accounted for in R_{eff} . We considered the effective resistance from each source of dissipation in the circuit during the design of the qubit.

In order to avoid energy relaxation, the electrodynamic environment of the junction must be carefully designed. One possibility is to isolate the qubit junction by means of an inductive isolation network [21], which can be realized from on-chip capacitors and superconducting inductors. The output impedance of a parallel LC-resonant filter at working frequencies beyond its resonance frequency of \sqrt{LC} grows with its inductance L . Therefore, effective isolation demands high values of both inductance and capacitance, which accordingly consume large space on chip. By exploiting the Josephson inductance of an additional junction which is connected in parallel to the smaller qubit junction [145], the circuit can be kept small and the amount of isolation can furthermore be adjusted *in situ*. A disadvantage of this approach, beneath the additional subgap resistance of the isolating junction, is that the qubit junction is still switching to a resistive state during the readout process. In the non-zero voltage state, the potential difference across the junction gives rise to generation of quasiparticles, which will persist for some time after the junction is reset to the superconducting state. These quasiparticles remain a source of decoherence, because they provide normal current channels effectively shunting the qubit, and give rise to shot-noise and charge fluctuations.

The above mentioned problems are avoided when the qubit junction is isolated from the bias circuitry by means of a superconducting impedance transformer [208].

We adopted this approach in our phase qubit design.

The simple technique outlined in [165] for analyzing the effect of the electromagnetic environment on the qubit is to consider the circuit elements as impedance transformers coupling environmental noise into the qubit circuit. The measurement of the SQUID's asymmetric three-junction design allows its effective mutual inductance with the qubit to be dynamically tuned by adjusting the SQUID bias current, thus avoiding decoherence during operation while still allowing strong coupling for readout. Similarly, other circuit elements that couple to the qubit must be designed, so that environmental noise is appropriately transformed and will not decohere the qubit.

It has been suggested by J. Martinis *et al.* [207] to send the current bias to the junction through a superconducting dc-flux transformer. This approach provides broadband isolation, limits the generation of quasiparticles, and can be realized in compact dimensions. The transformer is fabricated on-chip by placing two superconducting coils close to each other. A schematics is shown in Fig. 7.6. The primary coil is connected to the current source which generates a magnetic bias flux Φ_b proportional to the applied current I_b .

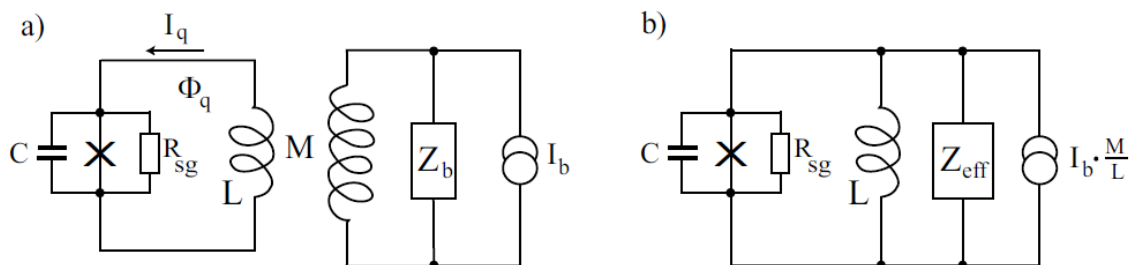


Figure 7.6: *a)* Schematics of the transformer circuit. The qubit junction is embedded in a superconducting loop of inductance L , which is coupled via a mutual inductance M to the primary coil. This coil is connected by wires of low impedance Z_b to the current source. *b)* Equivalent schematics of the transformer circuit. The junction remains isolated from the environment by a large effective impedance Z_{eff} . Figure from [135]

Since the two coils are coupled by the mutual inductance M , the secondary coil

receives a magnetic flux $\Phi_q = MI_b$, which induces a current I_q flowing through the qubit junction according to

$$I_q = \frac{\Phi_q}{L} = \frac{M}{L} I_b \quad (7.2.5)$$

where L is the inductance of the secondary coil, which will be referred to as the qubit loop in the following. Beneath the advantage that the qubit junction remains galvanically isolated from the electronics, also the impedance of the bias wires Z_b is transformed to an effective value Z_{eff} . For an ideal (non-dissipative) transformer, the output power P_q is equal to the input power P_b ,

$$P_q = I_q^2 Z_{eff} = P_b = I_b^2 Z_b \quad (7.2.6)$$

This results in an impedance transformation of

$$Z_{eff} = \left(\frac{M}{L}\right)^2 Z_b \quad (7.2.7)$$

where Eq. 7.2.5 has been used to find $I_q/I_b = M/L$. By assuming a practical ratio $M/L \approx 100$, the wire impedance $Z \approx 100\Omega$ is stepped up to $Z_{eff} \approx 1M\Omega$. In addition, the generation of quasiparticles is effectively reduced in this approach, because the dc voltage across the junction remains zero all the time due to the superconducting short. This not only increases the coherence time, but also renders an idle time after each measurement unnecessary, which is otherwise essential to allow unpaired electrons to recondense into Cooper pairs.

The same considerations could also be applied to the microwave lines and the readout DC SQUID, which are similarly inductively coupled to the inductance L of the qubit (see Fig. 7.3), in order to decouple the latter from additional decoherence.

7.2.3 Read-out DC SQUID

Several methods can be used to measure the flux state of the phase qubit. One of them [37] directly determines the circulation direction of the loop current by a measurement of the critical current of an additional junction incorporated in the

loop. Less invasive techniques are based on a measurement of the flux generated from the loop current by using an inductively coupled DC SQUID. In this section, the circuit design requirements for the widely used method of flux detection by a switching-current measurement of the DC SQUID are discussed.

The qubit state is measured by selectively tunnelling the qubit $|1\rangle$ state out of the cubic well of the phase qubit potential. The tunneled $|1\rangle$ and non-tunneled $|0\rangle$ states produce different amounts of magnetic flux in the qubit loop, the difference being about one flux quantum Φ_0 . The critical current of the measurement SQUID is sensitive to this difference in flux, allowing us to discriminate between the two qubit states by ramping the SQUID bias and measuring the current when the SQUID switches into the voltage state.

The readout DC SQUID is coupled by the mutual inductance M_{sq} to the qubit loop. The flux signal that must be detectable is

$$\Delta\Phi_{sq} = M_{sq}\Delta I_q \approx \frac{M_{sq}}{L}\Phi_0 \quad (7.2.8)$$

where $\Delta I_q \approx I_0$ is the change of the circulating current associated to a change of the qubit potential well. Sufficient qubit isolation requires the ratio M_{sq}/L to be $\approx 10^{-2}$, which limits the flux signal $\Delta\Phi_{sq}$ to the order of $10 \text{ m}\Phi_0$. The method to detect this small flux change is based on the magnetic field dependence of the DC SQUID critical current $I_{0,sq}$, which is periodic in Φ_0 . The mutual inductance mediates dissipation in the DC SQUID, but generates back-action to the qubit. While the back-action scales as M_{sq}^2/LL_{sq} , dissipation in the qubit is proportional to the inverse effective DC SQUID damping impedance Z_{sq}^{-1} , which is transformed to the qubit via $Z^{-1} = Z_{sq}^{-1}(M_{sq}/L)^2$. A detailed discussion of decoherence effects due to coupling to the readout SQUID is given in the previous section and in Ref. [231].

This sensitivity to qubit flux is only necessary during measurement, because it is detrimental during qubit operation. If the SQUID is sensitive to flux from the qubit, then the qubit is also sensitive to flux from the SQUID; noise and dissipation in the SQUID circuit, in particular from the shunt resistance of the DC SQUID bias line, will decohere the qubit state.

In order to be able to modulate the SQUID's flux sensitivity, turning off the coupling during qubit operation, and turning it on only for measurement, we chose the asymmetric three-junction layout introduced by J. Martinis's group in [165] for the design of the DC SQUID.

The asymmetric three-junction design allows the device to be biased in such a way that the effective mutual inductance between SQUID and qubit can be tuned by biasing the SQUID, despite the fixed geometric mutual inductance. In particular, by choosing a ratio $\alpha < 2$ between the critical currents of the one small and two large Josephson junctions in the SQUID, it is possible to tune the effective mutual induction to zero, thereby decoupling the SQUID and qubit. In practice we chose $\alpha \leq 1.7$ because of photolithographic constraints (the DC SQUID junction may have the diameters of 6 and 8 μm , respectively) and safety considerations with respect of unavoidable variations in junction size during the fabrication, in order to ensure that an insensitive point will exist, yet will not be too close to the critical current of the SQUID.

When bias current I_{sq} is applied to the SQUID, it divides into the upper and lower branches of the loop. The lower branch has a single Josephson junction with critical current I_0 , whereas the upper branch has two larger Josephson junctions each with critical current αI_0 . The total current is $I_{sq} = I_U + I_L = \alpha I_0 \sin(\varphi/2) + I_0 \sin(\varphi)$, where φ is the superconducting phase difference across the loop. The circulating current in the loop is $I_{circ} = I_U - I_L = \alpha I_0 \sin(\varphi/2) - I_0 \sin(\varphi)$. This circulating current couples via a fixed mutual inductance $M_{sq}/2$ in each branch to the qubit loop, causing current $I_q = (M_{sq}/2L_q)I_{circ}$ to flow.

During qubit operation, the SQUID is biased at this insensitive point in order to prevent fluctuations in the SQUID to cause decoherence in the qubit. As from [165], the SQUID and qubit are decoupled at insensitive point. Away from the insensitive point, the inductances become unbalanced, and the transfer function has non-zero slope, so that SQUID and qubit are again coupled. When measuring the qubit, the current I_{sq} is ramped toward the critical current, turning the coupling on and allowing

the SQUID to discriminate between the tunnelled and non-tunnelled qubit states.

The point at which the SQUID switches into the voltage state will depend on the final qubit state, allowing to distinguish between qubit states by measuring the time it takes the SQUID to switch for a fixed bias ramp.

The small value chosen for M_{sq} , even if it is too little to allow single-shot state-readout distinguishability, reduces the decoherence induced by the SQUID, and reduces the SQUID self-inductance L_{sq} to ~ 230 pH. Lower self-inductance keeps the SQUID potential single-valued, resulting in more controlled switching behavior. The design without any overlap between the qubit loop and the SQUID guaranteed negligible capacitive coupling between the two circuit elements, due to the crossovers, which could be another harmful source of decoherence [218].

The SQUID junctions are fabricated in the same process step as the qubit junctions, thus with the same improved design presented in chapter 6.

7.2.4 Flux Bias

The other primary circuit element required for the phase qubit is the flux bias coil which is used to bias the qubit circuit and apply measurement pulses. The mutual inductance between qubit loop and flux bias coil is chosen to be $M_q \sim 2$ pH. This gives an impedance transform such that dissipation from the 50Ω environmental noise limits the qubit lifetime to $\sim 10 \mu\text{s}$, which is far from being a limiting factor with current devices. At the same time, this mutual inductance allows us to vary the flux bias by $\sim 2 \Phi_0$ with the accessible range of bias currents, which gives a sufficient flux range for the qubit characterization. A coil current of 1 mA results in an induced qubit flux of about one Φ_0 . Although a smaller mutual inductance would increase the qubit isolation, it is impractical to apply larger currents to on-chip coils, due to the risk of heating the sample. While the risk of exceeding the critical current of thin superconducting films is limited by designing the flux line with a larger width, heating in the non-superconducting wire sections which are thermally anchored to the mixing chamber may be strong enough to increase the reachable base temperature

by tens of milliKelvin. The dissipated power grows quadratically with the applied current. Furthermore, if contact resistances were present in the aluminum bonds, heating would occur directly on the sample chip [194].

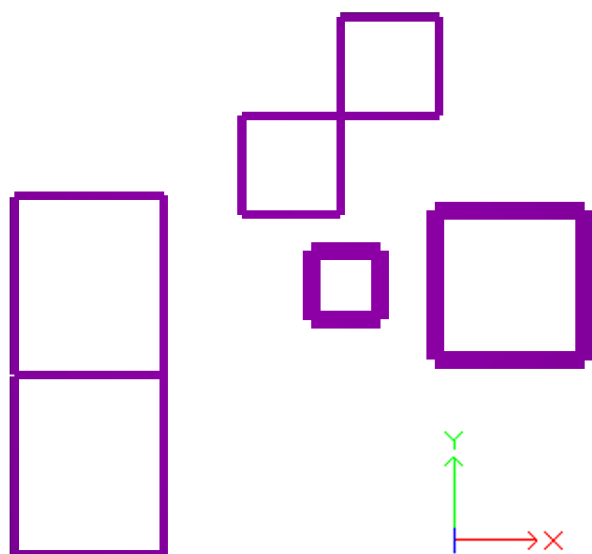


Figure 7.7: The geometries from which the self- and mutual-inductances were calculated by FastHenry.

The coil to apply bias flux to the qubit is designed gradiometrically in the form of an "8", so that the current will flow in counter-rotating directions in its branches (Fig. 7.1). The readout DC SQUID is placed symmetrically with respect to this biasing coil-branches, such that the flux received from each half of the "8"-shaped coil is of same magnitude but opposite direction. This decouples the DC SQUID from the flux-bias.

On the other hand, the qubit is placed asymmetrically, allowing the flux coil to couple to the qubit as desired. All these mutual inductances were simulated using the FastHenry [74] and have been found to be very close to the experimentally observed values in real devices.

Typically when operating a qubit, the flux bias is adjusted to give a barrier height $\Delta U \sim 4E_{10}$, so that about 4 quantum levels exist in the well, as showed in the potential-well energy-level simulator made by J. Lisenfeld in Fig 7.8.

Due to the non linear Josephson inductance, the energy levels are not evenly spaced, that is, the energy difference E_{21} between the first and the second excited

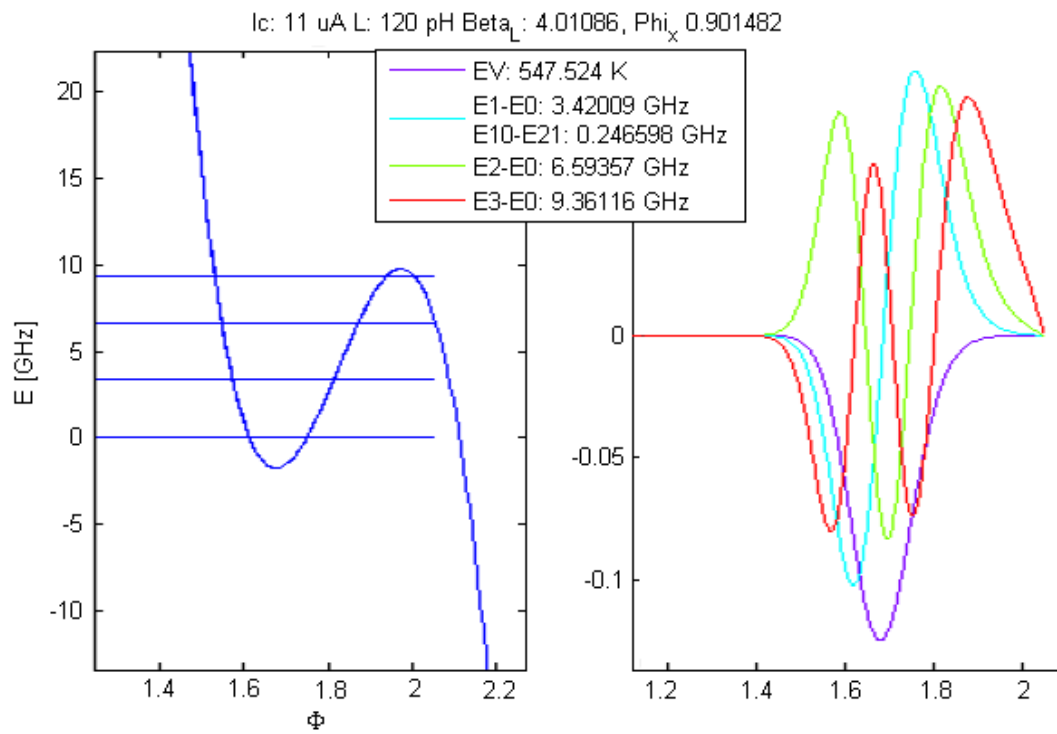


Figure 7.8: Potential-well energy-level simulator made by J. Lisenfeld at KIT. Given I_c and L as input, the Matlab routine computes the energy and splittings of the quantized level in the potential well, together with their wavefunctions [135].

states is different from the qubit energy E_{10} between the ground state and the first excited state.

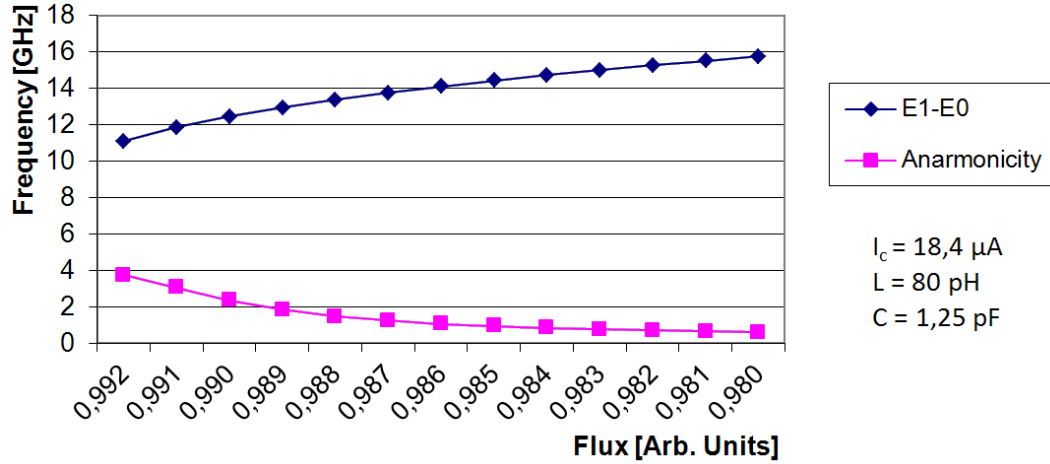


Figure 7.9: Calculated anharmonicity versus flux bias.

This nonlinearity $\Delta \equiv (E_{21} - E_{10})/\hbar$, called anharmonicity, is a crucial feature of the circuit that allows the system to be operated as an effective two-level system. For typical operating parameters, the nonlinearity is on the order of 300 MHz, small but sufficient for reasonably fast operation. In Fig. 7.9 it is reported the calculated anharmonicity versus flux bias in order to check the occurrence of sufficiently large energy difference ($E_{21} - E_{10}$) to operate the qubit with the indicated values.

7.2.5 Microwave Transmission Line

In order to cause transitions between qubit levels, microwaves should be applied at the qubit frequency $\omega_{10} = E_{10}/\hbar$ by means of a on-chip coplanar waveguide structures to provide high frequencies radiation (110GHz) to the qubit sample.

The microwave transmission line is patterned in coplanar configuration as a 12 μm wide central-conductor separated from the ground planes by 7 μm , resulting for a Si substrate with $\varepsilon_r = 11.9$ in an impedance of $\approx 50 \Omega$, as simulated by *tx line* software [227] at the characteristic microwave frequencies used (1-10 GHz) to excite

the qubit, so that it is well matched to the load impedance.

Ground and inner conductor are inductively connected to the qubit loop. According to computer simulations, the CPW terminated by a large inductor of the order of 300 pH couples to the qubit loop with a mutual inductance of $M_{MW} = 1$ pH.

The microwave-line positioning with respect of the qubit loop is not trivial, because several recent experiments suggest that the relaxation time was being limited by spurious coupling to the microwave line [191, 218]. For this reason, we chose to place the MW-bias at a distance of $\sim 100\mu\text{m}$ [218], while keeping the mutual inductance at sufficient level.

Moreover, a grid of ground-holes has been realized in order to provide extra pinning to the vortices that are eventually trapped in the ground area during the cool-down or during microwave excitation [212].

7.2.6 Shunt Capacitor

It would be interesting to operate a qubit at lower-than-usual frequencies, say at 2-3 GHz. In order to realize this condition, a shunt capacitor was placed in parallel to some of the realized qubit junction.

A parallel-plate capacitor was extensively used for the realization of LC resonators (see chapter 5), and the losses due to dielectrics in the capacitor have been minimized by utilizing hydrogenated amorphous silicon (a-Si:H) dielectric for its realization. Accurate calibration of the thickness of the PECVD deposited dielectrics guarantees a good predictability of the resulting shunting capacitance C_s .

The minimum frequency at which a phase qubit may be operated could be determined by calculating the the occupation-probability of thermal-excited levels. In the simplest case, we consider only the occupancy of the first excited level, which maps the qubit's $|1\rangle$ state, as a lower bound

$$P(1) = e^{-\left(\frac{\hbar\omega}{k_b T}\right)}; \quad (7.2.9)$$

for a temperature $T = 30$ mK, and for the frequencies of 6 GHz, 3 GHz, 2 GHz,

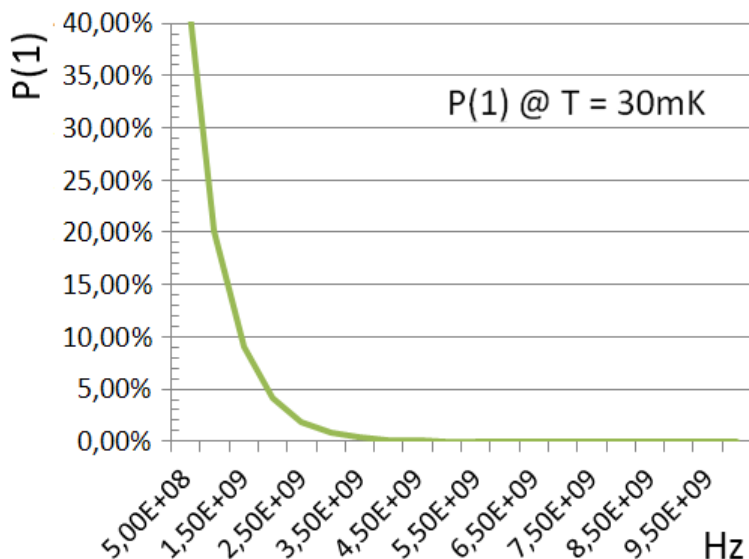


Figure 7.10: Occupation-probability of thermal-excited levels calculated from 7.2.9.

and 1 GHz, we obtain a thermal population of 0.00068 %, 0.56%, 4 %, and 20 %, respectively, as from Fig 7.10.

Considering this probabilities, it seems considerably safe to design a shunted qubit with a targeted operating frequency $\omega_{10} = 3$ GHz, in order to avoid the thermal-population of the qubit's excited states. Calculations for all the values of qubit inductances L and critical currents J_s have been done with the potential-well energy-level simulator, in order to compute the optimal shunting capacitor for each case.

As an example, a qubit with $L = 120$ pH and $J_s = 30$ A/cm², would normally have $\omega_{10} = 5-8$ GHz (depending on the flux-bias). With a shunt capacitance of $C_s = 6.6$ pF, the operating frequencies would be reduced of 50%, namely resulting 2.5-4 GHz, with preserved anharmonicity.

Chapter 8

Qubit Fabrication

As we saw from a vast amount of examples, all over chapters 2 and 3, the fabrication process is critical for the realization of low-decoherence superconducting qubit, with a large number of technological aspects which could be optimized.

Since many of the implemented fabrication processes have been developed *ad-hoc* for the qubit realization, extensive testing and trial-and-error were required for each fabrication (manufacture) step. Indeed, fabricating circuits with non-standard protocols require continue feedback at every level of the fabrication chain: from etching processes back to the design of the circuits, from circuit characterization back to its dimensioning, and so on.

Our objectives were:

to test the influence of **different substrates** (and pre-treatments):

- Si (111) 600 Ωcm (ultrasonically cleaned in IPA bath)
- Si (100) high resistivity $> 10000\Omega\text{cm}$ (cleaned by HF dip and fast-load)
- R-plane sapphire (custom acid etch, HNO_3 and HF)
- M-plane sapphire (custom acid etch, HNO_3 and HF)

to test the influence of different **superconducting materials**:

- Niobium
- Niobium Nitride
- Aluminum

to test the influence of different **barrier materials** (and N_2 plasma treatment):

- Nb/ AlO_x /Nb
- NbN/ AlN /NbN
- NbN/ SiN_x /NbN
- Al/ AlN /Al

to test the influence of different **wiring insulators**:

- Standard SiO
- Hydrogenated amorphous silicon (a-Si:H).

In the following sections, we will analyze the fabrication flow-chart presented in Fig. 8.1, with an emphasis on the processes that were custom-developed in order to realize working qubit from all the possible combination of the above mentioned materials, for a total of 24 completed chips.

8.1 Substrates

For the realization of the qubit devices, specific types of silicon and sapphire substrates have been chosen. For what it concerns the silicon ones, the usual $600 \Omega\text{cm}$ Si (111), a good substrate for polycrystalline Nb growth, has been teamed up with a high resistivity $> 10000 \Omega\text{cm}$ Si (100), indicated in literature as the lowest lossy substrate in the field of CPWs and low-noise SIS mixer application [15] (see section 3.1).

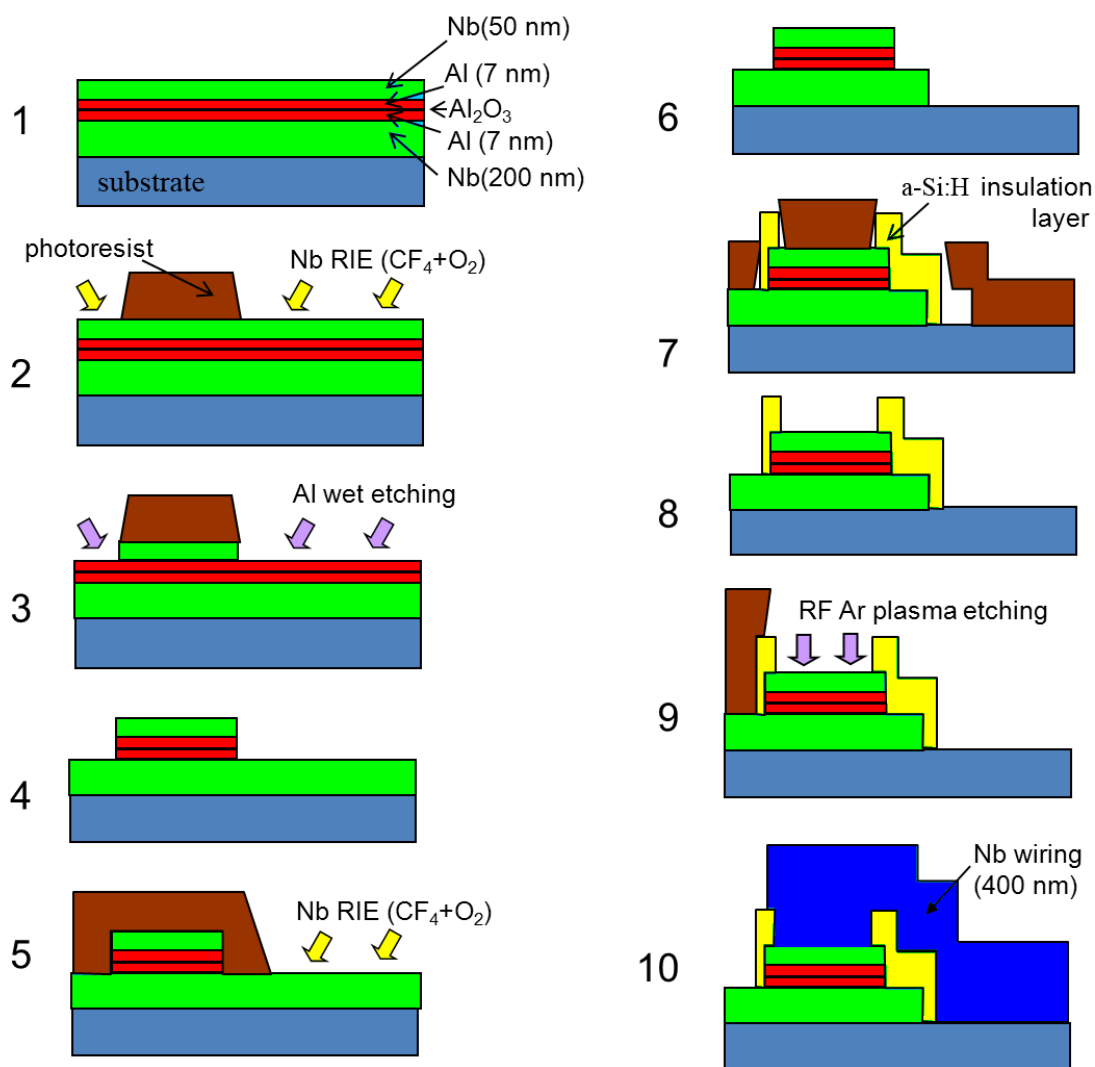


Figure 8.1: ICIB-CNR Nb/AlO_x/Nb fabrication process without anodization and with high temperature a-Si:H lift-off processes.

For what it concerns the sapphire ones, the usual R-plane ($1\bar{1}02$), a good substrate for room temperature NbN growth, has been teamed up with a M-plane sapphire ($10\bar{1}0$), indicated in literature as a better crystalline seed for the growth of un-twinned NbN crystalline grains. In Fig. 8.2 it is shown the AFM surface characterization of the as-delivered substrates from CrysTec GmbH, in order to ensure the absence of mismatch in the crystal-cut angle.

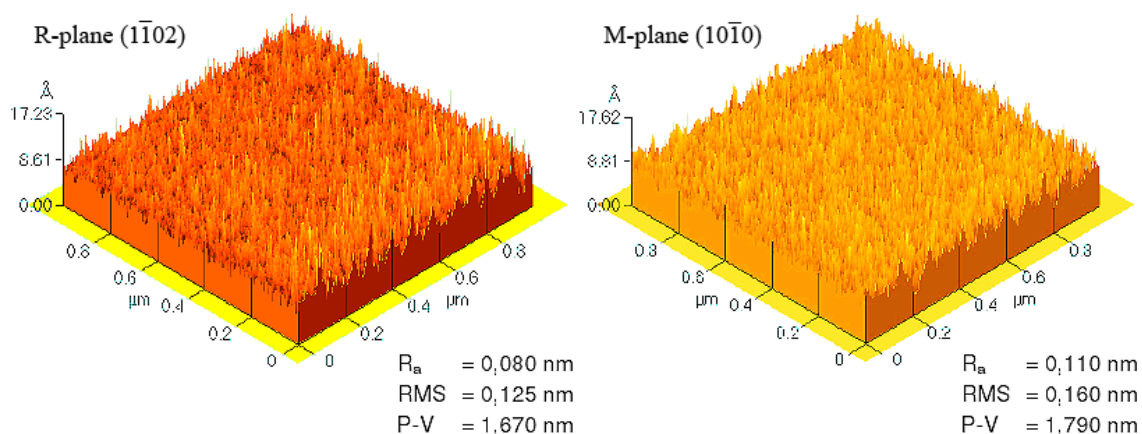


Figure 8.2: AFM analysis to certificate the sapphire quality: R_a (average roughness), RMS (root-mean-square-roughness), and P-V (maximum peak-to-valley range in the area).

All the substrates have been cut in 10 x 10 mm tiles with diamond scribe before any other processes. We deliberately chose to avoid any argon cleaning process to the substrate's surfaces prior of the first metal layer deposition, in order to prevent the damage of the crystalline structure and its transformation in an amorphous layer.

The Si (100) was ultrasonically cleaned in IPA bath, so that its surface was still covered by thermal SiO_x when the trilayers were deposited. The high resistivity Si (100) was prepared by a diluted HF etch, to remove the oxide layer, followed by a fast-load, in a controlled N_2 atmosphere, into the load-lock of the sputter system. This process, if the loading time is less than three minute and specially is done in a controlled atmosphere, is said to leave the silicon surface H-terminated.

R-plane and M-plane sapphire were cleaned with a custom-recipe HNO_3 and HF

wet etch, and their resulting surface is O-terminated.

8.2 Trilayers

The trilayers were all deposited in one *in situ* DC magnetron sputtering session (see Fig. 8.1.1). Together with the Nb/ AlO_x /Nb and the NbN/ AlN /NbN trilayers, we chose to introduce also the NbN/ SiN_x /NbN and the Al/ AlN /Al ones.

To our knowledge, NbN/ SiN_x /NbN junctions have never been realized, and the TLSs associated with material defect of the un-hydrogenated, rf reactive-magnetron sputtered SiN_x , may have a different properties than the well-characterized AlO_x ones. "Bulk" silicon nitride, Si_3N_4 , is a hard, dense, refractory material. Its structure is quite different from that of silicon dioxide or aluminum oxide: instead of flexible, adjustable Si-O-Si bridge bonds, the Si-N-Si structure is rendered rigid by the necessity of nitrogen forming three bonds rather than two. CVD or reactive-sputtered silicon nitride is generally amorphous, but the material is much more constrained in structure than the oxide. As a consequence, the nitride is harder, has higher stress levels, and cracks more readily. The dense structure of silicon nitride does not provide the open channels found in oxide structures; thus, the nitride is widely employed in electronics as a barrier material. Even hydrogen diffuses slowly in a densified nitride film, and other small positive ions (Na^+ or K^+) are effectively blocked by thin nitride layers. Since oxygen diffuses very slowly through nitride, the deposited nitride can prevent oxidation of underlying silicon. Nitride layers are also employed as etch stop layers both for wet etching and plasma etching.

Moreover, silicon nitride seems to be a valid choice as barrier material in all-NbN tunnel junctions, both from the point of view of a sufficiently low loss tangent of these materials (see Table 3.1), and from the point of view of the compatibility with NbN technology. Furthermore, the high melting temperature and the common nitrogen in each compound, are expected to limit inter-diffusion, and make the NbN/ SiN_x an ideal interface to be studied, with remarkably uniform and smooth interfaces [36].

Moreover, also Al/AlN/Al junctions have not been typically employed for qubit's realization. AlN barrier could be grown either by *in situ* N₂ plasma process of clean Al surfaces [202], or by the Al reactive sputter deposition in N₂ + Ar atmosphere. We opted for the second approach.

Finally, we realized a set of NbN/AlN/NbN and NbN/SiN_x/NbN trilayers with an *in situ* N₂ plasma process of clean barrier surfaces, in order to improve their uniformity and fill their nitrogen vacancies [202].

8.3 Junctions and Base Layer

The next step of the fabrication process continues with the standard photolithographic definition of the junction's area, and its patterning by means of Cf₄ + O₂ reactive ion etching (Fig. 8.1.2).

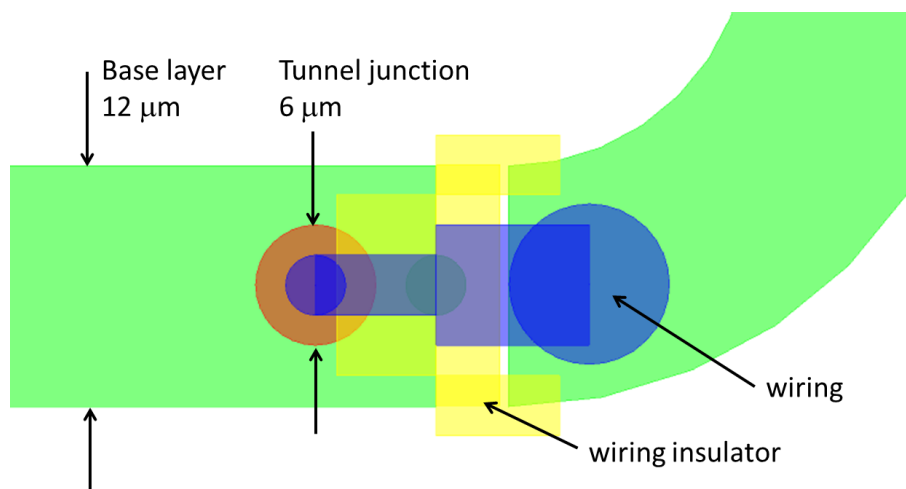


Figure 8.3: Detail of the layout of the qubit junction area.

Since some of the junction's barrier-materials are stoppers of the RIE process, AlO_x and AlN barrier layers had to be etched away by a strong wet etch based on HF/HNO₃ chemistry, followed by another 30 nm of exposed base-layer RIE (Fig. 8.1.3).

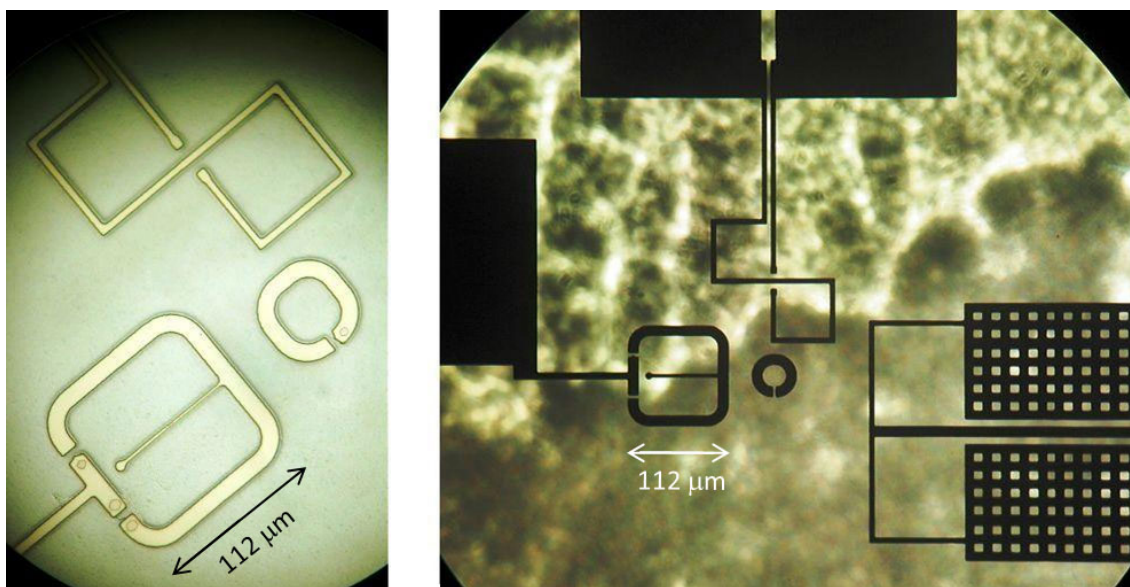


Figure 8.4: Left: Junctions and base layer of a NbN/SiN_x/NbN chip on Si (100). Right: the same trilayer deposited on M-plane sapphire (transparent).

Only for the Al/AlN/Al samples, the junction area definition was done in a hot (50° C) wet etch process based on H₃PO₄/HNO₃/acetic-acid chemistry.

Standard photolithographic definition of the base layer and the relative etch followed (Fig. 8.1.5-6 and Fig. 8.4).

At this step, it would be very interesting to process the freshly exposed surfaces by an *in situ* treatment, in the same RIE (or Ion mill, in case of other fabrication protocols) chamber. These treatment processes were introduced in section 3.5, and could comprise, among the vast possibilities, a plasma surface carbidization or fluoridization, a deposition of a ferromagnetic layer, controlled ion-implantation of impurities, or the deposition of a low-temperature antiferromagnetic CuO layer.

8.4 a-Si:H liftoff

In order to reduce the contamination of the superconductor's surfaces during the fabrication of the capacitor dielectric (as described in section 5.2.3), we developed

and tested a high-temperature a-Si:H lift-off process (Fig. 8.1.7-8). In fact, in order to realize high quality superconducting resonators or qubits, it is preferable to reduce the dielectric coverage of the underlying superconductor [147, 32, 14], limiting the contamination of the superconducting surfaces by hydrogen and dielectric inclusions.

We developed a fabrication protocol that is suitable for both the resonators and the qubits fabrication and, as I showed in section 7.1.1, the photolithographic masks allow the resonators to be co-fabricated on the same chip with the qubit, in order to investigate in the same experimental condition both the dielectric losses and the decoherence of the qubits.

Here I will describe in detail the process, together with the difficulties that had to be solved in order to develop a reliable method.

In order to perform lift-off at the high-required temperature, we demonstrated that a PMGI/Nb bilayer, suitably patterned and conditioned, is capable of high temperature (up to 200° C) lift-off of a-Si:H. Moreover, the developed high-temperature lift-off process is capable to integrate the high-temperature PECVD deposition of a-Si:H with existing Nb Josephson technology, fulfilling the above mentioned requirements of reduced coverage of the underlying superconducting films.

In the following, I will describe the high temperature lift-off process, basing the discussion on the realization of a shunting capacitor, nevertheless the method applies in the same way for wiring crossover and junction insulation. The goal of the process is to PECVD deposit the a-Si:H on the top of pre-existing patterned structures, and selectively choose the areas where the dielectric should not be deposited.

The process was set-up in a month of work, in parallel of the other qubit fabrication processing, nevertheless many have been the challenges to be solved in order to let the protocol to be reliable.

The first choice was on which PMGI to use: different concentrations of the solvent imply different obtainable thickness-ranges, as from Fig. 8.8.

Moreover, the most critical steps for the the process success were step 2 and 4.

Step 2 required the optimization of the PMGI pre-bake temperature, and the

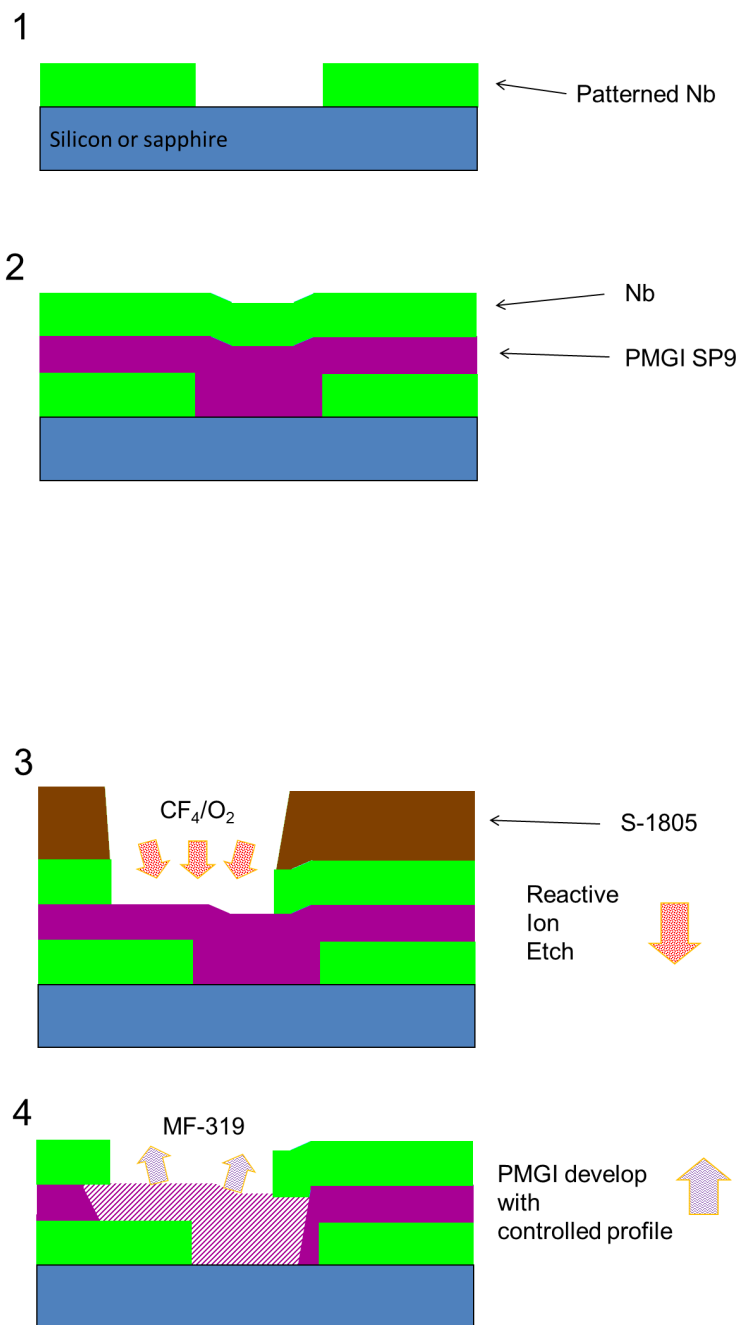


Figure 8.5:

1) Pre-existing circuit on the substrate, *e.g.* patterned Nb thin films.

2) HDMS priming of the surfaces, to improve the adhesion; spinning the PMGI resist to obtain a thickness of 1.3 times the thickness of the final a-Si:H film; PMGI pre-baking; depositing a Nb hard-mask.

Figure 8.6:

3) Standard photolithography and RIE of the Nb Hard mask.

4) Controlled development of the PMGI resist.

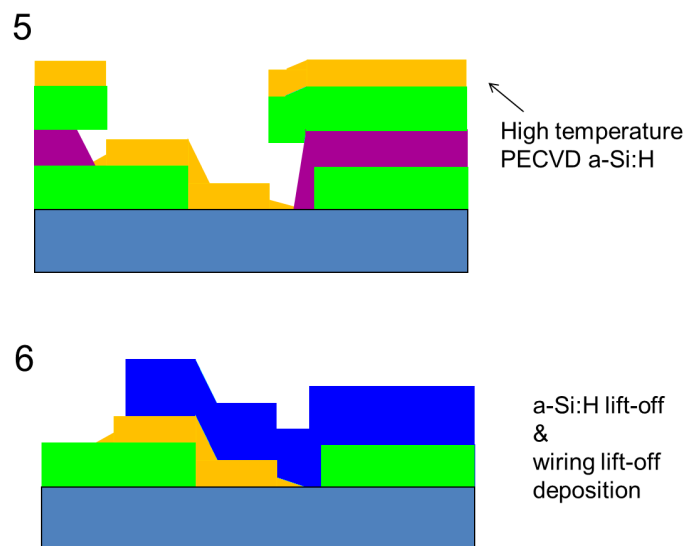


Figure 8.7:

5) High temperature deposition (max 200° C) of a-Si:H by PECVD.

6) Liftoff in hot PG remover; standard photolithography for wiring lift-off; wiring deposition and lift-off.

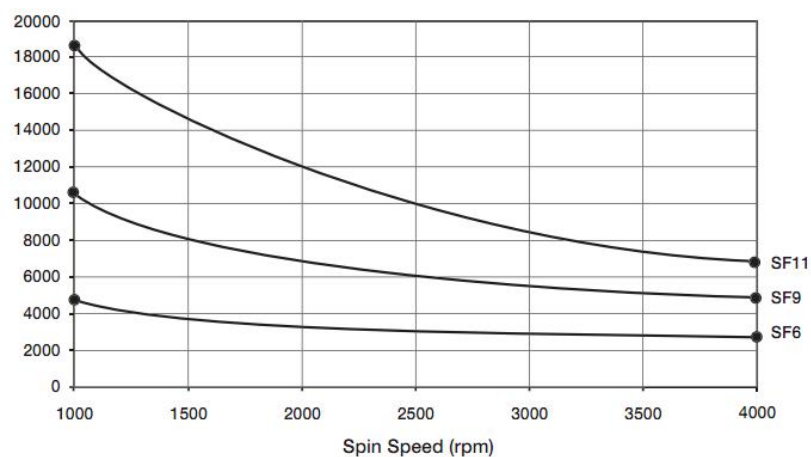


Figure 8.8: Spin speed versus PMGI thickness (in Å) for various solvent concentrations.

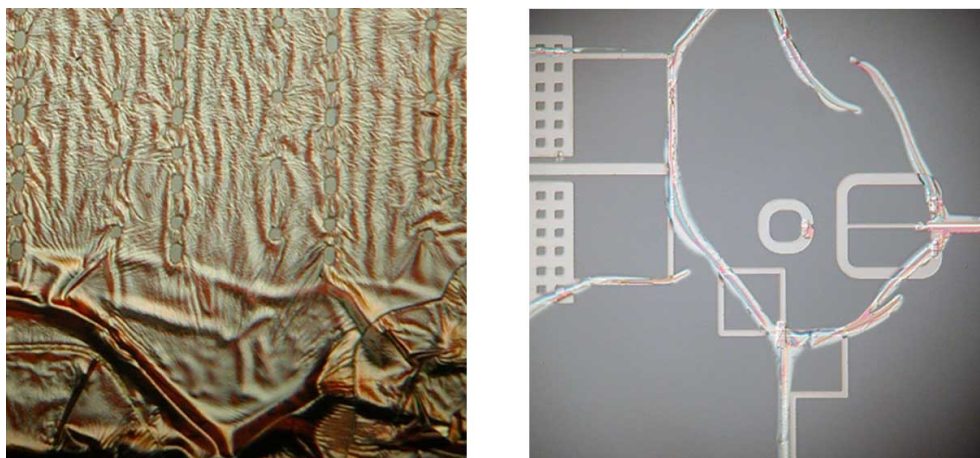


Figure 8.9: Left: Stressed niobium on an unstable surface. Right: a-Si:H deposited in the hard mask stress-fissurae.

concomitant optimization of the argon pressure during the Nb deposition: in fact, the Nb is sputtered on an unstable polymeric surface as PMGI and, thus, it is critical to be able to deposit stress-free niobium [226] on a more rigid surface (the results of an unsuccessful realization of this process is shown in Fig. 8.9).

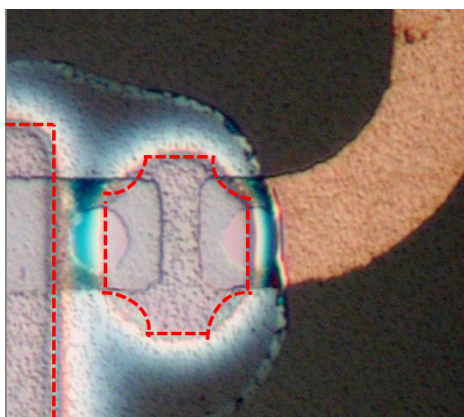


Figure 8.10: Consequences of over-developed PMGI at step 4. The a-Si:H "aprons" are in average 150 Å thick. The dashed line is the targeted deposition area.

On the other hand, step 4 required the optimization of the developing times for the PMGI layer. If the time is too small, polymeric residues will affect a-Si:H adhesion and quality, while if the time is too large, over-developed PMGI will allow the formation of lateral "aprons" of a-Si:H with a mean thickness of 150 Å (the results of an unsuccessful process realization of this is shown in Fig. 8.10).

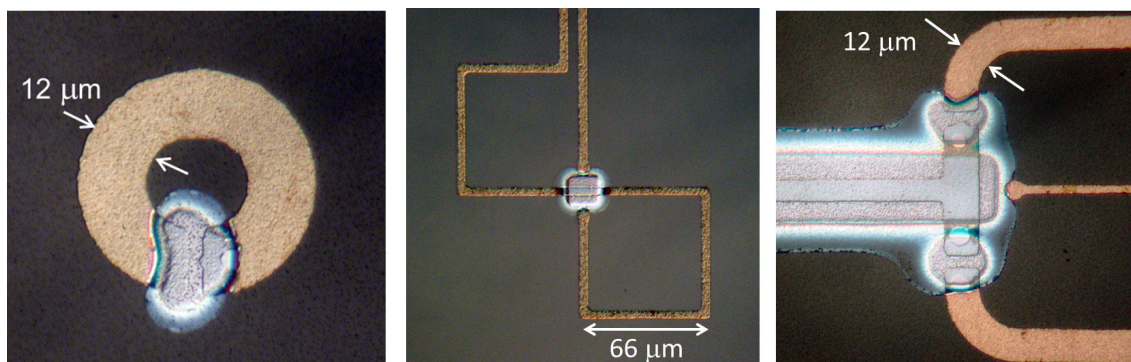


Figure 8.11: Details of the insulating regions for the qubit realization. Left: the rf SQUID junction insulator. Center: flux-bias wiring-crossover. Right: DC SQUID junctions and line insulation.

The maximum substrate-temperature during PECVD is $\sim 190^\circ\text{C}$, provided that the glass-transition temperature for PMGI resists is $T_g = 190^\circ\text{C}$.

In section 6.0.2, Fig. 8.6, we show that the NbN/AlN/NbN Josephson junctions could sustain the annealing during the high-temperature PECVD a-Si:H deposition, with no detrimental effects due to hydrogenation and, this is *per se* an exciting result.

8.5 Wiring

The concluding fabrication-steps are the photolithography and the sputter deposition of the wiring layer, followed by the lift-off process. Finally, the samples are completed (Fig. 8.12 and 8.13) and are ready to be characterized.

8.6 Preliminary Test of Fabricated Qubits

Some of the fabricated qubits were tested at 4.2 K in terms of the current-voltage curve of the read-out DC SQUID. Figure 8.14 shows the I-V characteristic of the three junctions of a NbN/AlN/NbN DC SQUID with SiO wiring insulator.

Moreover we also measured NbN/AlN/NbN junctions with a-Si:H wiring insulator.

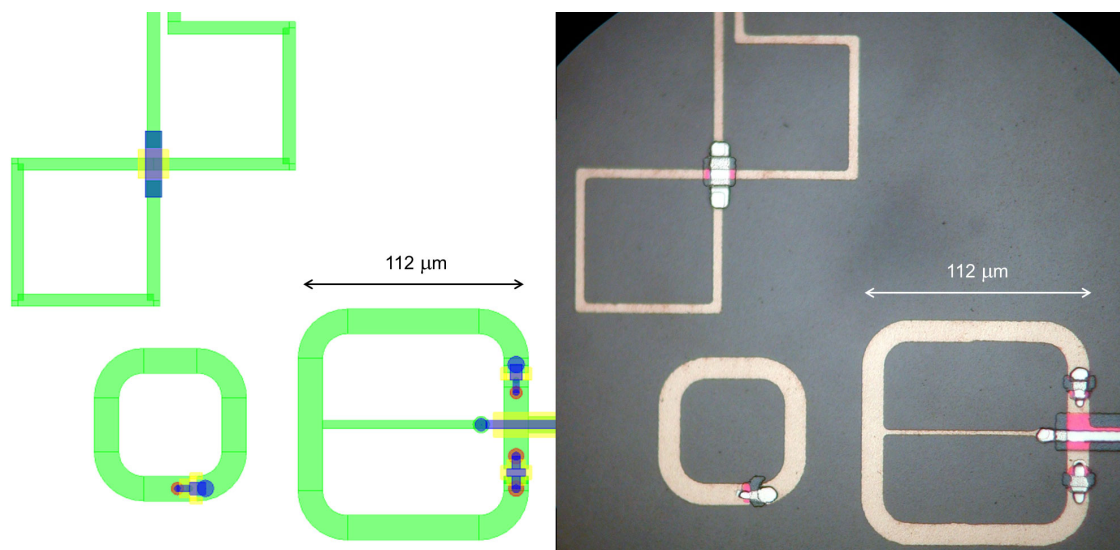


Figure 8.12: A complete NbN/AlN/NbN phase qubit, from the project to the realization.

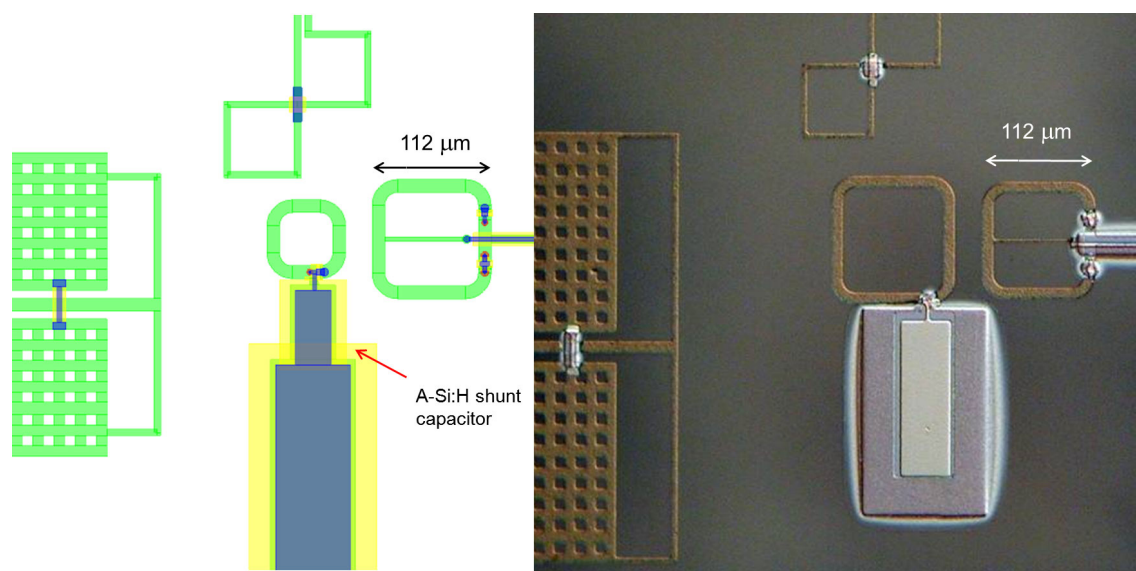


Figure 8.13: A complete NbN/AlN/NbN shunted phase qubit, from the project to the realization.

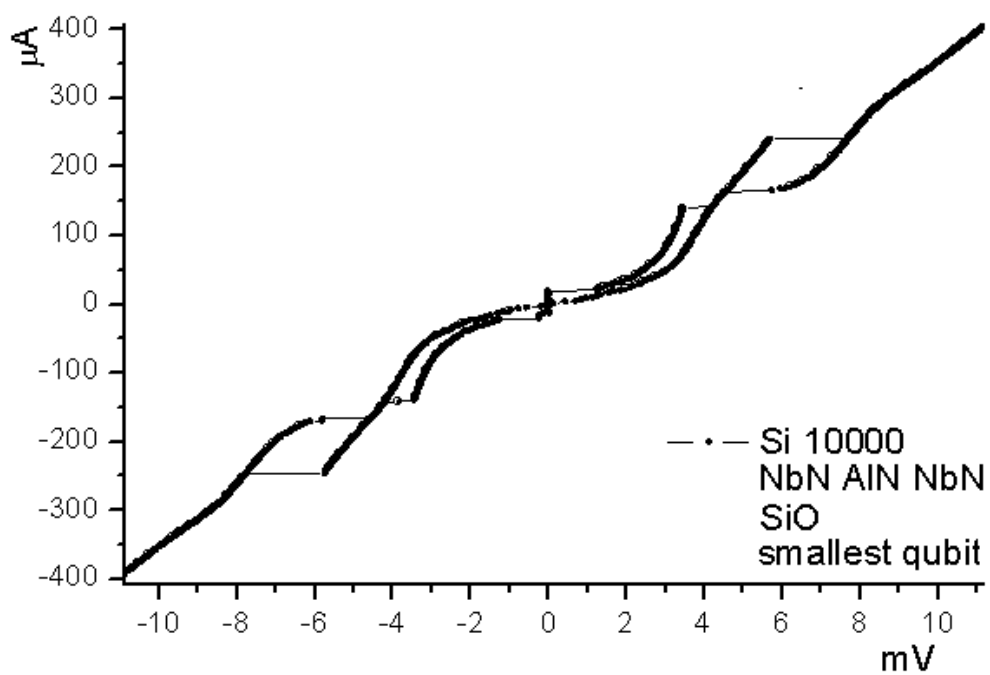


Figure 8.14: I-V characteristic of a read-out DC SQUID of a NbN/AlN/NbN DC SQUID fabricated on a Si (100) substrate and with SiO wiring insulator, measured at $T = 4.2$ K.

Thus, we demonstrated that the junction were still working after the a-Si:H PECVD at $\sim 150^\circ$ C. In Fig. 8.6 we compare the I-V curve of such a junction with the I-V curve of a NbN/AlN/NbN junction with SiO wiring insulator.

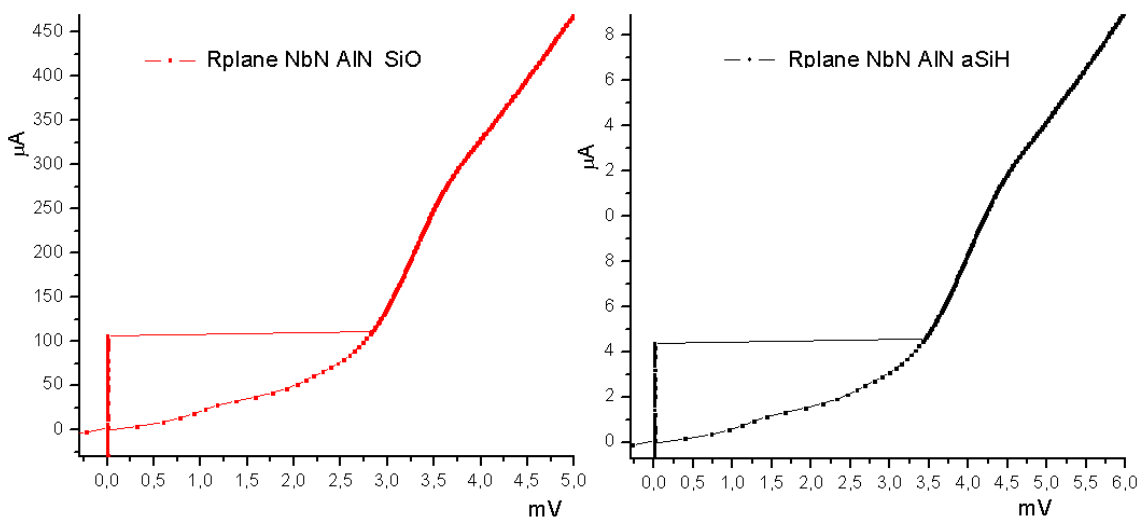


Figure 8.15: I-V characterization of two NbN/AlN/NbN junctions, having different diameter and wiring insulator, measured at $T = 4.2$ K. In red: $20 \mu\text{m}$ junction with SiO wiring insulator; in black: $6 \mu\text{m}$ junction with a-Si:H wiring insulator (after annealing at 250° C for 30 minutes and hydrogen contamination due to the PECVD process).

We note that the critical current densities were respectively: 34 A/cm^2 for the $20 \mu\text{m}$ NbN/AlN/NbN junction with SiO wiring insulator, and 16 A/cm^2 for the $6 \mu\text{m}$ NbN/AlN/NbN junction with a-Si:H wiring insulator, but the two junctions are from a different fabrication run.

Chapter 9

Conclusions

The research activity of the present thesis work was dedicated to the experimental investigation of materials (both dielectric and superconducting) involved in superconducting qubits based on Josephson tunnel junctions, with the final goal to improve the coherence time of these devices. To our best knowledge, a major intrinsic source of decoherence in superconducting qubits is the presence of microscopic defects [two-level states (TLSs) defects] in the dielectric materials utilized for their fabrication. Therefore the wiring crossover insulator, superconductor/insulator interfaces, and tunnel barrier were studied and optimized in order to reduce decoherence in the fabricated superconducting qubits.

Hydrogenated amorphous silicon (a-Si:H) is the dielectric material with the lowest dielectric losses ($\tan \delta$) among the known amorphous dielectrics (SiO, SiO₂, SiN_x), and it was chosen as the dielectric for the fabrication of the wiring-insulation layer. The deposition conditions of the a-Si:H fabricated by PECVD, *e.g.* different substrate temperatures and the SiH₄/H₂ ratio, were optimized in such a way to achieve the lowest dielectric losses. In order to characterize such losses, we used lumped-element LC superconducting resonators, which are reliable and powerful tools for the loss tangent characterization of any dielectric at the typical conditions at which a qubit device is operated, namely at low cryogenic temperatures (20 mK), microwave frequencies

(150 MHz-12 GHz), and low excitation power (10^{-7} - 10^{-3} V).

In order to measure the low $\tan \delta$ expected for the a-Si:H, the measurement set-up was improved: the initial measurements, performed in brass-housings, were somehow "limited" (by unknown reasons) to quality factor (Q_0) values lower than 9000, instead of the expected unloaded quality factor $Q_0 \sim 30000$ for such resonators at 4.2 K. Accurate simulations using Sonnet Electromagnetic Field Solver pointed out that the limiting factor had to be found in the sample housing and, in particular, in the choice of its constituting material. Simulations of the housing effect on the resonator's quality factor showed that the use of a superconducting housing reduces the housing influence to an absolute minimum. Test measurements of housings made of copper, and then of superconducting lead confirmed the necessity to utilize a superconductor as the housing material. Indeed, the very low losses in the a-Si:H resonators (as low as $\tan \delta = 2,5 \times 10^{-5}$ at the highest frequencies) were measured by using superconducting niobium housings.

For the resonator realization, the Nb technology was successfully incorporated with the a-Si:H PECVD process. The fabricated resonators have been characterized at $T = 4.2$ K, $T = 300$ mK, and $T = 20$ mK, while we studied the dependence of the dielectric loss on frequency, temperature and power. Experimental results on a-Si:H were compared to those on other investigated dielectrics (Nb_2O_5 , SiO, SiN_x).

In addition to the conventional RIE process for definition of the a-Si:H layer, a high temperature lift-off process based on the PMGI resist was developed and successfully applied for patterning the a-Si:H film. In fact, in order to realize high-quality superconducting resonators or qubits, it is preferable to reduce the dielectric coverage of the underlying superconductor, in order to limit the contamination of the superconducting surfaces by hydrogen and dielectric inclusions. In order to perform lift-off at the high-required temperature, we demonstrated that a PMGI/Nb bilayer, suitably patterned and conditioned, is capable of high temperature (up to 200° C) lift-off of a-Si:H. As a result, we developed a fabrication protocol that is suitable for both the resonators and the qubits fabrication.

The influence of the annealing at 250° C, and of the PECVD a-Si:H deposition on the superconducting and crystalline properties of a 20 nm thin Nb films was studied. By observing the correlation between the degradation of the superconducting Nb properties and the increase of the niobium lattice parameter (caused by oxygen and hydrogen diffusion), it was demonstrated that the predominant suppression mechanism for the Nb superconducting critical temperature (T_c) was the decomposition of the Nb native surface oxides, and the subsequent oxygen diffusion into the Nb bulk, due to the heating of the sample at 250° C.

Furthermore, in order to protect the superconductor's surfaces from the natural-oxide growth and from hydrogen diffusion, we developed and studied two surface protection methods: plasma nitridation, and deposition of a thin a-Si layer. We demonstrated that an *in situ* sputtered thin a-Si layer works well as a protective method against both the oxygen and hydrogen diffusion. Moreover, we found that the extent of the T_c suppression, caused by the annealing and by the complete PECVD process depends inversely on the Nb film thickness. This implies that for the 200 nm thick superconducting-wires present in the fabricated samples, the bulk superconducting properties will not be affected by the annealing, nor by the PECVD a-Si:H deposition.

Moreover, we demonstrated the feasibility of the integration of Nb and NbN Josephson junction technology with the a-Si:H dielectric as a wiring insulator. It is well known that passing from SiO to a-Si:H for wiring's insulators and capacitor's dielectric has dramatic effects in terms of the improvement of the qubit's coherence-times. Having demonstrated that the junctions could sustain the annealing during the high-temperature PECVD a-Si:H deposition, with no detrimental effects due to hydrogenation, is for us a considerable result. The conventional fabrication processes based on Nb/AlOx/Nb trilayer, incorporated with the a-Si:H deposited by PECVD, was improved and optimized in order to minimize the circuital loss sources. The main features of these optimizations were: the avoidance of any anodization step, the compatibility with a-Si:H PECVD technology for junction shunting capacitor and wiring

crossover insulator, the reduction of the dielectric area in contact with the superconductors, and the reduction of the wiring layer dimensions. We successfully tested at $T=4.2$ K the feasibility of all the mentioned improvements by realizing several Josephson Junctions, whose parameters were already optimized for the application in superconducting phase qubits.

In order to test qubits fabricated with material which differs from the traditional Nb/ AlO_x and Al/ AlO_x , we chose to develop the NbN/ AlN / NbN fabrication technology. NbN is considered as a promising material in order to increase the superconducting qubits coherence time, because it can be epitaxially grown at room temperature and, in addition, it is a superconducting material that forms a smaller amount of a native surface-oxide in comparison with Al and Nb, has a high superconducting transition temperature ($T_c \approx 17$ K), and has a large superconducting gap ($2\Delta = 5.9$ mV). We successfully fabricated Josephson junctions based on a NbN/ AlN / NbN trilayer, with the current-voltage characteristic suitable for preliminary qubit realization.

In order to improve both the surface properties of the NbN film and the interface between the NbN and the substrate, we compared the growth of NbN films on R-plane and on M-plane sapphire in terms of the superconducting properties and of the crystalline structure of those films (the latter was investigated by means of Θ - 2Θ X-ray diffraction, and rocking curve analysis). It was found that NbN films grown on M-plane sapphire were un-twined, in contrast with those grown on R-plane sapphire. As a result, the un-twined NbN film on M-plane sapphire allowed the growth of a 3 nm thin polycrystalline-AlN film, while in case of the NbN on R-plane sapphire, the AlN film with the same thickness was grown as an amorphous layer.

As an alternative junction barrier, in the context of NbN technology, we realized trilayers having SiN_x as tunnelling barrier, deposited by means of RF-reactive magnetron sputtering in Ar/N_2 atmosphere.

We designed highly-optimized superconducting phase qubit-layout in collaboration with the group of Prof. A. Ustinov at KIT, Germany. We fabricated a set of photolithographic masks containing both LC resonators and qubit devices in order to

characterize the losses of the LC resonators and the coherence times of the qubits in the same measurement, and to correlate the two phenomena at the same experimental conditions and within the same deposited dielectric material.

The fabrication protocol that we developed was flexible enough to allow the simultaneous fabrication of four kind of trilayer, in order to investigate the effects on the qubit coherence of a vast number of materials' combination. We realized qubits based on the following trilayers: Nb/AlO_x/Nb, NbN/AlN/NbN, NbN/SiN_x/NbN, Al/AlN/Al, both with SiO and a-Si:H as wiring crossover insulator. In this context, the developed high temperature (150° C) a-Si:H lift-off process was used to integrate the PECVD deposition of a-Si:H with Nb and NbN junction technologies, fulfilling the requirements of reduced dielectric coverage of the underlying superconducting films.

Some of the fabricated qubits were preliminary tested at $T = 4.2$ K, in terms of the measurement of the current-voltage curve of the DC SQUID read-out magnetometer. Working Josephson junction were observed for the NbN/AlN/NbN qubits, with a-Si:H wiring crossover deposited by the high-temperature a-Si:H lift-off process. This result confirmed the compatibility of the high-temperature a-Si:H lift-off process with the NbN junction fabrication technology.

Bibliography

- [1] E. Abrahams, Physical Review **107**, 491 (1957).
- [2] D.S. Abrams, and S. Lloyd, Phys. Rev. Lett. **83**, 5162 (1999).
- [3] D.S. Abrams, and C.P. Williams (1999), quant-ph/9908083v1
- [4] Aeroflex / Inmet Inc., Ann Arbor, MI 48103, U.S.A.,
<http://www.aeroflexinmet.com>
- [5] M.S. Allman, F. Altomare, J.D. Whittaker, K. Cicak, D. Li, A. Sirois, J. Strong, J.D. Teufel, and R.W. Simmonds, arXiv:1004.2738v1 (2010).
- [6] P.W. Anderson, B. I. Halperin, and C.M. Varma, Philos. Mag. **25**, 1 (1972).
- [7] M. Ansmann, H. Wang, R.C. Bialczak, M. Hofheinz, E. Lucero, M. Neeley, A.D. O'Connell, D. Sank, M. Weides, J. Wenner, A.N. Cleland, and J.M. Martinis, Nature **461**, 504 (2009).
- [8] C.Z. Antoine, and S. Berry, AIP Conf. Proc. **671**, 176 (2003).
- [9] W. Arnold, and S. Hunklinger, Phys. Acoust. **12**, 155 (1976).
- [10] O. Astafiev, Y.A. Pashkin, Y. Nakamura, T. Yamamoto, and J.S. Tsai, Phys. Rev. Lett. **96**, 137001 (2006).
- [11] J. Aumentado, M.W. Keller, J.M. Martinis, and M.H. Devoret, Phys. Rev. Lett. **92**, 066802 (2004).

- [12] M.C. Banuls, R. Orus, J.I. Latorre, A. Perez, and P. Ruiz-Femenia, *Phys. Rev. A* **73**, 22344 (2006).
- [13] R. Barends, J.J.A. Baselmans, J.N. Hovenier, J.R. Gao, S.J.C. Yates, T.M. Klapwijk, H.F.C. Hoevers, *IEEE Trans. Appl. Supercond.* **17**, 263 (2007).
- [14] R. Barends, H.L. Hortensius, T. Zijlstra, J.J.A. Baselmans, S.J.C. Yates, J.R. Gao, and T.M. Klapwijk, *Appl. Phys. Lett.* **92**, 223502 (2008).
- [15] R. Barends, H.L. Hortensius, T. Zijlstra, J.J.A. Baselmans, S.J.C. Yates, J.R. Gao, and T.M. Klapwijk, *IEEE Trans. Appl. Supercond.* **19**, 3 (2009).
- [16] R. Barends, N. Vercruyssen, A. Endo, P.J. de Visser, T. Zijlstra, T.M. Klapwijk, and J.J.A. Baselmans, *Appl. Phys. Lett.* **97**, 033507 (2010).
- [17] R. Barends, J. Wenner, M. Lenander, Y. Chen, R.C. Bialczak, J. Kelly, E. Lucero, P. O'Malley, M. Mariani, D. Sank, H. Wang, T.C. White, Y. Yin, J. Zhao, A.N. Cleland, J.M. Martinis¹, and J.J.A. Baselmans, *Appl. Phys. Lett.* **99**, 113507 (2011).
- [18] A. Barone, and G. Paternò, *Physics and Applications of the Josephson Effect*, Wiley, New York (1982).
- [19] D.A. Bennett, L. Longobardi, V. Patel, W. Chen, and J.E. Lukens, *Supercond. Sci. Technol.* **20**, S445 (2007).
- [20] A. Berkley, Ph.D. thesis, University of Maryland (2003).
- [21] A.J. Berkley, H. Xu, R.C. Ramos, M.A. Gubrud, F.W. Strauch, P.R. Johnson, J.R. Anderson, A.J. Dragt, C.J. Lobb, and F.C. Wellstood, *Science* **300**, 154 (2003).
- [22] D. Bermejo, and M. Cardona, *J. Non-Cryst. Sol.* **32**, 405 (1978).
- [23] P. Bertet, I. Chiorescu, G. Burkard, K. Semba, C.J.P.M. Harmans, D.P. DiVincenzo, and J.E. Mooij, *Phys. Rev. Lett.* **95**, 257002 (2005).

- [24] R.C. Bialczak, R. McDermot, M. Ansmann, H. Hofheinz, N. Katz, E. Lucero, M. Neeley, A.D. O'Connell, H. Wang, A.N. Cleland, and J.M. Martinis, *Phys. Rev. Lett.* **99**, 187006 (2007).
- [25] H. Bluhm, J.A. Bert, N.C. Koshnick, M.E. Huber, and K.A. Moler, *Phys. Rev. Lett.* **103**, 026805 (2009).
- [26] M.F. Bocko, A.M. Herr, and Feldman M.J., *IEEE Trans. Appl. Supercond.* **7**, 3638 (1997).
- [27] B.M. Boghosian, and W. Taylor, *Physica D* **120**, 30 (1998).
- [28] D. Bothner, T. Gaber, M. Kemmler, D. Koelle, and R. Kleiner, *Appl. Phys. Lett.* **98**, 102504 (2011)
- [29] V. Bouchiat, Ph.D. thesis, Université Paris VI (1997),
<http://www.drecam.cea.fr/drecam/spec/Pres/Quantro/>
- [30] V.B. Braginsky, and V.I. Panov, *IEEE Trans. Magn.* **15**, 30 (1979); V.B. Braginsky, V.S. Ilchenko, and K.S. Bagdassarov, *Phys. Lett. A* **120**, 300 (1987).
- [31] J.R. Bray, and L. Roy, *IEEE Proc. Microw. Antennas Propag.* **151**, 345 (2004).
- [32] A. Bruno, P. Mengucci, L.V. Mercaldo, and M.P. Lisitskiy, in preparation for *Appl. Phys. Lett.* (2011).
- [33] T. Byrnes, and Y. Yamamoto, *Phys. Rev. A* **73**, 022328 (2006).
- [34] G. Catelani, J. Koch, L. Frunzio, R.J. Schoelkopf, M.H. Devoret, and L.I. Glazman, *Phys. Rev. Lett.* **106**, 077002 (2011).
- [35] W. Chen, D.A. Bennett, V. Patel, and J.E. Lukens, *Supercond. Sci. Technol.* **21**, 075013 (2008).
- [36] J. Chen, E.D. Rippert, S.N. Song, M.P. Ulmer, and J.B. Ketterson, *J. Mater. Res.* **9**, 1678 (1994).

- [37] F. Chiarello, P. Carelli, M.G. Castellano, C. Cosmelli, L. Gangemi, R. Leoni, S. Poletto, D. Simeone, and G. Torrioli, *Supercond. Sci. Tech.* **18**, 1370 (2005).
- [38] A.M. Childs, E. Farhi, J. Goldstone, and S. Gutmann, *Quant. Info. Comp.* **2**, 181 (2002).
- [39] I. Chiorescu, Y. Nakamura, C.J.P.M. Harmans, and J.E. Mooij, *Science* **299**, 1869 (2003).
- [40] S. Choi, D.H. Lee, S.G. Louie, and J. Clarke, *Phys. Rev. Lett.* **103**, 197001 (2009).
- [41] K. Cicak, D. Li, J.A. Strong, M.S. Allman, F. Altomare, A.J. Sirois, J.D. Whittaker, J.D. Teufel, and R.W. Simmonds, *Appl. Phys. Lett.* **96**, 093502 (2010).
- [42] J.I. Cirac, and P. Zoller, *Nature* **404**, 579 (2000).
- [43] J.I. Cirac, and P. Zoller, *Phys. Rev. Lett.* **74**, 4091 (1995).
- [44] J. Clarke, and A. Braginski, *SQUID Handbook*, vol. 1, Wiley, New York (2004).
- [45] J.H. Cole, C. Müller, P. Bushev, G.J. Grabovskij, J. Lisenfeld, A. Lukashenko, A.V. Ustinov, and A. Shnirman, *Appl. Phys. Lett.* **97**, 252501 (2010).
- [46] M. Constantin, and C.C. Yu, *Phys. Rev. Lett.* **99**, 207001 (2007).
- [47] K.B. Cooper, M. Steffen, R. McDermott, R. Simmonds, S. Oh, D. Hite, D. Pappas, and J. Martinis, *Phys. Rev. Lett.* **93**, 180401 (2004).
- [48] D. Cory, A. Fahmy, and T. Havel, *Proc. Nat. Acad. Sci.* **94**, 1634 (1997).
- [49] N.A. Court, A.J. Ferguson, R. Lutchyn, and R.G. Clark, *Phys. Rev. B* **77**, 100501 (2008).
- [50] R. Cristiano, E. Esposito, L. Frunzio, M.P. Lisitskii, C. Nappi, G. Ammendola, A. Barone, L. Parlato, D.V. Balashov, and V.N. Gubankov, *Appl. Phys. Lett.* **74**, 3389 (1999).

- [51] P.K. Day, H.G. LeDuc, B.A. Mazin, A. Vayonakis, and J. Zmuidzinas, *Nature* **425**, 817 (2003).
- [52] M. Delheusy, A. Stierle, N. Kasper, R.P. Kurta, A. Vlad, H. Dosch, C. Antoine, A. Resta, E. Lundgren, and J. Andersen, *Appl. Phys. Lett.* **92**, 101911 (2008).
- [53] P. Delli Veneri, L.V. Mercaldo, and C. Privio, *Ren. Energy* **33**, 42 (2008).
- [54] P. Delli Veneri, and L.V. Mercaldo, Thin film Silicon Solar Cells, in *Thin film solar cells*, A. Bosio, A. Romeo, Nova Science Publishers Inc, New York (2011).
- [55] W. DeSorbo, *Phys. Rev.* **132**, 107 (1963).
- [56] R. de Sousa, *Phys. Rev. B* **76**, 245306 (2007).
- [57] D. Deutsch, *Proc. Roy. Soc. London A* **400**, 97 (1985).
- [58] P.J. de Visser, J.J.A. Baselmans, P. Diener, S.J.C. Yates, A. Endo, and T.M. Klapwijk, *Phys.Rev.Lett.* **106**, 167004 (2011).
- [59] M.H. Devoret, J.M. Martinis, and J. Clarke, *Phys. Rev. Lett.* **55**, 1908 (1985).
- [60] L. DiCarlo, J.M. Chow, J.M. Gambetta, L.S. Bishop, B.R. Johnson¹, D.I. Schuster, J. Majer, A. Blais, L. Frunzio, S.M. Girvin, and R.J. Schoelkopf, *Nature* **460**, 240 (2009).
- [61] D.P. DiVincenzo, *Fortsch. Phys.* **48**, 771 (2000).
- [62] D.P. DiVincenzo, *Science* **270**, 255 (1995).
- [63] S.K. Dutta, F.W. Strauch, R.M. Lewis, K. Mitra, H. Paik, T.A. Palomaki, E. Tiesinga, J.R. Anderson, A.J. Dragt, C.J. Lobb, and F.C. Wellstood, *Phy. Rev. B* **78**, 104510 (2008).
- [64] P. Dutta, and P.M. Horn, *Rev. Mod. Phys.* **53**, 497 (1981).

- [65] Eccosorb – Emerson & Cuming Microwave Products,
<http://www.eccosorb.com/resource-technical-notes.htm>
- [66] A. Ekert, and R. Jozsa, *Rev. Mod. Phys.* **68**, 733 (1996).
- [67] C. Enss, S. Hunklinger, *Low-Temperature Physics*, Springer, Berlin Heidelberg (2005).
- [68] J. Eroms, L.C. van Schaarenburg, E.F.C. Driessen, J.H. Plantenberg, C.M. Huizinga, R.N. Schouten, A.H. Verbruggen, C.J.P.M. Harmans, and J.E. Mooij, *Appl. Phys. Lett.* **89**, 122516 (2006).
- [69] R. Espiau de Lamaestre, Ph. Odier, and J.C. Villégier, *Appl. Phys. Lett.* **91**, 232501 (2007).
- [70] L. Faoro, and L.B. Ioffe, *Phys. Rev. Lett.* **96**, 047001 (2006).
- [71] L. Faoro, and L.B. Ioffe, *Phys. Rev. B* **75**, 132505 (2007).
- [72] L. Faoro, and L.B. Ioffe, *Phys. Rev. Lett.* **100**, 227005 (2008).
- [73] E. Farhi, J. Goldstone, S. Gutmann, J. Lapan, A. Lundgren, and D. Preda, *Science* **292**, 472 (2001).
- [74] Whiteley Research Inc., Sunnyvale, CA 94086, U.S.A.,
<http://www.wrcad.com/ftp/pub/fasthenry-3.0wr-setup.exe>
- [75] S.A. Fenner, and Y. Zhang, *Proc. 9th IC-EATCS Italian Conference on Theoretical Computer Science*, 215 (2005), [quant-ph/0408150](http://arxiv.org/abs/quant-ph/0408150).
- [76] R.P. Feynman, *Int. J. Theor. Phys.* **21**, 467 (1982).
- [77] V. Foglietti, W.J. Gallagher, M.B. Ketchen, A.W. Kleinsasser, R.H. Koch, S.I. Raider, and R.L. Sandstrom, *Appl. Phys. Lett.* **49**, 1393 (1986).
- [78] J.R. Friedman, V. Patel, W. Chen, S.K. Tolpygo, and J.E. Lukens, *Nature* **406**, 43 (2000).

- [79] L. Frunzio, A. Wallraff, D. Schuster, J. Majer, and R. Schoelkopf, *IEEE Trans. Appl. Supercond.* **15**, 860 (2005).
- [80] J. Gao, J. Zmuidzinas, B.A. Mazin, H.G. LeDuc, and P.K. Day, *Appl. Phys. Lett.* **90**, 102507 (2007).
- [81] J. Gao, M. Daal, A. Vayonakis, S. Kumar, J. Zmuidzinas, B. Sadoulet, B.A. Mazin, P.K. Day, and H.G. Leduc, *Appl. Phys. Lett.* **92**, 152505 (2008).
- [82] J. Gao, M. Daal, J.M. Martinis, A. Vayonakis, J. Zmuidzinas, B. Sadoulet, B.A. Mazin, P.K. Day, and H.G. Leduc, *Appl. Phys. Lett.* **92**, 212504 (2008).
- [83] N.A. Gershenfeld, and I.L. Chuang, *Science* **275**, 350 (1997).
- [84] G. Giovannetti, S. Kumar, A. Stroppa, J. van den Brink, S. Picozzi, and J. Lorenzana, *Phys. Rev. Lett.* **106**, 026401 (2011).
- [85] M.F. Goffman, R. Cron, A.L. Yeyati, P. Joyez, M.H. Devoret, D. Esteve, and C. Urbina, *Phys. Rev. Lett.* **85**, 170 (2000).
- [86] G.J. Grabovskij, J. Lisenfeld, A. Lukashenko, and A.V. Ustinov, in preparation (2011).
- [87] C. Granata, B. Ruggiero, M. Russo, A. Vettoliere, V. Corato, and P. Silvestrini, *Appl. Phys. Lett.* **87**, 172507 (2005).
- [88] C. Granata, A. Vettoliere, and M. Russo, *Appl. Phys. Lett.* **88**, 212506 (2006).
- [89] D. L. Griscom, *J. Non-Cryst. Solids* **73**, 51 (1985).
- [90] L.K. Grover, *Proc. Twenty-Eighth Annual ACM Symposium on the Theory of Computing*, 212 (1996), quant-ph/9605043.
- [91] M. Gurwitsch, W.A. Washington, and H.A. Huggins, *Appl. Phys. Lett.* **42**, 472 (1983).

- [92] G. Hammer, S. Wünsch, K. Ilin, M. Siegel, *Journal of Physics: Conference Series* **97**, 012044 (2008).
- [93] S. Haroche, M. Brune, and J.M. Raimond, *Phil. Trans. Roy. Soc. Lond. A* **355**, 2367 (1997).
- [94] M.A. Hein, D.E. Oates, P.J. Hirst, R.G. Humphreys, and A.V. Velichko, *Appl. Phys. Lett.* **80**, 1007 (2002).
- [95] F.H. Horn, and W.T. Zeigler, *J. Am. Chem. Soc.* **69**, 2762 (1947).
- [96] T. Hoss, C. Strunk, and C. Schonenberger, *Microel. Eng.* **46**,149 (1999).
- [97] A.A. Houck, J.A. Schreier, B.R. Johnson, J.M. Chow, J. Koch, J.M. Gambetta, D.I. Schuster, L. Frunzio, M.H. Devoret, S.M. Girvin, and R.J. Schoelkopf, *Phys. Rev. Lett.* **101**, 080502 (2008).
- [98] H. How, R.G. Seed, C. Vittoria, D.B. Chrisey, J.S. Horwitz, C. Corosella, and V. Folen, *IEEE Trans. Micro. Theo. and Tech.* **40**, 1668 (1992).
- [99] Huber+Suhner GmbH, D-82024 Taufkirchen, Germany,
<http://www.hubersuhner.de>
- [100] B.D. Hunt, H.G. LeDuc, S.R. Cypher, J.A. Stern, and A. Judas, *Appl. Phys. Lett.* **55**, 81 (1989).
- [101] T. Imamura, and S. Hasuo, *IEEE Trans. Mag.* **25**, 1119 (1989).
- [102] Intel Company, 2200 Mission College Blvd. Santa Clara, CA, USA
http://download.intel.com/newsroom/kits/22nm/pdfs/22nm-Details_Presentation.pdf
- [103] L.B. Ioffe, V.B. Geshkenbein, C.Helm, and G. Blatter, *Phys. Rev. Lett.* **93**, 057001 (2004).

- [104] G. Ithier, E. Collin, P. Joyez, P.J. Meeson, D. Vion, D. Esteve, F. Chiarello, A. Shnirman, Y. Makhlin, J. Schrie, and G. Schön, Phys. Rev. B **72**, 134519 (2005).
- [105] P. Jaksch, and A. Papageorgiou, Phys. Rev. Lett. **91**, 257902 (2003).
- [106] A.C. Johnson, J.R. Petta, J.M. Taylor, A. Yacoby, M.D. Lukin, C.M. Marcus, M.P. Hanson, and A. C. Gossard, Nature **435**, 925 (2005).
- [107] A.K. Jonscher, J. Phys. D: Appl. Phys. **32**, R57 (1999).
- [108] B.D. Josephson, Phys. Lett. **1**, 251 (1962).
- [109] Ch. Kaiser, S.T. Skacel, S. Wünsh, R. Dolata, B. Mackrodt, A. Zorin, and M. Siegel, Supercond. Sci. Technol. **23**, 075008 (2010).
- [110] B.E. Kane, Nature **393**, 133 (1998).
- [111] T. Kato, A.A. Golubov, and Y. Nakamura, Phys. Rev. B **76**, 172502 (2007).
- [112] M. Kenyon, C.J. Lobb, and F.C. Wellstood, J. Appl. Phys. **88**, 6536 (2000).
- [113] H.J. Kimble, M. Dagenais, and L. Mandel, Phys. Rev. Lett. **39**, 691 (1977).
- [114] A.Y. Kitaev, Tech. Rep. TR **96**, 3 (1996), quantph/9511026.
- [115] J. Koch, T.M. Yu, J. Gambetta, A.A. Houck, D.I. Schuster, J. Majer, A. Blais, M.H. Devoret, S.M. Girvin, and R.J. Schoelkopf, Phys. Rev. A **76**, 042319 (2007).
- [116] R.H. Koch, D.P. DiVincenzo, and J. Clarke, Phys. Rev. Lett. **98**, 267003 (2007).
- [117] R.H. Koch, J. Clarke, W.M. Goubau, J.M. Martinis, C.M. Pegrum, and D.J. van Harlingen, J. Low Temp. Phys **51**, 207 (1983).
- [118] R.H. Koch and R.J. Hamers, Surf. Sci. **181**, 333 (1987).

- [119] A.G. Kofman, Q. Zang, J.M. Martinis, and A. N. Korotkov, *Phys. Rev. B* **75**, 014524 (2007).
- [120] H.A. Kramers, and K.N.A. Wetenschap, *Proc. Acad. Sci. Amsterdam* **33**, 959 (1930).
- [121] H. Kroger, L.N. Smith, D.W. Jillie, J.B. Thaxter, R. Aucoin, L.W. Currier, C.N. Potter, D.W. Shaw, and P.H. Willis, *IEEE Trans. Mag.* **21**, 870 (1985).
- [122] V.A. Krupenin, D.E. Presnov, M.N. Savvateev, H. Scherer, A.B. Zorin, and J. Niemeyer, *J. Appl. Phys.* **84**, 3212 (1998).
- [123] S. Kumar, J. Gao, J. Zmuidzinis, B.A. Mazin, H.G. LeDuc, P.K. Day, *Appl. Phys. Lett.* **92**, 123503 (2008).
- [124] S. K. Lamoreaux, *Phys. Rev. Lett.* **78**, 5 (1997).
- [125] K.M. Lang, S. Nam, J. Aumentado, C. Urbina, and J.M. Martinis, *IEEE Trans. Appl. Supercond.* **13**, 2 (2003).
- [126] T. Lanting, A.J. Berkley, B. Bumble, P. Bunyk, A. Fung, J. Johansson, A. Kaul, A. Kleinsasser, E. Ladizinsky, F. Maibaum, R. Harris, M.W. Johnson, E. Tolkacheva, and M.H.S. Amin, *Phys. Rev. B* **79**, 060509 (2009).
- [127] D.P. de Lara, M.P. Lisitskiy, C. Nappi, and R. Cristiano, *Phys. Rev. B*, **73**, 214530 (2006).
- [128] V. Lefevre-Seguin, E. Turlot, C. Urbina, D. Esteve, and M.H. Devoret, *Phys. Rev. B*. **46**, 5507 (1992).
- [129] K.W. Lehnert, K. Bladh, L.F. Spietz, D. Gunnarsson, D.I. Schuster, P. Delsing, and R.J. Schoelkopf, *Phys. Rev. Lett.* **90**, 027002 (2003).
- [130] E.M. Levenson-Falk, R. Vijay, I. and Siddiqi, *Appl. Phys. Lett.* **98**, 123115 (2011).

- [131] D. Li, F.C.S. da Silva, D.A. Braje, R.W. Simmonds, and D.P. Pappas, *Appl. Phys. Lett.* **97**, 102507 (2010).
- [132] T. Lindström, J.E. Healey, M.S. Colclough, and C.M. Muirhead, *arXiv:0905.1481v1* (2009).
- [133] K.K. Likharev, *Rev. Mod. Phys.* **51**, 101 (1979).
- [134] M.P. Lisitskiy, C. Camerlingo, M. Salvato, A. Vecchione, and M. Russo, *Journal of Physics: Conference Series* **43**, 1135 (2006).
- [135] J. Lisenfeld, PhD Thesis, Universität Erlangen-Nürnberg (2007).
- [136] J. Lisenfeld, A. Lukashenko, M. Ansmann, J.M.Martinis, and A.V.Ustinov, *Phys. Rev. Lett.* **99**, 170504 (2007).
- [137] S. Lloyd, *Science* **273**, 1073 (1996).
- [138] L. Longobardi, S. Pottorf, V. Patel, and J.E. Lukens, *IEEE Trans. Appl. Supercond.* **17**, 88 (2007).
- [139] D. Loss, and D.P. DiVicenzo, *Phys. Rev. A* **57**, 120 (1998).
- [140] A. Lukashenko, and A.V. Ustinov, *Rev. Sci. Instrum.* **79**, 014701 (2008).
- [141] P. Macha, S.H.W. van der Ploeg, G. Oelsner, E. Il'ichev, and H.G. Meyer, *Appl. Phys. Lett.* **96**, 062503 (2010).
- [142] Y. Makhlin, G. Schön, and A. Shnirman, *Rev. Mod. Phys.* **73**, 357 (2001).
- [143] V.E. Manucharyan, J. Koch, L.I. Glazman, and M.H. Devoret, *Science* **326**, 113 (2009).
- [144] M. Mariantoni, H. Wang, T. Yamamoto, M. Neeley, R.C. Bialczak, Y. Chen, M. Lenander, E. Lucero, A.D. O'Connell, D. Sank, M. Weides, J. Wenner, Y. Yin, J. Zhao, A.N. Korotkov, A.N. Cleland, and J.M. Martinis, *Science* **334**, 61 (2011).

- [145] J.M. Martinis, S. Nam, J. Aumentado, and C. Urbina, Phys. Rev. Lett. **89**, 117901 (2002).
- [146] J.M. Martinis, S. Nam, J. Aumentado, K.M. Lang, and C. Urbina, Phys. Rev. B **67**, 094510 (2003).
- [147] J.M. Martinis, K.B. Cooper, R. McDermott, M. Steffen, M. Ansmann, K.D. Osborn, K. Cicak, S. Oh, D.P. Pappas, R.W. Simmonds, and C.C. Yu, Phys. Rev. Lett. **95**, 210503 (2005).
- [148] J.M. Martinis, M. Ansmann, and J. Aumentado, Phys. Rev. Lett. **103**, 097002 (2009).
- [149] J.M. Martinis, Quantum Inf. Process **8**, 81 (2009).
- [150] J.M. Martinis, M.H. Devoret, and J. Clarke, Phys. Rev. Lett. **55**, 1543 (1985).
- [151] D.C. Mattis, and J. Bardeen, Phys. Rev. **III**, 412 (1958).
- [152] R. McDermott, R.W. Simmonds, M. Steffen, K.B. Cooper, K. Cicak, K.D. Osborn, S. Oh, D.P. Pappas, and J.M. Martinis, Science **307**, 1299 (2005).
- [153] R. McDermott, IEEE Trans. Appl. Supercond. **19**, 2 (2009).
- [154] W.L. McMillan, Phys. Rev. **167**, 331 (1968).
- [155] T.H. Metzger, U. Schubert, and J. Peisl, J. Phys. F **15**, 779 (1985).
- [156] C. Monroe, D.M. Meekhof, B.E. King, W.M. Itano, and D.J Wineland, Phys. Rev. Lett. **75**, 4714 (1995).
- [157] J.E. Mooji, T.P. Orlando, L. Levitov, L. Tian, C.H. Van der Wal, and S. Lloyd, Science **285**, 1036 (1999).
- [158] J.E. Mooij, and C.J.P.M Harmans, New J. Phys. **7**, 219 (2005).

- [159] M. Mosca, and A. Ekert, Lecture Notes in Computer Science **1509**, 174 (1999), quantph/9903071.
- [160] M. Mück, M.Korn, C.G.A. Mugford, J.B.Kycia, and J. Clarke, Appl. Phys. Lett. **86**, 012510 (2005).
- [161] K. Munakata, T.H. Geballe, and M.R. Beasley, Phys. Rev. B **84**, 161405 (2011).
- [162] Y. Nakamura, Y.A. Pashkin, and J.S. Tsai, Phys. Rev. Lett. **87**, 246601 (2001).
- [163] Y. Nakamura, H. Terai, K. Inomata, T. Yamamoto, W. Qiu, and Z. Wang, Appl. Phys. Lett. **99**, 212502 (2011).
- [164] Y. Nakamura, Y.A. Pashkin, and J.S. Tsai, Nature **398**, 786 (1999).
- [165] M. Neeley, M. Ansmann, R.C. Bialczak, M. Hofheinz, N. Katz, E. Lucero, A.D. O'Connell, H. Wang, A.N. Cleland, and J.M. Martinis, Phys. Rev. B **77**, 180508 (2008).
- [166] M. Neeley, M. Ansmann, R.C. Bialczak, M. Hofheinz, N. Katz, E. Lucero, A.D. O'Connell, H. Wang, A.N. Cleland, and J.M. Martinis, Nature Physics **4**, 523 (2008).
- [167] K.L. Ngai, A.K. Jonscher, and C.T. White, Nature **277**, 185 (1979).
- [168] M.A. Nielsen, and I.L. Chuang, *Quantum Computation and Quantum Information*, Cambridge University Press, Cambridge, U.K. (2000).
- [169] A.D. O'Connell, M. Ansmann, R.C. Bialczak, M. Hogheinz, N. Katz, E. Lucero, C. McKenney, M. Neeley, H. Wang, E.M. Weig, A.N. Cleland, and J.M. Martinis, Appl. Phys. Lett. **92**, 112903 (2008).
- [170] S. Oh, K. Cicak, R. McDermott, K.B. Cooper, K.D. Osborn, R.W. Simmonds, M. Steffen, J.M. Martinis, and D.P. Pappas, Supercond. Sci. Technol. **18**, 1396 (2005).

- [171] S. Oh, K. Cicak, J.S. Kline, M.A. Sillanpää, K.D. Osborn, J.D. Whittaker, R.W. Simmonds, and D.P. Pappas, *Phys. Rev. B* **74**, 100502 (2006).
- [172] A. Oliva, R. Monaco, *IEEE Trans. Appl. Sup.* **4**, 1 (1994).
- [173] H. Paik, S.K. Dutta, R.M. Lewis, T.A. Palomaki, B.K. Cooper, R.C. Ramos, H. Xu, A.J. Dragt, J.R. Anderson, C.J. Lobb, and F.C. Wellstood, *Phys. Rev. B* **77**, 214510 (2008).
- [174] H. Paik, and K.D. Osborn, *Appl. Phys. Lett.* **96**, 072505 (2010).
- [175] H. Paik, D.I. Schuster, L.S. Bishop, G. Kirchmair, G. Catelani, A.P. Sears, B.R. Johnson, M.J. Reagor, L. Frunzio, L.I. Glazman, S.M. Girvin, M.H. Devoret, and R.J. Schoelkopf, *Phys. Rev. Lett.* Accepted for publication (2011).
- [176] E. Paladino, L. Faoro, G. Falci, and R. Fazio, *Phys. Rev. Lett.* **88**, 228304 (2002).
- [177] T.A. Palomaki, S.K. Dutta, R.M. Lewis, H. Paik, K. Mitra, B.K. Cooper, A.J. Przybysz, A.J. Dragt, J.R. Anderson, C.J. Lobb, and F.C. Wellstood, *IEEE Trans. Appl. Sup.* **17**, 162 (2007).
- [178] D.P. Pappas, M.R. Vissers, D.S. Wisbey, J.S. Kline, and J. Gao, *IEEE ASC Conference Series* **1**, (2010).
- [179] V. Patel, W. Chen, S. Pottorf, and J.E. Lukens, *IEEE Trans. Appl. Supercond.* **15**, 117 (2005).
- [180] U. Patel, S. Sendelbach, J. Kline, D.P. Pappas, M. Weides, J.M. Martinis, R. McDermott, American Physical Society meeting, abstract Y26.00014, May (2010).
- [181] J. Pettersson, P. Wahlgren, P. Delsing, D.B. Haviland, T. Claeson, N. Rorsman, and H. Zirath, *Phys. Rev. B* **53**, R13272 (1996).

- [182] G. Pfeiffer, and H. Wipf, J. Phys. F **6**, 167 (1976).
- [183] H. Pfeiffer, PhD Thesis, Munich University (1976).
- [184] W.A. Phillips, *Amorphous Solids: Low-Temperature Properties*, Springer, New York (1981).
- [185] W.A. Phillips, J. Low Temp. Phys. **7**, 351 (1972).
- [186] W.A. Phillips, Reports on Progress in Physics **50**, 1657 (1987).
- [187] P.M. Platzman, M.I. Dykman, Science **284**, 1967 (1999).
- [188] R.O. Pohl, X. Liu, and E.J. Thompson, Rev. Mod. Phys. **74**, 991 (2002).
- [189] V. Polushkin, Nuclear Electronics. Superconducting Detectors and Processing Techniques, John Wiley & Sons Ltd. (2004).
- [190] V. Privman, I.D. Vagner, and G. Kventsel, Phys. Letters A **239**, 141 (1998).
- [191] A.J. Przybysz, H. Kwon, R. Budoyo, B.K. Cooper, E. Crowe, A.J. Dragt, J.R. Anderson, C.J. Lobb, and F.C. Wellstood, IEEE Trans. Appl. Supercond. **21**, 867 (2011).
- [192] E.M. Purcell, Phys. Rev. **69**, 681 (1946).
- [193] W. Qiu, Ph.D. thesis, University of Kansas (2007).
- [194] T.L. Robertson, Ph.D. Thesis, University of California, Berkely (2005).
- [195] C.T. Rogers, and R.A. Buhrman, Phys. Rev. Lett. **53**, 1272 (1984).
- [196] R. Rouse, S. Han, and J.E. Lukens, Phys. Rev. Lett. **75**, 1614 (1996).
- [197] E. Sarnelli, G. Testa, D. Crimaldi, A. Monaco, M. Adamo, and M.A. Navacerada, IEEE Trans. Appl.Sup. **15**, 2 (2005).

- [198] J. Schneider, A. Anders, B. Hjörvarsson, I. Petrov, K. Macák, U. Helmersson, and J.E. Sundgren, *Appl. Phys. Lett.* **74**, 200 (1999).
- [199] S. Sendelbach, D. Hover, A. Kittel, M. Mück, J.M. Martinis, and R. McDermott, *Phys. Rev. Lett.* **100**, 227006 (2008).
- [200] M.D. Shaw, R.M. Lutchyn, P. Delsing, and P.M. Echternach, *Phys. Rev. B* **78**, 024503 (2008).
- [201] T. Shiota, T. Imamura, and S. Hasuo, *J. Appl. Phys.* **70**, 6958 (1991).
- [202] T. Shiota, T. Imamura, and S. Hasuo, *Appl. Phys. Lett.* **61**, 1228 (1992).
- [203] T. Shiota, T. Imamura, and S. Hasuo, *Appl. Phys. Lett.* **60**, 3051 (1992).
- [204] A. Shnirman, G. Schön, I. Martin, and Y. Makhlin, *Phys. Rev. Lett.* **94**, 127002 (2005).
- [205] A. Shnirman, G. Schn, and Z. Hermon, *Phys. Rev. Lett.* **79**, 2371 (1997).
- [206] P.W. Shor, *Proc. 35th Annual Symposium on Foundations of Computer Science*, 124 (1994).
- [207] R. Simmonds, K. Lang, D.A. Hite, S. Nam, D.P. Pappas, and J. Martinis, *Phys. Rev. Lett.* **93**, 0770031 (2004).
- [208] R. Simmonds, K. Lang, D.A. Hite, S. Nam, D.P. Pappas, and J.M. Martinis, *Phys. Rev. Lett.* **93**, 0770031 (2004).
- [209] S. Skacel, *Diplomarbeit, Institut für Mikro- und Nanoelektronische Systeme and Physikalisches Institut, Karlsruher Institut für Technologie (KIT)* (2010).
- [210] C.P. Slichter, *Principles of Magnetic Resonance*, Springer, Berlin (1996).
- [211] A.H.M. Smets, J.H. van Helden, and M.C.M. van de Sanden, *Mater. Res. Soc. Symp. Proc.* **664**, A22.4.1 (2001).

- [212] C. Song, T.W. Heitmann, M.P. Defeo, K. Yu, R. McDermott, M. Neeley, J.M. Martinis, and B.L.T. Plourde, *Phys. Rev. B* **75**, 174512 (2009).
- [213] C. Song, M.P. Defeo, K. Yu, B.L.T. Plourde,
- [214] Sonnet [©], 3D Planar High-Frequency Electromagnetic Software,
<http://www.sonnetsoftware.com>
- [215] A.T. Sornborger, and E.D. Stewart, *Phys. Rev. A* **60**, 1956 (1999).
- [216] M. Steffen, M. Ansmann, R.C. Bialczak, N. Katz, E. Lucero, R. McDermott, M. Neeley, E.M. Weig, A.N. Cleland, and J.M. Martinis, *Science* **313**, 1423 (2006).
- [217] M. Steffen, M. Ansmann, R. McDermott, N. Katz, R.C. Bialczak, E. Lucero, M. Neeley, E.M. Weig, A.N. Cleland, and J.M. Martinis, *Phys. Rev. Lett.* **97**, 050502 (2006).
- [218] M. Steffen, F. Brito, D. DiVincenzo, S. Kumar, and M. Ketchen, *New J. Phys.* **11**, 033030 (2009).
- [219] R.B. Stephens, *Phys. Rev. B* **8**, 2896 (1973).
- [220] U. Strom, M. von Schickfus, S. Hunklinger, *Phys. Rev. Lett.* **41**, 910 (1978).
- [221] V. Subramaniam, and P. Ramadevi (2002), [quant-ph/0210095](https://arxiv.org/abs/quant-ph/0210095)
- [222] T. Szkopek, V. Roychowdhury, and E. Yablonovitch, *Phys. Rev. A* **72**, 62318 (2005).
- [223] A. Taylor, and N.J. Doyle, *J. Less-Common Metals* **13**, 313 (1967).
- [224] C. Tesche, K. Brown, A. Callegari, M. Chen, J. Greiner, H. Jones, M. Ketchen, K. Kim, A. Kleinsasser, H. Notarys, G. Proto, R. Wang, and T. Yogi, *IEEE Trans. Mag* **21**, 1032 (1985).

- [225] M. Tinkham, *Introduction to Superconductivity*, 2nd ed., McGraw-Hill, New York (1996).
- [226] K. Tsukada, J. Kawai, G. Uehara, and H. Kado, *IEEE Trans. App. Sup.* **3**, 2944 (1993).
- [227] tx line – AWR Corporation,
<http://web.awrcorp.com/Usa/Products/Optional-Products/TX-Line/>
- [228] Vacuumschmelze GmbH & Co. KG, D-63450 Hanau,
<http://www.vacuumschmelze.de>
- [229] L.M.K. Vandersypen, M. Steffen, G. Breyta, C.S. Yannoni, M.H. Sherwood, and I.L. Chuang, *Nature* **414**, 883 (2001).
- [230] C.H. van der Wal, A.C.J. ter Haar, F.K. Wilhelm, R.N. Schouten, C.J.P.M. Harmans, T.P. Orlando, S. Lloyd, and J.E. Mooij, *Science* **290**, 773 (2000).
- [231] C. van der Wal, F. Wilhelm, C. Harmans, and J. Mooij, *Eur. Phys. J. B* **31**, 111 (2003).
- [232] D.J. Van Harlingen, T.L. Robertson, B.L.T. Plourde, P.A. Reichardt, T.A. Crane, and J. Clarke, *Phys. Rev. B* **70**, 064517 (2004).
- [233] N. Vercruyssen, R. Barends, T.M Klapwijk, J.T. Muhonen, M. Meschke, *Appl. Phy. Lett.* **99**, 062509 (2011).
- [234] R. Vijay , J.D. Sau, M.L. Cohen, and I. Siddiqi, *Phys. Rev. Lett.* **103**, 087003 (2009).
- [235] R. Vijay, E.M. Levenson-Falk, D.H. Slichter, and I. Siddiqi, *Appl. Phys. Lett.* **96**, 223112 (2010).
- [236] V.M. Vinokur, T.I. Baturina, M.V. Fistul, A.Y. Mironov, M. Baklanov, and Ch. Strunk, *Nature* **452**, 613 (2008).

- [237] D. Vion, A. Aassime, A. Cottet, P. Joyez, H. Pothier, C. Urbina, D. Esteve, and M.H. Devoret, *Science* **296**, 886 (2002).
- [238] E.H. Visscher, S.M. Verbrugh, J. Lindeman, P. Hadley, and J.E. Mooij, *Appl. Phys. Lett.* **66**, 3 (1995).
- [239] M.R. Vissers, J. Gao, D.S. Wisbey, D.A. Hite, C.C. Tsuei, A.D. Corcoles, M. Steffen, and D.P. Pappas, *Appl. Phys. Lett.* **97**, 232509 (2010).
- [240] M. von Schickfus, and S. Hunklinger, *J. Phys. C* **9**, L439 (1976).
- [241] R.V. Voss, and R.A. Webb, *Phys. Rev. Lett.* **47**, 265-8 (1981).
- [242] A. Wallraff, D.I. Schuster, A. Blais, L. Frunzio, R.S. Huang, J. Majer, S. Kumar, S.M. Girvin, and R.J. Schoelkopf, *Nature* **431**, 162 (2004).
- [243] H. Wang, M. Hofheinz, J. Wenner, M. Ansmann, R.C. Bialczak, M. Lenander, E. Lucero, M. Neeley, A.D. O'Connell, D. Sank, M. Weides, A.N. Cleland, and J.M. Martinis, *Appl. Phys. Lett.* **95**, 233508 (2009).
- [244] S. Weber, K.W. Murch, D.H. Slichter, R. Vijay, I. Siddiqi, *Appl. Phys. Lett.* **98**, 172510 (2011).
- [245] W. Qui, Y. Yu, B. Mao, S. Li, and S. Han, *IEEE Trans. Appl. Supercond.* **19**, 977 (2009).
- [246] M.B. Weissman, *Rev. Mod. Phys.* **60**, 537 (1988).
- [247] F.C. Wellstood, C. Urbina, and J. Clarke, *Appl. Phys. Lett.* **85**, 5296 (2004).
- [248] F.C. Wellstood, C. Urbina, and J. Clarke, *Appl. Phys. Lett.* **50**, 772 (1987).
- [249] T. Wirth, J. Lisenfeld, A. Lukashenko, and A.V. Ustinov, *arXiv:1010.0954v1* (2010).
- [250] D.S. Wisbey, J. Gao, M.R. Vissers, F.C.S. da Silva, J.S. Kline, L. Vale, and D.P. Pappas, *J. Appl. Phys.* **108**, 093918 (2010).

- [251] C.D. Wiseman, J. Appl. Phys., **37** 3599 (1966).
- [252] P. Wocjan, and J. Yard (2006), quant-ph/0603069
- [253] T. Yamamoto, Y.A. Pashkin, O. Astafiev, Y. Nakamura, and J.S. Tsai, Nature **425**, 941 (2003).
- [254] F. Yoshihara, K. Harrabi, A.O. Niskanen, Y. Nakamura, and J.S. Tsai, Phys. Rev. Lett. **97**, 167001 (2006).
- [255] Y. Yu, S. Han, X. Chu, S. Chu, and Z. Wang, Science **296**, 889-92 (2002).
- [256] R.C. Zeller, and R.O. Pohl, Phys. Rev. B **4**, 2029 (1971).
- [257] Q. Zhang, A.G. Kofman, J. Martinis, and A.N. Korotkov, Phys. Rev. B **74**, 2145181 (2006).
- [258] J. Zimmermann, and A. Silver, Phys. Rev. **157**, 317 (1967).
- [259] G. Zimmerli, T.M. Eiles, R.L. Kautz, and J.M. Martinis, Appl. Phys. Lett. **61**, 237 (1992).
- [260] A.B. Zorin, F.J. Ahlers, J. Niemeyer, T. Weimann, H. Wolf, V.A. Krupenin, and S.V. Lotkhov, Phys. Rev. B **53**, 13682 (1996), and references therein.